Multivariate B-Spline Scheduling for Linear Parameter Varying Model

Sasho Angelovski

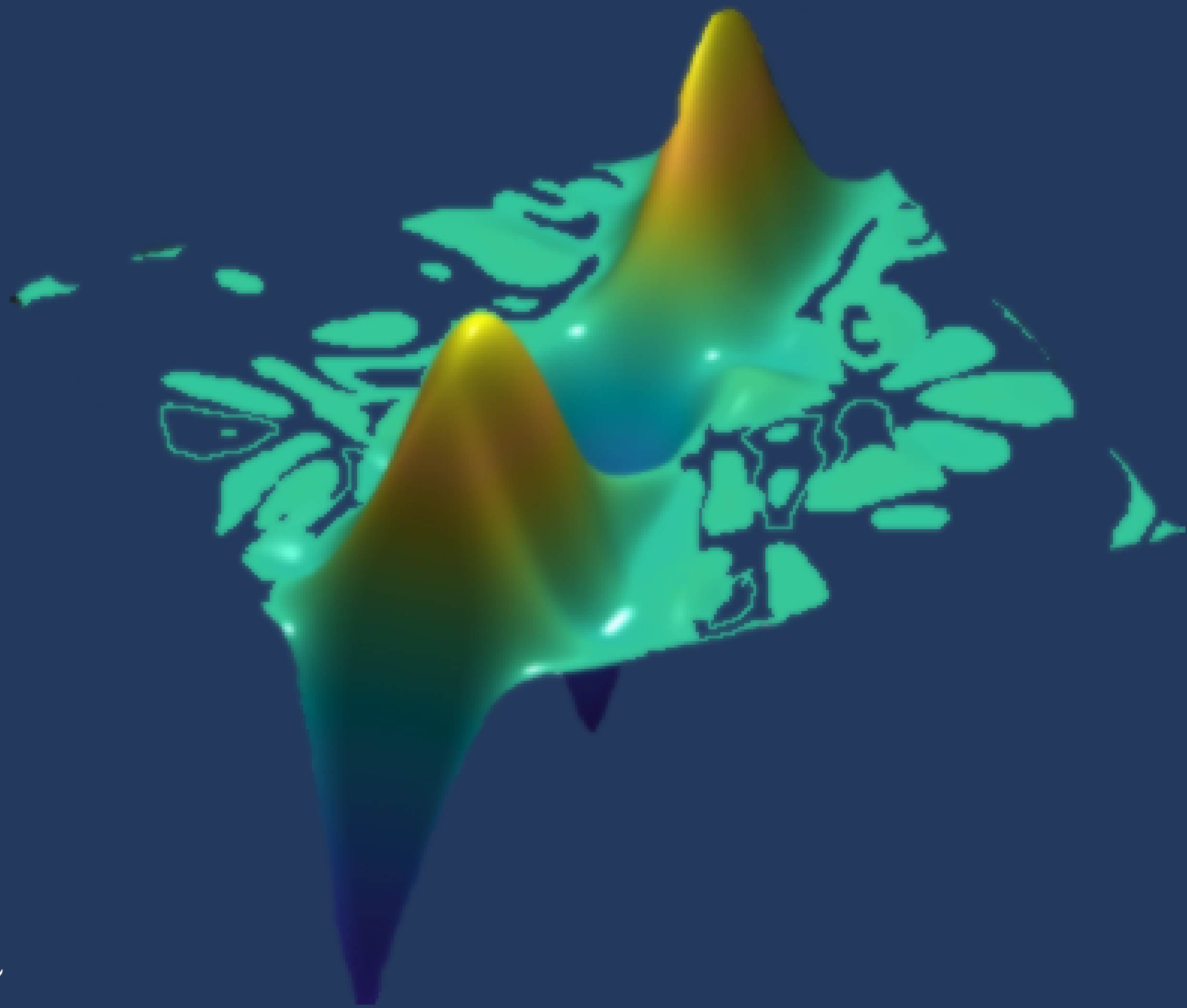

TU Delft

Multivariate B-Spline Scheduling for Linear Parameter Varying Model

MSc Thesis report

by

Sasho Angelovski

to obtain the degree of Master of Science
at the Delft University of Technology
to be defended publicly on April 09, 2025 at 13:00

Thesis committee:	
Chair:	Dr.Ir. E.van Kampen
Supervisor:	Dr.Ir. C.C. de Visser
External examiner:	Dr. S. Wang
Place:	Faculty of Aerospace Engineering, Delft
Project Duration:	October, 2024 - April, 2025
Student number:	4055403

An electronic version of this thesis is available at `http://repository.tudelft.nl/`.

Faculty of Aerospace Engineering · Delft University of Technology

Preface

This Master thesis marks the culmination of a significant chapter in my life. During a period of global world uncertainty, I made the decision to pursue and complete my academic journey, an endeavor that has remained an important goal on my personal and professional agenda. Finishing this project, which at one point seemed distant, has brought a deep sense of accomplishment and, hopefully, will provide momentum for future personal endeavors. Throughout this work, my goal has been to bridge two domains: Robust control in the form of Linear Parameter Varying (LPV) systems and System identification with multivariate simplex B-splines, a pursuit that has proven to be highly challenging. I hope that the insights presented here will contribute to future research in this field and aid in the development of next-generation controllers, enhancing the performance and autonomy of aerospace vehicles.

I would like to express my sincere gratitude to my supervisor, Dr. Ir. C.C. de Visser, whose guidance and encouragement have been key in expanding my knowledge and enabling me to successfully complete this project, despite my initial limited familiarity with some of its topics. I owe my deepest gratitude to my mother, Snezhana, for her unconditional support and motivation on my path to becoming an academically accomplished individual, an aspiration I have always had, inspired by her example. I would like to thank Silvia for being by my side throughout this journey, as well as my family, friends and colleagues for their support and encouragement during one of the most challenging but satisfying projects of my life.

SAGR. Tali [facili da intendersi] sono tutte le cose vere, doppo che son trovete; ma il punto sta nel saperle trovare.[1]

- Galileo Galilei, ”Dialogo sopra i due massimi sistemi” -

Tuesday 25th March, 2025 — *Sasho Angelovski*
Veldhoven, The Netherlands

[1] So [easy to understand] are all truths, once they are discovered; the point is in being able to discover them.[Stilmann Drake transl., p.225]

Summary

This study had a main task to investigate the use of Linear Parameter-Varying (LPV) models to approximate nonlinear and time-varying system dynamics by interpolating multiple Linear Time-Invariant (LTI) models through a smooth multi variable scheduling function. Furthermore, it investigates the effectiveness of multivariate simplex B-splines as such scheduling function within a specific type of LPV models, namely State-Space quasi-LPV (SS-qLPV) models. These B-splines offer a global approximation using local basis functions, ensuring smooth transitions across the system's operating range which make them a very good candidate for such application. Additionally, the level of smoothness is determined by the continuity conditions, which represent a parameter that can be freely selected when working with splines.

In Part I, the main research article has been constructed where an application of an SS-qLPV representation to an Inverted Pendulum on a Cart Model (IPCM) in an open-loop setting is created. The scheduling parameters used are the cart's velocity and the pendulum's angle. Multiple scheduling function estimation methods are compared, including piecewise-constant Zero-Order Hold (ZOH), polynomial uni- and multi-variate Ordinary Least Squares (OLS), and multivariate simplex B-splines. The findings indicate that B-splines achieve better approximation accuracy than polynomial methods at the same polynomial order, as shown by lower root mean squared error (RMSE) values. However, under broader simulation conditions, LPV-ZOH can be computationally less demanding and sometimes results in lower RMSE, despite its discontinuities at switching points, which may affect closed-loop performance.

In Part II, the literature review conducted for this study is shown in detail, that also researches the feasibility of the approach to a highly non-linear aircraft model of the Innovative Control Effectors (ICE) aircraft. It shows the existing research of constructing LPV model of ICE and shows the ways a multivariate simplex B-spline function can be incorporated as a scheduling function. This review has also indicated the gap in the current state of litertature, such that multivariate simplex splines have not been considered as a scheduling function. A review of the literature shows that tensor-product, cubic splines, and single-variable splines have been commonly applied. However, simplex-based triangulation offers a more efficient and adaptive representation of the scheduling parameter space for multivariate B-spline approximations in nonlinear systems.

In Part III, additional results from the study are explored, including a preliminary Linear Quadratic Regulator (LQR) control scheme applied in a closed-loop setting of the LPV model of the IPCM. This section highlights the trade-offs between different scheduling function methods and suggests further research on optimizing simplices for enhanced performance. This topic is also addressed in Part I, where it is noted that optimization of scheduling grid is needed for open-loop results, noting Constrained Delaunay Triangulation (CDT) or Type I/II hypercube triangulation method as proposed techniques. As discussed in Part III, the closed-loop performance grid of scheduling parameters differs significantly from that of the open-loop, highlighting the need for further simplex optimization, which is recommended for future research.

Contents

Nomenclature

List of Abbreviations

AMT All-moving tips

ARX Autoregressive model (AR) with an exogenous input (X)

BLUE Best Linear Unbiased Estimator

BMI Bilinear Matrix Inequality

CA Control Allocation

CGI Cascaded Generalized Inverse

CT Continuous-time

DI Dynamic Inversion

DOF Degree of freedom

DT Discrete-time

DynCA Dynamic Control Allocation

ECGLS Equality Constrained Generalized Least Squares

ECOLS Equality Constrained Ordinary Least Squares

ELE Elevons

EOM Equations of motion

GLS Generalized Least Squares

ICE Innovative Control Effectors

iLEF Inboard Leading Edge Flap

INCA Incremental Nonlinear Control Allocation

IPCM Inverted Pendulum on a Cart Model

IQC Integral Quadratic Constraint

KKT Karush-Kuhn-Tucker

LFT Linear Fractional Transformation

LMI Linear Matrix Inequality

LPV Linear Parameter Varying

LPV-A Affine Linear Parameter Varying

LPV-IO Linear Parameter Varying Input-Output

LPV-SS Linear Parameter Varying State-Space

LQR Linear Quadratic Regulator

LSQ Least Squares

LTI Linear Time Invariant

LTV Linear Time Varying

MC Monte Carlo

MIMO Multi-Input Multi-Output

MLTI Multi Linear Time Invariant

MPC Model Predictive Control

ODE Ordinary Differential Equation

oLEF Outboard Leading Edge Flap

OLS Ordinary Least Squares

PF Pitch Flaps

PID Proportional-Integral-Derivative

qLPV quasi - Linear Parameter Varying

RMSE Root Mean Square Error

SIMO Single-Input Multi-Output

SISO Single-Input Single-Output

SS State-Space

SSD Spoiler Slot Deflector

TV (P&Y) Thrust Vectoring (Pitch & Yaw)

WLS Weighted Least Squares

WPI Weighted Pseudo Inverse

ZOH Zero-Order Hold

List of Symbols

α Angle of attack (deg)

β Angle of sideslip (deg)

δ^*	Generalized control or moment command vector
δ_i	Control Effector deflection
$\nu(t)$	Virtual control input
Ω	Angular velocity
ϕ	Roll angle (deg)
ψ	Yaw angle (deg)
$\rho_d(k)$	Discrete-time scheduling signal
$\tilde{q}$	Dynamic pressure (N/m^2)
$\underline{u}$	Control input vector
C_i	Dimensionless moment coefficient
$E(X_i)$	Absolute error per dynamic state
M	Mach number
$M_{\text{uni}}/M_{\text{multi}}$	Optimal Uni/Multi-variate polynomial degree
N_{pts}	Optimal number of scheduling points
p	Roll rate (deg/s)
q	Pitch rate (deg/s)
r	Yaw rate (deg/s)
T	Thrust vector
u	Forward velocity component (m/s)
$u_d(k)$	Discrete-time input
V	True airspeed (m/s)
v	Sideways velocity component (m/s)
w	Vertical velocity component (m/s)
X_i	Dynamic state vector
$y_d(k)$	Sampled output
$\hat{\lambda}$	Lagrange multiplier initial estimate
$\hat{\Theta}$	Linear regression estimator
$\hat{c}_p$	Physical coefficients vector
$\hat{d}$	Total number of valid permutations
κ	Multi-index
Λ	Transformation matrix
$\mathcal{K}(\rho(t))$	Nonlinear terms matrix
$\mathcal{T}_J$	Triangulation of J simplices
ν_i	Non-degenerate vertex
$\overline{X}$	Linear regression matrix function
ρ_i	Scheduling parameter
Σ	Residual covariance matrix
σ	Noise standard deviation
σ^2	Variance of the residual
$\tilde{\nu}_{i,j}$	Out-of-edge vertex
$\zeta(t)$	Scheduled states vector
$A(\rho)$	Linear matrix parameter varying state function
B	Global regression matrix
$B(\rho)$	Linear matrix parameter varying input function
$B(x)$	Control effectiveness matrix
B^+	Pseudo-inverse of the control effectiveness matrix
$B_{\text{lin}}(x)$	Linear control effectiveness matrix
b_i	Barycentric coordinates
B_{t_J}	Per-simplex regression matrix
$C(\rho)$	Linear matrix parameter varying output function
c^{t_J}	Per-simplex B-coefficient vector
d	Polynomial degree
$D(\rho)$	Linear matrix parameter varying feed-forward function
g_i	Normalized interpolation scheduling functions
$H(t)$	Heaviside step function
J_{lqr}	Quadratic performance index
n	Spline dimension
N_θ	Set of LTI models
S_u	Selector function of input vector
S_x	Selector function of state vector
T_d	Discrete sampling interval (s)
u_i	Physical control surface deflections
W	Constant noise scaling matrix
$W(t)$	Non-Scheduled states vector

List of Figures

List of Tables

1 Introduction

In a constantly growing and evolving aerospace industry, the need for enhancing safety, efficiency, performance and autonomy of aerospace vehicles enables the development of control architectures that remain robust to uncertainties. In the cases where failure or damage occurs, the aircraft model radically changes, which makes it unfeasible to use a single controller to guarantee stability and performance. This has been realised ever since 1970, where the focus has been switched to multi-variable feedback methods, that recognize the importance of model uncertainties which, in turn, induce limits on the control performance [1]. Complex aerodynamic interactions in high-performance aircraft involve significant nonlinear changes of the aerodynamic model in terms of aerodynamic forces and moments, large spectrum of speeds, and operation at high angles of attack where stall and post-stall behaviors significantly impact their control and stability. This enables them to operate close to their aerodynamic limits at the expense of increased control complexity, such as a high number of control inputs vs. measured outputs, increased computational load, and sophisticated control algorithms. When the full flight envelope is considered, a method is needed to guarantee stability and robustness over its entirety (globally stable) and should enable multi-objective, multiple-input multiple-output (MIMO) controller designs [2].

A well-established framework for describing dynamical systems is provided in the form of Linear Time-Invariant (LTI) systems, which constitute a fundamental basis for control design. LTI models are extensively researched, and while they can approximate nonlinear systems well, L.Ljung explains that as the number of data points increases, the uncertainties in LTI systems, when estimated in Bode/Nyquist plots, converge to zero [3]. Furthermore, the region of validity of the linear model might be exceeded with changes in the operating conditions, resulting in poor performance [4]. Other clear shortcomings of LTI systems come from the fact that complex nonlinear systems show position or operating condition-dependent dynamics [5], such as is the case for high performance aircraft with sudden changes in operating conditions in typical mission flight profiles.

One way to overcome these limitations is the use of more advanced control approaches, such as Linear Parameter Varying (LPV) that require specifying the parameter dependence on the scheduling variables over a wide envelope. Using LPV systems instead of LTI or Linear-Time-Varying (LTV) systems is based on the causal knowledge of the system's dynamics. In the LPV framework, the causal relationship between the scheduling variables and the plant enables to customize the controller dynamics to account for variations in the plant's characteristics [6]. This dependency can take various forms - affine, polynomial, rational, piece-wise etc. Choosing the appropriate structure is crucial to avoid under/over-fitting and structural biases, that would obstruct the handling of dynamic and complex environments effectively. As demonstrated in [2], LPV control synthesis allows a guarantee for stability and performance for all parameter trajectories within the bounds outlined by the scheduling parameter. LPV approach models the aircraft dynamics as a set of (LTI) systems, each corresponding to an equilibrium point (trim point). Individual linear controllers are then designed at these operating points and interpolated based on the current flight parameters in order to obtain a global solution. The interpolating fitting function, such as a least-squares (LSQ) multi-variable polynomial (as in [7]), or B-splines (as in [8]) can be used, in an improvised manner, to interpolate between these trim points in order to form a global model, which is closely related to local-linear-modeling framework [4]. It has been shown in [8], that the B-splines structure effectively handles piecewise polynomial parameterizations of both the LPV system and the optimization variables, enabling more accurate modeling compared to polynomial or LSQ parametrization. Multivariate simplex splines, as indicated in [9], facilitate local model identification, in a way that they exhibit high approximation power and allow for flexible selection of continuity order such that a smooth dependence of the LPV systems on the scheduling function is achieve while at the same time creating a global model.

To analyze the complexities of high performing aircraft, a statically unstable, tailless and over-actuated (with highly non-linear control effectiveness matrix) aircraft, such as the Innovative Control Effectors (ICE), is used. It is part of a research project, which is a collaboration between the Control & Simulation (of TU Delft Aerospace Engineering faculty) division and Lockheed-Martin Skunkworks, which aims to explore new flight control and control allocation methodologies. What makes this project challenging is that the ICE fighter aircraft has 13 axis-coupled control effectors, shown in Figure 3.5, that are strongly redundant, and more importantly, also non-linearly influence each others functions. Thus the model possesses a unique actuator configuration, with a highly non-linear control effectiveness matrix that is also more sensitive to sources of uncertainties than conventional aircraft. The control effort required to manage all these actuators simultaneously is very high and makes it impossible for a pilot to manage with manual control. Additionally, the lack of a vertical tail reduces both directional stability and control authority, leading to tightly coupled and highly nonlinear dynamics, where yaw motion is coupled with pitch. This complex coupling necessitates that controllers account for the aircraft's dynamics across all three axes simultaneously [10].

A way to manage control effector redundancies is to use non-linear control allocation approaches that requires the ICE aerodynamic model to be parametrized using multivariate splines. This is due to the assumption that conventional control allocation methods use linear relationship between control actuator positions and control-induced forces and moments. However, this performance is insufficient for tailless aircraft such as the ICE, as discussed in [11]. Multivariate spline approaches have already been researched at Control & Simulation, and include a multivariate simplex B-spline aerodynamic model [12] and a multivariate simplotope B-Spline model [13], [14] of the ICE aircraft. They provide efficient means to fit scattered data on non-rectangular domains, as indicated in [15], which should make them good candidates for a development of a scheduling function for a LPV system.

First, a study on the effectiveness of multi-variable LPV system, using multivariate splines as a scheduling function, which should eventually provide robustness to the non-affine system dynamics of the selected model has to be made. This should unravel the research gap that currently exists in this field and is supported by relevant literature in Chapter 3. Succeeding, is the Preliminary Research Methodology described in Chapter 4, which explains the models being used for the rest of the thesis and is subdivided into: LPV Model Selection in 4.1, selection of spline basis function in 4.2 and the ICE aerodynamic model in 4.3. Additionally Section 4.4, explains the example to IPCM where this methodology is demonstrated. In Chapter 5 additional results are presented, which should support the main work done in Part I. Finally, conclusions and are drawn in Chapter 6 and recommendations for future research in Chapter 7.

1.1. Research Objective

The main objective of this research is to investigate the connection between a robust method of nonlinear control, which leverages the well-established Linear-Time-Invariant (LTI) system framework to solve non-linear problems, known as the Linear Parameter Varying (LPV) method, and the potential of using global nonlinear model identification method based on multivariate splines, as a scheduling function of the LPV model. Multivariate simplex B-splines show potential for better performance than existing polynomial based methods, while still using standard parameter estimation techniques in a linear regression setting.

A suitable candidate for this comparison is the application on a highly non-linear, non-conventional aerodynamic model of Innovative Control Effectors (ICE) aircraft. Multivariate Spline formulations for the aerodynamic model on ICE have already been created in previous work in Control & Simulation department ([12], [13], [14]), but research on connecting this model with a robust global control method such as LPV is absent. However, to first understand the concepts of LPV models on a non-linear model and the combination with multivariate splines as scheduling function a suitable demonstrator is needed. As shown in Part I, the inverted pendulum on a cart model (IPCM) serves as a widely studied example due to its nonlinear dynamics, which closely aligns with real-world control challenges and present complexity in the application of robust control models, such as LPV, with an additional complexity coming from the application of multivariate simplex B-splines. Researching both LPV and B-spline methodologies already constitutes a substantial body of work, and for the purposes of this study, the IPCM provides an adequate and representative system for analysis.

Therefore, the main research statement reflects the goal of this thesis, which is shown below.

Research Objective

How can a Linear Parameter Varying (LPV) control method combined with a multivariate simplex B-spline scheduling function address the gap in connecting robust control methods with the complex, non-affine dynamic models?

To answer this question, the main research directions need to be split into smaller sub-questions in a way that they are relevant, anchored and precise to the research study and are formulated in the next Section.

1.2. Research Questions

The answer to the first research question leads to the development of a LPV model for non-affine dynamic model that allows the use of a global nonlinear model identification method based on multivariate splines.

Research Question 1

What form of LPV mathematical model is applicable to a non-affine dynamic model that can guarantee a certain level of robustness?

With the subsequent questions derived as follows:

1.1 How can the LPV model be parameterized to obtain full state predictions of the dynamics of the non-affine model?

1.2 What model LPV structure can be used to enable the application of multivariate splines?

1.3 What validation methods should be employed to ensure that the identified LPV model meet requirements?

The second research question is related with the model identification of the non-linear model with multivariate simplex splines, and how can it be combined with a global LPV model.

Research Question 2

How does the application of multivariate splines enhance the accuracy of the LPV model in predicting the performance of a non-affine system across varying operating regimes?

With the subsequent questions derived as follows:

2.1 How do multivariate splines compare to polynomial methods in terms of root mean square error (RMSE) in parameter estimation?

2.2 What is the impact of parameter variability over the entire operating range on the accuracy of spline-based LPV models?

1.3. Research Approach

To answer the first research question, several steps need to be taken to develop an applicable mathematical model for the true global LPV. They are indicated as follows:

- Starting from the non-affine dynamic model, a set of model states based on the model's Equations of Motion that approximate the longitudinal and lateral dynamics need to be derived.
- Based on these equations, a set of scheduling states needs to be selected, whose combination can also constrain the operating envelope of the model.
- Explore different forms of global LPV models (e.g.,State-Space, Input/Output LPV representations) that can be applied to the non-linear model.

- ▷ Creation of linearized rigid body models, evaluated at the set of operating points of the scheduled parameter of the operating envelope, in order to obtain a set of LTI models of the non-linear system that can be interpolated to form a global LPV model.
- ▷ Identify key parameters (scheduling variables, parameter grid) that influence the non-affine behavior and consider their uncertainty in order to evaluate robustness of the LPV model. Evaluation of whether the fidelity of the model will be affected if some parameters are relaxed.
- ▷ *Specific for implementation of the ICE model:* A determination of the type of control allocation that can be implemented needs to be done. Simplifying the ICE model to longitudinal/lateral motion, with limited inputs, as done in literature is an effective way to asses the model.
- ▷ The type of basis functions and polynomial structures for the model, to enable the comparison with multivariate simplex splines, needs to be determined.
- ▷ The data generated will need to be split into separate identification and validation datasets, with a specific split ratio to make sure that the validation set contains sufficient dynamics. Several model validation methods can be employed such as analysis of model residuals and parameter co-variances or B-coefficient bounds: $p(x) = \{\text{min}(\hat{c}), \text{max}(\hat{c})\}$.

For the answer of the second research question, the following steps need to be determined:

- ▷ Numerical simulations using both multivariate simplex spline models and polynomial models have to be performed and Root-Mean-Squared-Error for both methods across various operating points in the operating envelope needs to be compared.
- ▷ To assess how perturbations in spline parameters affect the approximation error of the spline-based LPV model, it is essential to identify and analyze key parameters such as the spline dimension, spline degree, continuity near the spline edges and the triangulation settings in terms of number of datapoints and size of grid.
- ▷ A trade-off needs to be conducted between these spline-specific parameters and the critical parameters of the LPV model across the specified operating envelope to evaluate their impact on model performance. Model performance should show how effectively the system's model predicts the real system's behavior, focusing on model accuracy, response time and error minimization.
- ▷ Estimation of the size and type of scheduling grid spanned by the scheduling variables also needs to be determined. By varying the scheduling parameter grid, the accuracy of the spline-based approximation to the true LPV model, as well as the system's response to reference inputs can be examined.

Part I

Scientific Article

Multivariate B-Spline Scheduling for Linear Parameter Varying Model

S. Angelovski*
Delft University of Technology, 2629HS Delft, The Netherlands

Linear Parameter-Varying (LPV) models provide means to approximate complex, nonlinear, and time-varying system dynamics using a set of Linear Time-Invariant (LTI) models, interpolated by a scheduling function to ensure smooth transitions across the system's operating envelope. This study demonstrates that multivariate simplex B-splines can serve as such function, evaluated for State-Space quasi-LPV (SS-qLPV) models by providing a global approximation using local basis functions. The Inverted Pendulum on a Cart Model (IPCM) is used as a demonstrator in an open-loop setting, with an affine LPV representation based on cart velocity and pendulum angle as scheduling parameters. Several scheduling function estimation methods: piecewise-constant Zero-Order Hold (ZOH), polynomial uni and multi-variate Ordinary Least Squares (OLS), and multivariate simplex B-splines are evaluated. Results indicate that, at the same polynomial order, B-splines show higher approximation capabilities compared to polynomial methods, as shown by the root mean squared error (RMSE) of the residuals. However, under broader simulation conditions, LPV-ZOH can be computationally less expensive and can achieve lower RMSE, although piecewise constant methods have discontinuities at the switching points, which can have an impact to closed-loop performance. The study highlights trade-offs in scheduling function selection and suggests future research in optimizing simplices for improved performance. Applying B-spline scheduling functions with gain scheduled controllers in closed-loop control is the next direction for increasing control performance in complex, high-dimensional systems.

Nomenclature

α = pendulum angular acceleration (rad/s^2)
$\hat{\lambda}$ = lagrange multiplier initial estimate
$\hat{d}$ = total number of valid permutations
$\mathcal{T}_J$ = triangulation of J simplices
v = cart velocity (m/s)
v_i = non-degenerate vertex
Ω = pendulum angular velocity (rad/s)
ω_n = pendulum natural frequency (s^{-1})
ρ_i = scheduling parameter
θ = pendulum angle (rad)
θ_{00} = initial pendulum angle (rad)
$\tilde{v}_{i,j}$ = out-of-edge vertex
a = cart's acceleration (m/s^2)
A_m = amplitude of input force (N)
b = friction coefficient
b_i = barycentric coordinates
C^r = continuity order
d = polynomial degree
h = fixed time step (s)
J = total number of simplices
l = length of pendulum rod (m)
M = mass of cart (kg)
m = mass of pendulum bob (kg)
N_ρ = number of data points per parameter
N_{sim} = number of simulations
T_d = discrete sampling interval (s)
T_{sim} = simulation time (s)
X = cart position (m)

*MSc Student, Control and Simulation Division, Faculty of Aerospace Engineering, Kluyverweg 1, 2629HS Delft, The Netherlands, s.angelovski@student.tudelft.nl

I. Introduction

LINEAR Parameter Varying (LPV) models have gained considerable attention in the field of control systems over the past two decades, due to their ability to approximate nonlinear dynamics, while utilizing the well-established framework of Linear Time-Invariant (LTI) systems. They extend the LTI framework to systems whose dynamics depend on measurable, time-dependent parameters known as scheduling variables, by introducing a scheduling function that interpolates the locally linearized LTI models, in order to form a global solution to the entire operating regime [1]. This approach enables LPV models to capture the local dynamics represented by LTI systems while adapting to changing operating conditions. If a true LPV system exhibits smooth dependence on its scheduling parameter, its overall parameter-dependent model can be directly reconstructed from identified local models, highlighting the importance of having a smooth and continuous interpolation function, as noted in [2]. Since LPV models maintain convexity in the parameter space, sparse data can make this challenging. In particular, sparse data makes it difficult to ensure smoothness, especially when interpolating across regions with limited data points. Moreover, there is a risk of overfitting the available data, leading to a model that becomes sensitive to small variations in the local data points, which can result in unrealistic or unstable behavior. Searching for modeling techniques that provide smooth dependence of the scheduling parameters, flexibility, and approximation power, the use of multivariate simplex B-splines is examined. B-Splines, particularly piecewise polynomial splines, are used to model smooth, non-linear relationships between scheduling variables and system parameters. They allow local control over the operating envelope by dividing the domain into intervals (simplices) and fitting a polynomial function within each interval. This posses the question to be answered in this paper: *How can a Linear Parameter Varying (LPV) control method combined with a multivariate simplex B-spline scheduling function address the gap in connecting robust control methods with the complex, non-affine dynamic models?*

The modeling of LPV systems using multivariate B-splines is insufficiently researched as manifested by existing literature. In [3], tensor-product polynomial splines are used to parameterize Lyapunov functions and reduce the infinite-dimensional parameter-dependent LMI problem to a finite-dimensional form via LMI relaxations. However, this approach assumes that all state-space matrices depend on a single parameter through tensor-product splines, which limits its application to systems with structured, grid-based data. For scattered data or continuous physical systems, tensor-product splines are not well suited [4]. Cubic splines have been applied in [5] for LPV modeling of an arm-driven inverted pendulum, with a simplification of two dependent scheduling variables, by keeping one variable fixed. Despite improved performance for some variables, cubic splines require nonlinear optimization and struggle with C^1 discontinuities, exhibiting similarities to Gibbs' phenomenon of Fourier series [6]. Simplex splines, however, address discontinuities by adjusting the triangulation density [4]. In [7] a general B-spline-based LPV modeling approach is presented with strategies for knot optimization, which leads to reduced model complexity for univariate splines. Yet, the extension to multivariate B-splines has the same tensor-product limitations as in [3]. Simplex-based triangulation should enable efficient and adaptive scheduling parameter space representation of multivariate B-spline approximations for nonlinear systems.

In terms of application, a linearized LPV model is derived and estimated using a multivariate B-spline model, which is then applied to a case study involving a two-variable inverted pendulum on a cart. This example demonstrates the efficacy of B-spline-based LPV modeling in capturing nonlinear system dynamics with improved flexibility and accuracy compared to piecewise constant or polynomial least squares methods. The inverted pendulum on a cart serves as a simplified nonlinear control problem similar to aircraft dynamic models, making it a promising tool for future aerospace applications.

This paper is outlined as follows: The methodology is explained in Sections II and III, where a brief theory and overview on LPV models and multivariate B-splines is provided, concluding with the explanation of the global LPV Model and ways to approximate it using spline spaces. Section IV, shows the experiment setup of the applied LPV model and goes in detail to estimate it using multivariate B-splines. In Section V the results are described.

II. Linear Parameter Varying Model Representation

Linear Parameter-Varying (LPV) systems represent a class of linear systems with state-space descriptions that are functions of time-varying parameters. These parameters possess causal dependence on the trajectory of their time-varying values and affect the system dynamics in a way that allows the system to capture nonlinear behaviors or time-varying characteristics through a linear representation. The general continuous-time state-space representation of an LPV system is shown in Equation 1[8].

$$G(\rho) : \begin{cases} \dot{x}(t) = A(\rho)x(t) + B_1(\rho)\omega(t) + B_2(\rho)u(t) \\ z(t) = C_1(\rho)x(t) + D_{11}(\rho)\omega(t) + D_{12}(\rho)u(t) \\ y(t) = C_2(\rho)x(t) + D_{21}(\rho)\omega(t) + D_{22}(\rho)u(t) \end{cases} \tag{1}$$

where $x(t) \in \mathbb{R}^{n_x}$, $y(t) \in \mathbb{R}^{n_p}$, $u(t) \in \mathbb{R}^{n_m}$, $z(t) \in \mathbb{R}^{n_z}$ are the state, output, input and controlled output vectors respectively. The term $\omega(t)$ contains the exogenous inputs. The linear matrix functions $A \subset \mathbb{R}^{n_x \times n_x}, B \subset \mathbb{R}^{n_x \times n_\omega}, C \subset \mathbb{R}^{n_y \times n_x}, D \subset \mathbb{R}^{n_y \times n_\omega}$ depend on the parameter space:

$$\mathcal{P} := \left\{\rho := [\rho_1, \rho_2, ..., \rho_k]^T \in \mathbb{R}^k, \rho_i \in \left[\ \underline{\rho_i}, \overline{\rho_i}\right] \forall i = 1, ..., n_\rho\right\}$$

which represents the set of k-dimensional vectors where each element ρ_i is bounded by its respective lower $\underline{\rho_i}$ and upper limits $\overline{\rho_i}$. The vector $\rho \in \mathbb{R}^{n_\rho}$ has dimension n_ρ and consists of the measurable varying parameters that belong to $\mathcal{P}$. Depending on the type of system, the different possibilities of the varying parameters are indicated in Table 1.

Condition	**Function**	**System Type**
ρ is constant	$\rho = c$	Linear Time-Invariant (LTI)
ρ has variation with time known explicitly	$\rho = \rho(t)$	Linear Time-Varying (LTV)
ρ varies with internal system states	$\rho = \rho(x(t))$	Quasi-Linear Parameter-Varying (qLPV)
ρ is an external parameter	$\rho = \rho_e(t)$	Linear Parameter-Varying (LPV)

Table 1. Classification of systems based on the behavior of the varying parameter ρ.

A. Quasi-LPV Representation

Quasi-Linear Parameter Varying (qLPV) systems are suitable for modeling physical systems due to their ability to closely represent the nonlinear dynamics by internal state dependent parameters. In many aerospace applications, quasi-LPV (qLPV) models are preferred because they allow for the derivation of a linearized structure that includes the internal state varying parameters. This reduces the complexity of the nonlinear model and enables the application of more straightforward control strategies [9].

Selection of a qLPV model, changes the structure of the general LPV description, from Equation 1, by first dividing the state vector $x(t)$ into scheduling $\zeta(t)$ and non-scheduling states $W(t)$ as shown:

$$x(t) = \begin{bmatrix} \zeta(t) & W(t) \end{bmatrix}^T$$

Since the varying parameter trajectory (or scheduling map) $\rho(t)$ is endogenous rather than exogenous, $\omega(t)$ in Equation 1 can be assumed to be a part of the scheduling variable vector, when written in qLPV form, without the loss of generality, as described in [10]. An additional simplification can be made by neglecting the controlled output $z(t)$. Since the LPV model is being analyzed in open-loop (see Figure 1), the primary focus is on the system's internal dynamics and outputs, making $z(t)$ not relevant to the analysis. Therefore the general qLPV model is derrived and shown with Equation 2.

$$G(\rho(x(t))) : \begin{cases} \dot{\zeta}(t) = A_{11}(\rho(t))\zeta(t) + A_{12}(\rho(t))W(t) + B_1(\rho(t))u(t) \\ \dot{W}(t) = A_{21}(\rho(t))\zeta(t) + A_{22}(\rho(t))W(t) + B_2(\rho(t))u(t) \\ y(t) = C_1(\rho(t))\zeta(t) + C_2(\rho(t))W(t) + D(\rho(t))u(t) \end{cases} \tag{2}$$

In Figure 1, the block diagram of qLPV model is depicted, where a feedback loop between the LPV model and the scheduling map $\rho(t)$ exist in terms of the scheduled states $\zeta(t)$ and inputs u.

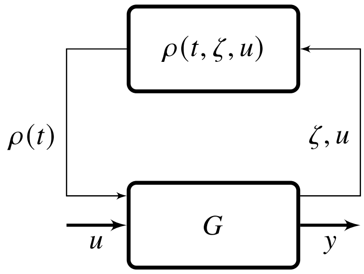

Figure 1. Block diagram illustrating the general qLPV model of a nonlinear plant G. The scheduling map $\rho(t)$ is determined endogenously by the scheduling states ζ and the input u, with $\rho(t) = \rho(t, \zeta, u)$ serving is the scheduling function that defines the parameter trajectory.

The benefit of expressing Equation 2 in this way is that it is applicable to a class of nonlinear systems that can be represented in the form given by Equations 3a - 3b. This formulation assumes that both the states and control inputs enter the system linearly. However, this assumption can be relaxed by treating the states and control inputs as scheduling parameters, which can then be integrated into the nonlinear terms matrix $\mathbf{f}(\rho(t))$ [10]. Additionally, this form makes a straightforward first-order linearization around the equilibrium or off-equilibrium point, as discussed in Section IV.A.1.

$$\begin{bmatrix} \dot{\zeta}(t) \\ \dot{W}(t) \end{bmatrix} = A(\rho(t)) \begin{bmatrix} \zeta(t) \\ W(t) \end{bmatrix} + B(\rho(t))u(t) + \mathbf{f}(\rho(t)) \tag{3a}$$

$$y(t) = C(\rho(t)) \begin{bmatrix} \zeta(t) \\ W(t) \end{bmatrix} + D(\rho(t))u(t) \tag{3b}$$

The resulting model provides a local approximation of the nonlinear plant's dynamics near a particular set of equilibrium points. To apply first-order linearization to the plant, an appropriate interpolation scheme is also necessary. Interpolation approaches in system identification of LPV systems usually use the classical gain-scheduling concept, where models are derived for constant scheduling trajectories and interpolated to form a global model. These methods, often using polynomial or spline interpolation, are closely related to the local-linear-modeling framework [1].

B. Global LPV Model

To derive a *global* Linear Parameter-Varying (LPV) model from a set of Linear Time-Invariant (LTI) models that describe the system dynamics, a method is required to estimate unknown values between the given LTI setpoints. *Interpolation*, a method that involves constructing a function that either passes through or approximates the known data points, is widely used in LPV literature as the primary approach for predicting these values (see [1], [2]). This method allows for merging individual LTI models (local model structure) and a set of scheduling functions which combines them, in order to form the global LPV model.

Figure 2 illustrates an example of a 2-dimensional parameter space defined by two scheduling parameters, forming a grid. Each point on the grid represents a local, 'frozen' Linear Time-Invariant (LTI) model, and the connecting curves are there to resemble the interpolation rules between these models.

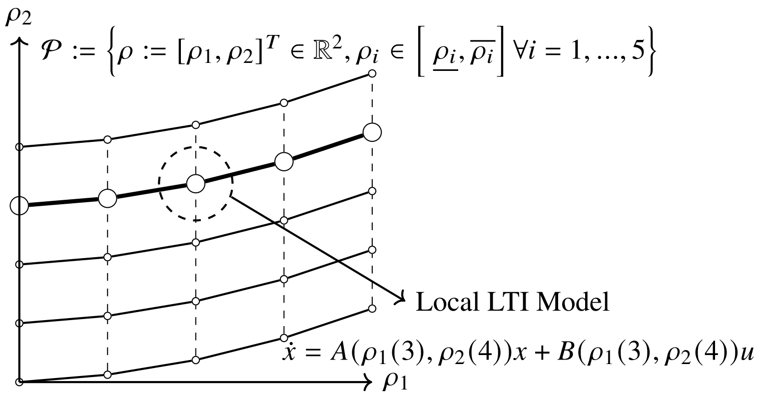

Figure 2. Example of the parameter space $\mathcal{P}$, created by two scheduling variables ρ_1 and ρ_2 where the local LTI models of the plant are connected with interpolation rules to form a global approximation of the scheduling space.

To interpolate between the locally derived LTI models, suitable *regressor* Υ, formed from the linear or nonlinear combinations of the elements of ρ, needs to be fitted to the state-space matrices. This is done usually in *Affine* form and is represented by Equations 4 and 5.

$$\dot{x} = \left(A_0 + \sum_{i=1}^{n_\Upsilon} A_i(\Upsilon_i)\right) x + \left(B_0 + \sum_{i=1}^{n_\Upsilon} B_i(\Upsilon_i)\right) u \quad (4) \quad y = \left(C_0 + \sum_{i=1}^{n_\Upsilon} C_i(\Upsilon_i)\right) x + \left(D_0 + \sum_{i=1}^{n_\Upsilon} D_i(\Upsilon_i)\right) u \quad (5)$$

where the state-space matrices are represented by the transfer function:

$$G_k(s) = C\left(\Upsilon(k)\right)\left(sI - A(\Upsilon(k))\right)^{-1} B(\Upsilon(k)) + D\left(\Upsilon(k)\right)$$

for $k = 1 \dots N_\rho$, where k is the scheduling index of the $\mathrm{k^{th}}$ identified local model. When the entries of Equations 4 and 5, a combined matrix $F(\gamma(k))$ can be obtained using Equation 6.

$$F(\Upsilon(k)) = \begin{bmatrix} A(\Upsilon(k)) & B(\Upsilon(k)) \\ C(\Upsilon(k)) & D(\Upsilon(k)) \end{bmatrix}, \quad k = 1 \dots N_\rho \tag{6}$$

Among the various possible suitable regressors, which can be linear or nonlinear combinations of ρ, a global regression matrix, formed by B-spline local basis functions, is proposed. These functions are composed of piecewise polynomials that are interconnected to ensure continuity of derivatives up to a specific order, determined by the degree of the polynomials. The benefit of doing this is: high approximation power, the flexibility to freely choose the spline continuity order, and the ability to fit scattered datasets on non-rectangular domains [4]. Additionally, the spatially localized spline parameters make them suitable for interpolation problems requiring smooth approximations. B-splines also possess the linear-in-the-parameters property, enabling the use of least squares solvers for parameter estimation, which is explained in detail in Section IV. The concept of simplex B-splines is explained in the next section.

III. Preliminaries on Multivariate B-splines

In the following section, a concise overview of the theory behind simplex splines is presented, providing the foundation for formulating a simplex B-spline model. This overview focuses on simplices and barycentric coordinates (Sec. III.A), spline basis functions (Sec. III.B), triangulations (Sec. III.C), continuity constraints (Sec. III.D) and general definition of spline function and spline space (Sec. III.E). These concepts are the basis for the derivation of a spline-based scheduling function for the model described in Section IV.A. For a more in-depth understanding of the simplex B-spline theory, refer to [11], [4], [12], and [13].

A. Simplices and Barycentric Coordinates

Multivariate *simplex* splines consist of B-form polynomials defined over adjacent triangular bases, known as simplices. These simplices are geometric structures that minimally span a given set of dimensions, forming the simplest convex shapes in the corresponding dimensional space. Mathematically, a simplex t in n-dimensional space is the convex hull of its $n+1$ non-degenerate vertices v, shown in Equation 7[4].

$$t := \langle v_0, v_1, ..., v_n \rangle \in \mathbb{R}^n \tag{7}$$

If the set of vertices is given by $\mathcal{V}_t = (v_0, v_1, ..., v_n)$, it is important to note, that the elements within this set are ordered based on the vertex index. Additionally, the non-degenerate property of the vertices implies that every vertex in $\mathcal{V}_t$ must contribute to the n-dimensional structure of the simplex [4].

The local coordinate system of the simplices t is represented using barycentric coordinates. This includes all points x that are the weighted sum of the vertices v_i in the set $\mathcal{V}_t$, where each weight b_i is unique and is shown in 8. An additional property of barycentric coordinates, is that they are normalized, as provided by Equation 9[12].

$$x = \sum_{i=0}^{n} b_i v_i \tag{8}$$

$$\sum_{i=0}^{n} b_i = 1 \tag{9}$$

The usefulness of the normalization property of the barycentric coordinates is that it reduces the dimensionality of the barycentric coordinate transformation by one, as any single component of b_i can be expressed in terms of the others [4]. For example, the b_0 barycentric coordinate can be expressed as: $b_0 = 1 - \sum_{i=1}^{n} b_i$.

B. Bernstein basis polynomials and the B-form of the multivariate simplex spline

Polynomials expressed in terms of barycentric coordinates, defined locally on a single simplex, are referred to as Bernstein basis polynomials of a certain degree d, as shown in Equation 10[4].

$$B^d_\kappa(b_{t_j}(x)) = \frac{d!}{\kappa!}(b_{t_j}(x)) \tag{10}$$

where $b_{t_j}(x)$ ($\mathbf{b} \in \mathbb{R}^{n+1}$) is the barycentric coordinate of the point $x \in \mathbb{R}^n$ with respect to the n-dimensional simplex t. The multi-index κ has the following properties: $|\kappa| = \kappa_0 + \kappa_1 + \cdots + \kappa_n$ and $\kappa! = \kappa_0!\kappa_1! \ldots \kappa_n!$, which allows to simplify the notation of the basis polynomials to $B^d_\kappa(b_{t_j}(x))$ in Equation 10. In order for the basis functions of simplex splines, in the form of Bernstein polynomials ($\mathbf{b}$) be a *Stable Local Basis*, the properties in Equations 11[4] and 12[11] must hold.

$$\sum_{|\kappa|=d} B^d_\kappa(b_{t_j}(x)) = 1 \tag{11}$$

$$B^d_\kappa(b_{t_j}(x)) = \begin{cases} \frac{d!}{\kappa!}(b_{t_j}(x)), & \forall x \in t \\ 0 & \forall x \notin t \end{cases} \tag{12}$$

The significance of the stable local basis of Bernstein polynomials, derived by Carl de Boor in [14], lies in the fact that any polynomial of degree d can be uniquely represented as a linear combination of Bernstein basis polynomials. Consequently, any polynomial $p(x)$ of degree d can be expressed in the *B-form*, as shown in Equation 13[14].

$$p(x) = \sum_{|\kappa|=d} c_{\kappa}^{t_j} B_{\kappa}^{d}(b_{t_j}(x)) \tag{13}$$

where $c_{\kappa}^{t_j}$ are the polynomial, or *B-coefficients* with $b = (b_0, b_1 \dots b_n)$ the barycentric coordinates of x with respect to an n-simplex t_j. The strength of B-splines lies in the fact that each B-coefficient has a unique spatial location, allowing the coefficients to locally control the shape of the simplex polynomial. The spatial location in barycentric coordinates is given by Equation 14. The variable κ is the multi-index introduced with Bernstein basis polynomials with $|\kappa| = d$, and d is the polynomial degree. The structure formed by the B-coefficients, within a single simplex t, is referred to as *B-net*. For a given degree d and dimension n, within a single simplex t, the amount of B-coefficients can be determined using the relation that corresponds to the total number of valid permutations $\hat{d}$ of the multi-index κ, as shown in Equation 15[14].

$$b(c_k) = \frac{\kappa}{d} \tag{14}$$

$$\hat{d} = \begin{pmatrix} d+n \\ n \end{pmatrix} = \frac{(d+n)!}{n!d!} \tag{15}$$

The set of basis polynomials of degree d, each defined on a individual simplex t_j is represented by a simplex spline function, given by the per-simplex vector notation shown in Equation 16[12].

$$p^{t_j}(x) = \begin{cases} c^{t_j} B^d\left(b_{t_j}(x)\right), & \forall x \in t_j \\ 0 & \forall x \notin t_j \end{cases} \tag{16}$$

where $B^d(b)$ represents the sorted vector of basis polynomials, described with barycentric coordinates b and is obtained by the relation shown in Equation 17a[13]. The vector c^{t_j} contains the correspondingly sorted B-coefficents, as shown in Equation 17b.

$$\begin{aligned} B^d\left(b_{t_j}(x)\right) &= \left[B^d_{d,0\dots0}\left(b_{t_j}(x)\right)\ B^d_{d-1,1\dots0}\left(b_{t_j}(x)\right)\cdots B^d_{0,1\dots d-1}\left(b_{t_j}(x)\right)\ B^d_{0,0\dots d}\left(b_{t_j}(x)\right)\right] && \text{(17a)} \\ c^{t_j} &= \left[c^{t_j}_{d,0,0}\ c^{t_j}_{d-1,1,0}\cdots c^{t_j}_{0,1,d-1}\ c^{t_j}_{0,0,d}\right]^T && \text{(17b)} \end{aligned}$$

C. Triangulations

The approximation capability of a spline function depends on the *triangulation* configuration, which consists of multiple simplices connected across all dimensions of the simplex spline. A triangulation involves partitioning a bounded domain $\Omega \subset \mathbb{R}^n$ into a set of J non-overlapping simplices, as illustrated in Equation 18[13].

$$\mathcal{T} := \cup_{j=1}^{J} t_j, \quad t_i \cap t_j \in \{\emptyset, \widetilde{t}\}, \quad \forall t_i, t_j \in \mathcal{T} \tag{18}$$

Delaunay triangulation is a geometric method for dividing a set of points in n-dimensional space into non-overlapping simplices, such that no point in the set lies inside the circumsphere in n-dimensions of any simplex. The advantage of using it over other triangulation techniques is its lack of assumptions about the configuration of the points to be triangulated, aside from requiring them to be non-degenerate [4].

D. Continuity constraints

Two simplices, t_i and t_j, share a unique *edge-facet*, $\tilde{t}_{ij}$, of dimension $n-1$, which is defined by the n vertices forming the common edge between the two simplices. This is described with Equations 19a - 19c[4].

$$\begin{aligned} t_i &= \langle v_0, v_1, ..., v_{n-1}, \tilde{v}_{i,j} \rangle && \text{(19a)} \\ t_j &= \langle v_0, v_1, ..., v_{n-1}, \tilde{v}_{j,i} \rangle && \text{(19b)} \\ \tilde{t}_{ij} &= t_i \cap t_j = \langle v_0, v_1, ..., v_{n-1} \rangle && \text{(19c)} \end{aligned}$$

The vertices $\tilde{v}_{i,j}$ and $\tilde{v}_{j,i}$ are not part of $\tilde{t}_{ij}$ and are named *out-of-edge vertices*. Each simplex contains a single vertex that lies outside the shared edge-facet. The *continuity constraints* are equations that establish relationships between the B-coefficients on either side of the edge-facet. These constraints make sure that the model maintains a smooth surface, up to a specified order of continuity, between the polynomial segments of the simplex spline. For general orders of continuity $r < d$ between two neighboring simplices t_i and t_j, the continuity conditions are formulated using Equation 20[4].

$$c^{t_i}_{\kappa_1,\dots,\kappa_{n-1},m} = \sum_{|\gamma|=m} c^{t_j}_{(\kappa_1,\dots,\kappa_{n-1},0)+\gamma} B^m_\gamma(b_{t_i}(\widetilde{v}_{i,j})), \quad 0 \le m \le r \tag{20}$$

where γ is a multi-index with the same size as κ and the sum of γ and κ is element-wise. The relations relating the polynomial degree d and sum of γ and κ are shown in Equations 21a - 21b.

$$\kappa_1 + \kappa_2 + \cdots + \kappa_{n-1} + m = d \tag{21a}$$

$$(\kappa_1 + \kappa_2 + \cdots + \kappa_{n-1}) + (\gamma_1 + \gamma_2 + \cdots + \gamma_n) = d \tag{21b}$$

The total amount of constraints per-edge in an n-dimensional triangulation of order C^r is calculated using Equation 22[4].

$$R = \sum_{m=0}^{r} \frac{(d-m-n-1)!}{(n-1)!(d-m)!} \tag{22}$$

It then becomes possible to write the continuity equations for all edges E in a set of linear equations shown in Equation 23[12].

$$H\mathbf{c} = 0, \quad H \in \mathbb{R}^{E\cdot R \times J\cdot \hat{d}} \tag{23}$$

where H is the *Smoothness Matrix*, with each row describing a single constraint between two simplices, making H a sparse and rank deficient matrix.

E. Spline Space

To approximate data on a triangulation, it is necessary to determine the optimal B-coefficients for each B-form polynomial. Using Equation 18, a spline function of degree d and continuity order r can be defined on a triangulation $\mathcal{T}$, which consists of J simplices, as described in Equation 24.

$$s^d_r(x) = B \cdot \mathbf{c} \in S^r_d(\mathcal{T}_J) \tag{24}$$

where B is the *global regression matrix* with dimension $\mathbb{R}^{N\times J\cdot\hat{d}}$ and $\mathbf{c} = [\mathbf{c}^{t_j}]^J_{j=1} \in \mathbb{R}^{J\cdot\hat{d}\times 1}$ is the *global B-coefficient vector*, consisting of the per-simplex vector of lexicographically sorted B-coefficients $\mathbf{c}^{t_j} \in \mathbb{R}^{\hat{d}\times 1}$. $S^r_d(\mathcal{T}_J)$ is known as the *spline space*. It is defined as the space of all spline functions $s^d_r(x)$ belonging to the space of polynomials $\mathbb{P}_d$ of a given degree d and continuity order C^r on a given triangulation $\mathcal{T}_J$, mathematically expressed with Equation 25[11].

$$S^r_d(\mathcal{T}_J) := \{s \in C^r(\mathcal{T}_J) : s|_t \in \mathbb{P}_d, \forall t \in \mathcal{T}_J\} \tag{25}$$

IV. Application of Splines to an LPV Model

This section is presented in two parts. The first part demonstrates the practical application of the theoretical framework established in previous chapters by implementing it on the Inverted Pendulum with Cart Model (IPCM), as detailed in Section IV.A. This implementation deals with the creation of the scheduling function and the parameter selection process, which are described in Section IV.A.2 together with the application of spline-based regression, presented in Section IV.A.3. The second part lists the methodologies used for comparative analysis. This includes a description of the Zero-Order Hold (ZOH) method (Section IV.B.1) and Ordinary Least Squares (OLS) regression (Section IV.B.2), along with the metrics used for model quality assessment, the details of which are provided in Section IV.B.3. These methods and metrics are applied throughout the study to evaluate model performance.

A. Model Formulation

The IPCM is a fundamental classroom example that is interesting in the study of global nonlinear control, as its dynamics are governed by nonlinear, dynamically coupled differential equations that exhibit an inherently unstable equilibrium. The IPCM is widely used for modeling various control systems, serving as benchmark for advanced techniques to stabilize and control nonlinear, unstable systems in real-world applications (see [15] for study on applications of IPCM).

The IPCM system has two degrees of freedom: the position x and pendulum angle θ, with a free-body-diagram depicted in Figure 3. The Equations of Motion (EoM), describing the nonlinear dynamics of this system, are shown in Equations 26a and 26b.

$$(M+m)\ddot{x} + ml\cos(\theta)\ddot{\theta} - ml\sin(\theta)\dot{\theta}^2 = F(t) - b\dot{x} \tag{26a}$$

$$ml^2\ddot{\theta} + ml\cos(\theta)\ddot{x} - mgl\sin(\theta) = 0 \tag{26b}$$

where M is the mass of cart, m is the mass of the bob and l is the length of the mass-less pendulum rod.

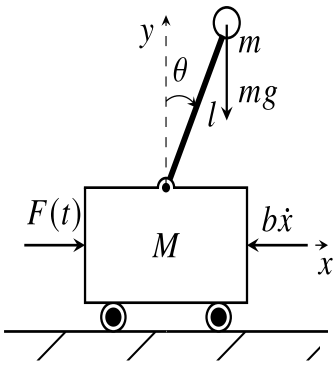

Figure 3. Free body diagram of the IPCM problem, depicting applied forces acting on the cart $F(t)$ and non-applied friction force ($b\dot{x}$) from the cart's wheels and pendulum gravity force (mg). There are 2 Degrees of Freedom (DOF): cart-position x and pendulum angle θ, creating a Single-Input-Multi-Output (SIMO) system.

From the EoM, four states can be distinguished, which provide a complete description of the system at any given time: cart's position (x), cart velocity ($\dot{x} := v$), pendulum's angle (θ) and angular velocity ($\dot{\theta} := \Omega$). These four states make the state vector $\mathbf{X}$, which leads to the description of the non-linear system with Equation 27.

$$\frac{d\mathbf{X}}{dt} = f(\mathbf{X}, u), \quad y = g(\mathbf{X}) \tag{27}$$

where $\mathbf{X} \in \mathbb{R}^n$, $u \in \mathbb{R}^r$, $y \in \mathbb{R}^m$ and f, g are smooth functions, with the state vector being $\mathbf{X} = [x\ v\ \theta\ \Omega]^{\mathrm{T}}$. The derivative of the state vector is $\frac{d\mathbf{X}}{dt} = [v\ a\ \Omega\ \alpha]^{\mathrm{T}}$, and is used to describe the non-linear matrix equation shown with Equation 28.

$$\begin{bmatrix} v \\ a \\ \Omega \\ \alpha \end{bmatrix} = \begin{bmatrix} v \\ -\frac{b}{mq}v - g\frac{\sin 2\theta}{2q} + \frac{l\sin\theta}{q}\Omega^2 \\ \Omega \\ \frac{b\cos\theta}{mlq}v + gK\frac{\sin\theta}{q} - \frac{\sin 2\theta}{q}\Omega^2 \end{bmatrix} + \begin{bmatrix} 0 \\ \frac{1}{mq} \\ 0 \\ -\frac{\cos\theta}{mlq} \end{bmatrix} F(t) \tag{28}$$

where $q = \frac{M}{m} + \sin^2\theta$ and $K = \frac{M+m}{ml}$. The dynamics of interest are fully captured by Equation 28, as the output equation y is defined solely in terms of the system states without any feed-forward terms. Specifically, the output is described by $y = \mathbf{I}\mathbf{X} + \mathbf{0}F(t)$, where I is the 4x4 identity matrix and $\mathbf{0}$ is the 4x1 zero matrix. Since the non-linear system is analyzed in an open-loop configuration, the output equations are not necessary for the analysis.

By setting Equation 28 equal to zero, two equilibrium points can be identified: the downward position ($\theta = \pi$) and the upward position ($\theta = 0$), both characterized by zero cart velocity and zero angular velocity. Among these, the upward position corresponds to an unstable equilibrium, where the downward position is stable. In the absence of a control force, a unperturbed pendulum will naturally return to the stable downward position. Only at the equilibrium points, a Taylor series approximation can be used, as shown in Equation 29, which would linearize the non-linear equations of motion, presented in Equation 28.

$$f(x) = f(x_0) + \frac{df(x_0)}{dx}(x - x_0) + \cdots + \frac{1}{n!}\frac{d^n f(x_0)}{dx^n}(x - x_0)^n \tag{29}$$

where for a first-order linearization, all $n > 1$ are treated as higher-order terms and can be neglected. At the equilibrium points, defined as $(\mathbf{X}, u) \in \mathbb{R}^{n+r} \mid f(\mathbf{X}, u) = 0$, the first-order linearized expression for the non-linear system can be derived using Equation 30.

$$\frac{d\mathbf{X}}{dt} = A_0\Delta\mathbf{X}_0 + B_0\Delta\mathbf{u}_0 = \frac{\partial f(\mathbf{X}_0, u_0)}{\partial\mathbf{X}}(\mathbf{X} - \mathbf{X}_0) + \frac{\partial f(\mathbf{X}_0, u_0)}{\partial u}(u - u_0) \tag{30}$$

where A_0 is the state-space matrix and B_0 is the input matrix of the equilibrium point $(\mathbf{X}_0, u_0)$. The resulting linearized system, in state-space form, is shown in Equation 31.

$$\begin{bmatrix} v \\ a \\ \Omega \\ \alpha \end{bmatrix} = \begin{bmatrix} 0 & 1 & 0 & 0 \\ 0 & -\frac{b}{M} & -\frac{mg}{M} & 0 \\ 0 & 0 & 0 & 1 \\ 0 & S_\theta\frac{b}{Ml} & S_\theta gK & 0 \end{bmatrix} \begin{bmatrix} x \\ v \\ \theta \\ \Omega \end{bmatrix} + \begin{bmatrix} 0 \\ \frac{1}{M} \\ 0 \\ -S_\theta\frac{1}{Ml} \end{bmatrix} F(t) \tag{31}$$

where $S_\theta = 1$ signifies the pendulum being in unstable equilibrium point, and $S_\theta = -1$ when the pendulum is in the stable equilibrium point. At the two equilibrium points, the system is time-invariant, as the members of the Jacobian matrix are constants. Describing the state-space using Equation 31 enables the application of the well-established theoretical framework for LTI systems (see [16] and [17]) to approximate the behavior of the nonlinear system for small deviations in initial conditions and inputs around the two equilibrium points. However, having only two equilibrium points is a drawback, as the transient dynamics—those occurring away from equilibrium—cannot be adequately represented by the LTI model alone due to the small-angle approximation not being valid anymore.

1. Off-Equilibrium Linearization

If the dynamics of the nonlinear plant are approximated near an operating point, $(\mathbf{X}_0, u_0) \in \mathbb{R}^{n+r}$, which is not necessarily an equilibrium point, the dynamics of the non-linear system, from Equation 28, can be reformulated into the *affine* form using Equation 32[18].

$$\frac{d\mathbf{X}}{dt} = f(\mathbf{X}_0, u_0) + \frac{\partial f(\mathbf{X}_0, u_0)}{\partial \mathbf{X}}(\mathbf{X} - \mathbf{X}_0) + \frac{\partial f(\mathbf{X}_0, u_0)}{\partial u}(u - u_0) := A_0\mathbf{X} + B_0\mathbf{u} + d_0 \tag{32}$$

where $d_0 = f(\mathbf{X}_0, u_0) - A_0 x_0 - B_0 u_0$ and represents an approximation of the function f by its tangent plane at the point $(\mathbf{X}_0, u_0)$, as analogized in [18]. The function $f(\mathbf{X}_0, u_0)$ for an LTI system equates to zero, but for an LPV system, is proportional to both the elapsed time and the derivative at the linearization point. It results in a locally linearized system along a trajectory, meaning that the system remains in motion while its behavior is analyzed in the vicinity of this trajectory. This approach of describing the system is part of the family of first-principle LPV representations for physical systems, named *Linearization Based Approximation Methods*, as stated in [1]. The Jacobian matrix, describing the changes of the non-linear function from Equation 28, with respect to the each state and input are shown in Equations 33a and 33b.

$$\frac{\partial f(\mathbf{X}_0, u_0)}{\partial \mathbf{X}} = \begin{bmatrix} 0 & 1 & 0 & 0 \\ 0 & -\frac{b}{mq} & -vb\frac{q-\dot{q}}{mq^2} - g\frac{q\cos 2\theta - \frac{1}{2}\dot{q}^2}{q^2} + \Omega^2 L \frac{q\cos\theta - \dot{q}\sin\theta}{q^2} & \frac{2\Omega\sin\theta}{q} \\ 0 & 0 & 0 & 1 \\ 0 & \frac{b\cos\theta}{mlq} & -vb\frac{(q\sin\theta - \dot{q}\cos\theta)}{q^2} + gK\frac{q\cos\theta - \dot{q}\sin\theta}{q^2} + \Omega^2\frac{q\cos(2\theta) - \frac{1}{2}\dot{q}^2}{q^2} & -\frac{\Omega\sin 2\theta}{q} \end{bmatrix} \tag{33a}$$

$$\frac{\partial f(\mathbf{X}_0, u_0))}{\partial u} = \begin{bmatrix} 0 & \frac{1}{mq} & 0 & -\frac{\cos\theta}{mlq} \end{bmatrix}^T \tag{33b}$$

where $\dot{q} := \frac{d}{d\theta}\left(\frac{M}{m} + \sin^2\theta\right) = 2\cos\theta\sin\theta = \sin(2\theta)$. Based on the Jacobian matrix, the linearized system does not explicitly depend on time, but it is a function of time-varying parameters, which also represent the states of the system.

If Equation 32 is evaluated at an initial point $\theta_{00} >> \theta_{\text{eq}}$, which is not the equilibrium point: $(\mathbf{X}_0, u_0) = \left([0\ 0\ \theta_{00}\ 0]^T, 0\right)$, the Jacobian matrix with respect to the state and input of the non-linear model, is shown with Equation 34.

$$\dot{\mathbf{X}} = \begin{bmatrix} 0 & 1 & 0 & 0 \\ 0 & -\frac{b}{mq_0} & -g\frac{q_0\cos(2\theta_0) - \frac{1}{2}\dot{q}_0^2}{q_0^2} & 0 \\ 0 & 0 & 0 & 1 \\ 0 & \frac{b\cos\theta_0}{mlq_0} & gK\frac{q_0\cos\theta_0 - \dot{q}_0\sin\theta_0}{q_0^2} & 0 \end{bmatrix}\mathbf{X} + \begin{bmatrix} 0 \\ \frac{1}{mq_0} \\ 0 \\ -\frac{\cos\theta_0}{mlq_0} \end{bmatrix}u + \begin{bmatrix} 0 \\ -g\theta_0\frac{q_0(\sin 2\theta_0 + \cos 2\theta_0) - \frac{1}{2}\dot{q}_0^2}{q_0^2} \\ 0 \\ gK\theta_0\frac{q_0(\sin\theta_0 - \cos\theta_0) + \dot{q}_0\sin\theta_0}{q_0^2} \end{bmatrix} \tag{34}$$

Evidently, the dynamics governing the non-linear system in the Jacobian matrix are functions of two states, namely the cart's velocity v, and the pendulum's angle θ, even when the system initializes at only the angle θ_0, while keeping the other states at zero.

2. Scheduling Parameter and Function Selection

The pendulum angle θ is a natural choice of a scheduling parameter as it directly influences both the pendulum and cart trajectories, provided they are coupled, thereby governing the overall dynamic behavior of the system. Additionally, as the non-linear equations, depend explicitly on trigonometric functions of θ, by bounding θ within a finite range, the system's nonlinear dynamics across the entire operating region can be captured. When an external input force $F(t)$ is applied to the system, the work done by this force, along with the non-conservative frictional dissipation, $b\dot{x}$, opposing the input, influences the velocity of the cart. To model the nonlinear system more effectively, the inclusion of ν as a scheduling parameter allows the LPV model to capture the system's response to these external disturbances and the time-varying nature of the system's dynamics.

This allows for the representation of the scheduling vector to contain the two aforementioned parameters, which are also internal states of the system, evaluated in a grid parameter space defined by:

$$\mathcal{P} := \left\{ \rho := \begin{bmatrix} \nu_0 \\ \theta_0 \end{bmatrix} \in \mathbb{R}^2 \middle| : \begin{array}{l} \nu_{0,k} = \nu_{0,\min} + \Delta\nu_0 \left(\left\lfloor \frac{k-1}{N_\rho} \right\rfloor \right) \\ \theta_{0,k} = \theta_{0,\min} + \Delta\theta_0 \left(k - 1 - N_\rho \left\lfloor \frac{k-1}{N_\rho} \right\rfloor \right) \end{array}, k = 1, \ldots, N_\rho^2 \right\}$$

where the single index k is mapping to pairs of $(\nu_{0,i}, \theta_{0,j})$ with $\nu_{0,i} = \nu_{0,\min} + (i-1)\Delta\nu_0$ and $\theta_{0,j} = \theta_{0,\min} + (j-1)\Delta\theta_0$ using the transformation $k = (i-1)N_\rho + j$. The vectors $\nu_{0,i}$ and $\theta_{0,j}$ are linearly spaced which allows for equidistant selection of scheduling parameter points drawn from a uniform distribution with $\Delta\nu_0 = \frac{\nu_{0,\max} - \nu_{0,\min}}{N_\rho - 1}$ and $\Delta\theta_0 = \frac{\theta_{0,\max} - \theta_{0,\min}}{N_\rho - 1}$. The number of data points per parameter is given by N_ρ. There are N_ρ points, but only $(N_\rho - 1)$ intervals between them and for the two- scheduling parameter grid, there are a total of $N_\rho \times N_\rho$ points. The expression $\left\lfloor \frac{k-1}{N_\rho} \right\rfloor$ is the floor function that accounts for rounding of k to the nearest integer that is less than or equal to k.

Therefore, it is possible to explicitly represent the state and input space functions of the qLPV model, since a quasi-LPV system is a linear time-varying plant whose state-space matrices are predefined functions of parameters that depend on the state variables as shown in Equation 35.

$$\dot{\mathbf{X}} = \begin{bmatrix} 0 & 1 & 0 & 0 \\ 0 & \widetilde{\mathbf{A}}_{22}(\theta_0) & \widetilde{\mathbf{A}}_{23}(\nu_0, \theta_0) & 0 \\ 0 & 0 & 0 & 1 \\ 0 & \widetilde{\mathbf{A}}_{42}(\theta_0) & \widetilde{\mathbf{A}}_{43}(\nu_0, \theta_0) & 0 \end{bmatrix} \Delta\mathbf{X} + \begin{bmatrix} 0 \\ \widetilde{\mathbf{B}}_2(\theta_0) \\ 0 \\ \widetilde{\mathbf{B}}_4(\theta_0) \end{bmatrix} \Delta u + \widetilde{\mathbf{f}}_0(\nu_0, \theta_0) \tag{35}$$

where $\Delta\mathbf{X} = (\mathbf{X} - \mathbf{X}_0)$ and $\Delta u = (u - u_0)$. This expression aligns with the form of Equation 3a, where a distinction is made between scheduled and non-scheduled states (although not ordered as $x(t) = [\ \zeta(t) \quad W(t)\ ]^T$), and the dependence of the state and input matrices $A(\rho)$ and $B(\rho)$ on the scheduling vector is clear. Additionally, the affine non-linear terms are contained within $\mathbf{f}_0(\rho)$, thereby completing the description of the affine qLPV system.

Since the elements of the state and input space matrices are functions of the scheduling vector, evaluated at the scheduling parameter grid, expressing them as linear combinations of a set of B-spline basis functions allows for smooth interpolation across the parameter space. It also allows for continuous and differentiable transitions between grid points. Using the formal definition of the multivariate simplex spline, as outlined in Equation 24, the elements of these matrices can be estimated. Denoting the set of measurement points as $x_k := (\nu_{0,k}, \theta_{0,k})$ and total number of measurments $N := N_\rho^2$, the multivariate simplex B-spline $s_r^d(x_k) \in \mathbb{R}^{N\times 1}$ can be used to estimate all of the terms in the LPV model noted in Equation 35.

A matrix that concatenates all the terms from Equation 35, named $\mathbf{Z} \in \mathbb{R}^{N\times 7}$ is created, which is evaluated at every data point x_k. It contains all the relevant system parameters from the linearized model and is later used in the regression model, given by Equation 36.

$$\mathbf{Z} = \begin{bmatrix} \widetilde{\mathbf{A}}_{22}(x_1) & \widetilde{\mathbf{A}}_{42}(x_1) & \widetilde{\mathbf{A}}_{23}(x_1) & \widetilde{\mathbf{A}}_{24}(x_1) & \widetilde{\mathbf{B}}_2(x_1) & \widetilde{\mathbf{B}}_4(x_1) & \widetilde{\mathbf{f}}_0(x_1) \\ \vdots & \vdots & \vdots & \vdots & \vdots & \vdots & \vdots \\ \widetilde{\mathbf{A}}_{22}(x_N) & \widetilde{\mathbf{A}}_{42}(x_N) & \widetilde{\mathbf{A}}_{23}(x_N) & \widetilde{\mathbf{A}}_{24}(x_N) & \widetilde{\mathbf{B}}_2(x_N) & \widetilde{\mathbf{B}}_4(x_N) & \widetilde{\mathbf{f}}_0(x_N) \end{bmatrix} \tag{36}$$

An example is taken for the vector $\widetilde{\mathbf{A}}_{23}(\nu_0, \theta_0) \in \mathbf{R}^{N\times 1}$ where the estimation is achieved by representing $\widetilde{\mathbf{A}}_{23}$ with a spline $s_r^d(x_k)$ over a triangulation T_j consisting of J simplices, expressed as follows:

$$\left[\widetilde{\mathbf{A}}_{23}(x_k)\right]_{k=1}^{N} \approx s_r^d(x_k)$$

where each of the terms are expressed as follows:

$$\widetilde{\mathbf{A}}_{23}(x_k) = \left(-v_{0,k} b \frac{q_{0,k} - \dot{q}_{0,k}}{m q_{0,k}^2} - g \frac{q_{0,k} \cos 2\theta_{0,k} - \frac{1}{2}\dot{q}_{0,k}^2}{q_{0,k}^2}\right), \quad \begin{aligned} \dot{q}_{0,k} &= 2\cos\theta_{0,k}\sin\theta_{0,k} \\ q_{0,k} &= \frac{M}{m} + \sin^2\theta_{0,k} \end{aligned}$$

$$s_r^d(x_k) = \mathbf{B}\cdot\mathbf{c} = \begin{bmatrix} B_{t_1} & 0 & 0 & 0 \\ 0 & B_{t_2} & 0 & 0 \\ 0 & 0 & \ddots & 0 \\ 0 & 0 & 0 & B_{t_J} \end{bmatrix} \begin{bmatrix} c_{t_1} \\ c_{t_2} \\ \vdots \\ c_{t_J} \end{bmatrix}, \ \forall x_k \in t_j$$

The matrix $\mathbf{B}$, is the block diagonal global matrix, which consists of each $B_{t_J} \in \mathbb{R}^{N_j \times \hat{d}}$, the per-simplex, basis polynomials in terms of the barycentric coordinates b_{t_j} provided by Equation 37.

$$B_{t_J} = \begin{bmatrix} B^d_{d,0,0}\left(b_{t_j}(x_1)\right) & B^d_{d-1,1,0}\left(b_{t_j}(x_1)\right) & \dots & B^d_{0,1,d-1}\left(b_{t_j}(x_1)\right) & B^d_{0,0,d}\left(b_{t_j}(x_1)\right) \\ \vdots & \vdots & \vdots & \vdots & \vdots \\ B^d_{d,0,0}\left(b_{t_j}(x_{N_j})\right) & B^d_{d-1,1,0}\left(b_{t_j}(x_{N_j})\right) & \dots & B^d_{0,1,d-1}\left(b_{t_j}(x_{N_j})\right) & B^d_{0,0,d}\left(b_{t_j}(x_{N_j})\right) \end{bmatrix} \tag{37}$$

where N_j is the total number of data points x_k inside the simplex j. This estimation with a global spline is performed for every column $\mathbf{Z}_{N,m}$ of the matrix $\mathbf{Z}$, with columns $m = 1 \dots 7$ and rows $N := N_\rho^2$.

3. Linear Regression and Least Squares estimator for B-coefficients

Following from Equation 24, the global regression matrix $\mathbf{B}$ reformulates the standard linear regression model such that it integrates into the full-triangulation regression matrix for all observations $\mathbf{X} \in \mathbb{R}^{N \times J \cdot \hat{d}}$ to form Equation 38.

$$\mathbf{Y} := \mathbf{Xc} + \epsilon \in \mathbb{R}^{N\times 1} \tag{38}$$

where $\mathbf{Y}$ is the column vector containing all observations of column $\mathbf{Z}_{N,m}$ of the matrix $\mathbf{Z}$ and ϵ is the column vector containing all the residuals. This structure ensures that the regression model takes into account the complete triangulation of the spline basis, while estimating the B-coefficient vector in n-dimensional spaces. Since B-form polynomials are linear in the parameters, linear solvers such as the Equality Constrained Ordinary Least Squares (ECOLS) can be used which for B-splines define the cost function using the global parameters, with Equation 39[4].

$$J(\mathbf{c}) = \frac{1}{2}(\mathbf{Y} - \mathbf{Bc})^T(\mathbf{Y} - \mathbf{Bc}) \tag{39}$$

In order to enforce smoothness constraints between individual spline pieces, the constrained cost linear regression estimator is determined using Equation 40[12].

$$\hat{\mathbf{c}} = \arg\min_{\mathbf{c}} J(\mathbf{c}), \quad \text{subject to} \quad \mathbf{H}\cdot\mathbf{c} = 0 \tag{40}$$

This relation can be solved with the *Lagrange Multiplier Method*, which augments the optimization problem with the Lagrangian, as described with Equation 41.

$$L(\mathbf{c}, \lambda) = \frac{1}{2}(\mathbf{Y} - \mathbf{Bc})^T(\mathbf{Y} - \mathbf{Bc}) + \lambda^T \cdot \mathbf{H}\cdot\mathbf{c} \tag{41}$$

The vector λ contains the Lagrangian Multipliers. The optimum is then found at location (c, λ), which is located at the bottom of the convex multi-dimensional cost function $J(\mathbf{c})$. At this point, the partial derivatives with respect to the B-coefficients, $\frac{\partial L}{\partial c}$ and with respect to the Lagrange multipliers $\frac{\partial L}{\partial \lambda}$, equate to zero. It then becomes possible to reformulate the optimization problem using the Karush-Kuhn-Tucker (KKT) matrix, as shown in Equation 42.

$$\begin{bmatrix} \mathbf{B}^T \cdot \mathbf{B} & \mathbf{H}^T \\ \mathbf{H} & 0 \end{bmatrix} \begin{bmatrix} \hat{\mathbf{c}} \\ \lambda \end{bmatrix} = \begin{bmatrix} \mathbf{B}^T \cdot \mathbf{Y} \\ 0 \end{bmatrix} \tag{42}$$

If the *Gram (dispersion) matrix* is defined as $\mathbf{Q} = \mathbf{B}^T \cdot \mathbf{B}$, then the KKT matrix is non-singular if $\mathbf{Q}$ is positive definite on the kernel of the smoothness constraint matrix $\mathbf{H}$. This means that for $\mathbf{c} \neq 0$, satisfying $\mathbf{H} \cdot \mathbf{c} = 0$, $\mathbf{c}^T\ \mathbf{Q}\mathbf{c} > 0$ must hold and the rank of $\mathbf{Q}$ and $\mathbf{H}$ must be full [12]. This ensures that no unconstrained directions remain in which $\mathbf{Q}$ is singular, preventing degeneracy in the system. Furthermore, it has been proven in [4] and [12] that the dispersion matrix $\mathbf{Q}$ is non-singular if every simplex in the triangulation $\mathcal{T}$ contains at least $\hat{d}$ non-coplanar data points, so that $N_J \geq \hat{d}$. This condition imposes constraints on both the volume and configuration of the data, which is an important bound for the simulation of the IPCM.

The rank of $\mathbf{H}$ is full, when there are no redundant continuity conditions, however, if $\mathbf{H}$ is rank-deficient, then KKT matrix is singular and a different approach is needed to solve the optimization problem, like the Moore-Penrose pseudo inverse, which is shown in Equation 43.

$$\begin{bmatrix} \hat{\mathbf{c}} \\ \lambda \end{bmatrix} = \begin{bmatrix} \mathbf{Q} & \mathbf{H}^T \\ \mathbf{H} & 0 \end{bmatrix}^+ \begin{bmatrix} \mathbf{B}^T \cdot \mathbf{Y} \\ 0 \end{bmatrix} = \begin{bmatrix} \mathbf{C}_1 & \mathbf{C}_2 \\ \mathbf{C}_3 & \mathbf{C}_4 \end{bmatrix} \begin{bmatrix} \mathbf{B}^T \cdot \mathbf{Y} \\ 0 \end{bmatrix} \tag{43}$$

As long as $\mathbf{Q}$ is positive definite and on the kernel of $\mathbf{H}$, an efficient, fast-converging method for solving the KKT matrix is used as proposed in [19] and [20]. This iterative method is shown in Equations 44a and 44b.

$$\hat{\mathbf{c}}_1 = \left(2\mathbf{Q} + \frac{1}{\varepsilon}\mathbf{H}^T H\right)^{-1} \left(2\mathbf{B}^T \cdot \mathbf{Y} - \mathbf{H}^T \cdot \hat{\lambda}_0\right), \quad 0 \leq \varepsilon \leq 1 \tag{44a}$$

$$\hat{\mathbf{c}}_{k+1} = \left(2\mathbf{Q} + \frac{1}{\varepsilon}\mathbf{H}^T H\right)^{-1} \left(2\mathbf{Q} \cdot \hat{\mathbf{c}}_k\right), \quad 0 \leq \varepsilon \leq 1 \tag{44b}$$

where $\hat{\lambda}_0$ is the initial estimate for the Lagrange multipliers. Important to note is that the convergence rate of the iterative solver depends on the continuity order relative to the degree.

B. Model Implementation

The following Section presents the setup of four different methods used to compare the performance of a B-spline with degree $d = 4$ and continuity $r = 2$ defined on a Delaunay 3×3 grid triangulation of $\mathcal{T}_{18}$ simplices, applied as a scheduling function of the IPCM. These methods were selected because they represent varying levels of dependence on the scheduling parameter, particularly in terms of differentiability. The comparison starts with the piecewise constant Zero-Order Hold (ZOH), in Section IV.B.1, which remains constant within an interval, and continues to single and multi-variable smooth polynomial OLS estimators in Section IV.B.2. The accuracy of the spline approximation is evaluated through residual analysis and statistical methods described in section IV.B.3.

1. Zero-Order Hold

Using a ZOH LPV method means that a piecewise-constant behavior on the scheduling parameter $\rho(t)$ is created, which results in switching between each discrete sampling interval T_d. Therefore, $\rho(t)$, remains constant within each interval $[kT_d, (k+1)T_d)$ and switches instantaneously at $t_{switch} = kT_d$, where $k \in \mathbb{Z}^+$. This is illustrated with Equation 45.

$$\rho := \theta_0 = \sum_{k=0}^{\infty} H(t - kT_d) \left(\theta_{0,j}(k) - \theta_{0,j}(k-1)\right), \qquad \begin{array}{l} \forall t \in [kT_d, (k+1)T_d) \\ k \in \mathbb{Z}^+ \end{array} \tag{45}$$

where $H(t)$ is the Heaviside step function: $H(t) = \begin{cases} 1 & \text{if } t < 0 \\ 0 & \text{if } t \geq 0 \end{cases}$ and $\theta_{0,j} = \theta_{0,\min} + (j-1)\Delta\theta_0$ with N_ρ total amount of points.

Evaluating the state and input matrices from Equation 35 results in finite set of linear models $(A_{0,j}, B_{0,j})$ corresponding to a specific point $\theta_{0,j}$ in the parameter space $\mathcal{P}$. Scheduling the models at each time step is done by taking the minimum of the difference between the actual $\theta(t)$ and parameter value $\theta_{0,j}$, shown by Equation 46.

$$\theta_j = \arg\min |\theta(t) - \theta_{0,j}| \tag{46}$$

where for each value of at θ_j, $(\mathbf{A}_0, \mathbf{B}_0)$ are retrieved and used to solve the differential equation. Additionally, the angle θ_j undergoes a de-wrapping process to ensure it remains within the interval $[0 \leq \theta \leq 2\pi]$. If the angle falls outside this range, appropriate multiples of 2π are either added or subtracted until the angle is confined to the interval.

2. Univariate and Multivariate Ordinary Least-Squares

For the second method, a univariate polynomial structure, with dependence on the pendulum angle as a single scheduling parameter is constructed such that Equations 47 and 48 are used to estimate $(\mathbf{A}_0, \mathbf{B}_0)$. The scheduling vector takes the form:

$$\rho_d(\theta_0) := \theta_0^d \quad d \in [0, D_{\text{uni}}]$$

where d is the maximum degree for each scheduling variable θ_0. The pendulum angle is chosen in this form because, as seen in Equation 35, all matrix functions to be estimated are functions of θ_0.

$$\widetilde{\mathbf{A}}(\theta_0) = \sum_{d=0}^{D_{\text{uni}}} \mathbf{A}_d \rho_d(\theta_0) \tag{47}$$

$$\widetilde{\mathbf{B}}(\theta_0) = \sum_{d=0}^{D_{\text{uni}}} \mathbf{B}_d \rho_d(\theta_0) \tag{48}$$

The term D_{uni} is the maximum order of the univariate polynomial and A_d and B_d contain the unknown model parameters. A model that best fits a sequence of N_ρ measurements per column of the sub-matrix $\mathbf{Z}_{\text{uni}}$ is constructed and shown with Equation 49.

$$\mathbf{Z}_{\text{uni}} = \begin{bmatrix} \widetilde{\mathbf{A}}_{23}(\theta_{0,1}) & \widetilde{\mathbf{A}}_{43}(\theta_{0,1}) & \widetilde{\mathbf{B}}_4(\theta_{0,1}) & \widetilde{\mathbf{f}}_0(\theta_{0,1}) \\ \vdots & \vdots & \vdots & \vdots \\ \widetilde{\mathbf{A}}_{23}(\theta_{0,N_\rho}) & \widetilde{\mathbf{A}}_{43}(\theta_{0,N_\rho}) & \widetilde{\mathbf{B}}_4(\theta_{0,N_\rho}) & \widetilde{\mathbf{f}}_0(\theta_{0,N_\rho}) \end{bmatrix} \tag{49}$$

The reason why $\mathbf{Z}_{\text{uni}}$ is a sub-matrix containing only the Jacobian matrix terms directly connected to θ from Equation 26b is due to the limitations of OLS as estimation method for this problem. The terms derived from Equation 26a, which represent the cart dynamics, show dependency on the cart velocity v, which happens because the state evolution of the pendulum angle is not isolated but dynamically influenced by the motion of the cart, even if this influence is not explicitly represented in the mathematical form of the Jacobian terms. The assumption of OLS is that the independent variable θ fully captures the variance needed to explain the dependent variable, however for cross-coupled terms, which are parameters influenced by both (v, θ), this assumption does not hold. Therefore the parameter estimates which are required to be unbiased and consistent, restrict the application of univariate OLS to only these four terms in $\mathbf{Z}_{\text{uni}}$.

Continuing the example of $\widetilde{\mathbf{A}}_{23}$ from Section IV.A.2, each column of $\mathbf{Z}_{\text{uni}}$ can be estimated using Equation 50, where each component $a_{23,j}$ is a constant global model parameter, contained in $\mathbf{A}_d$. Similarly, the same notation is valid for $\mathbf{B}_d$ with coefficients $b_{4,j}$ and affine function $f_{0,j}$ part of the $\mathbf{f}_0$ vector.

$$\begin{bmatrix} \widetilde{\mathbf{A}}_{23}(\theta_{0,1}) \\ \widetilde{\mathbf{A}}_{23}(\theta_{0,2}) \\ \vdots \\ \widetilde{\mathbf{A}}_{23}(\theta_{0,N_\rho}) \end{bmatrix} = \begin{bmatrix} \rho_0(\theta_{0,1}) = 1 & \rho_1(\theta_{0,1}) = \theta_{0,1} & \cdots & \rho_d(\theta_{0,1}) = \theta_{0,1}^{D_{\text{uni}}} \\ \rho_0(\theta_{0,2}) = 1 & \rho_0(\theta_{0,2}) = \theta_{0,2} & \cdots & \rho_d(\theta_{0,2}) = \theta_{0,2}^{D_{\text{uni}}} \\ \vdots & \vdots & \vdots & \vdots \\ \rho_0(\theta_{0,N_\rho}) = 1 & \rho_1(\theta_{0,N_\rho}) = \theta_{0,N_\rho} & \cdots & \rho_d(\theta_{0,N_\rho}) = \theta_{0,N_\rho}^{D_{\text{uni}}} \end{bmatrix} \begin{bmatrix} a_{23,0} \\ a_{23,1} \\ \vdots \\ a_{23,d} \end{bmatrix} + \begin{bmatrix} \epsilon_1 \\ \epsilon_2 \\ \vdots \\ \epsilon_{N_\rho} \end{bmatrix} \tag{50}$$

This form can be represented as in Equation 38, where the regression matrix is represented by $\mathbf{X} \in \mathbb{R}^{N_\rho \times D}$, with $D = D_{\text{uni}} + 1$. This formulation accounts for all the predictors, including the intercept term. To solve the OLS problem, the cost function to minimize is similar to the one described with Equation 40, where instead of the spline parameters, the regression matrix $\mathbf{X}$ is used and the expression has the form shown in Equation 51.

$$J(\Theta) = \frac{1}{2}(\mathbf{Y} - \mathbf{X}\Theta)^T(\mathbf{Y} - \mathbf{X}\Theta) \tag{51}$$

$$\hat{\Theta} = \left(\mathbf{X}^T \cdot \mathbf{X}\right)^{-1} \cdot \mathbf{X}^T \cdot \mathbf{Y} \tag{52}$$

The constant parameter vector Θ depends on which global parameter is being estimated and $\hat{\Theta}$ is the ordinary least squares estimator indicated with Equation 52. When an OLS estimator is introduced, assumptions about the residuals are made, including constant variance of residuals across all measurements together with uncorrelated residuals, as shown in Equation 53. Additionally, a zero mean for ϵ, shown in Equation 54, is required, such that best linear unbiased estimator (BLUE) is obtained.

$$E\{\epsilon \cdot \epsilon^T\} = \sigma^2 I \tag{53}$$

$$E\{\epsilon\} = 0 \tag{54}$$

The term σ^2 is the variance of the residuals, and I is the $N \times N$ identity matrix. In the IPCM experiment, noise on the scheduling parameter is not taken into account for the estimation process. Similar to many LPV approaches, linear regression is used as an optimization tool, without using stochastic estimation that explicitly accounts for the noise and disturbances [1]. This approach overlooks the potential impact of noise, as a deterministic model is assumed. Additionally. since IPCM is an open-loop system, without feedback control, noise has a lower impact when compared to model uncertainties or scheduling parameter variations. Noise inserted into the input will propagate through the system, but without a feedback mechanism, there is no way to correct or mitigate it, thus is not considered in the analysis.

The addition of the cart's velocity as a variable, makes it possible to have the full estimation matrix $\mathbf{Z}$ of the entire set of non-linear terms, which equals the matrix shown with Equation 36. The scheduling vector will then take the form:

$$\rho_{ij}(v_0, \theta_0) := \; v_0^i \theta_0^j \quad i + j = d \quad d \in [0, D_{\text{multi}}]$$

where d is the maximum degree for the possible combinations of the two scheduling parameters. The term D_{multi} represents the order of the multivariate polynomial. The relation that is used to estimate the non-linear function with the multivariate scheduling vector is then rewritten and shown in Equations 55 and 56.

$$\widetilde{\mathbf{A}}(v_0, \theta_0) = \sum_{d=0}^{D_{\text{multi}}} \sum_{i+j=d} \mathbf{A}_{ij} \rho_{ij}(v_0, \theta_0) \tag{55}$$

$$\widetilde{\mathbf{B}}(v_0, \theta_0) = \sum_{d=0}^{D_{\text{multii}}} \sum_{i+j=d} \mathbf{B}_{ij} \rho_{ij}(v_0, \theta_0) \tag{56}$$

The terms $\mathbf{A}_{ij}$ and $\mathbf{B}_{ij}$ contain the constant global model parameters a_{ij}, b_{ij}, similar to the univariate case. However, the regression matrix $\mathbf{X}$, will now contain a slightly different form than the univariate OLS, in order to account for the additional variable. The same definition of $x_k := (v_{0,k}, \theta_{0,k})$ is used as in Section IV.A.2, with the same defined index k, and total amount points $N := N_\rho^2$. The regression matrix is shown in Equation 57.

$$
\mathbf{X} = \begin{bmatrix} \rho_{00}(x_1) = 1 & \rho_{01}(x_1) = \theta_{0,1} & \rho_{10}(x_1) = v_{0,1} & \cdots & \rho_{dd}(x_1) = v_{0,1}^{D_{\text{multi}}} \theta_{0,1}^{D_{\text{multi}}} \\ \rho_{00}(x_2) = 1 & \rho_{01}(x_2) = \theta_{0,2} & \rho_{10}(x_2) = v_{0,2} & \cdots & \rho_{dd}(x_2) = v_{0,1}^{D_{\text{multi}}} \theta_{0,1}^{D_{\text{multi}}} \\ \vdots & \vdots & \vdots & \vdots & \\ \rho_{00}(x_N) = 1 & \rho_{01}(x_N) = \theta_{0,N} & \rho_{10}(x_2) = v_{0,N} & \cdots & \rho_{dd}(x_N) = v_{0,N}^{D_{\text{multi}}} \theta_{0,N}^{D_{\text{multi}}} \end{bmatrix} \tag{57}
$$

Equivalently to the univariate case, the solution of this linear regression problem comes from minimizing the cost function shown in Equation 51 and obtaining the OLS estimator in Equation 52.

3. Model Quality

The residual analysis consists of evaluating the Root Mean Squared Error (RMSE) of the residuals, which is a standard metric for model evaluation, or in this case, spline data fitting. Following from Equation 38, the residuals of the spline estimation are calculated by:

$$
\epsilon = \mathbf{Z}_m - \mathbf{X}\hat{\mathbf{c}} \quad \in \mathbb{R}^{N \times 1}
$$

The RMSE of the residuals is given by Equation 58, which uses a logarithmic function due to the very low magnitude of the RMS values for the estimated matrix functions (orders up to 10^{-15}). However, when validation data contains extremely small or large values, the relative RMS, $RMS_{rel}(\epsilon)$, is a more informative metric, which normalizes the RMS score to the range of the validation observations.

$$
RMS(\epsilon) = \sqrt{\frac{1}{N} \sum_{k=1}^{N} \epsilon_k^2}, \quad \log(RMS_{\text{rel}}(\epsilon)) = \log\left(\frac{RMS(\epsilon)}{\max \mathbf{Z}_m - \min \mathbf{Z}_m}\right) \tag{58}
$$

This metric measures how well the spline model's predicted values match the estimated values. A lower RMSE indicates a better fit, meaning the predictions are closer to the estimated values. On the other hand, a higher RMSE suggests a poor fit with greater differences between predictions and estimated values.

As uncertainty is controlled by the spline basis structure, the variance of B-splines is global and independent of the estimated function values in the matrix $\mathbf{Z}$. Following from Equation 43, if the smoothness matrix $\mathbf{H}$ is of full rank, and the pseudo inverse is also equal to the true inverse, the parameter covariance matrix of $\hat{\mathbf{c}}$ can by determined by Equation 59[4].

$$
Cov(\hat{\mathbf{c}}) = \mathbf{C}_1 \tag{59}
$$

$$
Cov(\hat{\mathbf{c}}_{OLS}) = \sigma^2 \mathbf{C}_1 \tag{60}
$$

The B-coefficient variances can be computed from the main diagonal as: $Var(\hat{\mathbf{c}}_q) = Cov(\hat{\mathbf{c}})_{q,q} \ \forall \ q = 1, \ldots J \cdot \hat{d}$. For the univariate and multivariate OLS estimations, the parameter covariance matrix includes the global variance of the residuals σ^2 as shown in Equation 60. As discussed in [4], a more useful statistical measure for evaluating the global quality of a spline model is the logarithm of the mean variance of all B-coefficients within a single spline function, which is computed as shown in Equation 61[4].

$$
\log(\overline{Var(\hat{\mathbf{c}})}) = \log\left(\frac{1}{\mathcal{T}_J \cdot \hat{d}} \sum_q Var(\hat{\mathbf{c}})_q\right) \tag{61}
$$

4. Simulation Setup

Following the equations of motion in Equation 28, the constant parameters used in the simulation are listed in Table 2. To maintain a reasonable balance and responsiveness of the inverted pendulum, which starts with a significant initial offset of $\theta_0 = \frac{\pi}{4}$, the factor K, defined as $K = \frac{M+m}{ml}$, is kept at a moderate value. This prevents the pendulum being dominated by gravity (due to $gK\frac{\sin\theta}{q}$ term) or having high responsiveness to the cart (relative effect of the $\frac{b\cos\theta}{mlq}$ term becomes stronger).

Parameter	Symbol	Value	Unit
Cart Mass	M	5	kg
Pendulum Mass	m	1	kg
Pendulum Length	l	2	m
Friction coefficient	b	0.1	-
Gravitational Acceleration	g	9.81	m/s^2

Table 2. Numerical values of constant parameters used in the simulation of the IPCM.

The response to sinusoidal input force can help visualize the tipping points and natural oscillatory behavior of the IPCM. The applied force is provided by Equation 62, where a Heaviside function is introduced at half the simulation time $T = T_{sim}$, indicated in 63. By applying a sinusoidal force at the linearized system natural frequency ω_n, the fundamental mode can be excited and observations can be made if the system exhibits resonant behavior, which should show excessive displacements.

$$F(t) = A_m \sin\sqrt{\frac{g}{l}}\left(t - \frac{T}{2}\right) H\left(t - \frac{T}{2}\right) \tag{62}$$

$$H\left(t - \tfrac{T}{2}\right) = \begin{cases} 0 & \text{if } t < \frac{T}{2} \\ 1 & \text{if } t \geq \frac{T}{2} \end{cases} \tag{63}$$

The term $\omega_n = \sqrt{\frac{g}{l}}$ is the pendulum natural frequency. Additionally, a sinusoidal input force allows for better comparison of methods than, for instance, using a step input. The sinusoidal input constrains the cart position within bounds, avoiding the abrupt changes and large displacements caused by a step input, which can mask the differences between methods as cart position and velocity will keep increasing.

The ordinary differential equations (ODEs) presented in Equation 28 are linearized and solved numerically using a fourth-order Runge-Kutta method, that follows the rule:

$$x_{t+1} = x_t + \frac{h}{6}\left(f_1 + 2f_2 + 2f_3 + f_4\right)$$

The term x_t is the state vector at time step t and x_{t+1} is the state vector at time step $t+1$, with the difference between the two of $h = 0.01$ seconds representing the fixed time step. The intermediate values are computed as follows:

$$f_1 = f(x_t, u_t), \quad f_2 = f(x_t + \tfrac{h}{2} f_1, u_t), \quad f_3 = f(x_t + \tfrac{h}{2} f_2, u_t), \quad f_4 = f(x_t + h f_3, u_t)$$

with $f(x_t, u_t) = f_0 + A\Delta x + B\Delta u$, shown with Equation 35, the LPV function of the corresponding abovementioned linearization methods.

V. Results & Discussion

This section presents the results of the main objective in this paper, which is to investigate the applicability of splines as scheduling functions applied to a LPV model. First, considering the experiment setup, a multivariate simplex B-spline has been created to estimate $\mathbf{Z}$ from Equation 36 with $s_2^4(x_{2601}) \in \mathbb{R}^{2601\times 1}$, with a total number of datapoints x_k, from $N := N_\rho^2 = 51^2$. The data points are spread on a square grid $(v, \theta) \in \mathbb{R}^2$, $[v_{\min}, v_{\max}] \times [\theta_{\min}, \theta_{\max}] = [-2, 2] \times [0, 2\pi]$ with the triangulation and structure of continuity indicated in Figure 4. The use of 51 points per scheduling parameter, generated by the linearly spaced vectors (as described in Section IV.A.2) ensures that the two equilibrium LTI points at $(v_0, \theta_0) = (0, \pi)$ and $(0, 0)$ are included.

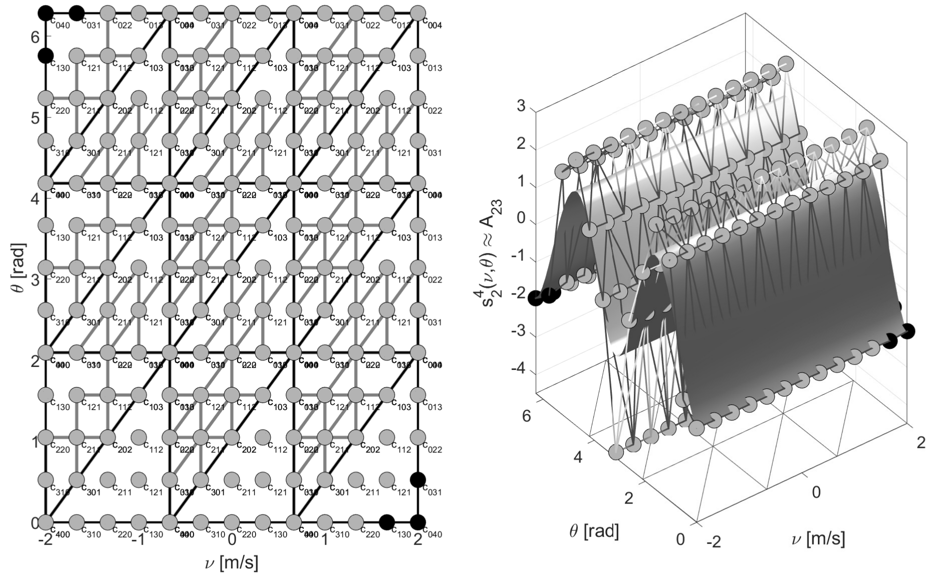

Figure 4. Triangulation of 18 simplices on a $[3 \times 3]$ square grid with the structure of continuity C^2 showing the relations between the 270 $(J \cdot \hat{d})$ B-coefficients of B-spline with degree $d = 4$. Circles on the edges of the domain (black) show B-coefficients that are not part of continuity structure, while circles in gray build the continuity structure. The B-Net of the polynomial estimating $\mathbf{A}_{23}$ is shown on the right.

For the LPV model, the requirement of continuity is at least C^1, as the Jacobian matrices are being estimated, which requires continuity at the first derivative. Furthermore, the Jacobian and Input matrices from Equations 33a and 33b contain sines and cosines, which require higher continuity from the approximating B-spline. This is due to the nature of the trigonometric functions, that are smooth, infinitely differentiable, and periodic, which necessitates differentiability at the triangulation edges.

However, the cost of enforcing continuity constraints, as shown in Figure 4, by linking the splines B-coefficients, is on the expense of the spline's flexibility. Each increase in the desired level of continuity decreases the number of free B-coefficients available, lowering the spline's ability to precisely fit a given function [4]. Therefore, the Degrees of Freedom (DOF) of the spline represent the number of B-coefficients, $\hat{\mathbf{c}}$, that are free to be varied to control its shape, which are constrained to lie within the null-space of $\mathbf{H}$. The basis for the null space of the smoothness constraints, Γ, is given by:

$$\mathbf{c} = \Gamma \cdot \tilde{\mathbf{c}}, \quad \Gamma = \mathrm{null}(\mathbf{H})$$

where $\tilde{\mathbf{c}}$ are the (free) unconstrained B-coefficients. With this relation, the spline coefficients $\mathbf{c}$ can be expressed as a linear combination of basis vectors, such that the number of free parameters $\tilde{\mathbf{c}}$ controlling the spline's shape is equal to the number of columns in Γ. For the selected continuity C^2 of the selected spline $s_2^4(x_k)$, the number of DOF of the spline $\tilde{\mathbf{c}} = 46$ out of a total number of $\hat{\mathbf{c}} = 270$ B-coefficients, obtained by total number of simplices $J = 18$ multiplied with total number of valid permutations $\hat{d} = 15$ calculated with Equation 15.

Figure 5 illustrates the variance of the B-coefficients, which is notably higher at the B-coefficients that do not belong to the continuity structure, as depicted in Figure 4. These coefficients are located at the edges of the scheduling parameter space as depicted by the 3D representation. This is expected as the variance of B-spline coefficients is higher at the edges because fewer basis functions overlap, resulting in increased variance compared to the interior. It can also be observed from Figure 5 and the calculation of the mean variance for varying spline spaces, that increasing the continuity order, at a fixed degree, leads to a decrease in the mean variance.

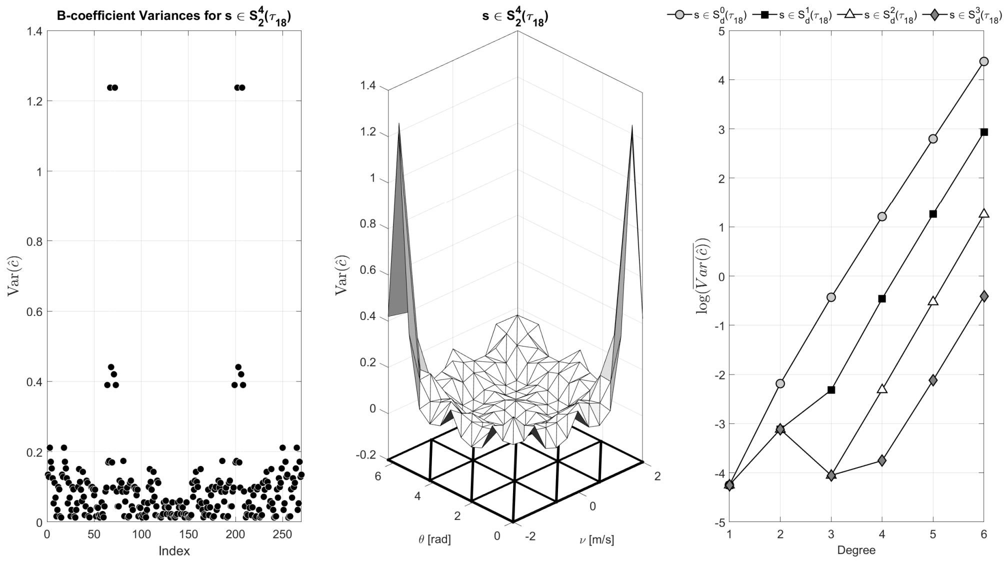

Figure 5. Variance of B-spline estimated B-coefficients shown versus the total number ($J \cdot \hat{d} = 270$) of indices (left) and over the triangulation of 18 simplices (middle). The logarithm of the mean of the global variance per varying continuity level and degree is shown on the right.

The B-spline per estimated parameter of LPV model, given **Z** matrix of estimated parameters in Equation 36, is shown in Figure 6. It can be seen that a spline with a relatively low degree, $s \in S_4^2$ provides an accurate fit to the datapoints x_k generated by **Z**. This specific spline parametrization was selected because, through simulation, it demonstrated best performance measured with the lowest RMSE among the tested methods for the provided simulation time.

Figure 7 displays the log(RMSE) for four spline spaces, varying in degree and continuity, compared to the multivariate OLS degree per estimated parameter of **Z**. Results have been obtained for varying simplex grid triangulations but a $\mathcal{T}_{18}$ triangulation was chosen as the minimum triangulation exhibiting significant differences between multivariate OLS and spline space performance across all estimated parameters. As similarly obtained in [4] and [12], increasing spline order correlates with decreasing RMSE. Additionally, increasing the continuity C^r does decrease the approximation power, as the RMSE for increasing continuity orders is increased, as can be observed from Figure 7. Comparing the B-spline values with those obtained from multivariate OLS, all examined levels of continuity have higher approximation power than the OLS, which for a polynomial approximation, means that B-splines outperform OLS methods. Similar observation, that the selected B-spline shows better performance, can be made for the relative RMSE of the residuals for all the polynomial methods, when compared at $d = 4$ with $N_\rho = 51$ points, with results shown in Table 3.

While the relative RMS provides a general measure of model quality, it does not reveal local accuracy (per data point), which is important for regions of the dataset that might be approximated better or worse. A small error in a region where values are near zero, can have a significant impact on estimation accuracy. To address this, the relative model residual ϵ_{rel} is scaled using the maximum of the model values and the model value range around each data point as depicted in Equation 64.

$$\epsilon_{rel}(\nu, \theta) = \frac{\mathbf{Z} - \mathbf{X}\hat{\mathbf{c}}}{\max(\max \mathbf{Z} - \min \mathbf{Z}, \max |\mathbf{Z}|)} \tag{64}$$

This approach of calculating the ϵ_{rel} is similar to what has been done in [21], where the term $\max |\mathbf{Z}|$, ensures that if the range is too small, or even zero, the maximum absolute value is used as the scaling factor. Choosing the maximum ensures the denominator remains nonzero, while providing a normalization factor. Similarly to

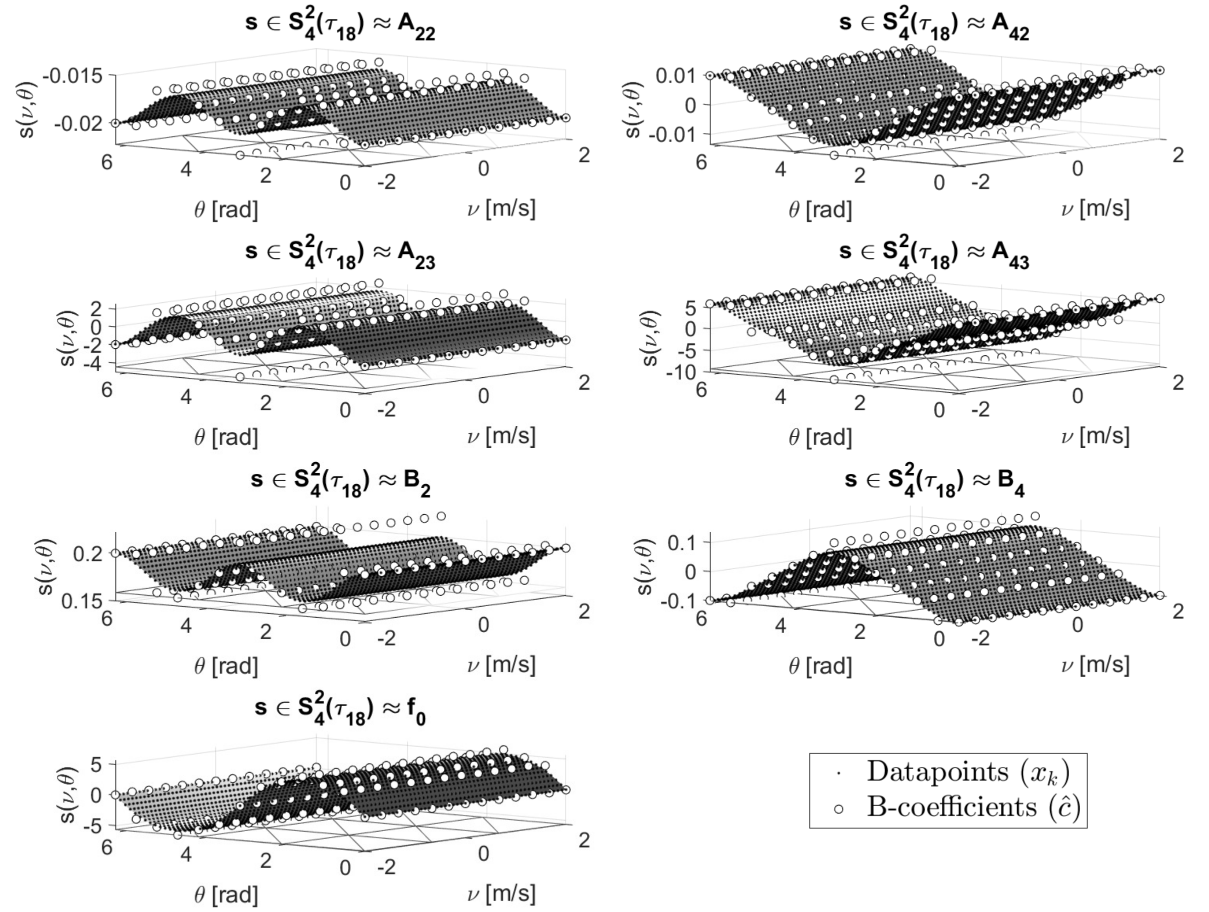

Figure 6. Multivariate spline model with degree 4, continuity 2 on 18 simplices per estimated LPV state space, input matrix and non-linear function terms. The grid is 3×3 with a total of 2601 data points with 270 $(J \cdot \hat{d})$ estimated B-coefficients.

Figure 6, the scaled residuals are plotted for all the estimated functions and shown in Figure 8.

Looking at the plots, several observations can be made. First, the scaled residuals indicate that the applied B-spline, $s_2^4(x_{2601})$, approximates the estimated LPV state-space, input matrix, and nonlinear function terms well, by observing that the magnitude of the residuals remains relatively small. Second, the scaled residuals for the terms $\widetilde{\mathbf{A}}_{23}(\nu_0, \theta_0)$, $\widetilde{\mathbf{A}}_{43}(\nu_0, \theta_0)$, and $\widetilde{\mathbf{f}}_0(\nu_0, \theta_0)$ are an order of magnitude higher than the other estimated parameters. This is expected from the model, as these terms, according to Equation 34, represent the most strongly coupled components that contain the primary modes of the dynamics of the nonlinear system. For example, the coupling between the cart's acceleration and the pendulum's angular motion is embedded in these terms. Additionally, they describe the potential energy of the system because they are only terms containing the effects of gravity. These reasons also provide an explanation to the question why single-parameter estimators, depending exclusively on θ, such as zero-order hold and univariate OLS, approximate the system to high level of accuracy, as observed in the simulation results in Figure 9.

An additional observation for the residuals per estimated parameter is that, due to the term q_0, which is itself a trigonometric function appearing in all estimated functions, they exhibit sinusoidal behavior in θ. Specifically, for angles in the range $\theta_0 \in \left(\frac{\pi}{2}, \frac{3\pi}{2}\right)$, the system experiences the highest residual magnitude, reflecting the greatest instability, as can be seen in Figure 8. This aligns with the physical interpretation that

	$\log(\mathbf{RMS}_{\text{rel}}(\epsilon))$						
Method	$\mathbf{A}_{22}$	$\mathbf{A}_{42}$	$\mathbf{A}_{23}$	$\mathbf{A}_{43}$	$\mathbf{B}_{2}$	$\mathbf{B}_{4}$	$\mathbf{f}_{0}$
P_{uniOLS}	/	/	-1.6134	-3.1549	/	-3.8963	-3.2286
$\text{P}_{\text{multiOLS}}$	-1.5852	-3.8963	-1.6273	-3.1545	-1.5852	-3.8963	-3.2286
$s \in S_4^2(\mathcal{T}_{18})$	-4.7137	-6.7188	-3.9461	-5.4953	-4.7137	-6.7188	-4.8473

Table 3. Comparison of the Root Mean Squared Error (RMSE) of the residuals per estimated parameter for a 4^{th} degree polynomial and $N_\rho = 51$ ponits.

when θ_0 is within this range, the tangential component of gravity ($mg \sin\theta$) is maximized, producing the greatest torque and driving the strongest motion of the pendulum, due rapid conversion of potential into kinetic energy. This, in turn, results in the strongest interaction with the cart, as the pendulum's torque is transferred, via the pivot point, proportional to the force acting on the cart increasing or decreasing its acceleration.

The results of the Simulation, with the setup explained in Section IV.B.4, is shown in Figure 9. The metric used for comparison between the four LPV methods is Root Mean Square difference between the non-linear model states and the estimated states, computed by:

$$\text{RMS} = \sqrt{\frac{1}{T_s}(\mathbf{X} - \hat{\mathbf{X}})^T(\mathbf{X} - \hat{\mathbf{X}})}$$

where T_s is the total simulation time, $\mathbf{X}$ is the non-linear state vector, while $\hat{\mathbf{X}}$ is the estimated LPV state vector. It can be observed that for a fourth-degree polynomial approximator, the simplex B-spline $s \in S_4^2(\mathcal{T}_{18})$ outperforms the other three methods at $x_k = 51$ data points per scheduling parameter. While increasing the order of the ordinary least squares (OLS) polynomial improves estimation accuracy, the advantage of having piecewise lower-order polynomials lies in favor of the use of the B-spline approach. As noted in [3], increasing the number of internal knots (equivalent to triangulation of simplices in higher-dimensions) in a B-spline representation allows for a lower polynomial order while improving approximation quality. This results in a solution that is closer to the true optimum while maintaining a similar numerical complexity compared to using a higher-degree polynomial and lower amount of knots.

Additionally, as expected, the addition of an external force in the open-loop simulation leads to deviations in the cart's position, as it perturbs the starting IPCM dynamics, which is solely due to the induced motion of the pendulum. Since the equations of motion do not explicitly contain the cart's position in Equation 28), as it is obtained through the integration of velocity, any discrepancies in velocity accumulate over time, leading to amplified deviations. This effect is particularly pronounced in open-loop simulations, where the errors are not corrected (controlled), leading to significant variations across different methods. This trend can be observed in Figure 7, which after 20 seconds, shows the impact of the force on the cart's position. The numerical RMSE values of the simulation are presented in Table 4.

It should be noted that the number of data points depends on the number of scheduling parameters being estimated. This implies that if the number of points in the piecewise constant approach increases, the ZOH method achieves higher estimation accuracy, yielding the lowest RMS observed (order 10^{-4}) across a range of simulations, varying in simulation time and number of datapoints. Notably, this holds only with a single scheduling parameter θ_0. As argued earlier, the primary modes in the Jacobian matrix of the IPCM dynamical system can be accurately estimated using only the pendulum angle, so these results are not surprising.

The main challenge of using the piecewise constant approach arises in the case if closed-loop control is applied for the pendulum. At any $t_{switch} = kT_d$, where switching occurs, discontinuities (i.e., sudden jumps between values) are introduced. These discontinuities can significantly affect the stability of a control

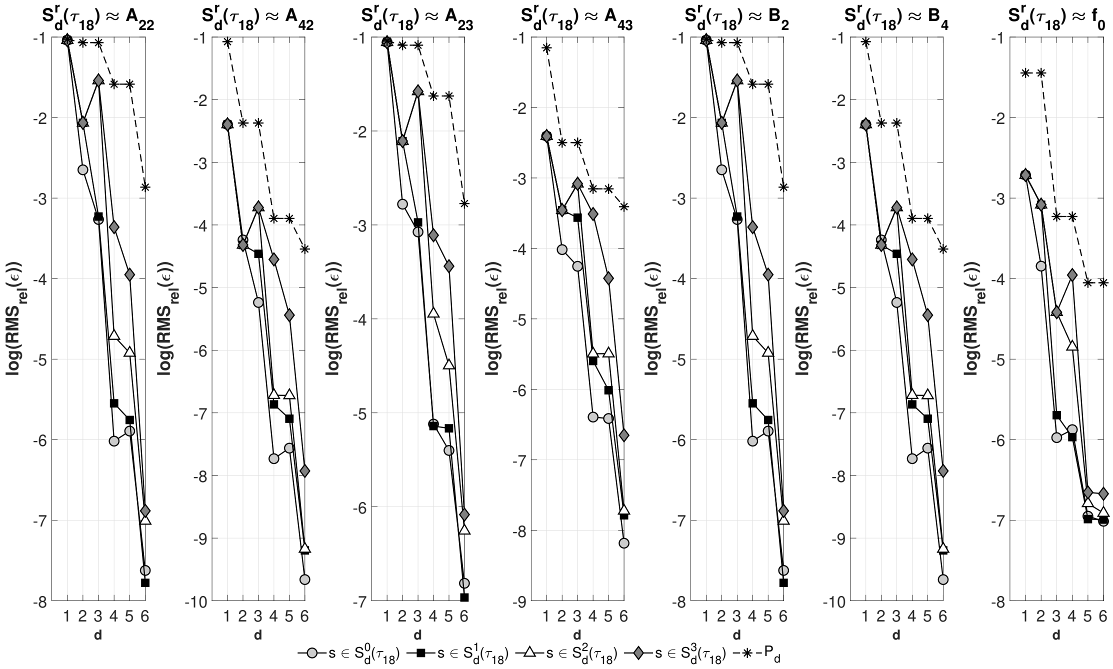

Figure 7. Logarithm of the relative Root Mean Squared Error of the residuals for all estimated functions of the LPV model for different spline spaces with varying spline continuity and degree, over a triangulation of 18 simplices ($[3 \times 3]$ grid) compared to multivariate OLS polynomial of varying degree P_d.

system, particularly in the case of a proportional-integral-derivative (PID) controller, where the derivative component of such controller is especially sensitive to abrupt changes, potentially leading to severe instability at the switching points. As recently observed in [22], the occurrence of chatter, which is characterized by high-frequency oscillations in the control input due to discontinuities or constraints in the control law, further exacerbates this issue. Specifically, the first-order actuator dynamics model fails to accurately capture the resulting second-order actuator behavior. In contrast, B-splines perform significantly better in this regard, as they allow for flexible selection of the spline continuity order, mitigating the adverse effects of such discontinuities. One important consideration, as previously mentioned, is that increasing continuity comes at price, which is reduced ability to approximate the data points.

Figure 10 presents the trajectory of the B-spline estimated scheduling parameters plotted on the simplex grid, providing an alternative perspective on the simulation. The trajectory is divided into two distinct phases: the first 20 seconds correspond to data points obtained only from pendulum motion (named unforced), while the remaining 20 seconds reflect the system's response to the applied external force (named forced data points). Additionally, the scheduling parameters are then substituted into Equation 28, to obtain a 3D trajectory plot of the cart acceleration and pendulum angular motion. Two things can be observed: first, as expected, the applied force is moving the data towards the edge simplices, but due to C^2 continuity of the selected spline, this does not pose an issue, as long as the data points are within the defined scheduling parameter grid. The second is that corner simplex pairs (t_1/t_2, t_5/t_6, t_{14}/t_{15}, and t_{17}/t_{18}), either contain no data points or only have them at the vertex edges. As shown in Figure 5, having simpices with datapoints only at the edges will result in loss of smoothness and reduced accuracy in the interior of the said simplices, which will make them badly defined. This indicates a need of optimizing the simplex shape, such that simplices that contain no data are removed. Multiple methods are proposed in literature, with Type I/II hypercube triangulation method explained in [4] or constrained Delaunay triangulation [23] among the many approaches to this problem.

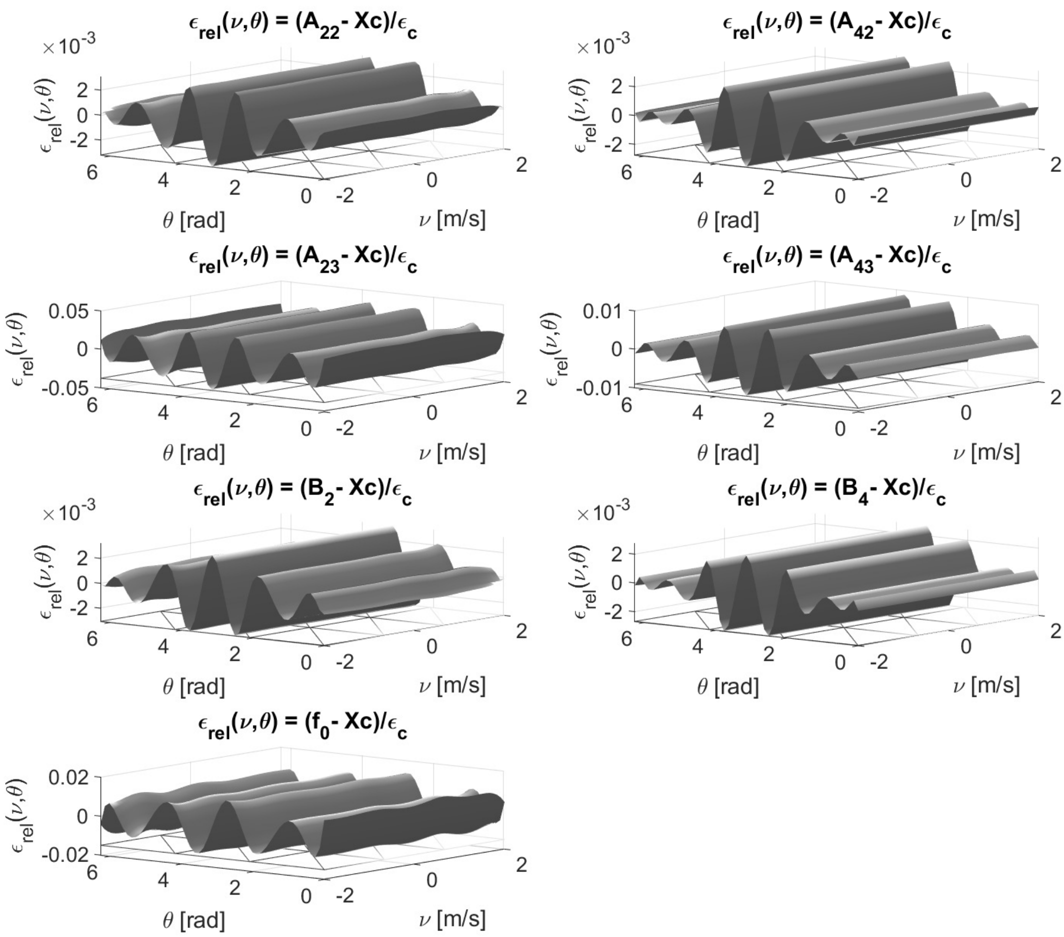

Figure 8. Scaled Relative residuals $\epsilon_{rel}(\nu, \theta)$ for a simplex B-spline $s \in S_4^2$ of the estimated LPV state space, input matrix and non-linear function terms. In the expression, the scaling term is given by: $\epsilon_c = \max(\max \mathbf{Z} - \min \mathbf{Z}, \max |\mathbf{Z}|)$.

As a final result, a variation of the initial conditions is performed, in order to see the spread of the scheduling parameter on the simplex grid $\mathcal{T}_{18}$ which is illustrated in Figure 11. The initial state vector $\mathbf{X}_0 = [0\ 0\ \theta_{00}\ 0]^T$ is varied in a linear fashion within the bounds $\theta_{0,\text{lin}} \in [0.1, 1.95\pi]$ and is sampled across $N_{\text{sim}} = 1000$ simulations with added noise. The noise initial angle $\theta_{0,\text{noisy}}$ follows a standard Gaussian distribution with mean $\mu = 0$ and standard deviation $\sigma = 1$, scaled by $\sigma = 0.05$ (ensuring 99.7% of values fall within $\pm 3\sigma$):

$$\theta_{0,\text{noisy}} = \sigma \cdot Z, \quad Z \sim \mathcal{N}(0, 1).$$

The final perturbed initial values are obtained by adding the noise to the linear samples $\theta_{00} = \theta_{0,\text{lin}} + \theta_{0,\text{noisy}}$. The pendulum angle θ_0 exhibits oscillations across the parameter grid in response to varying cart velocities. While fluctuations are observed, the pendulum remains within a confined bounds of the scheduling parameter grid, with largest swings at positive cart velocities. This motion follows a periodic trend, despite the injected random noise. As cart velocities increase, the variation becomes grater, indicative of greater instability in the system, but still within the confined bound. Thus, the system's deterministic nature enables accurate prediction of its trajectory based on initial conditions. Since the dynamics are heavily influenced by these initial parameters, bounding the scheduling parameters within a specific range, which is derived from an

	RMS $\times 10^{-3}$			
LPV Method	X [m]	v [m/s]	θ [rad]	Ω [rad/s]
Zero-Order Hold	12.45	5.04	5.45	9.18
Univariate OLS	10.17	5.40	5.98	9.83
Multivariate OLS	8.93	11.04	14.82	23.68
B-Spline	8.19	3.85	3.99	6.74

Table 4. Root Mean Square Error (RMSE) of the state vector **X** compared at $x_k = 51$ datapoints per scheduling parameter and polynomial degree $d = 4$ for the polynomial estimating methods.

apriori understanding of the system dynamics, can possibly lead to the development of a robust controller.

VI. Conclusion

This paper explored the parametrization of nonlinear models using the affine quasi-Linear Parameter-Varying (qLPV) approach, with a particular focus on the identification of an appropriate scheduling function. A key challenge was selecting a scheduling function that ensures a smooth and accurate transition between local Linear Time-Invariant (LTI) models while accurately estimating the underlying system behavior. The findings demonstrate that multivariate simplex B-splines can serve as a scheduling function for State-Space quasi-Linear Parameter-Varying (SS-qLPV) models, which are commonly used for representing nonlinear physical systems. Their key advantage is providing a global approximation of the linearized parameter varying model while making use of overlapping local basis functions over the entire scheduling parameter domain.

A demonstrator, Inverted Pendulum on a Cart Model (IPCM), has been used to model the nonlinear behavior of the system in an open-loop setting. The model has been linearized to first order using an affine LPV representation, where the cart's velocity v and pendulum angle θ serve as scheduling parameters to construct a scheduling grid. Over this defined parameter grid, various methods for generating the scheduling function have been explored, including single-variable zero-order hold (ZOH), ordinary least squares (OLS), and multivariate OLS with B-splines.

The results show that, compared to polynomial estimation methods like multivariate OLS at the same polynomial order, taken as $d = 4$, a B-spline in the spline space $s \in S_4^2(\mathcal{T}_{18})$ offers greater approximation power, as shown by the logarithm of RSME of the residuals for the estimated functions in Figure 7. This advantage comes from the spline continuity of derivatives C^2, enabling a smoother interpolation between local LTI models at a relatively small number of data points $N_\rho = 51$ per estimated scheduling parameter. Furthermore, a simulation was conducted over a duration of $T_{\text{sim}} = 40$ seconds, with a sinusoidal input force (at resonant frequency $\omega_n = \sqrt{\frac{g}{L}}$) applied at the midpoint of the simulation time. The true nonlinear model has been integrated using the `ode45` solver, while the various approximation methods were evaluated using a 4th-order Runge-Kutta integration scheme. Analysis of the root mean square error (RMS) of the simulation results demonstrated that B-splines were better estimator than the other methods.

There are several limitations to this study that should be considered. It was observed that B-splines offer greater accuracy under a specific set of conditions, such as the number of datapoints, total simulation time, and the specific input force applied. However, for the majority of other cases, the Zero-Order Hold (ZOH) method for LPV systems proves that with a single scheduling parameter θ, to be computationally less expensive and results in a lower simulation root mean square error (RMSE) across a broader range of varying simulation conditions, including T_{sim} and N_ρ. Nevertheless, one significant disadvantage of the ZOH method is that it varies the scheduling parameters in a piecewise constant manner, switching at time instants $t_{switch} = kT_d$, where k is an integer. This switching introduces discontinuities in scheduling parameters,

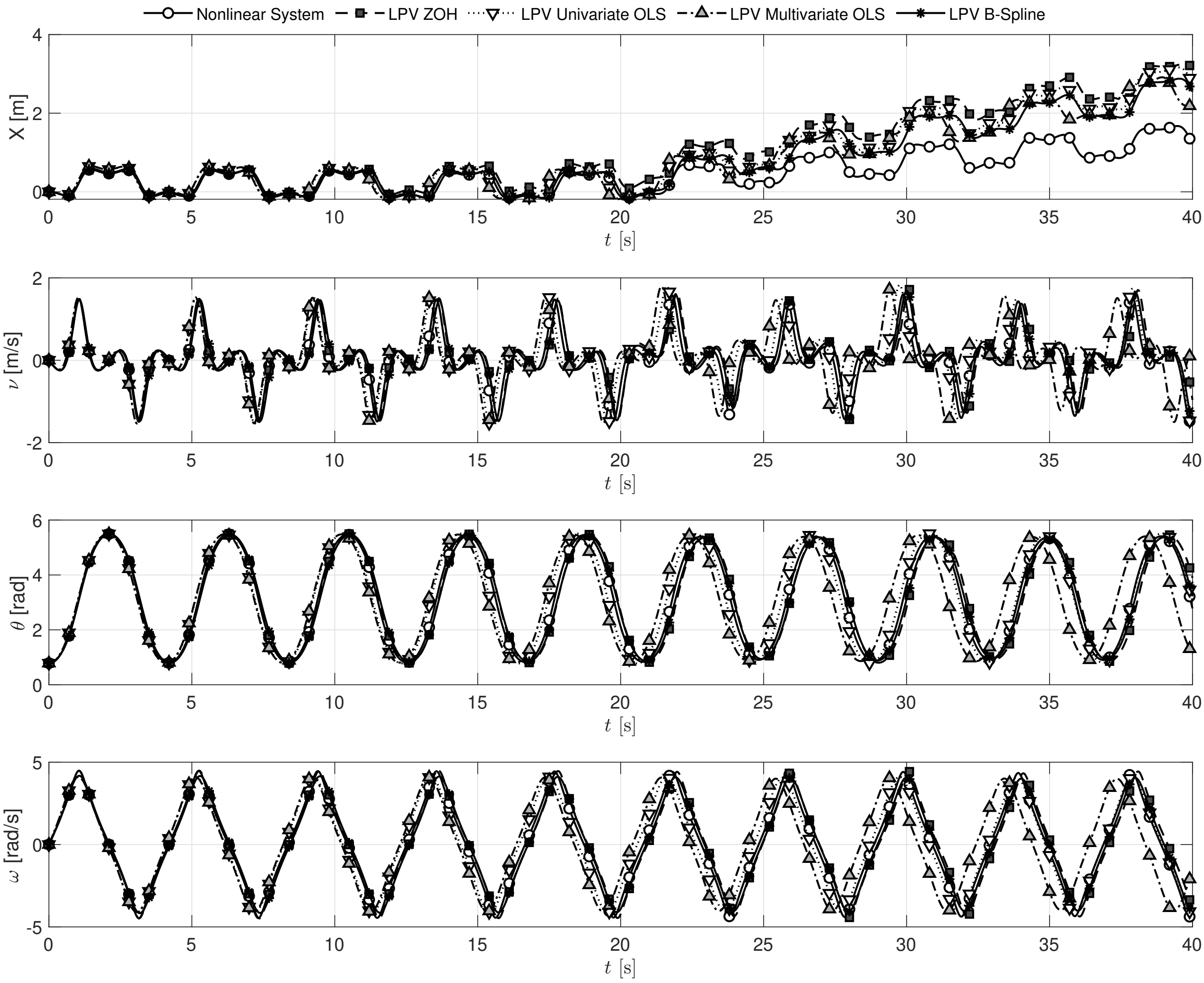

Figure 9. Simulation results of the nonlinear cart-pendulum model, showcasing the state vector **X** of the linearized LPV model integrated using 4^{th} order Runge-Kutta for the 4 LPV methods. The order of the polynomial approximating methods is selected as $d = 4$ and $x_k = 51$ datapoints per scheduling parameter. A input force, with amplitude $A_m = 1$ is applied at 20 seconds.

which can cause abrupt changes in the system's dynamics and negatively affect controller performance. In closed-loop settings, these discontinuities may lead to instability or oscillations, especially in systems that require smooth and continuous adjustments for stable control.

This work opens possibilities for further exploration of multivariate simplex B-splines as scheduling functions for LPV systems, particularly in applications involving highly coupled aerodynamic models with multivariate parameters in multiple dimensions. Given that simplex B-splines are inherently scalable to any number of dimensions, they offer significant potential for modeling complex, high-dimensional aerodynamic systems. In this experiment, a grid was employed as the scheduling parameter domain, which did not appear to fully utilize all of the simplices, as evidenced by spread of error in the residuals. To improve on this, it would be beneficial to optimize the simplices using Constrained Delaunay Triangulation (CDT) or Type I/II hypercube triangulation method. A subsequent step in this research direction should focus on applying the proposed scheduling function within a closed-loop LPV framework (e.g., Gain-scheduled Proportional-Integral-Derivative (PID), Linear Quadratic Regulator (LQR) or Model Predictive Control (MPC)

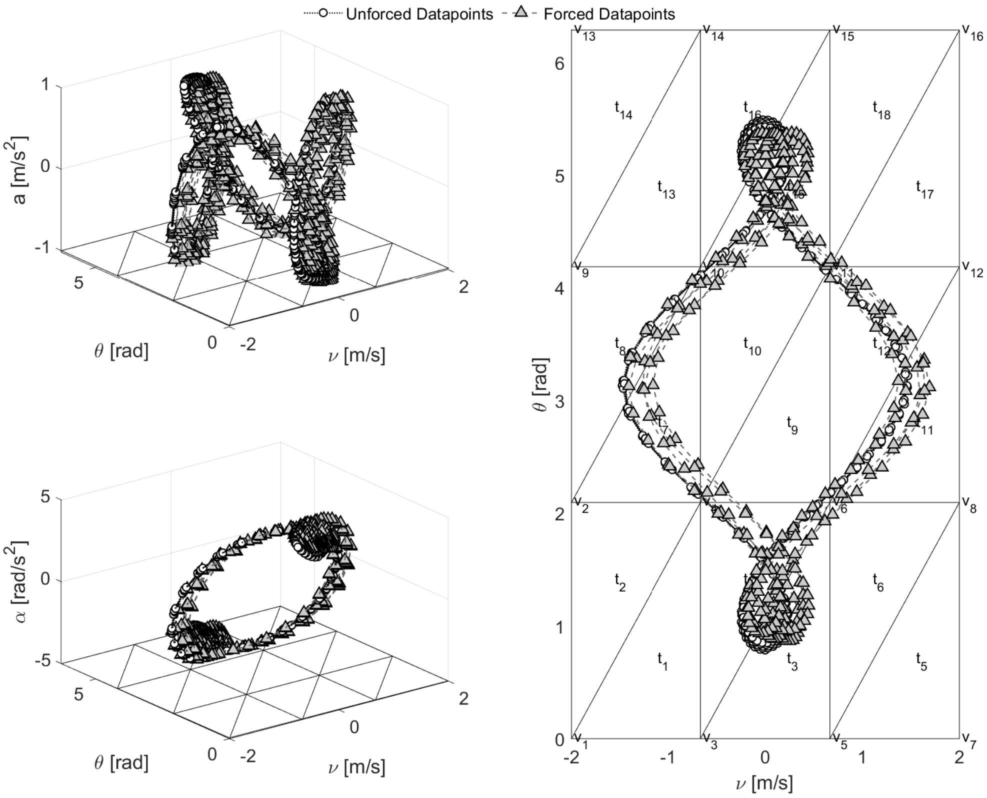

Figure 10. Trajectory of the B-spline estimated scheduling parameters *nu* and θ ploted over the simplex grid. 3D plots of the acceleration of the cart a and angular acceleration α are shown on the left, with a difference between datapoints before force application at 20 sec, and after. 2D plot over the triangulation of $\mathcal{T}_{18}$ simplices, with the same distinction of forced/unforced data points is shown on the right.

controllers), with a primary area of investigation being the evaluation of control stability and performance when the operational and scheduling parameter conditions are varied.

References

[1] Toth, R., *Modeling and identification of Linear Parameter-Varying systems*, Springer, Germany, 2010. DOI:10.1007/978-3-642-13812-6.

[2] Olivier Sename, P. G., and Bokor, J., *Robust Control and Linear Parameter Varying approaches: Application to Vehicle Dynamics*, Springer Berlin, Heidelberg, 2013. DOI:10.1007/978-3-642-36110-4.

[3] Hilhorst, G., Lambrechts, E., and Pipeleers, G., "Control of linear parameter-varying systems using B-splines," *2016 IEEE 55th Conference on Decision and Control (CDC)*, 2016, pp. 3246–3251. DOI:10.1109/CDC.2016.7798757.

[4] de Visser, C. C., "Global Nonlinear Model Identification with Multivariate Splines," Phd thesis, Control & Operations (Aerospace Engineering) (TU Delft), 2011. Available at `https://resolver.tudelft.nl/uuid:6bc0134a-0715-4829-903d-6479c5735913`.

[5] Boonto, S., and Werner, H., "Closed-loop identification of LPV models using cubic splines with application to an arm-driven inverted pendulum," *Proceedings of the 2010 American Control Conference, ACC 2010*, 2010, p. 3100 – 3105. DOI:10.1109/acc.2010.5531139.

[6] Zhang, Z., and Martin, C. F., "Convergence and Gibbs' phenomenon in cubic spline interpolation of discon-

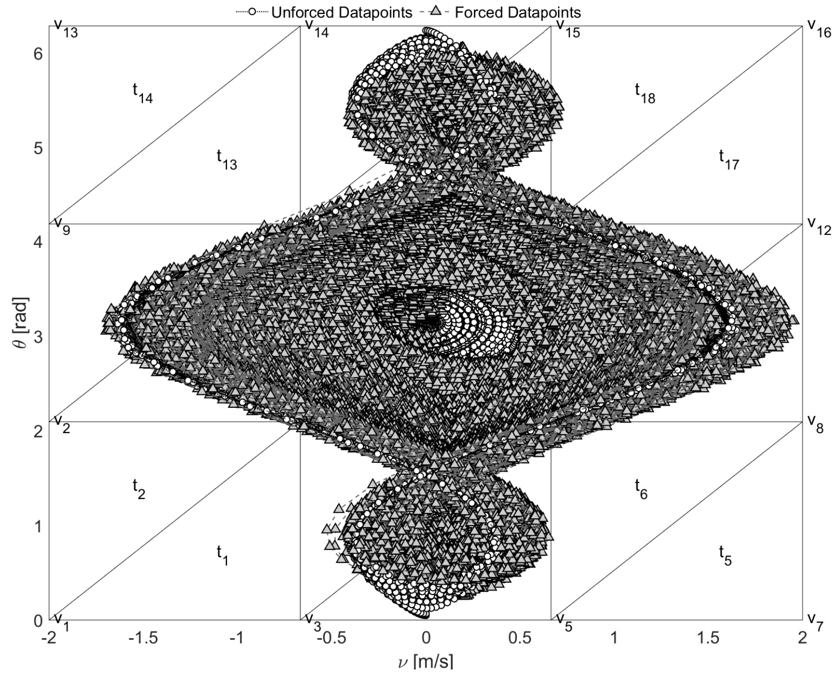

Figure 11. Simulation results of a noise added initial pendulum angle, θ_{00}, over the triangulation of $\mathcal{T}_{18}$ simplices, with the same distinction between datapoints before force application at 20 sec, and after plotted over $N_{sim} = 1000$.

tinuous functions," *Journal of Computational and Applied Mathematics*, Vol. 87, No. 2, 1997, pp. 359–371. DOI:10.1016/S0377-0427(97)00199-4.

[7] Turk, D., Jacobs, L., Singh, T., Decré, W., and Swevers, J., "Identification of Linear Parameter-Varying Systems Using B-splines," *2019 18th European Control Conference (ECC)*, 2019, pp. 3316–3321. DOI:10.23919/ECC.2019.8795917.

[8] Atoui, H., Sename, O., Milanes, V., and Martinez Molina, J., "Toward switching/interpolating LPV control: A review," *Annual Reviews in Control*, Vol. 54, 2022. DOI:10.1016/j.arcontrol.2022.07.002.

[9] Armanini, S. F., Karásek, M., and de Visser, C. C., "Global Linear Parameter-Varying Modeling of Flapping-Wing Dynamics Using Flight Data," *Journal of Guidance, Control, and Dynamics*, Vol. 41, No. 11, 2018, pp. 2338–2360. DOI:10.2514/1.G003505.

[10] Marcos, A., and Balas, G. J., "Development of Linear-Parameter-Varying Models for Aircraft," *Journal of Guidance, Control, and Dynamics*, Vol. 27, No. 2, 2004, p. 218 – 228. DOI:10.2514/1.9165.

[11] Lai, M., and L.L.Schumaker, *Spline Functions on Triangulations*, Cambridge University Press, 2010. DOI:https://doi.org/10.1017/CBO9780511721588.

[12] de Visser, C. C., Chu, Q. P., and Mulder, J., "A new approach to linear regression with multivariate splines," *Automatica*, Vol. 45, No. 12, 2009, pp. 2903–2909. DOI:10.1016/j.automatica.2009.09.017.

[13] Tol, H. J., de Visser, C. C., van Kampen, E., and Chu, Q. P., "Nonlinear Multivariate Spline-Based Control Allocation for High-Performance Aircraft," *Journal of Guidance, Control, and Dynamics*, Vol. 37, No. 6, 2014, pp. 1840–1862. DOI:10.2514/1.G000065.

[14] de Boor, C., "B-form basics. In:G. Farin, ed., Geometric modeling: Algorithms and new trends," *Society For Industrial and Applied Mathematics*, 1987, pp. 131–148.

[15] Krishnan, A., U, P. K., Bukya, M., Randhawa, P., and Piromalis, D., "A Comparative Study on Intelligent & Adaptive Control Techniques on a Nonlinear Inverted Pendulum Cart Mechanism," *2021 9th International Conference on Reliability, Infocom Technologies and Optimization (Trends and Future Directions) (ICRITO)*, 2021, pp. 1–6. DOI:10.1109/ICRITO51393.2021.9596243.

[16] Olsder, G. J., van der Woude, J. W., Maks, J., and Jeltsema, D., *Mathematical Systems Theory*, 4th ed., VSSD,

Leeghwaterstraat 42, 2628 CA Delft, The Netherlands, 2011. URL https://resolver.tudelft.nl/uuid:021bd7b5-1a8f-4d60-9a75-298550222b62.

[17] Khalil, H., *Nonlinear Systems*, 3rd ed., Pearson Education, Prentice Hall, Upper Saddle River, NJ 07458, 2002.

[18] Johansen, T., Hunt, K., Gawthrop, P., and Fritz, H., "Off-equilibrium linearisation and design of gain-scheduled control with application to vehicle speed control," *Control Engineering Practice*, Vol. 6, No. 2, 1998, pp. 167–180. DOI:10.1016/S0967-0661(98)00015-X.

[19] Awanou, G., Lai, M.-J., and Wenston, P., "The multivariate spline mehtod for scattered data fitting and numerical solution of partial differential equations," *Wavelets and Splines*, 2005, p. 24–75.

[20] Awanou, G., and Lai, M., "On convergence rate of the augmented Lagrangian algorithm for nonsymmetric saddle point problems," *Applied Numerical Mathematics*, Vol. 54, No. 2, 2005, pp. 122–134. DOI:10.1016/j.apnum.2004.09.020, 6th IMACS.

[21] der Peijl, I., "Physical Splines for Aerodynamic Modelling of Innovative Control Effectors," Master's Thesis, Delft University of Technology, 2017.

[22] Stam, N., and de Visser, C. C., *Adaptive Dynamic Incremental Nonlinear Control Allocation for Aircraft With Innovative Control Effectors*, American Institute of Aeronautics and Astronautics, Inc., 2025. DOI:10.2514/6.2025-0082.

[23] Ruppert, J., "A Delaunay Refinement Algorithm for Quality 2-Dimensional Mesh Generation," *Journal of Algorithms*, Vol. 18, No. 3, 1995, pp. 548–585. DOI:https://doi.org/10.1006/jagm.1995.1021.

Appendix

Additional plots regarding the simulation results are shown in this Section, such that the difference between methods is made more visible in the first seconds of the animation. Figure 12 shows the first 4 seconds of the simulation which equates to one full pendulum swing from the initial condition $(\mathbf{X}_0, u_0) = \left([0\ 0\ \frac{\pi}{4}\ 0]^T, 0\right)$. Figure 13 shows the first 2 seconds and Figure 14 shows the first second of the simulation run.

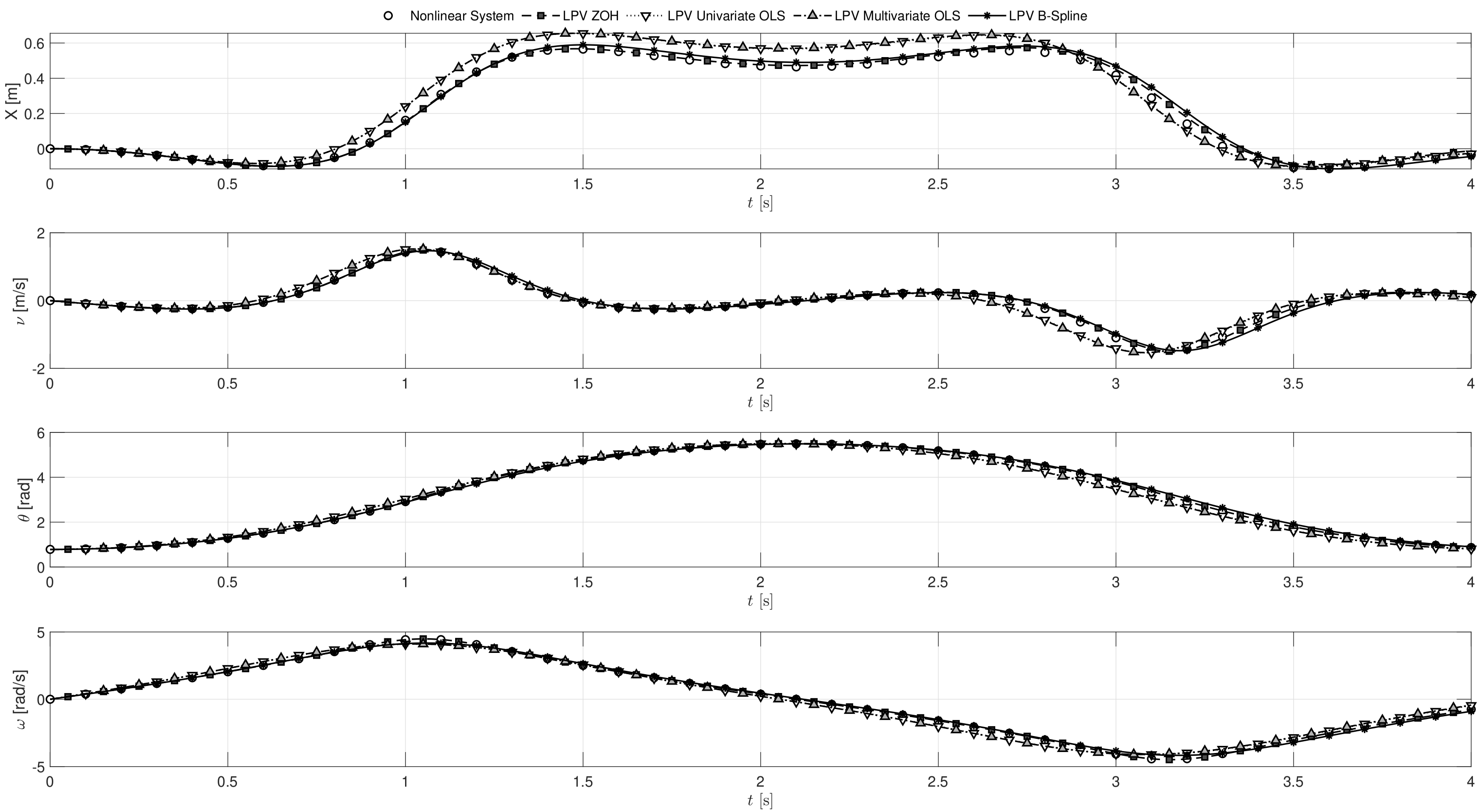

Figure 12. Slice of the first 4 seconds (equal to one full pendulum swing) of the simulation results in Figure 9 of the nonlinear cart-pendulum model, showcasing the state vector **X** of the linearized LPV model integrated using 4th order Runge-Kutta. The order of the polynomial approximating methods is selected as $d = 4$.

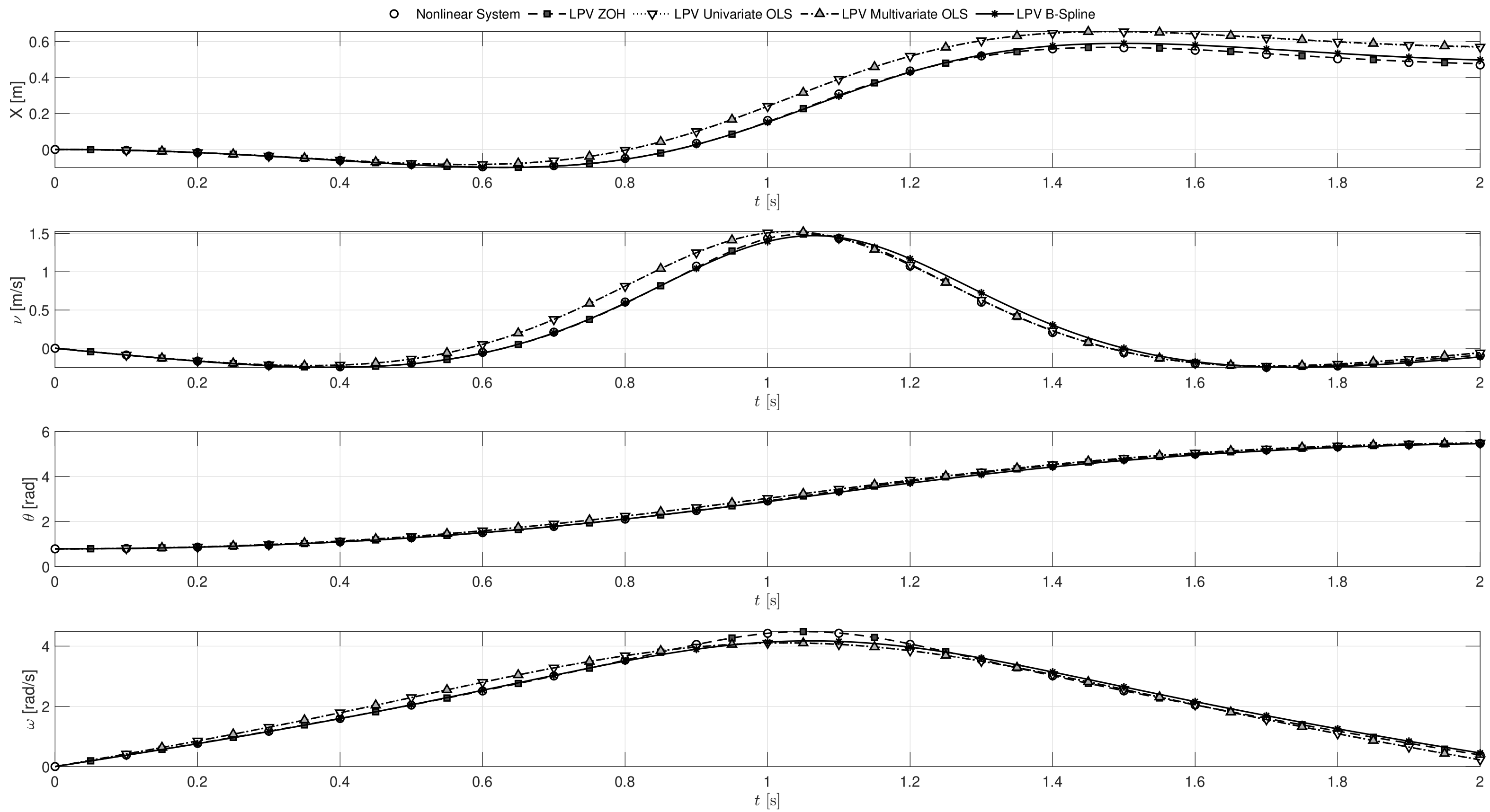

Figure 13. Slice of the first 2 seconds of the simulation results in Figure 9 of the nonlinear cart-pendulum model, showcasing the state vector **X** of the linearized LPV model integrated using 4$^{\text{th}}$ order Runge-Kutta. The order of the polynomial approximating methods is selected as $d = 4$.

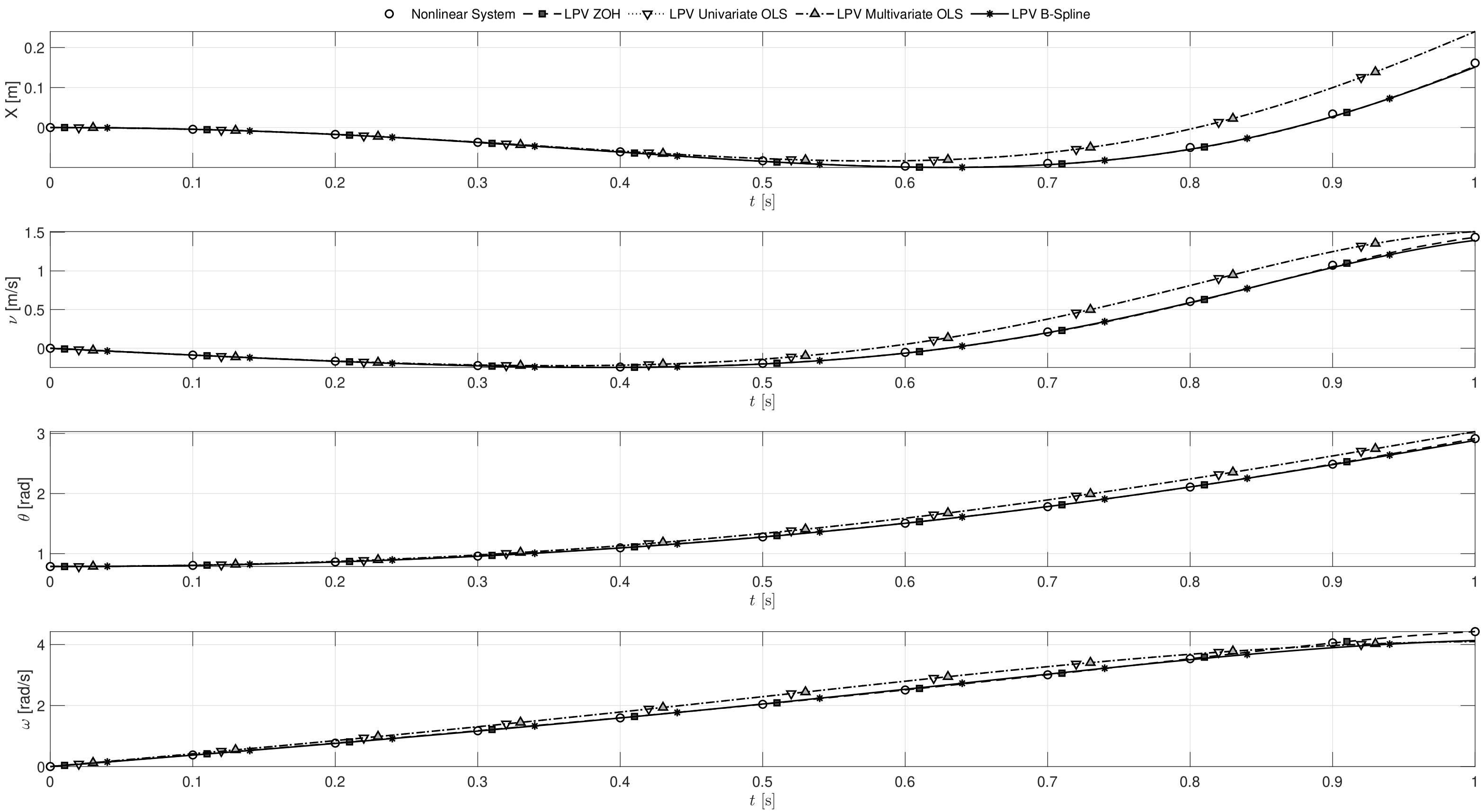

Figure 14. Slice of the first second of the simulation results in Figure 9 of the nonlinear cart-pendulum model, showcasing the state vector **X** of the linearized LPV model integrated using 4th order Runge-Kutta. The order of the polynomial approximating methods is selected as $d = 4$.

Part II

Preliminary Analysis

*This part has been assessed for the course AE4020 Literature Study.

Summary

The following Literature Review presents an in-depth analysis of the available literature, focusing on the core aspects of system modeling of robust Linear Parameter Varying (LPV) systems using multivariate scheduling functions. Its objective is to evaluate current knowledge, identify gaps, and provide a critical assessment of the methodologies and findings of whether multivariate simplex splines can be used as scheduling functions of state-space LPV systems, using data gathered and validated from an already available non-affine aerodynamic model. By using multivariate simplex splines, which facilitate local model identification and are fit scattered datasets in non-rectangular domains, the findings aim to demonstrate whether smooth dependence of the LPV systems on the scheduling function and for a global model can be achieved. This report also highlights the significance of these findings for ongoing research project of the Control & Simulation division, which aims to connect robust flight control and different classes of function approximators, such as the multivariate B-splines.

The literature review methodology involved a systematic search using SCOPUS, TU Delft Control and Simulation Reference Database and WorldCat to gather relevant studies published in the past two decades. This time frame was chosen because nonlinear robust control theory is a 'relatively' new field, as highlighted by [16] and further supported by the historical perspective provided in [17].The selected studies were categorized according to the relevant research areas, which were identified and depicted in Figure 3.1. Key findings from the literature suggest that while methods for LPV modeling are well-researched, with comprehensive references such as [18], [19], [20], and [21], there remains a notable gap in the application of multivariate splines as scheduling function approximators to these models. Although a few studies, including [8] and [22], explore splines as function approximators for LPV systems, their focus has been primarily on Tensor-product splines. These splines, however, are limited in their ability to handle scattered data due to their dependence on structured, grid-based input. This limitation poses a significant challenge, particularly in flight control problems, where the system dynamics can often be approximated as continuous physical processes.

Finally, this literature review highlights a research gap originating from the challenges in generating a global LPV model. The complexity occurs due to the high computational demands and stability restrictions associated with local models [23]. Moreover, because of the local nature of basis functions, the solution systems for multivariate B-splines tend to be highly sparse. This sparsity enables the use of efficient matrix solvers, making it feasible to approach LPV system modeling and identification with multivariate B-splines more effectively.

3

Literature Review

The following Chapter, includes the relevant areas of research for this thesis and gives an overview of what work has already been carried out to the field of research. Figure 3.1 depicts the intersections between Robust control, System Identification and literature on the ICE aircraft, to narrow down the link between the research question and this literature review in the next Chapter. Figure 3.1 illustrates how the literature references align within these intersections, highlighting the commonalities across different sources. Therefore, the relevant areas of research describe the work done in Robust control (3.1) and System Identification (3.2), while bisecting these areas into two smaller subsets: LPV Systems (Chapter 3.3) and Multivariate Splines (Section 3.3.4). Additionally, the application to ICE model is addressed with Subsection 3.4. Finally, Section 3.5 outlines the thesis's contribution to the body of research discussed in the preceding sections.

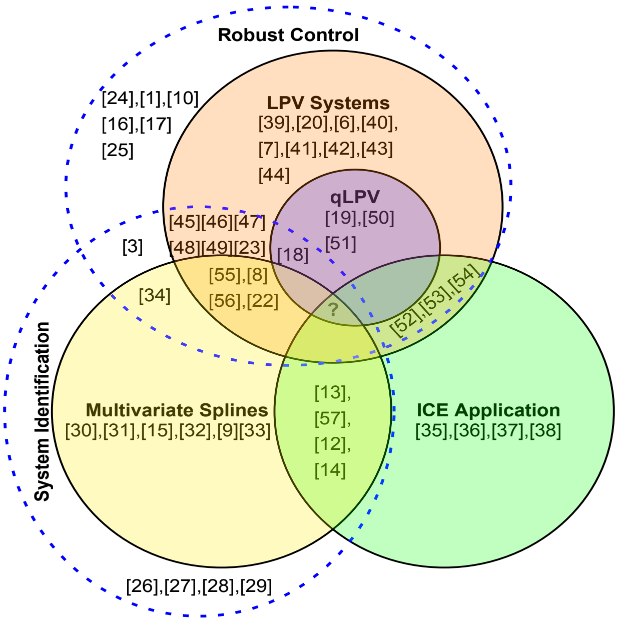

Figure 3.1: Venn diagram depicting the two general research directions: Robust Control and System Identification, while zooming in on the relevant sub-fields: LPV Systems, Multivariate Splines and the application to ICE. All the literature for this paper has been differentiated between its respective fields and intersections, which spans the entire research area of this report. The intersection in the middle of the diagram shows the literature gap that exists when the sub-fields interact with each other.

3.1. Robust Control

One of the main areas of research for this thesis, belongs to the field of robust control, which represents a branch of control theory that deals with the design of controllers for systems subjected to uncertainties. These uncertainties can arise from various sources, such as modeling errors, external disturbances, or changes in system parameters over time. This originates from the fact that the model chosen to represent the real system is never an exact one-to-one match. The primary goal of robust control is to ensure that the system remains stable and satisfies performance requirements under all possible conditions, despite these uncertainties.

As explained in [16], the period between the late 1970s to the early 2000s, robust control techniques such as H_∞, μ/K_m-synthesis and Bilinear Matrix Inequality (BMI)/Linear Matrix Inequalities (LMI)/Integral Quadratic Constraint (IQC) were established, that provided broader uncertainty regions and set-up of robustness margins that ultimately enhanced the reliability of control systems. However, a major challenge is that these fundamental robust control methods typically rely on precise prior assumptions about the size and structure of uncertainties. This means they lack the ability to adapt, in real-time, when newly acquired data contradicts these initial assumptions about uncertainty bounds [16]. Furthermore, all of these techniques have the assumption of regarding systems of linear (usually also finite-dimensional and time-invariant) static form [17]. A system is described as linear if it satisfies two properties: superposition and scaling. Superposition implies that if the system's response to input $x_1(t)$ is $y_1(t)$ and the response to input $x_2(t)$ is $y_2(t)$, then the response to a combination $ax_1(t) + bx_2(t)$ results in $ay_1(t) + by_2(t)$, where a, b are constants. Scaling corresponds to the property that if the input is multiplied by a constant factor, the output is also multiplied by that same factor. A system is static if its output at any given time depends only on the input at that same time. According to [24], a major stepping stone of modern control theory is the formulation of the H_∞ controller, but H_∞ robust controller designs are most effectively used when applied on uncertain linear systems [17].

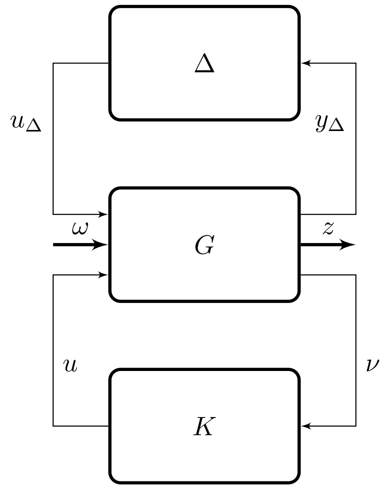

Figure 3.2: Uncertainty framework for controller synthesis of robust control systems. The plant (G), usually restricted to linear system, can contain single (LTI) or multiple (MLTI) models, linear parameter/time-varying (LPV/LTV) models, reference models, performance/specifications, etc. It is subjected to generalized disturbance input (w) and generalized output (z), while the Uncertainty (Δ) can depict structured or unstructured uncertain parameters, time-varying, nonlinearities or delays (encompassed into y_Δ) adding to the disturbed control input (u_Δ) to plant G. The Controller (K), can be full order or reduced order LTI controllers of any structure and complexity, gain scheduling, etc. that has sensor measures (ν) as input, and outputs (u) as control input to P.[58]

Alternative techniques exist, that directly address the nonlinearities to improve system performance for tailless aircraft, such as the feedback linearization approach. However, the fundamental assumption in this method is perfectly modeled plant dynamics and can be canceled exactly, which is not realistic and requires a robust controller to suppress undesired behavior due to plant uncertainties [10]. Nonlinear robust control theory offers techniques to deal with not-perfectly modeled plant than linear robust control, but most are focused on different measures for the "size" of an uncertainty, which have lead to different frameworks for robust control such as H_∞ method via game theory, $l1$, Lyapunov-based methods with invariant sets and many more. Figure 3.2 shows the block diagram depicting the robust control system design framework. As indicated in [25], the most common choice for the group of admissible uncertain systems is a set of uncertainties satisfying some norm bound, however, since the plant G is restricted to be linear, the group size has to be large enough, in order to capture the nonlinear phenomena. A disadvantage of this approach is that it ignores available information about existing nonlinearities, and the resulting controllers may be too conservative (especially when the nonlinearities are significant)[25].

A way to deal with the conservativity of nonlinear robust systems, while ensuring stability and performance across all possible variations of the system parameters and, in the meanwhile, maintaining linearity of the plant, is to use LPV methodology, whose research has peaked over the past two decades. This approach is particularly useful for systems where the uncertainties or nonlinearities can be captured by a set of time-varying parameters, rather than purely random or worst-case uncertainties [24]. LPV modeled systems have connected traditional linear control methods (LTI,MLTI,LTV) with non-linear robust control techniques, offering a structured way to handle variations while maintaining computational traceability. In this framework, the system dynamics are represented as a linear state-space model, with the coefficient matrices depending on external scheduling variables. Assuming these scheduling variables remain within a specified range, analytical results can guarantee a certain level of closed-loop performance and robustness [41].

3.2. System Identification

The second research area for this thesis encompasses the development of methods and techniques to build mathematical models of dynamic systems from observed data, referred to as System Identification. Its goal is to accurately capture the behavior of a system by estimating model parameters that best fit the measured input-output data. This involves, the so-called *Identification Cycle*, that can take multiple iterations and consists of the steps, as explained in [18]:

1. *Experiment design, data acquisition and manipulation*, which aims to select system excitation's that maximize the information content of measured signals and minimize estimation errors. Data pre-processing addresses disturbances and imperfections in measured data to ensure accurate model estimation.
2. *Model structure selection*, where the representation form of the model, parametrization, type of noise modeling are determined. Important factor is also the size of the model set including number of parameters or order of the model.
3. *Choice of Identification Criterion*, where selection of the performance measure is done. The most common measure is the Root Mean-Squared Error (RMSE) of the output prediction of the model estimate.
4. *Model Estimation*, which is the algorithmic solution of the estimation problem, expressed in terms of the selected model structure and the identification criterion.
5. *Validation of the model estimate*, where evaluation whether the model is sufficiently accurate for its intended application, is performed, which involves comparing the model's simulation results and predicted performance against experimental data and prior knowledge.

The choice of the model structure is crucial part of system identification, as it directly influences the maximum achievable accuracy or quality of the identified model. There are wide variety of model structures that can be chosen to model nonlinear dynamics and a subset, distinguished by parametric and non-parametric structures is shown in Figure 3.3. To create a sufficiently accurate models, high approximation power and sufficient flexibility on a global model scale is needed, which can be accomplished by four of the model structures shown in Figure 3.3: neural networks, kernel methods, polynomial models, and spline models [9]. Multi-layer neural networks can act as universal approximators, but in practice, they do not guarantee accurate results for reasonable dimensionalities. Achieving global and distributed approximation may require a high number of parameters, which can be computationally expensive.[28] In a similar fashion, kernel methods are non-parametric meaning that every significant data point is associated with a single kernel function, making large datasets computationally intractable [9]. Polynomial models, although the most commonly used, suffer from Runge's phenomenon, where a polynomial approximating a continuous function oscillates towards the ends of the function's interval, which increases with the order. By dividing the polynomial function in sub-domains, lower order polynomials can be used to accurately fit the data. However this leads to discontinuities which can be a problem for model based controllers [9].

Splines are piecewise polynomial functions with a predefined continuity between their pieces that circumvent the Runge's phenomenon. Simplex splines have arbitrarily high approximation power on a global model scale, which makes them an appealing candidate for LPV modelling and identification. A new method for linear regression of multivariate data with multivariate splines, was introduced in [9], which represents a powerful way to perform parameter estimation and system identification of complex time-variant nonlinear systems.

LPV model structures in literature (see [18], [19], [44]), are typically categorized as either *LPV Input-Output* (LPV-IO) or *LPV State-Space* (LPV-SS). LPV-IO models originate from the input-output (IO)

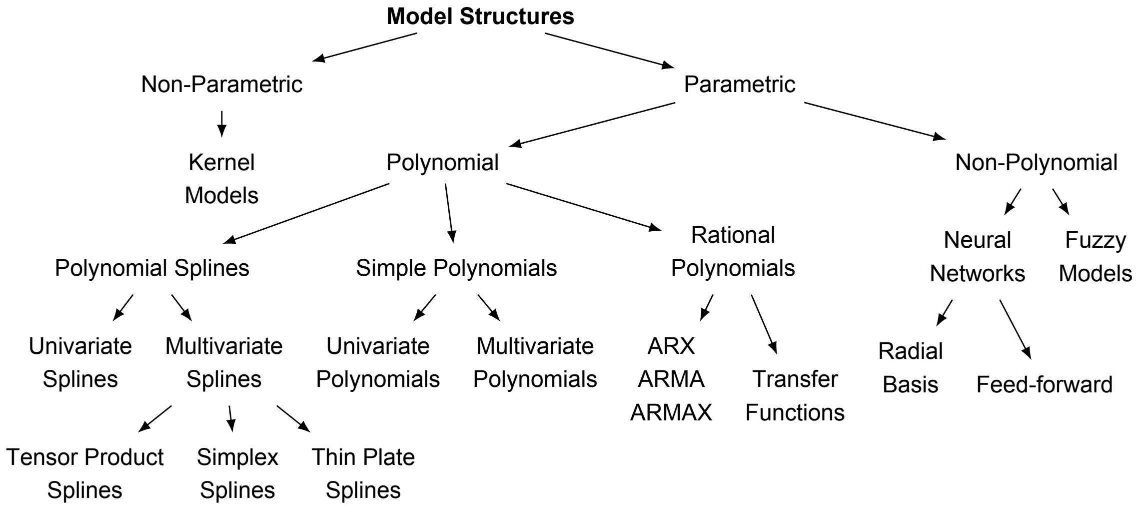

Figure 3.3: Classification of examples of relevant model structures for parameter estimation classified based on the type of estimating function.[59]

representation of the data-generating system within the LTI prediction-error framework. Approaches to model LPV-IO structures are primarily based on discrete-time models with static dependence, focusing on single-input single-output (SISO) scenarios. These methods can be categorized into four main approaches: Interpolation, Linear Regression, Set Membership, and Nonlinear Optimization. *Interpolation* approaches rely on the classical gain-scheduling concept, using ”frozen” models that are interpolated, either by polynomial or spline basis functions. *Linear Regression* methods use auto-regressive models with exogenous inputs (ARX) and employ linear parameterization techniques for coefficient estimation. *Set Membership* approaches deal with deterministic noise by calculating a feasible set of parameter values that satisfy the data with a bounded error. Lastly, *Nonlinear Optimization* methods enhance the estimation of coefficients by minimizing prediction errors through nonlinear parametrization, sometimes incorporating neural networks or separable least-squares strategies for improved accuracy.

LPV-SS model structures are similar to the state-space representation of LTI models and are accompanied with “innovation” type of noise model. LPV-SS methods identify systems using state-space representations with parameter-varying matrices, making them suitable for MIMO systems and LPV control applications. Identification methods for LPV-SS include *Gradient Methods*, which estimate matrices via nonlinear optimization and *Global Subspace Approaches* that handle uncertainties and large datasets through Linear Matrix Inequalities (LMI) and subspace identification. These two methods induce a significant computational load, which makes them limited for large scale systems [18].

Full-Measurement Methods use simplifying estimation to linear regression with measurable states and *Multiple-Model Methods*, which interpolate between LTI models. For Full-Measurement approach, an assumption is made that the state of the LPV-SS model is measurable and with linear dependence, which reduces the estimation problem to linear regression, often using least-squares.[18] Other techniques like *Set-Membership* and while *Observer-Based Grey-Box* Techniques utilize adaptive observers to estimate parameters of known nonlinear models and convert them to LPV-SS forms.

A new interpolation method for LPV system identification was proposed in [49], which allows the use of local models in any form (state-space, transfer function, etc.) without requiring coherence, making it suitable for fixed working points or slow transitions, but requiring real-time interpolation at each time instant. This means that even if the scheduling value has been interpolated before, it must be recalculated as local model outputs change over time. Drawbacks of this method is that it does not analyze the behavior of the local model or the underlying LPV model, which is never explicitly constructed.

3.2.1. Linear Regression

LPV models make use of LTI system theory and as indicated in literature, mainly focuses on Autoregressive Exogenous Input (ARX) models where coefficients are functions of the varying parameters, allowing the estimation to remain *linear-in-the-parameters*. However, an important benefit of using simplex splines is that they also use this property, as explained in [31].

This property is defined by a function $p(x, \Theta)$, consisting of Θ, a vector of the parameters and x, which is the state vector. For a function to be linear-in-the-parameters, Equation 3.1 must hold. This allows to rewrite Equation 3.1 as a multiplication of a parameter vector Θ and linear regression matrix function $\overline{X}(x)$ equaling the expression $p(x, \Theta) = \overline{X}(x)\Theta$.

$$\frac{\partial p(x, \Theta)}{\partial \Theta} = f(x) \tag{3.1}$$

The advantage of such property is the fact that optimization problems for linear-in-the-parameter models can be solved using simple linear solvers, which in general are easier to implement and have a lower computational complexity [59]. Using the widely used structure, a polynomial regression matrix, the linear regression model has the form shown with Equation 3.2[59].

$$Y = \begin{bmatrix} 1 & x_i(1) & \dots & x_i^n(1) & \dots & x_i^n(1)x_j^m(1) & \dots & x_k^M(1) \\ \vdots & \vdots & \vdots & \vdots & \vdots & \vdots & \vdots & \vdots \\ 1 & x_i(N) & \dots & x_i^n(N) & \dots & x_i^n(N)x_j^m(N) & \dots & x_k^M(N) \end{bmatrix} \Theta + \varepsilon \tag{3.2}$$

where M is the order/degree of the estimating polynomial and x_i, x_j, x_k are the regressor terms that represent the input dimensions, with total number of data points N.

It then becomes possible to derive the linear regression estimator $\hat{\Theta}$ with Equation 3.3[59], where J is a cost function.

$$\hat{\Theta} = \arg\min J\left(Y - p(x, \Theta)\right) = \arg\min J(\varepsilon) \tag{3.3}$$

The parameter estimation problem becomes a determination of the values for Θ that in some way minimizes the modeling error. The most widely used parameter estimation methods for identifying aerodynamic models are least squares and maximum likelihood methods in order to estimate the parameters of a polynomial regression model [29].

The least-squares (LSQ) method is a special case of the prediction-error identification method that uses the convex quadratic cost function, shown in Equation 3.4[59].

$$J(x, \Theta) = \varepsilon^T \varepsilon = \left(Y - \overline{X}(x)\Theta\right)^T \left(Y - \overline{X}(x)\Theta\right) \tag{3.4}$$

3.2.2. Least Squares Criterion

The Least Squares estimator is the solution to the optimization problem $\hat{\Theta} = \arg\min \varepsilon^{\mathsf{T}}\varepsilon$. The unique feature of this criterion, developed from the linear parametrization and the quadratic criterion, is that it is a quadratic function which can be minimized analytically, provided that $\left(\overline{X}^T(x) \cdot \overline{X}(x)\right)$ is invertible. A necessary condition for the residual ε of the least squares estimator is to be unbiased, which is only the case for the residual to be zero mean ($E\{\varepsilon\} = 0$). Another property, only valid for Ordinary Least Squares (OLS) estimators ($\hat{\Theta}_{\mathsf{OLS}}$), is that the residual posses a constant variance for all the measurements and is uncorrelated ($E\{\varepsilon\varepsilon^{\mathsf{T}}\} = \sigma^2 I$, where σ is the noise standard deviation and I the identity matrix). For a non-constant variance, Weighted Least Squares (WLS) estimator ($\hat{\Theta}_{\mathsf{WLS}}$) can be used, where the residuals are $\varepsilon = \sqrt{W}\nu$, where W is a constant noise scaling matrix and ν is a white noise residual. For a least squares estimator that allows correlated residuals ($E\{\varepsilon\varepsilon^{\mathsf{T}}\} = \Sigma$, where Σ the residual covariance matrix which can be used as a non-diagonal weighting matrix), generalized least squares (GLS) estimator ($\hat{\Theta}_{\mathsf{GLS}}$) can be used. These LS estimators are summarized with Equations 3.5a - 3.5c[59].

$$\hat{\Theta}_{\mathsf{OLS}} = \left(\overline{X}^T(x) \cdot \overline{X}(x)\right)^{-1} \cdot \overline{X}^T(x) \cdot Y \tag{3.5a}$$

$$\hat{\Theta}_{\mathsf{WLS}} = \left(\overline{X}^T(x) \cdot W^{-1} \cdot \overline{X}(x)\right)^{-1} \cdot \overline{X}^T(x) \cdot W^{-1} \cdot Y \tag{3.5b}$$

$$\hat{\Theta}_{\mathsf{GLS}} = \left(\overline{X}^T(x) \cdot \Sigma^{-1} \cdot \overline{X}(x)\right)^{-1} \cdot \overline{X}^T(x) \cdot \Sigma^{-1} \cdot Y \tag{3.5c}$$

3.2.3. Multivariate B-Spline Functions

The accuracy of ordinary polynomials in approximating nonlinear behavior is limited by their degree, as capturing highly nonlinear dynamics together with local irregularities would require a very high-order polynomial. Splines consist of multiple polynomials defined over adjacent triangular bases, known as simplices, which offer a higher approximation power than ordinary (global) polynomials [57]. A Comparison of the 4 different types of multivariate splines (Tensor, Thin plate, Polyhedral and Simplex) with respect to generality in all dimensions, handling scattered data and offering a simple and efficient implementation has already been done in the work of C.C.de Visser (see [9], [31]). The primary advantage of the multivariate simplex spline, in comparison to other multivariate approximation methods, has been determined to be the ability to approximate scattered multi-dimensional data over non-rectangular domains using polynomials. The usefulness of the unique properties of these polynomials makes them extremely good approximating functions when used inside a framework for system identification [9].

Any polynomial $p(x)$ of degree d can be written in the B-form as shown in Equation 3.6[32].

$$p(x) = \sum_{|\kappa|=d} c_{\kappa}^{t_j} B_{\kappa}^{d}(b_{t_j}(x)) \tag{3.6}$$

where $c_{\kappa}^{t_j}$ are the polynomial, or B-coefficients with $b = (b_0, b_1 \dots b_n)$ the barycentric coordinates of x with respect to an n-simplex t_j. The definition of these polynomials is done localy on simplices t_j, each n-simplex having $n+1$ non-degenerate vertices ν. The local coordinate system, in the form of barycentric coordinates contains all points x that are the sum of unique weights b which are multiplied with the vertices ν. Additionally, barycentric coordinates are normalized. This is depicted in Equation 3.7[60].

$$x = \sum_{i=0}^{n} b_i \nu_i \quad \ni \quad \sum_{i=0}^{n} b_i = 1 \tag{3.7}$$

The Bernstein basis polynomial $B_{\kappa}^{d}(b_{t_j}(x))$ is given by Equation 3.8[60].

$$B_{\kappa}^{d}(b_{t_j}(x)) = \frac{d!}{\kappa!}(b_{t_j}(x)) \tag{3.8}$$

where $b_{t_j}(x)$ (**b** $\in \mathbb{R}^{n+1}$) is the barycentric coordinate of the point $x \in \mathbb{R}^n$ with respect to the n-dimensional simplex t. The multi-index κ has the following properties: $|\kappa| = \kappa_0 + \kappa_1 + \cdots + \kappa_n$ and $\kappa! = \kappa_0!\kappa_1! \dots \kappa_n!$, which allows to simplify the notation of the basis polynomials to $B_{\kappa}^{d}(b_{t_j}(x))$ in Equation 3.8. In order for **b** to be a *Stable Local Basis*, the basis functions are only locally active and zero everywhere else, and stable only if the relation $\sum_{|\kappa|=d} B_{\kappa}^{d}(b_{t_j}(x)) = 1$, is true. Thus it is possible to form the per-simplex vector notation of Equation 3.6, shown with Equation 3.9[31].

$$p^{t_j}(x) = \begin{cases} c^{t_j} B^{d}\left(b_{t_j}(x)\right), & \forall x \in t_j \\ 0 & \forall x \notin t_j \end{cases} \tag{3.9}$$

The B-coefficients locally control the shape of the simplex polynomial and have a unique spatial location within each simplex. The structure formed by these coefficients within a simplex is known as the B-net [9]. The total number of B-coefficients for a given degree d and dimension n can be calculated using Equation 3.10[60].

$$\hat{d} = \begin{pmatrix} d+n \\ n \end{pmatrix} = \frac{(d+n)!}{n!d!} \tag{3.10}$$

The approximation power of a spline function is determined by the *triangulation* configuration, which refers to many simplices joined together across all simplex spline dimensions. A triangulation is the partitioning of a bounded domain $\Omega \subset \mathbb{R}^n$ into a set of J non-overlapping simplices, as shown in Equation 3.11[30].

$$\mathcal{T} := \cup_{j=1}^{J} t_j, \;\; t_i \cap t_j \in \{\varnothing, \widetilde{t}\}, \;\; \forall t_i, t_j \in \mathcal{T} \tag{3.11}$$

Solving a scattered data approximation problem on a triangulation involves finding the optimal B coefficients for each B-form polynomial. Using Equation 3.11, it is possible to define a spline function of degree d and continuity order r on a triangulation $\mathcal{T}$, consisting of J simplices with Equation 3.12[60], without the need to specify individual spline functions.

$$s_r^d(x) = B \cdot c \in S_d^r(\mathcal{T}_J) \tag{3.12}$$

where $S_d^r(\mathcal{T}_J)$ is known as the *spline space*. B is the global regression matrix with $B = \mathbb{R}^{N \times J \cdot \hat{d}}$ and c is the global B-coefficient vector.

Continuity constraints

Given the local nature of Bernstein polynomials, continuity equations are introduced to ensure the model has a smooth surface up to a specified order. For general orders of continuity $r < d$ between two neighbouring simplices t_1 and t_2, the continuity conditions are formulated using Equation 3.13[33]. These conditions include all continuity orders up to r, meaning that second-order continuity also implies first-order and zeroth-order continuity [13].

$$c^{t_2}_{m,\kappa_1,\ldots,\kappa_n} = \sum_{|\gamma|=m} c^{t_1}_{(0,\kappa_1,\ldots,\kappa_n)+\gamma} B^m_\gamma(b_{t_1}(\widetilde{\nu})) \tag{3.13}$$

where γ is a multi-index with the same size as κ and the sum of γ and κ is element-wise. It is assumed that $\widetilde{\nu}$ is out-of-edge vertex of simplex t_2. The total amount of smoothness constraints per-edge in an n-dimensional triangulation of order C^r is calculated using Equation 3.14[34].

$$R = \sum_{m=0}^{r} \frac{(d-m-n-1)!}{(n-1)!(d-m)!} \tag{3.14}$$

It then becomes possible to write the continuity equations for all edges E in a set of linear equations shown in Equation 3.15[34].

$$Hc = 0, \quad H \in \mathbb{R}^{E\cdot R \times J\cdot \hat{d}} \tag{3.15}$$

where H is the *Smoothness Matrix*, with each row describing a single constraint between two simplices, making H a sparse and rank deficient matrix.

B-Form Polynomials and Linear Regression

Using the per-simplex representation from Equation 3.9 it becomes possible to reformulate the Linear regression model, depicted in Equation 3.2, using the substitution of the polynomial regressor matrix ($\overline{X}$) with per-simplex regression matrix B_{t_j} and coefficient vector θ with per-simplex B-coefficient vector c^{t_j}, which is depicted in Equation 3.16[60].

$$Y = \begin{bmatrix} B^d_{d,0,0}\left(b_{t_j}(x(1))\right) & B^d_{d-1,1,0}\left(b_{t_j}(x(1))\right) & \ldots & B^d_{0,1,d-1}\left(b_{t_j}(x(1))\right) & B^d_{0,0,d}\left(b_{t_j}(x(1))\right) \\ \vdots & \vdots & \vdots & \vdots & \vdots \\ B^d_{d,0,0}\left(b_{t_j}(x(M))\right) & B^d_{d-1,1,0}\left(b_{t_j}(x(M))\right) & \ldots & B^d_{0,1,d-1}\left(b_{t_j}(x(M))\right) & B^d_{0,0,d}\left(b_{t_j}(x(M))\right) \end{bmatrix} c^{t_j} + \varepsilon \tag{3.16}$$

Indicating a spline function using the spline space formulation in Equation 3.12, a global linear regression structure for B-form polynomials can also be derived, which is depicted with Equation 3.17[60].

$$Y = \begin{bmatrix} B_{t_1} & 0 & 0 & 0 \\ 0 & B_{t_2} & 0 & 0 \\ 0 & 0 & \ddots & 0 \\ 0 & 0 & 0 & B_{t_J} \end{bmatrix} \begin{bmatrix} c_{t_1} \\ c_{t_2} \\ \vdots \\ c_{t_J} \end{bmatrix} + \varepsilon \tag{3.17}$$

Since B-form polynomials are linear in the parameters, it is possible to postulate the OLS cost function using the global parameters, shown in Equation 3.17 with Equation 3.18[60].

$$J(c) = \frac{1}{2}(Y - Bc)^T(Y - Bc) \tag{3.18}$$

In order to enforse smoothness constraints between individual spline pieces, the constrained cost linear regression estimator is determined using Equation 3.19[60].

$$\hat{c} = \arg\min J(c) = \arg\min \left[\frac{1}{2}(Y - Bc)^T(Y - Bc)\right], \quad \text{subject to} \quad H \cdot c = 0 \tag{3.19}$$

This relation can be solved with different methods, one of which is the *Lagrange Multiplier Method*. This method, augments the optimization problem with the Lagrangian: $L(c,\lambda) = \frac{1}{2}(Y - Bc)^T(Y - Bc) + \lambda^T \cdot H \cdot c$, where λ is a vector of Lagrangian Multipliers. The optimum is then found at location (c, λ), which means that the partial derivatives $\frac{\partial L}{\partial c}$ and $\frac{\partial L}{\partial \lambda}$, at this point, equate to zero. After some mathematical manipulation, the Lagrangian method results in Equality constrained OLS (ECOLS) or Equality constrained GLS (ECGLS) B-coefficients estimators showed in Equations 3.20a[60] and 3.20b[60].

$$\hat{c}_{ECOLS} = \left(B^T \cdot B\right)^{-1} \cdot B^T \cdot Y \tag{3.20a}$$

$$\hat{c}_{ECGLS} = \left(B^T \cdot \Sigma^{-1} \cdot B\right)^{-1} \cdot B^T \cdot \Sigma^{-1} \cdot Y \tag{3.20b}$$

3.3. Linear Parameter Varying Systems

In a general description, LPV systems constitute a class of linear systems characterized by state-space descriptions that are functions of time-varying parameters. The LPV framework includes systems in which the controller is constrained to a linear configuration, with state-space entries that are causally dependent on the past trajectory of the time-varying parameters. The general continuous-time state-space representation of an LPV system is shown in Equation 3.21[20].

$$G(\rho) : \begin{cases} \dot{x}(t) = A(\rho)x(t) + B_1(\rho)\omega(t) + B_2(\rho)u(t) \\ z(t) = C_1(\rho)x(t) + D_{11}(\rho)\omega(t) + D_{12}(\rho)u(t) \\ y(t) = C_2(\rho)x(t) + D_{21}(\rho)\omega(t) + D_{22}(\rho)u(t) \end{cases} \tag{3.21}$$

where $A \subset \mathbb{R}^{n_x \times n_x}, B \subset \mathbb{R}^{n_x \times n_\omega}, C \subset \mathbb{R}^{n_y \times n_x}, D \subset \mathbb{R}^{n_y \times n_\omega}$ are linear matrix functions that depend on the parameter space $\mathcal{P} := \{\rho := [\rho_1, \rho_2, ..., \rho_k^T] \in \mathbb{R}^k, \rho_i \in [\, \underline{\rho_i}, \overline{\rho_i}]\ \forall i = 1, ..., n_p\}$. $x(t) \in \mathbb{R}^{n_x}$, $y(t) \in \mathbb{R}^{n_p}$, $u(t) \in \mathbb{R}^{n_m}$, $z(t) \in \mathbb{R}^{n_z}$ are are the state, output, input, controlled output vectors respectively. $\omega(t)$ contains the exogenous inputs. The general relation shown in Equation 3.21, can be subdivided into a representation depending on the different cases of the scheduling function ρ: when ρ = constant, the system is represented as LTI. ρ = $\rho(t)$ where the variation of ρ with respect to time is explicitly known, the system is represented as LTV, or $\rho(t)$ is external parameter, then the system is LPV. ρ = $\rho(x(t))$ is the quasi-LPV (qLPV) representation, where $x(t)$ is the internal state vector of the system.

LPV control problems usually involve solving an infinite number of LMIs due to the parameter space. Some approaches to reduce the problem to a finite set include polytopic, grid-based, and Linear Fractional Transformation (LFT) approaches. The most used is the polytopic approach with the restriction to a limited number of scheduling parameters because the number of vertices increases exponentially with the number of parameters, making the approach less feasible as the system complexity grows [20]. However, most control synthesis problems cannot be expressed in the form of a Linear Matrix Inequality (LMI). Instead, they are often represented in a more general non-convex form known as a Bilinear Matrix Inequality (BMI), for which no complete or efficient methods to find global solutions are currently available [42].

3.3.1. Quasi-LPV (qLPV) form

The pure form of LPV shown with Equation 3.21, does not suit most flight control problems, which require the use of a quasi-LPV (qLPV) model, as the scheduling variables are measured states where the parameter can vary as a function of states, inputs or outputs and not just considered as exogenous inputs [20]. For qLPV systems, the internal state vector $x(t)$, can be split into scheduling states $\zeta(t) \in \mathcal{F}_{\mathcal{P}}$, where $\mathcal{F}_{\mathcal{P}}$ denotes the set of all piecewise continuous functions mapping $\mathbb{R}^+$ (time) into $\mathcal{P}$ with a finite number of discontinuities in any interval and non-scheduling states $W(t)$ [6]. Thus $x(t) = [\zeta(t)\ W(t)]^{\mathsf{T}}$. This division makes it possible to rewrite the qLPV into the form provided in Equation 3.22.

$$G(\rho(t)) : \begin{cases} \dot{\zeta}(t) = A_{11}(\rho(t))\zeta(t) + A_{12}(\rho(t))W(t) + B_1(\rho(t))u(t) \\ \dot{W}(t) = A_{21}(\rho(t))\zeta(t) + A_{22}(\rho(t))W(t) + B_2(\rho(t))u(t) \\ y(t) = C_1(\rho(t))\zeta(t) + C_2(\rho(t))W(t) + D(\rho(t))u(t) \end{cases} \tag{3.22}$$

Comparing Equation 3.21 with Equation 3.22, the exogenous inputs $\omega(t)$ can be assumed to be a part of the scheduling variable vector $\rho(t) = [\zeta(t)\ \omega(t)]^{\mathsf{T}}$, when written in qLPV form, without the loss of generality [6]. The system dynamics are linear with respect to the inputs and other states, and there are inputs to regulate the scheduling variables to arbitrary equilibrium values. However, practical application requires numerical testing across a grid of scheduling variables within the defined operating envelope and the analytical results are only strictly valid within the defined limits of the scheduling variables and their rates of change [41].

Another advantage of qLPV form of the nonlinear model is that global stability can be proven represented as a convex LMI optimization problem, by supposing there exists a positive definite matrix P such that Equation 3.23 is valid. Then, the system is globally stable over the operating envelope P.[50]

$$A(\zeta(t))^{\mathsf{T}} P + PA(\zeta(t)) < 0, \quad \forall \zeta(t) \in P. \tag{3.23}$$

Equation 3.23 is obtained by supposing that the system is described by a state-space representation given by $\dot{x}(t) = A(\zeta)x(t)$, where $x(t) = [\zeta(t)\ W(t)]^{\mathsf{T}}$ with parameters within the set $\mathcal{P}$. Then, the main goal is to find some Lyapunov function $V(x)$, defined as $V(x) = x^{\mathsf{T}}Px$. For the system to be globally stable, the time derivative of $V(x(t))$ along the trajectories of the system must be negative definite.[44] Thus, the time derivative of the Lyapunov function $V(x(t))$ is given by Equation 3.24. To ensure global stability, $\dot{V}(x) < 0 \ \ \forall x(t) \neq 0, \zeta(t) \in P$.

$$\dot{V}(x(t)) = \frac{d}{dt}(x(t)^{\mathsf{T}}Px(t)) = x(t)^{\mathsf{T}}\left(A(\zeta(t))^{\mathsf{T}}P + PA(\zeta(t))\right)x(t) \tag{3.24}$$

In practical applications, the LMI constraints in Equation 3.23 are evaluated at all grid points within the envelope P and choosing a Lypunov function that satisfies the conditions of $V(x(t))$ is non-trivial. As a result, the ”frozen” dynamics (fixing the scheduling states ζ at a specific value, to analyze the system as LTI) at a fixed parameter are crucial in determining both local and global stability of the original nonlinear dynamics.

Theoretical qLPV Modeling
The available literature on qLPV systems identifies two primary approaches for their theoretical derivation (see [6], [19], and [18]). Starting from the most common method, the *Linearization based approach*, which uses a family of LTI systems at different points within the operational envelope and relies on first-order Taylor Series approximations around a single or multiple equilibrium points. The other two methods are a part of a larger group of *Substitution Based Transformation Methods*, which involves inserting the scheduling parameters as a function of the total state vector $x : x(t) = [\zeta(t)\ \omega(t)]^{\mathsf{T}}$ and inputs u using some selector functions S_x and S_u of the components of (x,u) used for the substitution, creating the vector $\rho = [S_x x\ S_u u]^{\mathsf{T}}$ [18].

Linearization Based Methods The advantage of writing 3.22 in such form, is that, it is applicable to a class of non-linear systems that can be written as the form shown in Equations 3.25a - 3.25b. The assumptions made using this form is that the states and the control inputs must enter the system linearly, but this can be relaxed if they are considered as scheduling parameters and added to the nonlinear terms matrix $\mathcal{K}(\rho(t))$ [6]. This form can be easily first-order linearized with respect to the equilibrium/trim point using the relations indicated in Equation 3.26a and 3.26b.

$$\begin{bmatrix} \dot{\zeta}(t) \\ \dot{W}(t) \end{bmatrix} = A(\rho(t)) \begin{bmatrix} \zeta(t) \\ W(t) \end{bmatrix} + B(\rho(t))u(t) + \mathcal{K}(\rho(t)) \tag{3.25a}$$

$$y(t) = C(\rho(t)) \begin{bmatrix} \zeta(t) \\ W(t) \end{bmatrix} + D(\rho(t))u(t) \tag{3.25b}$$

The resulting model serves as a local approximation of the nonlinear plant's dynamics around a specific set of equilibrium points. Applying a Jacobian linearization to the plant also requires an appropriate interpolation scheme that should be applied to both the state-space matrices of the system and the equilibrium curve [19]. It is possible to obtain the state-space matrix of the linearized system by first considering the difference of the function for the scheduled states f_ζ and function evaluated at the trim point (ζ_0, W_0, u_0) with Equation 3.26a. The same is performed for the non-scheduled function f_W at the trim point shown in Equation 3.26b.

$$f_\zeta(\zeta, W, u) \approx f_\zeta(\zeta_0, W_0, u_0) + \frac{\partial f_\zeta}{\partial \zeta}(\zeta - \zeta_0) + \frac{\partial f_\zeta}{\partial W}(W - W_0) + \frac{\partial f_\zeta}{\partial u}(u - u_0) \tag{3.26a}$$

$$f_W(\zeta, W, u) \approx f_W(\zeta, W, u)|_{\zeta_0, W_0, u_0} + \frac{\partial f_W}{\partial \zeta}(\zeta - \zeta_0) + \frac{\partial f_W}{\partial W}(W - W_0) + \frac{\partial f_W}{\partial u}(u - u_0) \tag{3.26b}$$

Using the expressions derived in Equations 3.26a and 3.26b, we can rewrite the linearization in state-space form, which satisfies the qLPV form, using Equation 3.27[6].

$$\begin{bmatrix} \dot{\delta}_\zeta \\ \dot{\delta}_W \end{bmatrix} = \begin{bmatrix} \frac{\partial f_\zeta}{\partial \zeta} & \frac{\partial f_\zeta}{\partial W} \\ \frac{\partial f_W}{\partial \zeta} & \frac{\partial f_W}{\partial W} \end{bmatrix} \begin{bmatrix} \delta_\zeta \\ \delta_W \end{bmatrix} + \begin{bmatrix} \frac{\partial f_\zeta}{\partial u} \\ \frac{\partial f_W}{\partial u} \end{bmatrix} \delta_u \tag{3.27}$$

where $\delta_\zeta = \zeta - \zeta_0$, $\delta_W = W - W_0$ and $\delta_u = u - u_0$ while the matrix containing the partial derivatives with respect to ζ and W is equivalent to $A_{11}(\rho(t)) \cdots A_{22}(\rho(t))$ and the vector containing the partial derivatives with respect to u is equivalent to $B_1(\rho(t)) \cdots B_2(\rho(t))$ in Equation 3.22.

The disadvantages of Jacobian linearization stem from the fact that it is a first-order method, which for large control inputs, diverges from the non-linear model. This would also mean that the region in which the LTI approximations are valid for the nonlinear model is very limited when a small number of equilibrium points is considered. The linearization in the equilibrium points is a serious restriction that may lead to poor transient performance as the approximation requires slowly varying scheduling parameters [18]. For the application of flight control, the longitudinal and lateral dynamics would require fast varying parameters. Also, having considered a large operating envelope, the use of an LTI model, at each equilibrium point, for the desired dynamics could lead to a large mismatch between the reference system and the actual system, resulting in large uncertainties that could even cause control effector saturation, and consequently loss of stability or degraded performance [43].

A linearization method called *Multiple Linearizations around a Single Equilibrium Point* as indicated in [18], that solves the problem of the poor transient performance of the general Jacobian linearization. It makes it possible to use multiple linearizations in the vicinity of a single equilibrium point. Then the resulting local models can be interpolated to obtain a global LPV model. Regardless of how well it copes with transients, its principal disadvantage is that it cannot handle nonlinear models with multiple equilibria. Other methods exist, such as the *Linearization along a known trajectory*, where trajectory of the scheduled variables (ρ) is pre-defined, but these problems resemble LTV rather than LPV systems and evidently if ρ is far off the pre-defined trajectory, performance reduces. Another linearization method named *Off-Equilibrium Linearization around a Set of Operating Points*, looks at the Jacobian linearization of Equation 3.25a where not all points are considered as equilibrium points. Then, $\mathcal{K}(\rho(t))$ will contain a function $f(p_i)$ of all the non-equilibrium points (p_i), which is interpolated in the same way as in the previous linearization methods. The remainder terms are considered as disturbances, additional inputs or they are locally eliminated to form a global LPV model. This enables to obtain models that improve on the transient dynamics of the LPV approximation.

Substitution Based Transformation Methods Several ad-hoc substitution approaches exist, such as *Substitution by Virtual Scheduling*, which fails to provide a general estimation procedure and has the disadvantage of increasing system order drastically increases the number of scheduling parameters. It is also only applicable to non-linear systems that do not use an approximation of plant dynamics. *Velocity-Based Scheduling Technique* looks at a linear system considering all the operating points of a non-linear system. A partially differentiable nonlinear function $\hat{f}(\zeta(t))$, appears in Equation 3.25a, constricting the solution set to signals that are differentiable. It is then possible to mask the differentiation of the scheduled state vector $\zeta(t)$ and the control input $u(t)$ into new variables $\widetilde{\zeta}(t) = \frac{d\zeta(t)}{dt}$ and $\widetilde{u} = \frac{du(t}{dt}$ such that the behavior of the resulting quasi-LPV system is different. This however, can lead to amplification of noise when the control input u is differentiated, making identification difficult, which limits practical use.

The *State-transformation Method* involves state transformation using differentiable functions of non-scheduling states, where control inputs are used to eliminate nonlinear terms that are independent of the scheduling parameters. This formulation necessitates that the dimension of the scheduling states vector n_ζ must equal the dimension of the input vector n_u, in order to be able to rewrite Equation 3.25a to qLPV form [6]. Defining the trim functions, where the left-hand side of Equation 3.25a is $[\dot{\zeta}(t)\ \dot{W}(t)]^{\mathsf{T}} = \overline{0}$, and assuming there exist continuously differentiable functions $W_{eq}(\rho)$ and $u_{eq}(\rho)$ such that for every $\rho \in \mathcal{F}_{\mathcal{P}}$ the system is in steady state [6]. This is presented in Equation 3.28[19], where $\dot{W}_{eq}(\rho) = \frac{\partial W_{eq}(\rho)}{\partial \rho}\dot{\zeta}$ and $U = u - u_{eq}(\rho)$.

$$\begin{bmatrix} \dot{\zeta} \\ \dot{W} - \dot{W}_{eq}(\rho) \end{bmatrix} = \begin{bmatrix} 0 & A_{12}(\rho) \\ 0 & A_{22}(\rho) - \frac{\partial W_{eq}(\rho)}{\partial \zeta}|_\rho A_{12} \end{bmatrix} \begin{bmatrix} \zeta \\ W - W_{eq}(\rho) \end{bmatrix} + \begin{bmatrix} B_1(\rho) \\ B_2(\rho) - \frac{\partial W_{eq}(\rho)}{\partial \zeta}|_\rho B_1(\rho) \end{bmatrix} U \quad (3.28)$$

Writing the system in such form, as in Equation 3.28, is limited to the specific class of non-linear state space models (Equation 3.25a) and there is no constructive procedure to find the continuously differentiable functions $W_{eq}(\rho)$ and $u_{eq}(\rho)$ over the non-trim region.

The next approach, known as *Function Substitution*, has the advantage of ensuring that the solution to the nonlinear dynamics is satisfied at all grid points [50]. In this method, the system represented by Equation 3.25a is replaced with an unknown matrix function, $\mathcal{F}$, such that the approximation remains accurate for every trajectory. $\mathcal{F}$ has a linear combination of scheduling parameter-dependent functions and the scheduling vector. Using a substitution of coordinates around a chosen equilibrium point $(\zeta_{eq}, W_{eq}, u_{eq})$, Equation 3.29a is obtained. Looking only at the scheduled states $\rho(t) = \zeta(t)$, along with the transformation coordinates, Equation 3.29b is created, where the contents of the function $\mathcal{F}$ are shown in Equation 3.29c.

$$\begin{aligned} \widetilde{\zeta} &= \zeta - \zeta_{eq}, \quad \widetilde{W} = W - W_{eq}, \quad \widetilde{U} = u - u_{eq} && (3.29a) \\ \begin{bmatrix} \dot{\widetilde{\zeta}}(t) \\ \dot{\widetilde{W}}(t) \end{bmatrix} &= A(\rho(t)) \begin{bmatrix} \widetilde{\zeta}(t) \\ \widetilde{W}(t) \end{bmatrix} + B(\rho(t))\widetilde{U}(t) + \mathcal{F}(\rho(t)) && (3.29b) \\ \mathcal{F}(\rho(t)) &= A(\rho(t)) \begin{bmatrix} \zeta_{eq}(t) \\ W_{eq}(t) \end{bmatrix} + B(\rho(t))u_{eq}(t) + \mathcal{K}(\rho(t)) && (3.29c) \end{aligned}$$

The main goal of this method is to reformulate $\mathcal{F}$ into an qLPV problem that can minimize the variations of each matrix element over the entire operating envelope. It is achieved by considering $\mathcal{F}$ to be formed by an Unknown matrix function $E(\rho(t))$, with e_i being the i-th row vecor ($i = 1...n$) of the matrix $E(\rho(t))$ as presented with Equation 3.30.

$$\mathcal{F}(\rho(t)) = E(\rho(t))\widetilde{\zeta}(t) = \begin{bmatrix} e_1(\rho(t)) & \dots & e_n(\rho(t) \end{bmatrix}^T \widetilde{\zeta}(t) \quad (3.30)$$

This function can capture terms in the nonlinear system that are non-affine in the non-scheduling states and control inputs and are not just purely functions of the scheduling vector. This decomposition is carried out through a minimization procedure, which leads to a series of numerical optimisation problems [19]. Thus the final qLPV model is written as shown in Equation 3.31a where the reformulated state matrix $A_{\mathcal{F}}$ is shown in Equation 3.31b and $\bar{0}$ is the $n \times n_W$ zero matrix.

$$\begin{aligned} \begin{bmatrix} \dot{\widetilde{\zeta}}(t) \\ \dot{\widetilde{W}}(t) \end{bmatrix} &= A_{\mathcal{F}}(\rho(t)) \begin{bmatrix} \widetilde{\zeta}(t) \\ \widetilde{W}(t) \end{bmatrix} + B(\rho(t))\widetilde{U}(t) && (3.31a) \\ A_{\mathcal{F}}(\rho(t)) &= A(\rho(t)) + [E|\bar{0}] && (3.31b) \end{aligned}$$

The solution Equation 3.31a closely matches that of the nonlinear dynamics because the equality constraint in Equation 3.30 is satisfied at all grid points. A disadvantage of this method is its strong dependence on the reference point; different reference points can lead to different representations. Additionally, the model may fail to capture the local stability of the original nonlinear model at other equilibrium points [50].

Empirical qLPV Modeling
Empirical modeling involves developing models based on experimental data, as opposed to theoretical models explained above. The available literature on empirical modeling of qLPV systems identifies two primary approaches that differ mainly in the frequency of experimental runs: global and local. Global approaches collect input/output data, including parameter variations, in a single experimental run, leading to the direct derivation of an LPV model in one step. In contrast, local approaches conduct multiple experiments at fixed parameter values, resulting in several LTI models that need to be interpolated to form the complete LPV representation of the system [19]. Advantages of local approach is to use well-established LTI framework, but lack global stability and performance.

3.3.2. Interpolation of Local Models

Interpolation approaches in system identification utilize the classical gain-scheduling concept, where models are derived for constant scheduling trajectories and interpolated to form a global model. These methods, often using polynomial or spline interpolation, are closely related to the local-linear-modeling framework and they leverage the LTI prediction-error framework to estimate the frozen dynamics of LPV systems, even in closed-loop settings.[18] If the true LPV system demonstrates a smooth dependence on the scheduling parameter ρ, the overall parameter-dependent model can be directly reconstructed from the identified local models [19].

A very common approach to interpolation in literature (see [19]) is based on using already determined set of LTI models, N_θ and directly fitting suitable regressors γ (linear or non-linear combinations of θ), formed from the scheduling parameter $\theta \in \mathbb{R}^{n_\rho}$ to the state-space matrices. This is usually in *Affine* form and is represented by Equations 3.32a and 3.32b.

$$\dot{x} = \left(A_0 + \sum_{i=1}^{n_\gamma} A_i(\gamma_i)\right) x + \left(B_0 + \sum_{i=1}^{n_\gamma} B_i(\gamma_i)\right) u \quad (3.32a)$$

$$y = \left(C_0 + \sum_{i=1}^{n_\gamma} C_i(\gamma_i)\right) x + \left(D_0 + \sum_{i=1}^{n_\gamma} D_i(\gamma_i)\right) u \quad (3.32b)$$

where the state-space matrices are represented by transfer function:
$G_k(s) = C\left(\gamma(k)\right)\left(sI - A(\gamma(k))\right)^{-1} B(\gamma(k)) + D\left(\gamma(k)\right)$, for $k = 1 \dots N_\theta$, where k is the scheduling index of the kth identified local model. When the entries of Equations 3.32a and 3.32b, a combined matrix $F(\gamma(k))$ can be obtained using Equation 3.33.

$$F(\gamma(k)) = \begin{bmatrix} A(\gamma(k)) & B(\gamma(k)) \\ C(\gamma(k)) & D(\gamma(k)) \end{bmatrix}, \quad k = 1 \dots N_\theta \quad (3.33)$$

The polynomial interpolation of the elements of the matrix F can be performed by solving a least squares problem of the linear regression form provided by Equation 3.2, where Y contains the elements f_{ij} of F. Matrix $\overline{X}$ would contain the regressor terms γ and Θ would contain the polynomial coefficients. To express the fitting error, RMSE as a a standard metric for performance measure (identification criterion) is computed using Equation 3.34[19].

$$RMSE = \frac{||Y - \overline{X}\hat{\Theta}||_2}{||Y||_2} \quad (3.34)$$

Two pitfalls have been identified for interpolation applicable directly to state-space matrices. First, state transformations used to align the LPV representation with favorable interpolation forms, like cannonical form, can introduce dynamic dependencies not captured by local LTI snapshots, leading to substantial errors during interpolation. Furthermore, while polynomials are straightforward and efficient, the least squares (LSQ) method typically utilizes all available degrees of freedom, resulting in models that are nonsparse and frequently overly complex [8]. Second, in black-box approaches, the independent identification of local models results in incoherent state bases, reducing the performance of the interpolated LPV model in regions not covered by the data set.[23]

The first pitfall can be minimized by using a different interpolation form. This research proposes B-splines, which are local basis functions that consist of piecewise polynomials. The segments are connected such that their derivatives are continuous up to a specific order, which is determined by the degree of the polynomials [32]. These functions are advantageous due to their computational simplicity and the flexibility to achieve the desired level of smoothness [26]. Due to these properties, B-splines have been used in interpolation problems, where efficient and smooth approximations are needed. Another very important benefit, that differentiates B-splines with other model structures, such as non-polynomial Neural Networks, is that they posses the linear-in-the-parameters property. This means that Least squares solvers, with estimators shown in Equation 3.5a, can be used.

The second pitfall can be avoided if the aerodynamic model chosen possesses information about the relationships between variables, constraints on model behavior, or explicit equations representing system dynamics, making the model *'grey-box'*. The ICE aircraft posseses a 6-DOF aerodynamic mathematical model, explained in [37], which contains these relationships, thus it can avoid incoherent state bases due to data set unavailability.

3.3.3. Discrete Time LPV Systems

In the LPV modeling framework, continuous-time (CT) LPV models are crucial for guiding model structure selection in system identification. However, while CT models are commonly used in LPV control synthesis, existing LPV identification methods are predominantly designed for discrete-time (DT). This necessitates the efficient discretization of CT models for practical implementation in the system identification processes [18]. The emphasis is on LPV-SS models with static dependence (memoryless) on the scheduling parameter, as this distinguishes them from LPV-IO models in cases such as *Affine parameter dependence*. The affine assumption in commonly used in LPV systems since it simplifies the modeling and mathematical analysis by providing a linear relationship between parameters and scheduling variables. This assumption preserves convexity, making control synthesis more straightforward through convex optimization techniques.[44] Additionally, affine models often offer a good balance between accuracy and complexity in practical applications.

Equations 3.35a and 3.35b depict the DT LPV-SS form, with this affine assumption (LPV-A). $A(\rho_d)$ is a sum of constant matrices A_i multiplied by time-varying scheduling parameter $\rho_{d,i}$ at time step k. In a similar fashion, the same is done with the SS matrices $B(\rho_d)$,$C(\rho_d)$ and $D(\rho_d)$. By definition, y_d, u_d, ρ_d are the sampled signals of the CT signals $y(t)$, $u(t)$, $\rho(t)$ with sampling period $T_d > 0$. The scheduling parameter $\rho_d(k)$, is a vector with s being the the scheduling dimension.

$$x_d(k+1) = \left(A_0 + \sum_{i=1}^{s} A_i(\rho_{d,i})(k)\right) x_d(k) + \left(B_0 + \sum_{i=1}^{s} B_i(\rho_{d,i})(k)\right) u_d(k) \tag{3.35a}$$

$$y_d(k) = \left(C_0 + \sum_{i=1}^{s} C_i(\rho_{d,i})(k)\right) x_d(k) + \left(D_0 + \sum_{i=1}^{s} D_i(\rho_{d,i})(k)\right) u_d(k) \tag{3.35b}$$

The affine parameter dependence, can be immediately generalised to a polynomial parameter dependence. If the system matrix A and output matrix C are set to be constant, resulting in $A = A_0$ and $C = C_0$, while B and D can vary, then Equations 3.35a and 3.35b exhibit *Input-affine* (LPV-IA) parameter dependence. A discrete-time form of the the general LPV CT form shown in Equation 3.21, is known as LPV Linear Fractional Transformation (LPV-LFT) form and is represented in Equations 3.36a-3.36c[19].

$$x_d(k+1) = Ax_d(k) + B_0 w_d(k) + B_1 u_d(k) \tag{3.36a}$$

$$z_d(k) = C_0 x_d(k) + D_{00} w_d(k) + D_{01} u_d(k) \tag{3.36b}$$

$$y_d(k) = C_1 x_d(k) + D_{10} w_d(k) + D_{11} u_d(k) \tag{3.36c}$$

where $w_d(k) = \text{diag}\left(\rho_{r_1}(k)I_{r_1} \dots \rho_{r_s}(k)I_{r_s}\right) z_d(k)$, $r = r_1 \dots r_s$, $w, z \in \mathbb{R}^r$. The benefit of these discrete-time representations are that affine and linear transformation techniques are related to each other by denoting the composition of the system matrices, using LPV-IA state-space system, as shown in Equation 3.37[19].

$$M(\rho_d(k)) = \begin{bmatrix} A & B(\rho_d(k)) \\ C & D(\rho_d(k)) \end{bmatrix} = M_0 + M_1\rho_{d,1}(k) + \dots + M_r\rho_{d,r}(k) \tag{3.37}$$

where $M(\rho(k))$ is expressed by means of rank decomposition, shown in Equation 3.38. The derived form of the system matrices matches the specific case of a linear fractional transformation characterized by $D_{00} = 0$ thereby allowing the transformation between these two representations.

$$M(\rho(k)) = M_0 + [U_1 \dots U_s] \cdot \text{diag}\left(\rho_{r_1}(k)I_{r_1} \dots \rho_{r_s}(k)I_{r_s}\right) \cdot \left[V_1^T \dots V_s^T\right]^T \tag{3.38}$$

One major drawback of the LPV-LFT is the significant time and effort required to develop formal LFT models. The impact of LFT discretization on the validation of results is also not fully understood, which can introduce uncertainties in the outcomes [51].

Zero-Order Hold

In the existing literature on LPV discretization, nearly all approaches are based on an isolated framework, typically assuming an ideal Zero-Order Hold (ZOH) setting [48]. Multiple approaches have been introduced for discretizing CT systems with the goal of preserving the CT input-output behavior under a zero-order-hold setting, shown in Figure 3.4, where the variation of free CT signals is limited to piecewise-constant. Some of these approaches: *Complete*, *Euler forward*, and *Trapezoidal methods*, which were developed for the discretization of LPV-SS representations by extending concepts from the linear time-invariant (LTI) framework. Alternative approaches are Polynomial and Multi-step formulas like the Runge-Kutta, Adams-Moulton, or the Adams-Bashforth type. Polynomial methods achieve better approximation of the complete case, but at the expense of increasing complexity. For multi-step approaches, zero-order hold (ZOH) discretization with a fixed step size, data is available only at past and present sampling instances, limiting the applicability of Adams-Moulton. Additionally, as the input function can only be evaluated at integer multiples of the sampling period, single-rate system realization is necessary, so Runge-Kutta cannot be used. Adams-Bashforth family satisfies these constraints, but posses slower convergence (n[th]-order) and has smaller stability radius (than Trapezoidal method for example).[18]

The Zero-Order Hold assumption states that if we consider a CT system plant G, with input-output partition ($u_d(k)$,$y_d(k)$) and a scheduling signal $\rho_d(k)$, where $u(t)$ and $\rho(t)$ are CT signals generated by an ideal ZOH and $y(t)$ is sampled in a perfectly synchronized manner with sampling period or discretization time-step T_d where $T_d > 0$. The ZOH and the output sampling instrument have infinite resolution (no quantization error) and zero processing time [48].

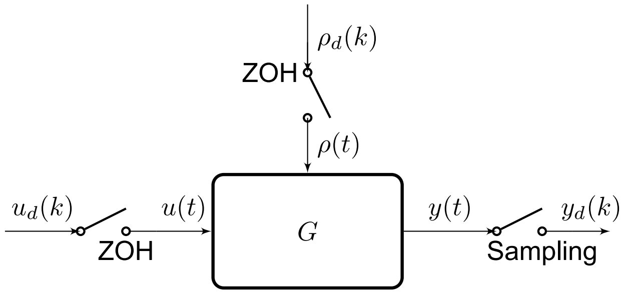

Figure 3.4: Zero-order hold discretization of a general continuous-time LPV system (LPV-ZOH) with plant G, Continuous-time inputs $u(t)$, scheduling signal $\rho(t)$ and outputs $y(t)$ and their discrete counterparts: Discrete-time inputs $u_d(k)$, scheduling signal $\rho_d(k)$ and sampled output $y_d(k)$ [48].

Based on the ZOH setting assumption, the relations in Equations 3.39a-3.39c[18] are derived, for each $k \in \mathbb{Z}$, which results in the constraint that $u(t)$ and $y(t)$ can only change at the end of each sampling interval.

$$u(t) = u_d(k) \quad \forall t \in [kT_d, (k+1)T_d), \tag{3.39a}$$
$$\rho(t) = \rho_d(k) \quad \forall t \in [kT_d, (k+1)T_d), \tag{3.39b}$$
$$y_d(k) = y(kT_d) \tag{3.39c}$$

Using this assumption imposes a piecewise-constant behavior on the scheduling parameter ρ_c, which may originate from external disturbances (general LPV) or be a function of the states of the plant G (qLPV), and may not be fully influenced by the digitally controlled actuators. While restricting these variables during the sampling period is necessary for deriving a DT description of the system, relaxing this assumption to allow more complex signal trajectories, such as first-order (piece-wise linear) or second-order holds (2^{nd}-order polynomial), can yield a more accurate DT representation. Though it may result in highly complicated discretization rules that are likely to end up with non-causal scheduling dependence.[48]

A basic property of LPV-ZOH is that due to the assumed ideal hold devices, at the beginning of each sample interval a switching effect occurs, shown with Equations 3.40a and 3.40b.

$$u(t) = \sum_{k=-\infty}^{\infty} H(t-kT_d)\left(u_d(k) - u_d(k-1)\right), \tag{3.40a}$$
$$\rho(t) = \sum_{k=-\infty}^{\infty} H(t-kT_d)\left(\rho_d(k) - \rho_d(k-1)\right), \tag{3.40b}$$

where $H(t)$ is the Heaviside step function, shown in Equation 3.41.

$$H(t) = \begin{cases} 1 & \text{if } t < 0 \\ 0 & \text{if } t \geq 0 \end{cases} \tag{3.41}$$

It is assumed that the switching effects are smooth and no dynamics are introduced with switching ρ_d.

The *Complete Method* of LPV-SS discretization entails solving an Ordinary Differential Equation (ODE), with the assumption that ρ_d and u_d are constant signals inside each sampling interval kT_d, which results in Equations 3.42a and 3.42b.

$$x_d(k+1) = e^{A(\rho_d)T_d} x_d(k) + A^{-1}(\rho_d)\left(e^{A(\rho_d)T_d} - I\right) B(\rho_d) u_d(k) \tag{3.42a}$$

$$y_d(k) = C(\rho_d) x_d(k) + D(\rho_d u_d(k) \tag{3.42b}$$

where $\rho_d = \rho(kT_d)$ and $A(\rho_d)$ is invertible. Looking at the term $e^{A(\rho_d)T_d}$, it becomes evident that this method introduces a non-linear relationship in ρ_d, as $A(\rho_d)$ is non-static. It makes the method be generally disfavoured as identification and control-synthesis procedures are often based on the assumption of linear, polynomial, or rational (static) dependence on $\rho(t)$ [48].

To avoid the appearance of the term $e^{A(\rho(kT_d))T_d}$, we can use the *Euler's method*, by using first order approximation: $e^{A(\rho_d)T_d} \approx I + A(\rho(kT_d))T_d$, which transforms Equation 3.42a into Equation 3.43.

$$x_d(k+1) = x_d(k) + T_d A(\rho(kT_d)) x_d(k) + T_d B(\rho(kT_d)) u_d(k) \tag{3.43}$$

This approximation leads to a good representation of the original behaviour while being less complex in the coefficient dependence.

A commonly used technique in LTI identification is the Trapezoidal rule, which can also be applied for ZOH systems as shown in Equation 3.44.

$$x_d(k+1) \approx x_d(k) + \frac{T_d}{2}\left(f(x,u,\rho)(kT_d) + f(x,u,\rho)((k+1)T_d)\right) \tag{3.44}$$

where $f(x,u,\rho)(\tau)$ is defined using Equation 3.45.

$$\int_{kT_d}^{(k+1)T_d} f(x,u,\rho)(\tau) d\tau = \int_{kT_d}^{(k+1)T_d} A(\rho(kT_d)) x(\tau) + B(\rho(kT_d)) u(kT_d) d\tau \tag{3.45}$$

Compared to methods like rectangular, which may simplify dependencies, or Adams-Bashforth that reduces discretization error, the trapezoidal method maintains a good compromise between complexity and accuracy. It provides a large stability radius and fast convergence, which can simplify model parametrization and controller design, especially if the important considerations are maintaining DT model quality and computational efficiency [18].

3.3.4. Multivariate Splines and LPV framework

The available literature on the modeling of LPV systems with multivariate splines is very limited. In [22], a LPV synthesis problem has been made numerically tractable by parameterizing the Lyapunov function and applying LMI relaxations, which reduce the infinite-dimensional parameter dependant LMI problem to a finite set of constraints and optimization variables. This is performed by using multivariate splines in the form of tensor product polynomial splines. The main limiting assumption is that all state-space system matrices in the continuous-time LPV system depend on the parameter-dependent variable α of the LMI problem through a tensor product polynomial spline. This assumption is very specific for problems that can express this dependence, but cannot be directly applied to the majority of continuous physical systems. Tensor product splines are inherently unsuitable for fitting scattered data due to their reliance on structured, grid-based input. While this limitation is not problematic for the application in this paper, where data can be arranged on a rectangular grid, it becomes a significant issue when modeling measurements from continuous physical systems, which are inherently scattered [9].

As investigated in [55], a cubic spline is used on a arm-driven inverted pendulum model identification of MIMO input-output LPV models, with polynomial dependance in closed-loop setting using separable least squares estimator. The simplification made in this paper, is that the scheduling variable is a previous sample of the angular position ϕ_1, which is the main source of the nonlinearity of the plant. Furthermore, a cubic spline function applied to two variables ϕ_1 and ϕ_2, shows better performance only for ϕ_1, when compared to the LPV polynomial model, while for ϕ_2, performance is matched to the LPV model. However, the disadvantage of using cubic spline functions was indicated to be that they are non-linear in their parameters, therefore non-linear optimization techniques have to be used [55]. Furthermore, cubic splines are generally not well-suited for approximating functions with C^1 discontinuities, such as step functions, as they tend to produce inaccurate approximations in the vicinity of the discontinuity and suffer from the Gibbs' phenomenon of splines [61]. Simplex splines, are capable of effectively modeling discontinuities in two ways. Either by locally increasing the density of the triangulation where discontinuities are present, or by aligning the triangulation so that areas of discontinuity coincide with the edges of the simplices [9].

In contrast to [22], the relationship between B-splines and LPV system models discussed in [8] offers a more general representation, focusing on identification and modelling that can be applied to any state-space LPV model. The paper also proposes strategies for selecting the optimal number and placement of knots, as the number of B-splines is directly proportional to the number of knots partitioning the domain over which the spline is defined. The numerical validation of the proposed methods showed a reduction in model complexity only on slight expense of the model accuracy. However, this is performed for univariate B-splines, and the extension to multiple scheduling parameters leads to tensor-product polynomial splines, which suffer the same drawbacks as in [22].

3.4. Innovative Control Effectors Aircraft

The final area of research focuses on the application of the methodologies discussed in preceding sections, by application to a non-affine, high-dimensional flight control problem. Such a candidate is the Lockheed Martin's ICE program, which was started in 1993 and split in two phases. The first phase, detailed in [35], focused on the conceptual design and analytical assessment of two baseline aircraft configurations with innovative control effectors. The second phase, described in [36], aimed to collect empirical data to develop accurate aerodynamic models at high Reynolds numbers, create control effector models, and analyze their interactions. The primary objective of the ICE study was to identify and quantify the aerodynamics and performance of various low-observable, tailless aircraft configurations featuring control effectors that have either never been applied to aircraft before or, at the very least, have not been used in combination with each other.[57] For the purpose of this paper, the land-based ICE model is used, which is depicted in Figure 3.5.

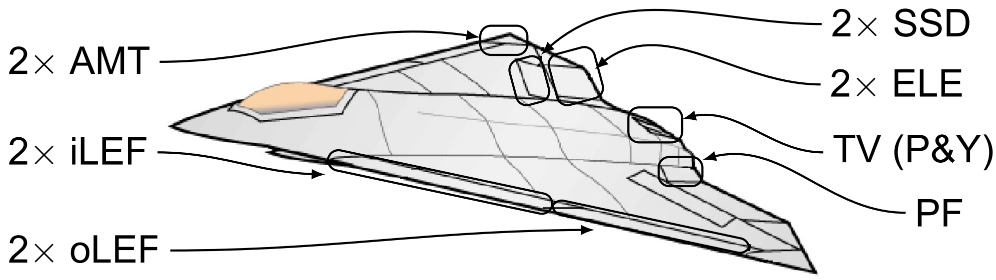

Figure 3.5: Depiction of the land-based version of ICE aircraft and its 13 control surfaces labeled as: AMT - All-Moving Tips, iLEF - inboard Leading Edge Flap, oLEF - outboard Leading Edge Flap, SSD - Spoiler Slot Deflector, ELE - Elevons, TV (P&Y) - Thrust Vectoring (Pitch & Yaw) and PF - Pitch Flaps.[37]

Lockheed Martin provided a full 6-DOF aerodynamic model based on wind tunnel tests conducted during the ICE research program in [37]. The model comprises of total force and moment coefficient build-up equations, in multiple axes, incorporating contributions from the bare airframe, isolated control effectors, interaction effects between control effectors, and dynamic derivatives.The conventional control effectors include elevons and pitch flaps, while the innovative or unconventional effectors comprise all-moving wingtips, as well as pitch and yaw thrust vectoring. Many of the 13 control surfaces generate moments along multiple axes to account for the loss of directional control induced by lack of vertical tail. The position of both conventional and innovative control effectors can also be seen in Figure 3.5. An overview of the deflection ranges of all of the control effectors is provided in [37] and show in Table 3.1.

It is evident from the number of control effectors listed in Table 3.1 that the system is over-actuated, necessitating the use of control allocation methods to distribute commands among the available actuators. One of the key advantages of an over-actuated system is the ability to utilize multiple effectors to achieve performance across all of its control axes. However, due to the coupling effects and the aerodynamic interactions between these effectors, the control effectiveness becomes highly nonlinear. The original ICE model presented in [37] employs linear interpolation for the majority of force and moment aerodynamic coefficients, with the exception of those depending on the Elevons (δ_{LEL}, δ_{REL}) and the Spoiler-Slot Deflectors (δ_{LSSD}, δ_{RSSD}), which are interpolated using cubic splines. This interpolation scheme was later modified in [12] by implementing a zero$^{\text{th}}$-order continuous (C^0) multivariate simplex B-spline model. While this method offers certain advantages, one of its drawbacks is the presence of discontinuities at the

Control Effector	Location	Notation	Positive Deflection	Position Limits [deg]	Rate Limits [deg/s]	Primary Effect on Axis
All Moving Tips	left right	δ_{LAMT} δ_{RAMT}	TED	$[0, 60]$	150	Roll & Yaw
Inboard Leading Edge Flaps	left right	δ_{LILEF} δ_{RILEF}	LED	$[0, 40]$	40	Pitch & Roll
Outboard Leading Edge Flaps	left right	δ_{LOLEF} δ_{ROLEF}	LED	$[-40, 40]$	40	Pitch & Roll
Spoiler-Slot Deflectors	left right	δ_{LSSD} δ_{RSSD}	TEU	$[0, 60]$	150	Pitch & Roll
Elevons	left right	δ_{LEL} δ_{REL}	TED	$[-30, 30]$	150	All axes
Multi-Axis Thrust Vectoring	pitch lateral	δ_{PTV} δ_{LTV}	$\dot{q} > 0$ $\dot{p} > 0$	$[-15, 15]$	150	Pitch & Yaw
Pitch Flaps		δ_{PF}	TED	$[-30, 30]$	150	Pitch

Table 3.1: Overview of all 13 ICE Control Effectors indicating the positive deflection per set (Trailing Edge (TE) or Leading Edge (LE) Up (U) or Down (D) including the positive pitch thrust vectoring defined as TED, positive yaw thrust vectoring TE left deflection), the rate limits and the primary effect of the effector on the ICE axis. Note that for thrust vectoring the effect of δ_{PTV}, δ_{LTV} on Pitch & Yaw axes is dependant on the trim thrust setting.

edges of neighboring simplices when taking derivatives, as noted in [14]. This led to the development of an Incremental Nonlinear Control Allocation (INCA) method, which leverages the Control Effectiveness Jacobian to account for control effector interactions. This approach, detailed in [11], not only exploits these interactions but also addresses both actuator position and rate constraints, significantly improving ICE control allocation performance. Further improving the spline model, in [13], a first order (C^1) continuous multivariate simplotope B-Spline model was constructed, estimated using a distributed approach. As a continuation to the work of [13], the method of multivariate simplotope B-Spline model is further extended to an online setting after modeling of a structural failure of ICE to demonstrate adaptive control, as explained in [14].

3.4.1. Control Allocation

A control allocator solves and underdetermined system of Equations, such that it determines $u(t)$ in $f[u(t)] = \nu(t)$, which i a function that maps the true control input $u(t)$ to a virtual control input $\nu(t)$. When $m > k$ from $u(t) \in \mathbb{R}^k$ and $\nu(t) \in \mathbb{R}^m$, system is overactuated. For linear cases, the relation described with Equation 3.46[62].

$$\nu(t) = B(x)u(t) \tag{3.46}$$

where $B(x) \in \mathbb{R}^{k\times m}$ is the control effectiveness matrix, depending on state x. The true control input is limited by position constraint: $u_{\text{min}} \leq u(t) \leq u_{\text{max}}$ and rate constraint: $\dot{u}_{\text{min}} \leq \dot{u}(t) \leq \dot{u}_{\text{max}}$. when $m > k$ is true, the control effectiveness matrix is non-square and cannot be inverted as in the case shown in Equation 3.47, where $m = k$.

$$u(t) = B(x)^{-1}\nu(t) \tag{3.47}$$

A number of methods exist to solve the control allocation problem when $m > k$. To limit the scope of the thesis, distinction is made to use methods that produce unique solution through optimization, named Optimization Based Control Allocation and not use methods that use geometric reasoning or Dynamic Control Allocation, that takes into account the actuator bandwidth (DynCA) when solving the problem. The optimization control allocation tries to find the best solution of Equation 3.46 and in the cases where no solution exists, it will generate control input, that approximates the solution of Equation 3.46 as close as possible according to the norm used [62].

The most commonly used norm for obtaining a solution for the control allocation problem is l_2, which is shown with Equation 3.48[62].

$$||u||_2 = \left(\sum_{i=1}^{m} |u_i|^2\right)^{\frac{1}{2}} \tag{3.48}$$

where m is the total number of actuators and i is the index of the actuator. The optimal control input is found in two steps indicated by Equations 3.49a[62] and 3.49b[62].

$$\Omega = \underset{\substack{u_{\text{min}} \leq u(t) \leq u_{\text{max}} \\ \dot{u}_{\text{min}} \leq \dot{u}(t) \leq \dot{u}_{\text{max}}}}{\arg\min} ||W_\nu(Bu - \nu)||_2 \tag{3.49a}$$

$$u = \underset{u \in \Omega}{\arg\min} ||W_u(u - u_d)||_2 \tag{3.49b}$$

where W_u is the weighting matrix for the actuators, W_ν is the weighting matrix for the virtual controls and u_d is the preferred steady state actuator deflection. In cases where Ω set is empty, the method determines the set of solutions, that minimizes the norm of the weighted difference between the virtual control input and the produced moments. The second step, as outlined in Equation 3.49b, refines the solution set from the first step by selecting the optimal solution based on the weighted difference between the desired steady-state actuator deflections and the actual control input [62]. For $W_\nu = W_u = I$, where I is the identity matrix, $u_d = 0$ as the steady state deflection and no constraints on the actuators, Equation 3.50[62], is derived.

$$u = B^+\nu = B^\mathsf{T}\left(BB^\mathsf{T}\right)^{-1}\nu \tag{3.50}$$

where B^+ is the pseudo-inverse of the control effectiveness matrix. The *Weighted Pseudo Inverse (WPI)* can be derived from Equation 3.49a, by reducing the problem to $\min_u ||e||_2$ subject to $Bu = \nu$. With $e = W_u(u - u_d)$. When B has full rank, the solution is given by Equations 3.51a - 3.51b[62].

$$u = (I - GB)u_d + G\nu \tag{3.51a}$$

$$G = W_u^{-1}\left(BW_u^{-1}\right)^+ \tag{3.51b}$$

Solving the over-actuated problem by pseudo-inverse control allocation can be done with standard linear algebra techniques. However, the assumption of unconstrained actuators, which for the ICE, have limits in rate and position, as seen in Table 3.1, will not hold. Inputs will be generated that can be beyond the capabilities of the actuators, making the solutions infeasible. A common method to avoid these solutions, which saturate the actuators beyond their limits, is to weigh each control input u with the inverse of its maximum value, using W_u [62]. Thus, the *Cascaded Generalized Inverse (CGI)* can be used, which tries to use the remaining free actuators to compensate for the saturated actuators. It provides two solutions to the problem with Equations 3.52a and 3.52b.

$$u_1 = (I - G_1B)u_d + G_1\nu \tag{3.52a}$$

$$u_2 = (I - G_2B_2)u_d + G_2(\nu - Bu_1)\nu \tag{3.52b}$$

where G_1 solved with Equation 3.51b and a new control effectivness matrix B_2 is computed that includes only the columns of the non-saturated actuators. And the process is repeated until a feasible solution is found. CGI is straightforward to implement and is generally an efficient method for constrained control allocation problems.

3.4.2. LPV framework applied to ICE model

The available literature on LPV application to ICE spans two papers ([63] and [52]) and dates back more than two decades ago, where advancements in LPV control methods and computing power were somewhat limited.

The first paper, [63], presents a comparison between two control methods: Dynamic Inversion (DI) and LPV control using parameter-dependent Lyapunov functions. These methods were selected due to their shared reliance on aerodynamic models of the aircraft, applied either on-board in real time (DI) or off-line (LPV). In the LPV control approach, a parameter-dependent Lyapunov function is computed off-line. To ensure the efficiency of the system, this function must be kept as simple and compact as possible, as both the size of the off-line optimization problem and the computational demands of on-line problem. In this paper, linear rigid body models are obtained by linearizing the equations of motion at 89 flight conditions across the flight envelope. A polynomial least squares scheduling function is employed to derive an LPV model for two parameters, specifically Mach number and altitude, $\rho = f(M, h)$. This approach is applied to the ICE five-state linear model utilizing aerodynamic data obtained from wind-tunnel experiments. The longitudinal dynamics were approximated using Equation 3.53a and the lateral dynamics with 3.53b

$$\begin{bmatrix} \dot{\alpha} \\ \dot{q} \end{bmatrix} = \begin{bmatrix} Z_\alpha(\rho) & 1 \\ M_\alpha(\rho) & M_q(\rho) \end{bmatrix} \begin{bmatrix} \alpha \\ q \end{bmatrix} + \sum_i \begin{bmatrix} Z_{u_i}(\rho) \\ M_{u_i}(\rho) \end{bmatrix} u_i \tag{3.53a}$$

$$\begin{bmatrix} \dot{\beta} \\ \dot{p} \\ \dot{r} \end{bmatrix} = \begin{bmatrix} Y_\beta(\rho) & Y_p(\rho) & Y_r(\rho) \\ L_\beta(\rho) & L_p(\rho) & L_r(\rho) \\ N_\beta(\rho) & N_p(\rho) & N_r(\rho) \end{bmatrix} \begin{bmatrix} \beta \\ p \\ r \end{bmatrix} + \sum_i \begin{bmatrix} Y_{u_i}(\rho) \\ L_{u_i}(\rho) \\ N_{u_i}(\rho) \end{bmatrix} u_i \tag{3.53b}$$

In each design, the physical control surface deflections, u_i, are replaced by generalized control or moment commands, dy. Control synthesis is then conducted using these generalized inputs, after which the resulting control laws will be integrated with a simplified control allocation scheme, which in turn translates the generalized control commands into individual surface deflections. A pseudo-inverse of the control effectiveness matrix was used for simplicity since the focus was not control allocation, using Equation. This technique can be useful to limit the dimensionality of this work, due to the large amount of 13 surface control actuators available to ICE, as in [63], the control input has been generalized and implemented in the control law, given by Equations 3.54a - 3.54c, where $A_c(\rho)$, $B_c(\rho)$, $C_c(\rho)$ are solutions to a set of LMI's.

$$\dot{x}_c = A_c(\rho)x_c + B_c(\rho) \begin{bmatrix} \omega_c(x_i - y) + \omega_c f_c y^c \\ x \end{bmatrix}, \tag{3.54a}$$

$$\dot{x}_i = -\omega_c f_i(y - y^c), \tag{3.54b}$$

$$d_y = C_c(\rho)x_c \tag{3.54c}$$

In [52], Barker and Ballas demonstrated that when an aircraft is trimmed for straight and level flight, the longitudinal and lateral-directional axes are effectively decoupled when the linear model is truncated to a sixth-order model composed of short period, roll, Dutch roll, and spiral modes. The control design methodology they employed closely resembles the standard H_∞ control design approach. Both longitudinal and lateral-directional LPV control laws were synthesized by minimizing the L_2 performance measure γ while adhering to a set of linear matrix inequalities. In this paper the Linear Models for longitudinal dynamics, shown in Equation 3.55a and the lateral dynamics shown in Equation 3.55b, differ in the application of the generalized moment commands q_{cmd}, p_{cmd} and r_{cmd} than in [63].

$$\begin{bmatrix} \dot{\alpha} \\ \dot{q} \end{bmatrix} = \begin{bmatrix} Z_\alpha & 1 \\ M_\alpha & M_q \end{bmatrix} \begin{bmatrix} \alpha \\ q \end{bmatrix} + \begin{bmatrix} 0 \\ q_{cmd} \end{bmatrix} \tag{3.55a}$$

$$\begin{bmatrix} \dot{\beta} \\ \dot{p} \\ \dot{r} \\ \dot{\phi} \end{bmatrix} = \begin{bmatrix} Y_\beta & Y_p & Y_r & Y_\phi \\ L_\beta & L_p & L_r & L_\phi \\ N_\beta & N_p & N_r & N_\phi \\ 0 & 1 & tan(\theta_t) & 0 \end{bmatrix} \begin{bmatrix} \beta \\ p \\ r \\ \phi \end{bmatrix} + \begin{bmatrix} 0 \\ p_{cmd} \\ r_{cmd} \\ 0 \end{bmatrix} \tag{3.55b}$$

The parameter space, in which the LPV model is valid is made gridded in this paper where the constraints are only solved at the gridpoints. Similarly to [63], control allocation via a pseudo-inverse of the B-matrix (B^+) to generate specific control surface commands from generalized moment commands is done: $\delta = B^+ B^* \delta^*$, by using a control selector.

The difficulty in applying LPV models to highly non-linear flight control systems using spline-based interpolation is outlined in [64]. In this work, a 6-DOF aerodynamic model is stabilized using a gain scheduled controller composed of 25 LQR controllers. This approach results in steady-state errors in the longitudinal dynamics, considering only two variables: forward and downward velocity. These errors occur because the control area does not consist of a sequence of equilibrium points across the analyzed flight envelope and extra scheduling parameters need to be considered. Adding a variable such as pitch angle in the gain scheduling, could help the controller design and stability radius, as recommended in the report.

3.5. Contribution of thesis to body of knowledge

Based on the conducted literature review, research and scientific work on the application of multivariate splines, which are a class of approximating functions, as scheduling parameter functions in the context of global LPV system identification problems is limited. Moreover, the application of multivariate B-splines in LPV modeling had been largely unexplored in existing literature, while simplex splines contain intriguing properties such as the ability to fit scattered datasets in non-rectangular domains. As demonstrated in the previous section, although B-splines provide smooth approximation capabilities, their flexibility can be limited when applied to general LPV or qLPV model. This limitation comes from the need for careful triangulation construction and tuning, which can be computationally intensive and susceptible to numerical issues.

The application of a LPV model, approximated using multivariate splines, to ICE aircraft has yet to be undertaken. ICE aircraft feature unconventional control surfaces and configurations, leading to highly nonlinear, coupled, and rapidly varying dynamics that pose significant challenges for accurate modeling. The control effectors in ICE aircraft often necessitate basis functions capable of addressing high-dimensional parameter spaces and abrupt shifts in dynamics. This requirement can be computationally intensive. The body of knowledge at the Control and Simulation department of TU Delft's Aerospace Engineering faculty, which has a defined research direction in the development of multivariate spline models for highly non-affine aircraft dynamics, will be enriched by the proposed work. This research contributes to the ongoing efforts to develop robust models for the ICE framework, with a particular focus on coping with highly transient and dynamic changes, which are characteristic of modern aircraft behavior. The research conducted in this thesis aims to evaluate the capacity of multivariate B-splines to achieve accurate approximations of the LPV model constructed for the highly non-affine models.

3.6. Concluding Remarks on Literature review

This literature review has examined the state-of-the-art in robust flight control by integrating it with the modeling of LPV systems, thereby bridging the gap between well-established local-linear modeling frameworks and non-linear systems. One promising direction identified is the use of multivariate simplex splines as a scheduling function for LPV systems, which, despite its potential, has received limited attention in the existing literature. The main objective would be to investigate the possibility of LPV model synthesis on a highly non-linear aircraft platform by using multivariate splines as a scheduling function. This would be an approach to LPV modeling that prioritizes the identification of an LPV system rather than closed-loop control, shifting the focus to system identification of nonlinear system descriptions.

Through an analysis of various theoretical and methodological frameworks, including Jacobian linearization for quasi-LPV systems around trim points and the incorporation of spline basis functions, it becomes evident that high levels of accuracy can be achieved when approximating with piecewise continuous functions, provided that the model's application supports such an approach. This work will investigate a highly non-affine overactuated ICE model that can be trimmed to obtain linearized state-space models, thus offering a suitable choice for scheduling parameters that are functions of the states, effectively transforming it into a quasi-LPV system. One of the main difficulties would be that the control input vector is $\mathbf{u} \in \mathbb{R}^{13}$, thus control allocation methods need to be applied. Although the literature demonstrates the use of spline basis functions to improve continuity and accuracy, and LPV controllers have been designed for ICE, there is currently no connection between these two approaches. This work aims to connect the two concepts by integrating spline-based methods with LPV system design for non-linear dynamical models, one of which is a highly non-affine aerodynamic model such as the ICE.

4

Preliminary Work

The following Chapter presents the selection of methodologies as a basis for the research conducted in this project based on the rigorous literature review performed in Chapter 3. It describes the proposed models for a global LPV system in Section 4.1, using system identification model structures, such as the multivariate simplex B-spline in Section 4.2 and their application to an non-affine aerodynamic model of the ICE aircraft in Section 4.3. Finally, this Chapter concludes with LPV model synthesis of cart-pendulum system in Section 4.4.

4.1. Linear Parameter Varying Model Selection

The selection of LPV model structure for the non-affine ICE aircraft depends on the measured data provided by wind tunnel tests performed in [37], which define the fundamental laws governing the ICE behavior that we aim to represent within the LPV framework. As shown in [37], it is possible to linearize the system across several operating/equilibrium points by creating a trim routine using MATLAB's constrained optimization function, `fmincon`, which minimizes the sum of the squared control effector deflections, also depicted by Equaton 3.48. By adjusting the initial aircraft velocities to match the desired freestream velocity, it drives both the linear and rotational accelerations to zero, resulting in a collection of local LTI descriptions that can be interpolated to form a global approximation of ICE. This allows for the linearization-based LPV modeling approcah that tries to approximate the non-linear system in a LPV state-space form.

The trim maps for each control effector were generated over a flight envelope that spanned altitudes from 0 to 50,000 feet in increments of 10,000 feet, and Mach numbers from 0.1 to 2.2 in increments of 0.1, as indicated in [37]. Since the LTI systems will be derived based on these two parameters, it is logical to select them as the scheduling variables, as it was done in [63] and [52]. Furthermore, the scheduling variables are not free parameters, or external disturbances of the aircraft, as do constitute the states of ICE (with some mathematical manipulation), thus the system becomes quasi-LPV with the form shown in Equation 3.22.

By defining the equilibrium points $p_i = \text{Col}(x_i, u_i) \in \mathbb{X} \times \mathbb{U},\ i \in \mathbb{I}_1^n$, it is possible to work with an LPV description of the the ICE model in the form of Equations 4.1a and 4.1b[18].

$$\frac{d}{dt}\tilde{x} = \sum_{i=1}^{n} g_i(p) A_i \tilde{x} + \sum_{i=1}^{n} g_i(p)(p) B_i u - \sum_{i=1}^{n} g_i(p)(A_i x_i + B_i u_i) \tag{4.1a}$$

$$\tilde{y} = \sum_{i=1}^{n} g_i(p) C_i \tilde{x} + \sum_{i=1}^{n} g_i(p) D_i \tilde{u} - \sum_{i=1}^{n} g_i(p)\left(C_i x_i + D_i u_i - \mathcal{G}(p_i)\right) \tag{4.1b}$$

where g_i is a set of normalized interpolation scheduling functions $g_i : \mathbb{P} \to [0,1]$, with $\sum_{i=1}^{n} g_i(p) = 1\ \forall p \in \mathbb{P}$ and $g_i(p_i) = 1\ \forall i \in \mathbb{I}_1^n$.

In order to make sure that the LPV model shown in Equations 4.1a and 4.1b is in state-space form, $n = 1$, so the system is linearized in only one point. In such case $\mathcal{G}_1 = 1$. Then by redefining the state as $\tilde{x} = x - x_1$ and the input as $\tilde{u} = u - u_1$ and the output as $\tilde{y} = y - \mathcal{G}_1$ an LTI-SS approximation is created. The selection of linearization points $\{p_i\}_{i=1}^{n}$ may initially suggest an equidistant distribution over the space $X \times U$. However, due to the dynamic variations of the ICE nonlinear system, a non-equidistant selection with denser sampling in certain regions of $X \times U$ may result in significantly improved approximations, as noted in [18]. The states $\mathbf{x} \in \mathbb{R}^{12}$, output $\mathbf{y} \in \mathbb{R}^{25}$ and input vectors $\mathbf{u} \in \mathbb{R}^{13}$ obtained from the model in [37] contain the variables shown in Equations 4.2a-4.2c.

$$x = \begin{bmatrix} x_e & y_e & z_e & u_b & v_b & w_b & \varphi & \theta & \psi & p & q & r \end{bmatrix} \tag{4.2a}$$

$$y = \begin{bmatrix} x_e & y_e & z_e & u_b & v_b & w_b & A_x & A_y & A_z & p & q & r & \dot{p} & \dot{q} & \dot{r} & u_e & v_e & w_e & M \end{bmatrix} \tag{4.2b}$$

$$u = \begin{bmatrix} \delta_{\text{LAMT}} & \delta_{\text{RAMT}} & \delta_{\text{LILEF}} & \delta_{\text{RIBLEF}} & \delta_{\text{LOLEF}} & \delta_{\text{ROLEF}} & \delta_{\text{LSSD}} & \delta_{\text{RSSD}} & \delta_{\text{LEL}} & \delta_{\text{REL}} & \delta_{\text{TV}} & \delta_{\text{PF}} \end{bmatrix} \tag{4.2c}$$

where the throttle control surfaces δ_{PTV} and δ_{LTV} are subject to the constraint as shown with Equation 4.3.

$$\sqrt{\delta_{\text{PTV}}^2 + \delta_{\text{LTV}}^2} \leq \delta_{\text{TV}_{\text{max}}} \tag{4.3}$$

4.2. Spline Basis Function

To apply the LPV system described in Equations 4.1a and 4.1b, the interpolating scheduling function neds to have the property $g_i : \mathbb{P} \to [0, 1]$, with $\sum_{i=1}^{n} g_i(p) = 1 \ \forall p \in \mathbb{P}$ and $g_i(p_i) = 1 \ \forall i \in \mathbb{I}_1^n$. As mentioned in Section 3.2.3, multivariate polynomial simplex B-splines can be used, as their barycentric coordinates are normalized in the way required by Equations 4.1a and 4.1b. The accuracy of using these type of splines can be determined, while the multivariate polynomial used can have a similar basis structure, as in [63], and is shown in Equation 4.4.

$$p(M, h, \Theta) = \Theta_0 + \Theta_{1,0}M + \Theta_{0,1}h + \Theta_{2,0}M^2 + \Theta_{1,1}Mh + \Theta_{0,2}h^2 + \cdots = \sum_{d=0}^{M_{\text{multi}}} \sum_{n+m=d} \Theta_{n,m}M^n h^m \tag{4.4}$$

where M is the Mach number, and h is the altitude in feet. The methodology followed in this research is already outlined in Subsection 3.2.3.

4.3. Innovative Control Effectors Aerodynamic Model

The aerodynamic model of ICE as described in [37], outputs dimensionless coefficients that are built-up from contributions of the dimensionless coefficients. The X-axis is in the symmetry plane of the aircraft and points forward, the Z-axis also lies in the symmetry plane and points downward. The Y-axis is directed to the right, perpendicular to the symmetry plane, completing the right-handed orthogonal axis-system. Each of these axes, has a respective moment, named L, M, N. The multi-axis thrust vectoring model is added additionally to the force and moment equation, by projecting the thrust vector T and thrust moment τ onto the body frame with l_n being the moment arm fixed at 18.75 ft, in [37]. The Equations of Motion for all six degrees of freedom, are then derived using Equation 4.5.

$$X = -C_A\tilde{q} + T\cos(\delta_{\text{PTV}})\cos(\delta_{\text{LTV}}) \tag{4.5}$$
$$Y = C_Y\tilde{q} + T\cos(\delta_{\text{PTV}})\sin(\delta_{\text{LTV}}) \tag{4.6}$$
$$Z = -C_N\tilde{q} - T\sin(\delta_{\text{PTV}})\cos(\delta_{\text{LTV}}) \tag{4.7}$$
$$L = C_l\tilde{q}b \tag{4.8}$$
$$M = C_m\tilde{q}\bar{c} - Tl_n\sin(\delta_{\text{PTV}})\cos(\delta_{\text{LTV}}) \tag{4.9}$$
$$N = C_n\tilde{q}b - Tl_n\cos(\delta_{\text{PTV}})\sin(\delta_{\text{LTV}}) \tag{4.10}$$

where $\tilde{q} = \frac{1}{2}\rho V^2$ (with true airspeed V [ft/s], local air density ρ in [slug/ft^3] and total wing surface area S in [ft^2] describes the dynamic pressure in the aerodynamic reference frame. b is the wing span and $\bar{c}$ is the mean aerodynamic chord in [ft]. To illustrate the complexity of the aerodynamic model, each dimensionless coefficients of the forces and moments in the six degrees of freedom, consist of between 17-19 sub-coefficients as indicated in [37]. The dimensionless moment coefficients are shown in Equations 4.11 - 4.13.

$$\begin{aligned}C_l &= C_{l_1}(\alpha, M) + C_{l_2}(\alpha, \beta, M) + C_{l_3}(\alpha, M, \delta_{\text{LEL}}, \delta_{\text{LSSD}}) - C_{l_4}(\alpha, M, \delta_{\text{REL}}, \delta_{\text{RSSD}}) - C_{l_5}(\alpha, \beta, \delta_{\text{LILEF}}) \\ &+ C_{l_6}(\alpha, \beta, \delta_{\text{RILEF}}) - C_{l_7}(\alpha, \beta, M, \delta_{\text{LILEF}}, \delta_{\text{LOLEF}}) + C_{l_8}(\alpha, \beta, M, \delta_{\text{RILEF}}, \delta_{\text{ROLEF}}) + C_{l_9}(\alpha, \delta_{\text{LOLEF}}, \delta_{\text{LAMT}}) \\ &- C_{l_{10}}(\alpha, \delta_{\text{ROLEF}}, \delta_{\text{RAMT}}) + C_{l_{11}}(\alpha, \delta_{\text{LAMT}}, \delta_{\text{LEL}}) - C_{l_{12}}(\alpha, \delta_{\text{RAMT}}, \delta_{\text{REL}}) + C_{l_{13}}(\alpha, M, \delta_{\text{PF}}, \delta_{\text{LSSD}}, \delta_{\text{RSSD}}) \\ &+ C_{l_{14}}(\alpha, \beta, \delta_{\text{LAMT}}) - C_{l_{15}}(\alpha, \beta, \delta_{\text{RAMT}}) + C_{l_{16}}(\alpha, \beta, \delta_{\text{LSSD}}) - C_{l_{17}}(\alpha, \beta, \delta_{\text{RSSD}}) + \frac{pb}{2V} C_{l_{18}}(\alpha, M) \\ &+ \frac{rb}{2V} C_{l_{19}}(\alpha, M)\end{aligned} \tag{4.11}$$

$$\begin{aligned}C_m &= C_{m_1}(\alpha, M) + C_{m_2}(\alpha, \beta, M) + C_{m_3}(\alpha, M, \delta_{\text{LEL}}, \delta_{\text{LSSD}}) + C_{m_4}(\alpha, M, \delta_{\text{REL}}, \delta_{\text{RSSD}}) + C_{m_5}(\alpha, \beta, \delta_{\text{LILEF}}) \\ &+ C_{m_6}(\alpha, \beta, \delta_{\text{RILEF}}) + C_{m_7}(\alpha, \beta, M, \delta_{\text{LILEF}}, \delta_{\text{LOLEF}}) + C_{m_8}(\alpha, \beta, M, \delta_{\text{RILEF}}, \delta_{\text{ROLEF}}) \\ &+ C_{m_9}(\alpha, \delta_{\text{LOLEF}}, \delta_{\text{LAMT}}) + C_{m_{10}}(\alpha, \delta_{\text{ROLEF}}, \delta_{\text{RAMT}}) + C_{m_{11}}(\alpha, \delta_{\text{LAMT}}, \delta_{\text{LEL}}) + C_{m_{12}}(\alpha, \delta_{\text{RAMT}}, \delta_{\text{REL}}) \\ &+ C_{m_{13}}(\alpha, M, \delta_{\text{PF}}, \delta_{\text{LSSD}}, \delta_{\text{RSSD}}) + C_{m_{14}}(\alpha, \beta, \delta_{\text{LAMT}}) + C_{m_{15}}(\alpha, \beta, \delta_{\text{RAMT}}) + C_{m_{16}}(\alpha, \beta, \delta_{\text{LSSD}}) \\ &+ C_{m_{17}}(\alpha, \beta, \delta_{\text{RSSD}}) + \frac{q\bar{c}}{2V} C_{m_{18}}(\alpha, M)\end{aligned} \tag{4.12}$$

$$\begin{aligned}C_n &= C_{n_1}(\alpha, M) + C_{n_2}(\alpha, \beta, M) + C_{n_3}(\alpha, M, \delta_{\text{LEL}}, \delta_{\text{LSSD}}) - C_{n_4}(\alpha, M, \delta_{\text{REL}}, \delta_{\text{RSSD}}) - C_{n_5}(\alpha, \beta, \delta_{\text{LILEF}}) \\ &+ C_{n_6}(\alpha, \beta, \delta_{\text{RILEF}}) - C_{n_7}(\alpha, \beta, M, \delta_{\text{LILEF}}, \delta_{\text{LOLEF}}) + C_{n_8}(\alpha, \beta, M, \delta_{\text{RILEF}}, \delta_{\text{ROLEF}}) + C_{n_9}(\alpha, \delta_{\text{LOLEF}}, \delta_{\text{LAMT}}) \\ &- C_{n_{10}}(\alpha, \delta_{\text{ROLEF}}, \delta_{\text{RAMT}}) + C_{n_{11}}(\alpha, \delta_{\text{LAMT}}, \delta_{\text{LEL}}) - C_{n_{12}}(\alpha, \delta_{\text{RAMT}}, \delta_{\text{REL}}) + C_{n_{13}}(\alpha, M, \delta_{\text{PF}}, \delta_{\text{LSSD}}, \delta_{\text{RSSD}}) \\ &+ C_{n_{14}}(\alpha, \beta, \delta_{\text{LAMT}}) - C_{l_{15}}(\alpha, \beta, \delta_{\text{RAMT}}) + C_{n_{16}}(\alpha, \beta, \delta_{\text{LSSD}}) - C_{n_{17}}(\alpha, \beta, \delta_{\text{RSSD}}) + \frac{pb}{2V} C_{n_{18}}(\alpha, M) \\ &+ \frac{rb}{2V} C_{n_{19}}(\alpha, M)\end{aligned} \tag{4.13}$$

The dimensionless force coefficients are shown in Equations 4.14 - 4.16.

$$\begin{aligned}C_A &= C_{A_1}(\alpha, M) + C_{A_2}(\alpha, \beta, M) + C_{A_3}(\alpha, M, \delta_{\text{LEL}}, \delta_{\text{LSSD}}) + C_{A_4}(\alpha, M, \delta_{\text{REL}}, \delta_{\text{RSSD}}) + C_{A_5}(\alpha, \beta, \delta_{\text{LILEF}}) \\ &+ C_{A_6}(\alpha, \beta, \delta_{\text{RILEF}}) + C_{A_7}(\alpha, \beta, M, \delta_{\text{LILEF}}, \delta_{\text{LOLEF}}) + C_{A_8}(\alpha, \beta, M, \delta_{\text{RILEF}}, \delta_{\text{ROLEF}}) + C_{A_9}(\alpha, \delta_{\text{LOLEF}}, \delta_{\text{LAMT}}) \\ &+ C_{A_{10}}(\alpha, \delta_{\text{ROLEF}}, \delta_{\text{RAMT}}) + C_{A_{11}}(\alpha, \delta_{\text{LAMT}}, \delta_{\text{LEL}}) + C_{A_{12}}(\alpha, \delta_{\text{RAMT}}, \delta_{\text{REL}}) + C_{A_{13}}(\alpha, M, \delta_{\text{PF}}, \delta_{\text{LSSD}}, \delta_{\text{RSSD}}) \\ &+ C_{A_{14}}(\alpha, \beta, \delta_{\text{LAMT}}) + C_{A_{15}}(\alpha, \beta, \delta_{\text{RAMT}}) + C_{A_{16}}(\alpha, \beta, \delta_{\text{LSSD}}) + C_{A_{17}}(\alpha, \beta, \delta_{\text{RSSD}})\end{aligned} \tag{4.14}$$

$$\begin{aligned}C_Y &= C_{Y_1}(\alpha, M) + C_{Y_2}(\alpha, \beta, M) + C_{Y_3}(\alpha, M, \delta_{\text{LEL}}, \delta_{\text{LSSD}}) - C_{Y_4}(\alpha, M, \delta_{\text{REL}}, \delta_{\text{RSSD}}) - C_{Y_5}(\alpha, \beta, \delta_{\text{LILEF}}) \\ &+ C_{Y_6}(\alpha, \beta, \delta_{\text{RILEF}}) - C_{Y_7}(\alpha, \beta, M, \delta_{\text{LILEF}}, \delta_{\text{LOLEF}}) + C_{Y_8}(\alpha, \beta, M, \delta_{\text{RILEF}}, \delta_{\text{ROLEF}}) \\ &+ C_{Y_9}(\alpha, \delta_{\text{LOLEF}}, \delta_{\text{LAMT}}) + C_{Y_{10}}(\alpha, \delta_{\text{ROLEF}}, \delta_{\text{RAMT}}) + C_{Y_{11}}(\alpha, \delta_{\text{LAMT}}, \delta_{\text{LEL}}) - C_{Y_{12}}(\alpha, \delta_{\text{RAMT}}, \delta_{\text{REL}}) \\ &+ C_{Y_{13}}(\alpha, M, \delta_{\text{PF}}, \delta_{\text{LSSD}}, \delta_{\text{RSSD}}) + C_{Y_{14}}(\alpha, \beta, \delta_{\text{LAMT}}) - C_{Y_{15}}(\alpha, \beta, \delta_{\text{RAMT}}) + C_{Y_{16}}(\alpha, \beta, \delta_{\text{LSSD}}) \\ &- C_{m_{17}}(\alpha, \beta, \delta_{\text{RSSD}})\end{aligned} \tag{4.15}$$

$$\begin{aligned}C_N &= C_{N_1}(\alpha, M) + C_{N_2}(\alpha, \beta, M) + C_{N_3}(\alpha, M, \delta_{\text{LEL}}, \delta_{\text{LSSD}}) + C_{N_4}(\alpha, M, \delta_{\text{REL}}, \delta_{\text{RSSD}}) + C_{N_5}(\alpha, \beta, \delta_{\text{LILEF}}) \\ &+ C_{n_6}(\alpha, \beta, \delta_{\text{RILEF}}) + C_{N_7}(\alpha, \beta, M, \delta_{\text{LILEF}}, \delta_{\text{LOLEF}}) + C_{N_8}(\alpha, \beta, M, \delta_{\text{RILEF}}, \delta_{\text{ROLEF}}) + C_{N_9}(\alpha, \delta_{\text{LOLEF}}, \delta_{\text{LAMT}}) \\ &+ C_{N_{10}}(\alpha, \delta_{\text{ROLEF}}, \delta_{\text{RAMT}}) + C_{N_{11}}(\alpha, \delta_{\text{LAMT}}, \delta_{\text{LEL}}) + C_{N_{12}}(\alpha, \delta_{\text{RAMT}}, \delta_{\text{REL}}) + C_{N_{13}}(\alpha, M, \delta_{\text{PF}}, \delta_{\text{LSSD}}, \delta_{\text{RSSD}}) \\ &+ C_{N_{14}}(\alpha, \beta, \delta_{\text{LAMT}}) + C_{N_{15}}(\alpha, \beta, \delta_{\text{RAMT}}) + C_{N_{16}}(\alpha, \beta, \delta_{\text{LSSD}}) + C_{N_{17}}(\alpha, \beta, \delta_{\text{RSSD}}) + \frac{q\bar{c}}{2V} C_{N_{18}}(\alpha, M)\end{aligned} \tag{4.16}$$

The dynamics of the leading edge flaps are provided by the ICE model, and are represented by the transfer function H_{LE} in Equaton 4.17a. All other effectors use the dynamics shown with the transfer function (H) in Equation 4.17b.

$$H_{\text{LE}} = \tfrac{(18)(100)}{(s+18)(s+100)} \tag{4.17a}$$

$$H = \tfrac{(40)(100)}{(s+40)(s+100)} \tag{4.17b}$$

4.3.1. Linear Control Allocation (LCA)

Following from the literature review in Subsection 4.3/LPV framework applied to ICE model, a commonly used method for control allocation of ICE assumes of affine functions of the inputs, such that a linear input dynamics are applied and shown in Equation 4.18.

$$\nu = h(x) + B_{\text{lin}}(x)u \tag{4.18}$$

where $h(x)$ consists of the aerodynamic forces and moments of ICE aircraft where all control effectors are trimmed. $B_{\text{lin}}(x)$ is the linear control effectiveness matrix that provides the contributions of the control effectors. In order for the inputs to be decoupled, the interactions between the 13 effectors are neglected, such that an affine aerodynamic model is obtained using Equations 4.19a - 4.19c.

$$C_l = C_{l,\alpha}(\alpha, M) + C_{l,\beta}(\alpha,\beta,M) + \frac{pb}{2V}C_{l,p}(\alpha,M) + \frac{rb}{2V}C_{l,r}(\alpha,M) + \sum_{i=1}^{13}\left(\frac{\partial C_l}{\partial u_i}u_i\right) \tag{4.19a}$$

$$C_m = C_{m,\alpha}(\alpha, M) + C_{m,\beta}(\alpha,\beta,M) + \frac{q\bar{c}}{2V}C_{m,q}(\alpha,M) + \sum_{i=1}^{13}\left(\frac{\partial C_m}{\partial u_i}u_i\right) \tag{4.19b}$$

$$C_n = C_{n,\alpha}(\alpha, M) + C_{n,\beta}(\alpha,\beta,M) + \frac{pb}{2V}C_{n,p}(\alpha,M) + \frac{rb}{2V}C_{n,r}(\alpha,M) + \sum_{i=1}^{13}\left(\frac{\partial C_n}{\partial u_i}u_i\right) \tag{4.19c}$$

where $C_{l,\alpha}, C_{l,\beta}, C_{m,\alpha}, C_{m,\beta}, C_{n,\alpha}, C_{n,\beta}$ are dimensionless nonlinear moments generated by the main aerodynamic frame. All the other p, q, r dependant terms, are rotational rate moment coefficients.

To solve Equation 4.18, the methods described in Subsection 3.4.1, using the pseudo-inverse of the control effectiveness matrix, can be employed. Equation 3.51a can be then written in the LCA form of Equation 4.20.

$$u = (I - G_{\text{lin}}B_{\text{lin}})u_d + G_{\text{lin}}(\nu - h(x)) \tag{4.20}$$

4.4. LPV Model Synthesis: Cart-Pendulum System

In order to investigate the applicability of LPV to non-linear systems and utilize the methods discussed in this Chapetr, the following Section deals with a control example, the inverted pendulum on top of cart, whose Free-Body-Diagram is shown in Figure 4.1. The example of the inverted pendulum is chosen, as it represents a classical problem within the domains of dynamics and control theory, serving as a benchmark of various control methodologies [65]. As it represents an underactuated mechanical system (UMS), there are two independent parameters, namely, the cart's position x and the pendulum angle θ, which, in total, define 4 states of the system. The decomposition of forces and angle, for the problem considered is indicated in Figure 4.1, where the forces acting on the cart are input force (F) and friction force ($b\dot{x}$), while the force due to gravity (mg) is exerted on the pendulum. Additionally, the constant parameters, mass of cart (M), mass of the bob (m) and length (l) of the mass-less pendulum rod, are also shown. Lastly, the direction of the two independent parameters, angle of pendulum θ and position of cart x with respect to the coordinate system xy are also noted. In the following Section, first the derivation of the governing Equations of Motion is described (sub-Section 4.4.1). Then, the derivation of the state-space model and application of the LPV identification model is presented with sub-Section 4.4.2.

4.4.1. Non-linear Equations of Motion

Since this problem depicts a dynamical system, whose time-dependent motion can be described as a relation to any chosen coordinate system to describe the position of the object (Lagrangian Mechanics), the first point of derivation is the kinematic constraints that relate the mass of the pendulum with the coordinate system indicated in Figure 4.1. The location of the pendulum's mass m with respect to the x and y-coordinates, defined in Figure 4.1, is expressed using Equation 4.21.

$$x_p = x + l\sin(\theta); \quad y_p = l\cos(\theta) \tag{4.21}$$

Defining the Lagrangian (L) as the difference between the total Kinetic Energy: $T = \frac{1}{2}\sum_i^N m_i v_i^2$ of the system and the Potential energy: $V = mgy$, specifically $L = T - V$, the kinematic relations can be related as shown in Equation 4.22.

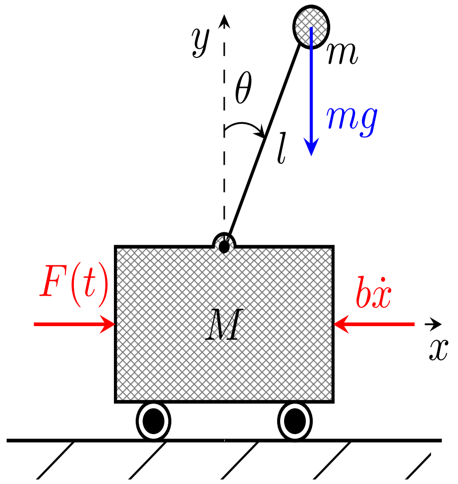

Figure 4.1: Free body diagram of inverted pendulum on top of a cart, showing forces acting on the cart in red and forces acting on the pendulum in blue.

$$\begin{aligned} L &= \frac{1}{2}M\dot{x}^2 + \frac{1}{2}m(\dot{x}_p^2 + \dot{y}_p^2) - mgy_p \\ L &= \frac{1}{2}(M+m)\dot{x}^2 + \frac{1}{2}ml^2\dot{\theta}^2 + ml\cos(\theta)\dot{x}\dot{\theta} - mgl\cos(\theta) \end{aligned} \tag{4.22}$$

Next, the Euler–Lagrange equation is formulated, shown in Equation 4.23, where q represents the complete and independent set of generalized coordinates which, in this example, represent the two independent parameters (degrees of freedom) $q_1 = x$ and $q_2 = \theta$.

$$\frac{d}{dt}\left(\frac{\partial L}{\partial \dot{q}_i}\right) - \left(\frac{\partial L}{\partial q_i}\right) = Q_i \tag{4.23}$$

On the right-hand side of Equation 4.23, the term Q_i represents the magnitude of the generalized force, associated with the virtual deflection of the system, obtained by the virtual work applied to the system by the non-constraint forces. The term Q_i is derived in Equation 4.24b from Equation 4.24a, as the dot product of the external force with the deflection component and additional component accounting for the contribution of the disipative friction force ($b\dot{x}$ in Figure 4.1). This force that is non-conservative in nature (does not depend only on position of the object, has zero potential and results in loss of energy), by definition, is not part of the Lagrangian formulation. However, with the use of Rayleigh's Dissipation Function, it is possible to account for friction, as explained in [66], and is shown in Equation 4.24b.

$$\delta W = \sum_{i=1}^{N-k}\left(\sum_{j=1}^{N} F_j \frac{\partial x_j}{\partial q_i}\right)\delta_{q_i} \tag{4.24a}$$

$$Q_i = \frac{\delta W}{\delta_{q_i}} = \sum_{j=1}^{N} F_j \frac{\partial x_j}{\partial q_i} - \sum_{i=1}^{N} b_i(q,t)\dot{q}_i \tag{4.24b}$$

Equation 4.24b, results in the forces exerted on the cart, $Q_1 = Q_x = F(t) - b\dot{x}$ and no external forces or moments on the pendulum bob, $Q_2 = Q_\theta = 0$.

Applying Equation 4.23 to the first independent variable - position x, Equation 4.25a is obtained. Furthermore, applying Equation 4.23 to the second variable - angle θ, Equation 4.25b is derived.

$$(M+m)\ddot{x} + ml\cos(\theta)\ddot{\theta} - ml\sin(\theta)\dot{\theta}^2 = F(t) - b\dot{x} \tag{4.25a}$$

$$ml^2\ddot{\theta} + ml\cos(\theta)\ddot{x} - mgl\sin(\theta) = 0 \tag{4.25b}$$

From these governing equations, it becomes clear that four states can be defined to provide a complete description of the system at any given time. These are the cart's position (x) and velocity ($\dot{x}$) and pendulum's angle (θ) and angular velocity ($\dot{\theta}$) and constitute the state vector (**x**). Equation 4.26 indicates the notation of the state variables and state variable derivatives used throughout the example.

$$\mathbf{X} = \begin{bmatrix} x \\ \dot{x} \\ \theta \\ \dot{\theta} \end{bmatrix} \Rightarrow \begin{bmatrix} X_1 \\ X_2 \\ X_3 \\ X_4 \end{bmatrix} \qquad \frac{d\mathbf{X}}{dt} = \begin{bmatrix} \dot{x} \\ \ddot{x} \\ \dot{\theta} \\ \ddot{\theta} \end{bmatrix} \Rightarrow \begin{bmatrix} \dot{X}_1 \\ \dot{X}_2 \\ \dot{X}_3 \\ \dot{X}_4 \end{bmatrix} \tag{4.26}$$

With this notation it becomes possible to represent the physical system in a state-space representation, where a mathematical model of it is presented as a set of input u, output y and state variables **x** related by first-order differential equations only.

$$\frac{d\mathbf{X}}{dt} = \mathbf{f}(\mathbf{X}) + \mathbf{b}(\mathbf{X})u \tag{4.27}$$

The contents of Equation 4.27 are shown in Equations 4.28a and 4.28b.

$$\frac{d\mathbf{X}}{dt} = \begin{bmatrix} X_2 \\ -\frac{b}{M+m\sin^2(X_3)}X_2 - \frac{g\sin(2X_3)}{2(\frac{M}{m}+\sin^2(X_3))} + \frac{l\sin(X_3)}{\frac{M}{m}+\sin^2(X_3)}X_4^2 \\ X_4 \\ \frac{b\cos(X_3)}{Ml+ml\sin^2(X_3)}X_2 + \frac{g(M+m)\sin(X_3)}{Ml+ml\sin^2(X_3)} - \frac{\sin(2X_3)}{2(\frac{M}{m}+\sin^2(X_3))}X_4^2 \end{bmatrix} + \begin{bmatrix} 0 \\ \frac{1}{M+m\sin^2(X_3)} \\ 0 \\ -\frac{\cos(X_3)}{Ml+ml\sin^2(X_3)} \end{bmatrix} F(t) \tag{4.28a}$$

$$y = \begin{bmatrix} X_1 & 0 & 0 & 0 \\ 0 & X_2 & 0 & 0 \\ 0 & 0 & X_3 & 0 \\ 0 & 0 & 0 & X_4 \end{bmatrix} + \begin{bmatrix} 0 \\ 0 \\ 0 \\ 0 \end{bmatrix} F(t) \tag{4.28b}$$

Note that the friction force has been moved to the left-hand-side of Equation 4.25a, as it dissipates the energy of the velocity $\dot{x}_2$. Therefore, the input u comprises only of the force $F(t)$. By equating Equation 4.28a to zero, it becomes possible to identify two equilibrium points: the downward position ($X_3 = \pi$) and the upward position ($X_3 = 0$), both of which are characterized by zero cart and angular velocities. Among these, the upward position represents an unstable equilibrium, while the downward position is stable. Therefore, unless a control force is applied, a disturbed pendulum will invariably return to the stable position. At these two equilibrium points, the system in 4.28a can be linearized to obtain an LTI representation at equilibrium by assuming small angle approximation, where $\cos(X_3) \approx 1$ and $\sin(X_3) \approx X_3$ and neglecting higher order derivatives like X_4^2. This is illustrated in Equation 4.29.

$$\begin{bmatrix} \dot{X}_1 \\ \dot{X}_2 \\ \dot{X}_3 \\ \dot{X}_4 \end{bmatrix} = \begin{bmatrix} 0 & 1 & 0 & 0 \\ 0 & -\frac{b}{M} & -\frac{gm}{M} & 0 \\ 0 & 0 & 0 & 1 \\ 0 & S_\theta \frac{b}{Ml} & S_\theta \frac{g(M+m)}{Ml} & 0 \end{bmatrix} \begin{bmatrix} X_1 \\ X_2 \\ X_3 \\ X_4 \end{bmatrix} + \begin{bmatrix} 0 \\ \frac{1}{M} \\ 0 \\ -S_\theta \frac{1}{Ml} \end{bmatrix} F(t) \tag{4.29}$$

where $S_\theta = 1$ signifies the pendulum being in unstable equilibrium point, and $S_\theta = -1$ when the pendulum is in the stable equilibrium point. In [67], a similar cart-pendulum problem has been investigated, while using LPV-LFT approach and focusing on a single varying parameter, the angle θ. The simplification made was that the control input u included the Force $F(t)$ and the nonlinear term $ml\sin(\theta)\dot{\theta}^2$ from Equation 4.25a. This simplifies the problem to make a reduced LFT-LPV state space form to perform H_∞ control. Since in this example, focus is put on modeling of the full dynamics of the pendulum-cart system, $ml\sin(\theta)\dot{\theta}^2$ remains part of the state-space matrix. This in turn has consequences on the numerical complexity of the derivatives of the state space matrix with respect to the scheduled states, as seen in the next Section.

4.4.2. LPV Representation

For this example, the Jacobian linearization method is used to illustrate the applicability of LPV on this Single-Input-Multi-Output (SIMO) system which will be estimated with a multivariable polynomial model structure. Applying Equations 3.26a and 3.26b on the non-linear model presented with Equation 4.28a results in a qLPV model, as the scheduling variable is selected to be the pendulum angle θ or X_3 and the cart's velocity $\dot{x}$ or X_2, which represent internal states of the system. The scheduling angle X_3 is a row vector of evenly spaced points $[0 \leq X_3 \leq 2\pi]$ rad, while the velocity is evenly spaced $[0 \leq X_2 \leq 4]$ m/s. The reason for using velocity instead of position is that position is not coupled with angle, as the non-linear unforced state matrix $f(x)$ in 4.28a contains no dependence on the state X_1.

The Jacobian Linearization form of the nonlinear equation in Equation 4.28a, is using the form shown in Equation 3.27, where instead of using an equilibrium point, the state vector is perturbed by $\tilde{X}$ which is given by $\widetilde{X} = X - X_0$, where the initial state vector is given by: $X_0 = [0\ 0\ \frac{\pi}{4}\ 0]^{\mathsf{T}}$. No perturbation in input is assumed, such that $\widetilde{U} = u$. This resembles the Off-Equilibrium approach mentioned in the Linearization Based Methods of Section 3.3.1. The first order derivatives of Equation 3.27 are shown in Equations 4.30 - 4.35, where as an example $A_{23} = \frac{\partial f_2(X)}{\partial X_3}$ with $f_2(X)$ is the second row of the non-linear unforced state matrix in Equation 4.28a and so forth.

$$A_{11} = 0,\ A_{12} = 1,\ A_{13} = 0,\ A_{14} = 0,\ A_{21} = 0, \tag{4.30}$$

$$A_{31} = 0,\ A_{32} = 0,\ A_{33} = 0,\ A_{34} = 1,\ A_{41} = 0, \tag{4.31}$$

$$A_{22} = -\frac{b}{mq},\ A_{24} = \frac{2\sin(X_3)}{q}X_4,\ A_{42} = \frac{b\cos(X_3)}{mlq}, A_{44} = -\frac{\sin(2X_3)}{q}X_4, \tag{4.32}$$

$$A_{23} = \frac{b\sin(2X_3)}{mq^2}X_2 - \frac{g}{q}\left[\sin(X_3) + \cos^2(X_3) + \frac{\sin^2(2X_3)}{2q}\right] + \frac{l\cos(X_3)}{q}\left[1 - \frac{2\sin^2(X_3)}{q}\right]X_4^2, \tag{4.33}$$

$$\begin{aligned} A_{43} = &-\frac{b\sin(X_3)}{mlq}\left[1 + 2\frac{\cos^2(X_3)}{q}\right]X_2 + \frac{cg\cos(X_3)}{q}\left[1 - \frac{2\sin^2(X_3)}{q}\right] + \\ &+ \quad \frac{1}{q}\left[\sin^2(X_3) - \cos^2(X_3) + \frac{\sin^2(2X_3)}{2q}\right]X_4^2, \end{aligned} \tag{4.34}$$

$$B_2 = \frac{1}{mq},\ B_4 = -\frac{\cos(X_3)}{mlq}. \tag{4.35}$$

where $q = \frac{M}{m} + \sin^2(X_3)$ and $c = \frac{M+m}{ml}$. As explained in [18], the Equations for A_{23} and A_{43} now contain a separate term which is a function of the scheduled state. Knowing the trajectory of the angle, equidistant selection of scheduling parameter points in the space $\mathbb{X} \times \mathbb{U}$ for the problem considered is possible, as there are no dense regions caused by dynamical changes. At the equilibrium points mentioned in Subsection 4.4.1, Equations 4.30 - 4.35 will simplify into Equation 4.29.

In this example, three distinct methods have been developed to interpolate the local models generated by Equations 4.30 to 4.35 at each scheduled point, ultimately constructing a global LPV model for the problem. The first two methods, ZOH and univariate polynomial parametric dependency use a single scheduling variable, while the last one, multivariate polynomial uses two scheduling variables. The performance of these methods is subsequently evaluated using the Root Mean Squared Error (RMSE) criterion for comparison.

The first approach employs a Zero-Order Hold (ZOH) method, as explained in Subsection 3.3.3/Zero Order Hold. In this method, the angle values θ_{ZOH} are substituted into the equations from Equations 4.30 to 4.35 in place of the state variable X_3. This substitution allows for the comparison of LPV models at each angle θ with the solution of the non-linear first-order differential equation described by Equation 4.28a. The method aims to identify the θ_{IDX} value of the Linear Time-Invariant (LTI) system that is closest to the scheduling parameter θ_{ZOH} in relation to the state X_3, while considering all available LTI systems that span N_θ number of scheduling points. This process conforms to the condition specified in Equation 4.36. Additionally, the method incorporates both the first-order Euler integration method, as outlined in Equation 3.43, and the second-order Trapezoidal method presented in Equation 3.44 to solve the non-linear first-order differential equation effectively.

$$\theta_{\text{IDX}} = \arg\min_{j} |\theta_{\text{ZOH}}(j) - X_3| \tag{4.36}$$

where $j = 1 \ldots N_t$, with N_t being the length of the simulation time vector t, which is discretized in time steps, T_d. Prior to solving the differential equation, the angle θ_{ZOH} undergoes a de-wrapping process to ensure it remains within the interval $[0 \leq \theta \leq 2\pi]$. If the angle falls outside this range, appropriate multiples of 2π are either added or subtracted until the angle is confined to the interval.

In the second method, a univariate polynomial structure with dependance on the angle $x = \theta$, as a single scheduling parameter is devised and and shown with Equation 4.37.

$$p(x, \Theta) = \Theta_0 + \Theta_1 x + \Theta_2 x^2 + \cdots + \Theta_d x^d = \sum_{d=0}^{M_{\text{uni}}} \Theta_d x^d \tag{4.37}$$

where M_{uni} is the order of the univariate polynomial and $\Theta_0, \ldots \Theta_d$ are the unknown model parameters. A linear regression model that best fits a sequence of N_θ measurements Y_{uni} is constructed, that consists of only the terms varying with the pendulum angle and creates the data to estimate the LPV scheduling functions for the true LPV model. This is presented with Equation 4.38

$$Y_{uni} = \begin{bmatrix} \frac{\partial f_2(X)}{\partial X_3} & \frac{\partial f_4(X)}{\partial X_3} & \frac{\partial b_4(X)}{\partial X_3} & \mathbf{f}(X_0) \end{bmatrix} \tag{4.38}$$

where $f_i(X), b_i(X)$ are the i^{th}-rows of the non-linear matrices shown with Equation 4.27. The evaluation of the non-linear function $\mathbf{f}$, at the initial vector X_0 equates to approximating the following term: $\mathbf{f}(X_0) \approx \frac{g(M+m)\sin(X_3)}{Ml+ml\sin^2(X_3)}$. Using Ordinary Least Squares estimator, as shown in Equation 3.5a, the estimated parameters of the global state-space LPV model become as depicted in Equation 4.39.

$$\frac{d\mathbf{x}}{dt} = \begin{bmatrix} 0 & 1 & 0 & 0 \\ 0 & -\frac{b}{mq} & p(X_3, \hat{\Theta}_{\text{OLS}}) & \frac{2\sin(X_3)}{q} \\ 0 & 0 & 0 & 1 \\ 0 & \frac{b\cos(X_3)}{mlq} & p(X_3, \hat{\Theta}_{\text{OLS}}) & \frac{-\sin(2X_3)}{q} \end{bmatrix} \begin{bmatrix} X_1 \\ X_2 \\ X_3 \\ X_4 \end{bmatrix} + \begin{bmatrix} 0 \\ \frac{1}{mq} \\ 0 \\ p(X_3, \hat{\Theta}_{\text{OLS}}) \end{bmatrix} F(t) \tag{4.39}$$

To serve a good point of comparison, Equation 4.39 is solved by the means of Euler and Trapezoidal integration. To perform Euler integration, first the difference between the perturbed state vector and the initial state vector is taken, with: $\widetilde{X} = X - X_0$, where X_0 needs to be updated, with every point along the trajectory of the angle θ. Therefore Equation 4.39, is solved by the expression in Equation 4.40.

$$X(k+1) = X(k) + h\left(\mathbf{f}(X_0) + A(p(X_3, \hat{\Theta}_{\text{OLS}}))\widetilde{X}(k) + B(p(X_3, \hat{\Theta}_{\text{OLS}}))\widetilde{U}\right) \tag{4.40}$$

where h is the step of the time vector $T(k+1) = T(k) + h$. The Trapezoid rule, has an additional step when compared with the Euler method, which is shown in Equation 4.41.

$$\begin{aligned} X(k+1) = X(k) + \frac{h}{2}\Big(&\mathbf{f}(X_0) + A(p(X_3, \hat{\Theta}_{\text{OLS}}))\widetilde{X}(k) + B(p(X_3, \hat{\Theta}_{\text{OLS}}))\widetilde{U} \\ &+ \mathbf{f}(X_0) + A(p(X_3, \hat{\Theta}_{\text{OLS}}))\widetilde{X}(k+1) + B(p(X_3, \hat{\Theta}_{\text{OLS}}))\widetilde{U}\Big) \end{aligned} \tag{4.41}$$

For the final method, a multivariate polynomial structure is constructed that depends on two variables, the pendulum angle $x = \theta$, and cart's velocity $y = \dot{x}$, represented in Equation 4.42.

$$p(x, y, \Theta) = \Theta_0 + \Theta_{1,0}x + \Theta_{0,1}y + \Theta_{2,0}x^2 + \Theta_{1,1}xy + \Theta_{0,2}y^2 + \cdots = \sum_{d=0}^{M_{\text{multi}}} \sum_{n+m=d} \Theta_{n,m} x^n y^m \tag{4.42}$$

where M_{multi} is the order of the multivariate polynomial. A linear regression model that best fits a grid of $N_\theta \times N_{\dot{x}}$ measurements Y_{multi} is constructed, expanded to include all coupled terms and consists of the structure shown in Equation 4.43.

$$Y_{multi} = \begin{bmatrix} \frac{\partial f_2(X)}{\partial X_2} & \frac{\partial f_2(X)}{\partial X_3} & \frac{\partial f_4(X)}{\partial X_2} & \frac{\partial f_4(X)}{\partial X_3} & \frac{\partial b_2(X)}{\partial X_2} & \frac{\partial b_4(X)}{\partial X_3} & \mathbf{f}(X_0) \end{bmatrix} \tag{4.43}$$

Same as in the previous method, the OLS estimator leads to a global state-space LPV model as shown in Equation 4.44.

$$\frac{d\mathbf{x}}{dt} = \begin{bmatrix} 0 & 1 & 0 & 0 \\ 0 & p(X_3, X_2, \hat{\Theta}_{\text{OLS}}) & p(X_3, X_2, \hat{\Theta}_{\text{OLS}}) & \frac{2\sin(X_3)}{q} \\ 0 & 0 & 0 & 1 \\ 0 & p(X_3, X_2, \hat{\Theta}_{\text{OLS}}) & p(X_3, X_2, \hat{\Theta}_{\text{OLS}}) & \frac{-\sin(2X_3)}{q} \end{bmatrix} \begin{bmatrix} X_1 \\ X_2 \\ X_3 \\ X_4 \end{bmatrix} + \begin{bmatrix} 0 \\ p(X_3, X_2, \hat{\Theta}_{\text{OLS}}) \\ 0 \\ p(X_3, X_2, \hat{\Theta}_{\text{OLS}}) \end{bmatrix} F(t) \tag{4.44}$$

By applying Equations 4.40 and 4.41,in a similar manner, it is noted that the state-matrix A is now defined as a function of the multivariate polynomial $A(p(X_3, X2, \hat{\Theta}_{\text{OLS}}))$. Similarly, the input matrix B, is expressed as $B(p(X_3, X2, \hat{\Theta}_{\text{OLS}}))$. As a result, it is possible to derive a solution to the first-order differential LPV state-space system.

4.4.3. Results Analysis and Discussion

With the three methods and two numerical integration schemes per method, explained in the preceding section, it becomes possible to do a simulation in MATLAB and compare the accuracy with the identification criterion Root Mean Squared Error, which has a formula written in Equation 3.34. To run the simulation, the constant terms are indicated in Table 4.1.

Parameter	Symbol	Value	Unit
Cart Mass	M	1	kg
Pendulum Mass	m	0.3	kg
Pendulum Length	l	2	m
Friction coefficient	b	0.1	-
Gravitational Acceleration	g	9.81	m/s^2
Integration time step	h	0.01	s
Simulation end time	T_{end}	10	s

Table 4.1: Constant parameters used in the simulation for the cart-pendulum system.

To integrate the non-linear differential equation in Equation 4.28a, MATLAB's `ode45` function is employed, which utilizes a six-stage, fifth-order Runge-Kutta method. A unit step force, $F(t)$, is applied as control input, at the midpoint of the simulation duration and is shown in Equation 4.45.

$$F(t) = u\left(t - \frac{T_{\text{end}}}{2}\right), \text{ where } u = \begin{cases} 1 & t \geq \frac{T_{\text{end}}}{2} \\ 0 & t < \frac{T_{\text{end}}}{2} \end{cases} \tag{4.45}$$

This timing is chosen because, during the first half of the simulation, the pendulum completes a full period of oscillation, allowing the system's behavior under the influence of the pendulum alone to be observed. All states, X_1 through X_4, are tracked, as outlined in the output matrix of Equation 4.28b and a plot of the different methods can be seen in Figure 4.2.

Looking through the results of Figure 4.2, several points can be noted. First, the linear integration on the ZOH-based LPV model is not accurate, which is expected as the approximation error is $\mathcal{O}(h)$, meaning the error scales linearly with the step size. If the step size is not sufficiently small, the accumulated error grows, making the integration inaccurate, which can be seen across all states, especially when the step input force is applied. The Trapezoid integration of the ZOH-based LPV model for the same number of 10 local LTI models for scheduling, shows an order of magnitude better approximation.

Furthermore, a high order polynomial for OLS estimation is needed, as the complexity of the original functions it tries to estimate have highly-nonlinear terms like $\cos(X_3) \cdot \sin^2(X_3) \cdot X_4^2$ in Equation 4.33, necessitating the use of additional polynomial terms to capture the system behaviour. This is a result from energy exchange between kinetic and potential energy that leads to non-linear oscillations which are not purely sinusoidal and contain harmonic content that can only be approximated by including higher-order polynomial terms. Using low-order polynomials will result in underfitting, which can be noticed in the grid-based search in Figures 4.4 and 4.5, where the RMSE at low orders is almost an order of magnitude higher. However, the use of high order polynomials comes with caveats such as overfitting and high sensitivity particularly near the boundaries of the data range, due to Runge's phenomenon. This is again evident in Figures 4.4 and 4.5, for a high degree (>15) of polynomial at low number of operating points, the RMSE is becomes an order magnitude higher accross all states.

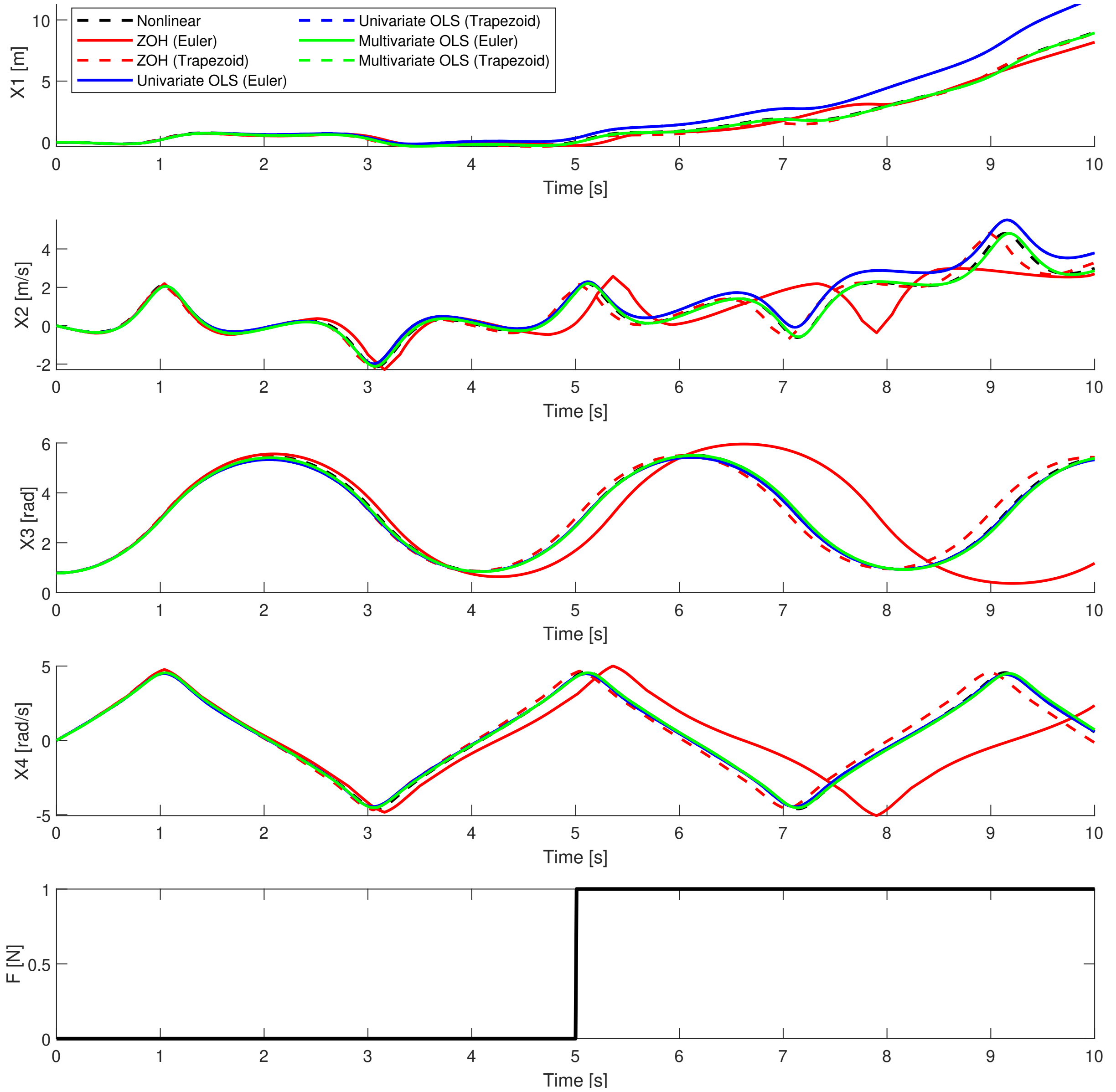

Figure 4.2: Simulation results of the nonlinear cart-pendulum model are presented, showcasing four states: the position (X_1) and velocity (X_2) of the cart, along with the angle (X_3) and angular velocity (X_4) of the pendulum, which are displayed in sub-plots. The comparison criteria are two integration techniques, Euler and Trapezoidal, applied to three different methods: Zero-Order Hold (ZOH), Univariate Ordinary Least Squares (Univariate OLS), and Multivariate Ordinary Least Squares (Multivariate OLS). The univariate polynomial order, M_{uni}, is set to 10, while the multivariate polynomial order, M_{multi}, is 12. The ZOH-based LPV model employs 10 local LTI models for scheduling. A total of 200 operating points were used to estimate the scheduling functions for both univariate and multivariate methods. A unit step force input is applied at $T_{\text{end}}/2$ seconds.

Notably, as illustrated in Figure 4.2, the absence of the state X_1, which represents the cart's position in the nonlinear equation given by Equation 4.28a, results in the worst performance of the OLS estimation for this state. State X_1 is simply an single integral of state X_2 and this observation holds true regardless of whether univariate or multivariate estimation methods are employed. Consequently, the inclusion of additional higher-order polynomial terms in the linear parameter varying (LPV) model becomes necessary. However, it is important to note that these terms may not necessarily improve the estimation of the other states $X_2 - X_4$. Furthermore, a comparison between the fixed-step methods, such as the Euler ($\mathcal{O}(h)$) and Trapezoid integration ($\mathcal{O}(h^2)$) schemes, and the adaptively adjusted step size of Runge-Kutta method ($\mathcal{O}(h^4)$) implemented in `ode45`, could explain the discrepancies in the accuracy of integrating state X_1 between the OLS models and the true nonlinear system, particularly following the application of a unit step force $F(t)$.

The estimated coefficients for a Univariate OLS polynomial function that approximates the true LPV model are shown in Table 4.2.

	Estimated Data			
OLS Coefficient	$\frac{\partial f_2(X)}{\partial X_3}$	$\frac{\partial f_4(X)}{\partial X_3}$	$\frac{\partial b_4(X)}{\partial X_3}$	$\mathbf{f}(X_0)$
$\hat{\Theta}_0$	-1.4782	7.4905	-0.5056	0.4790
$\hat{\Theta}_1$	-36.9794	-28.1000	0.1511	-3.6781
$\hat{\Theta}_2$	206.6224	140.1369	-0.4562	44.9137
$\hat{\Theta}_3$	-425.6707	-323.3804	1.9959	-84.1929
$\hat{\Theta}_4$	455.8488	370.3904	-2.6399	72.9152
$\hat{\Theta}_5$	-281.2179	-236.7066	1.7969	-33.8207
$\hat{\Theta}_6$	104.5742	89.7759	-0.7074	8.6757
$\hat{\Theta}_7$	-23.7765	-20.6608	0.1666	-1.1683
$\hat{\Theta}_8$	3.2333	2.8321	-0.0232	0.0606
$\hat{\Theta}_9$	-0.2416	-0.2127	0.0018	0.0021
$\hat{\Theta}_{10}$	0.0076	0.0067	-0.0001	-0.0003

Table 4.2: Values of the OLS coefficients for the Univariate polynomial model of optimal degree $M_{\text{uni}} = 10$.

The estimated coefficients for a Multivariate OLS polynomial function that approximates the true LPV model are shown in Table 4.3.

	Estimated Data						
OLS Coefficient	$\frac{\partial f_2(X)}{\partial X_2}$	$\frac{\partial f_2(X)}{\partial X_3}$	$\frac{\partial f_4(X)}{\partial X_2}$	$\frac{\partial f_4(X)}{\partial X_3}$	$\frac{\partial b_2(X)}{\partial X_2}$	$\frac{\partial b_4(X)}{\partial X_3}$	$\mathbf{f}(X_0)$
$\hat{\Theta}_0$	-0.1003	0.0498	-3.8009	5.6681	1.0025	-0.4975	-0.2949
$\hat{\Theta}_1$	0.0102	0.0096	31.8217	26.4702	-0.1015	-0.0963	11.1464
$\hat{\Theta}_2$	-0.0520	-0.1154	-230.2747	-209.4157	0.5195	1.1539	-31.7190
$\hat{\Theta}_3$	0.2715	0.2396	741.4889	616.7749	-2.7146	-2.3961	77.9388
$\hat{\Theta}_4$	-0.4907	-0.3750	-1211.1928	-980.6990	4.9068	3.7501	-101.6452
$\hat{\Theta}_5$	0.4826	0.3789	1152.0274	931.4441	-4.8256	-3.7886	70.8451
$\hat{\Theta}_6$	-0.2950	-0.2423	-686.8030	-558.5423	2.9497	2.4231	-26.0722
$\hat{\Theta}_7$	0.1172	0.0997	266.4737	218.2358	-1.1716	-0.9972	3.8428
$\hat{\Theta}_8$	-0.0306	-0.0267	-68.2472	-56.2540	0.3063	0.2670	0.5671
$\hat{\Theta}_9$	0.0052	0.0046	11.4429	9.4838	-0.0523	-0.0462	-0.3411
$\hat{\Theta}_{10}$	-0.0006	-0.0005	-1.2082	-1.0059	0.0056	0.0050	0.0603
$\hat{\Theta}_{11}$	0.0000	0.0000	0.0729	0.0609	-0.0003	-0.0003	-0.0050
$\hat{\Theta}_{12}$	-0.0000	-0.0000	-0.0019	-0.0016	0.0000	0.0000	0.0002

Table 4.3: Values of the OLS coefficients for the Multivariate polynomial model of optimal degree $M_{\text{multi}} = 12$.

Upon examining Figure 4.3, which presents a comparison of absolute errors exclusively for the Trapezoid integration scheme, which is more accurate than the Euler method, it is evident that the univariate ordinary least squares (OLS) estimation results in significantly large accumulated errors, particularly for the cart states X_1 and X_2. This observation aligns with expectations, as the polynomial estimation is constructed based on the scheduling variable θ, as shown in Equation 4.37. Estimating the cart's velocity using a polynomial derived solely from the pendulum's angle fails to account for the coupled dynamics, given that the pendulum's swing introduces transient effects that influence the cart's motion. Furthermore, this approach neglects the damping effect that opposes the applied force, which is further evidenced by the significant increase in accumulated error for X_1 following the application of the input force.

A noteworthy observation is that a uniform distribution of the scheduling parameter X_2 is a weaker approximator of the velocity of the cart than the uniformly distributed X_3 approximating the pendulum angle, even with the input force applied. One possible reason, is that there are no dissipating forces to the gravity force modeled that act on the pendulum bob ($Q_\theta = 0$), so that there is less uncertainty in the pendulum's motion.

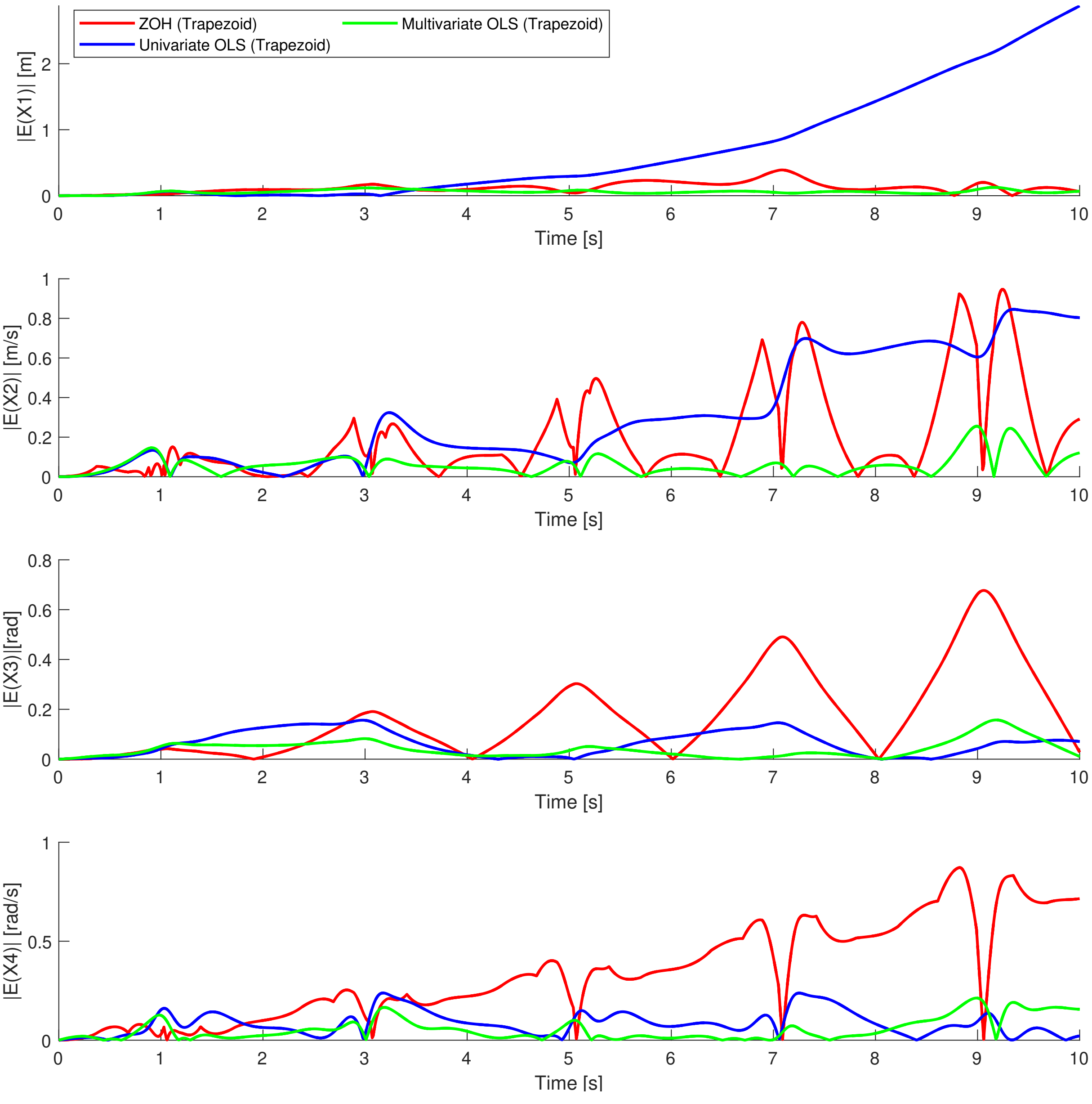

Figure 4.3: Absolute error of the nonlinear cart-pendulum model is presented, showcasing the error per state: the position ($E(X_1)$) and velocity ($E(X_2)$) errors of the cart, along with the angle ($E(X_3)$) and angular velocity ($E(X_4)$) errors of the pendulum, which are displayed in sub-plots. The criteria for comparison are the more accurate Trapezoid integration schemes applied to three different methods: Zero-Order Hold (ZOH), Univariate Ordinary Least Squares (Univariate OLS), and Multivariate Ordinary Least Squares (Multivariate OLS). The univariate polynomial order, M_{uni}, is set to 10, while the multivariate polynomial order, M_{multi}, is 12. The ZOH-based LPV model employs 10 local LTI models for scheduling. A total of 200 operating points were used to estimate the scheduling functions for both univariate and multivariate methods. A unit step force input is applied at $T_{\text{end}}/2$ seconds.

Table 4.4 presents the RSME calculated, using Equation 3.34 of the three methods presented, each per the integration technique used. It can be immediately noted that Euler and Trapezoid integration for the OLS methods yield almost identical results. This could be due to the step size h of 0.01 being too large, or too low end time T_{end} which will come at a cost of drastically increasing the computing time. Furthermore, a different set of initial conditions and constant parameters from Table 4.1, the approximation with the two integration techniques could yield a bigger difference, but experimenting with that would not be the purpose of this example. However, results do indicate that approximating the true LPV system with the multivariate OLS model in Equation 4.44 for the selected parameters and conditions are better when compared to univariate OLS or ZOH method.

		Root Mean Squared Error			
Method	**Integration**	X_1 [m]	X_2 [m/s]	X_3 [rad]	X_4 [rad/s]
Zero-Order Hold	Euler	0.0098716	0.027609	0.049658	0.060807
	Trapezoid	0.00451	0.0094404	0.0075498	0.013083
Univariate OLS	Euler	0.033502	0.01296	0.0025429	0.0032284
	Trapezoid	0.033535	0.012966	0.0025507	0.0032558
Multivariate OLS	Euler	0.0020799	0.0024805	0.0016867	0.0024838
	Trapezoid	0.0020643	0.0024397	0.0016603	0.0024417

Table 4.4: Root Mean Square Error (RMSE) of the four states: the position (X_1) and velocity (X_2) of the cart, along with the angle (X_3) and angular velocity (X_4) of the pendulum. The comparison criteria are two integration techniques, Euler and Trapezoidal, applied to three different methods: Zero-Order Hold (ZOH), Univariate Ordinary Least Squares (Univariate OLS), and Multivariate Ordinary Least Squares (Multivariate OLS).

The optimal estimating polynomial orders and optimal number of operating points selected for approximating the true LPV model, was determined by a grid-based search, spanning $N_{\text{pts}} \times M_{\text{uni/multi}}$, where $M_{\text{uni/multi}}$ is the order of the univariate or multivariate polynomial respectively. The criteria for optimization was the minimum RMSE value. These grid-based searches are depicted in Figure 4.4 for the univariate case and Figure 4.5 for the multivariate case. It can be seen that there is less confidence in finding an optimal value for the minimum RSME, when approximating the X_1 and X_2 states in contrast to states X_3 and X_4. As mentioned previously, this is the factor for increasing the number of polynomial terms, thus increasing the order, which leads to higher computational times. It is clearly evident, that for the univariate case the lowest RMSE for states X_1 and X_2 is at the edges of the grid, which was expected given the limitation of this method. However, changing the grid to an increased number of operating points > 300 or increased order of the polynomial > 15, does not improve performance and perhaps a different basis function is needed, which will be the focus of the subsequent work.

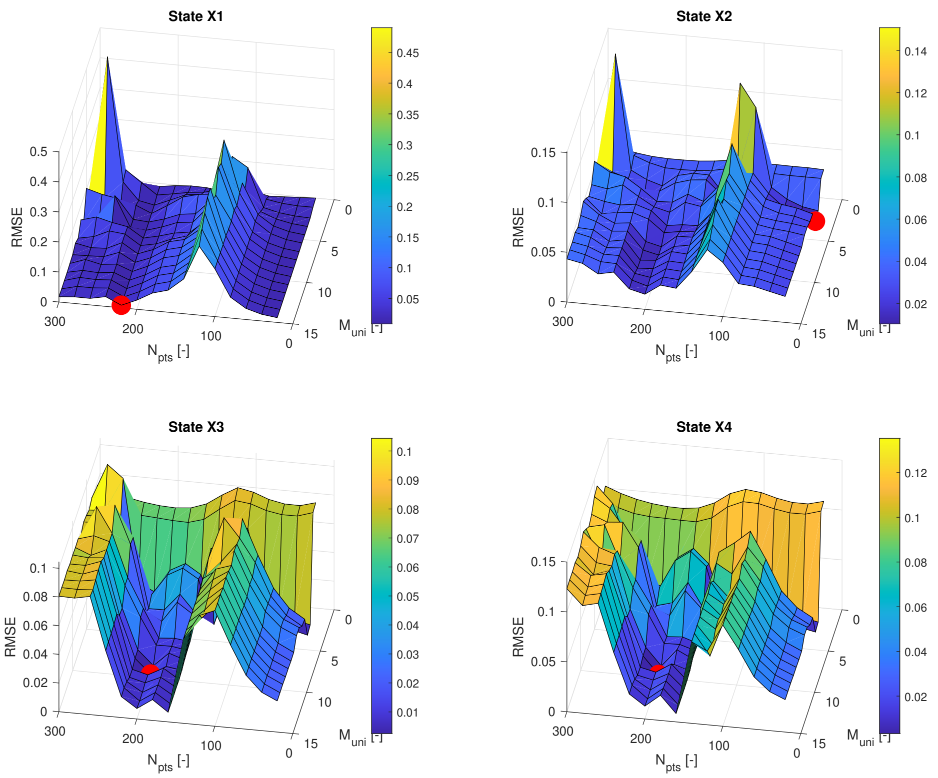

Figure 4.4: Minimum RMSE (indicated by the red dot) for the univariate polynomial approximation using the Trapezoidal Rule, shown across the four states of the cart-pendulum system. The results are displayed over a grid with varying polynomial orders (1:1:15) and total number of points (20:20:300).

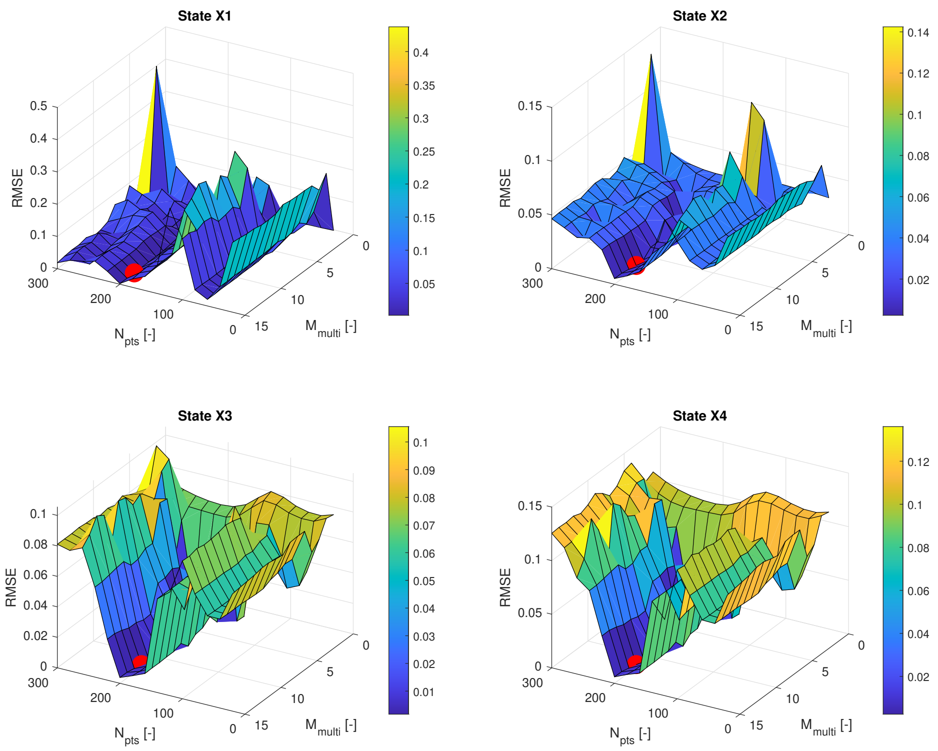

Figure 4.5: Minimum RMSE (indicated by the red dot) for the multivariate polynomial approximation using the Trapezoidal Rule, shown across the four states of the cart-pendulum system. The results are displayed over a grid with varying polynomial orders (1:1:15) and total number of points (20:20:300).

Part III

Additional Results

5

Supplementary Findings

In this Chapter additional results that have been obtained throughout the thesis work and support the scientific paper in Chapter 2 are presented. Starting with the discussion of the discontinuities for the piecewise constant method ZOH in Section 5.1, following the supplementary estimation results that support Section 2.5, for univariate and multivariate OLS in Section 5.2 for the same simulation conditions. Plots of comparing B-splines with the other polynomial methods are outlined in 5.3 and different triangulations in 5.4. Finally, an LQR controller is applied to the B-Spline LPV Model in Section 5.5.

5.1. Discontinuities of Zero-Order Hold

The first additional result for the ZOH method is checking discontinuities in ZOH due to the switching nature of ZOH. This has been explained in the Results and Discussion section of the scientific paper in Section 2.5. Compared to Multivariate OLS and B-spline in Figure 5.1, which show a smooth $f''(x)$ over 10 seconds, ZOH can cause instability in PID control due to switching. Abrupt changes lead to large, erratic outputs from the derivative term. A smooth error curve minimizes the effect of noise, leading to more stable control action. From Figure 5.1, it can be concluded that polynomial estimated methods show smoothness in the EOM approximation compared to the ZOH when using $N_\rho = 51$ points.

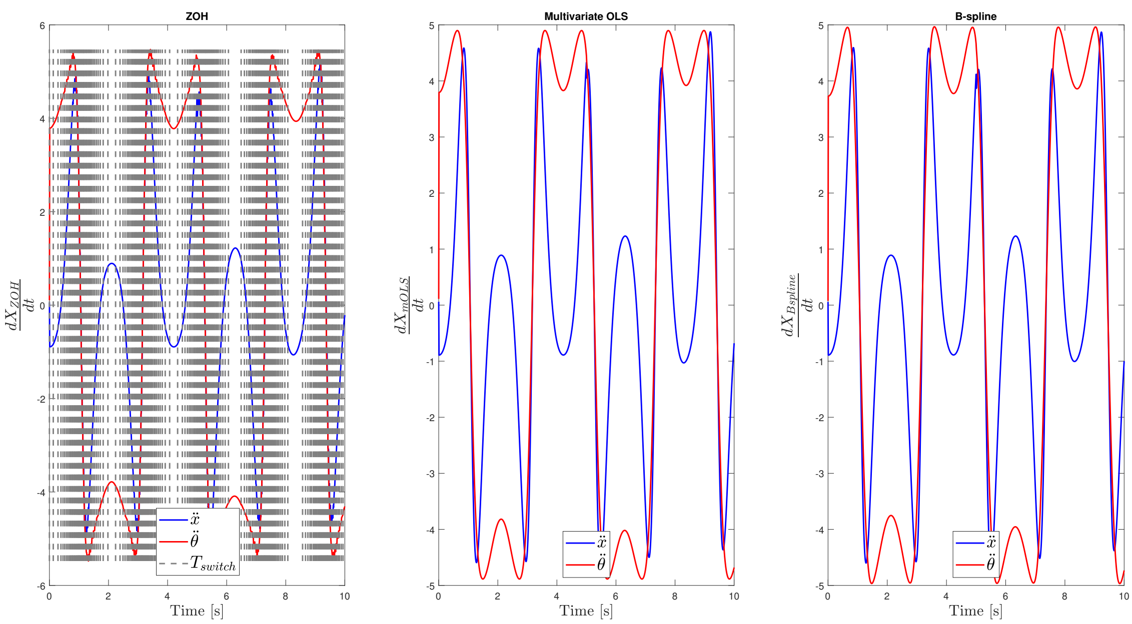

Figure 5.1: Comparison of the derivatives of velocity and angular rotation between ZOH and the polynomial methods for the IPCM. Additionally, the switching time between the constant values of the scheduling parameters in LTI systems for ZOH method is shown in the left plot.

The regions where scheduling parameters are switched are shown in Figure 5.1, with T_{switch} representing the switch time of an LTI model. This switch time is determined by substituting a subsequent value of the scheduling parameter, θ_0. It can be observed that there are regions that coincide with the values of θ_0 contained in the plot of the trajectory with simplices t_3/t_4 and t_{15}/t_{16} in Figure 10 of Section 2.5.

It is possible to check if increasing the number of scheduling points has an effect on the smoothness of the $f''(x)$ of the IPCM, by looking at Figure 5.2. It can be seen that at around 1000 points, the smoothness is almost matching the smoothness of the polynomial curves, however, the polynomial derivatives in Figure 5.2 are at 51 points, which shows the advantage of polynomial estimators.

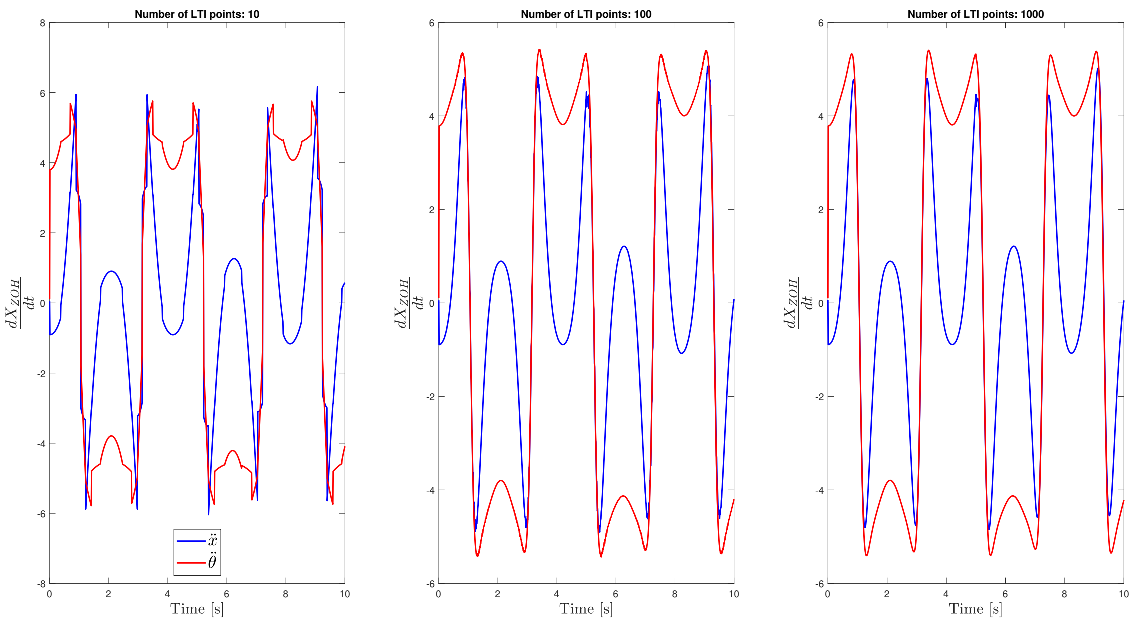

Figure 5.2: Comparison of the derivatives of velocity and angular rotation for increasing amount of scheduling points.

The computational cost of ZOH can be considered linear, $O(N)$ with N being the total number of parameters of a model using Matrix Vector multiplication (MVM): $A \cdot x \rightarrow O(N^2),\ x \in \mathbb{R}^{N\times N}$ [68]. Additionally, the ZOH algorithm performs each operation in constant discrete time, as each value is simply a lookup of the LTI system, obtained with a particular scheduling parameter data point. On the other hand, B-splines and OLS methods use matrix inverse operations $A^{-1} \rightarrow O(N^3),\ x \in \mathbb{R}^{N\times N}$, which is more expensive operation. However, as mentioned in [68], parameter estimators based on linear-in-the-parameter model structures, such as B-splines and OLS, have significantly lower computational complexity than those based on nonlinear-in-the-parameter model structure. Thus, while a ZOH scheduling approach might be more cost-effective in terms of performing mathematical operations, it does require more data points (LTI models) to get an increased level of smoothness, presenting a disadvantage when compared to interpolation methods like B-splines. A careful trade-off needs to be made when choosing ZOH as a coarse discretization may lead to loss of estimation accuracy of the non-linear system, while a fine discretization increases computational cost and complexity.

5.2. Additional OLS Results

.

Similarly to Figure 5 in the scientific paper in Section 2.5, the univariate OLS model that estimates the linearized LPV model function values of $\mathbf{Z}_{\text{uni}}$ is shown in Figure 5.3. These plots provide foundational context for the presentation and analysis of the preceding calculated simulation results presented in the scientific paper. Since the comparison of different polynomial methods in the scientific paper was conducted using the same polynomial degree ($d = 4$), the estimation over $N_\rho = 51$ is presented to illustrate why the univariate OLS estimation achieves a low RMSE value.

Figure 5.4 illustrates the multivariate ordinary least squares (OLS) estimation for the same parameters

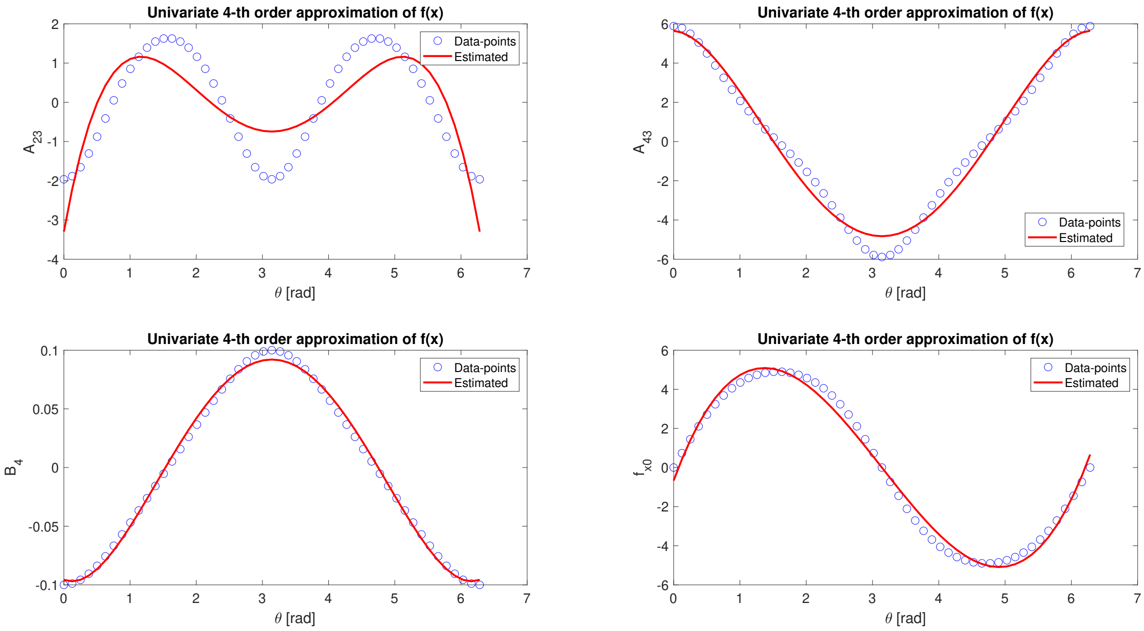

Figure 5.3: Estimation of $\mathbf{Z}_{\text{uni}}$ with univariate OLS of 4[th] degree D_{uni} over $N_\rho = 51$ data points.

examined previously. Observed data points are depicted in red, while the OLS estimation is visualized as a surface. This surface represents the estimated polynomial, approximating a grid of points, analogous to the B-spline model, due to the two-parameter estimation process resulting in a three-dimensional representation. The 4[th]-degree polynomial model exhibits a difference in OLS estimation capability between function matrix coefficients. Looking at the figure, the state space matrix coefficients associated with the cart's acceleration ($\widetilde{\mathbf{A}}_{22}$, $\widetilde{\mathbf{A}}_{23}$, and $\widetilde{\mathbf{B}}_2$) demonstrate lower estimation capability compared to those associated with the pendulum's angular acceleration ($\widetilde{\mathbf{A}}_{42}, \widetilde{\mathbf{A}}_{43}, \widetilde{\mathbf{B}}_4$).

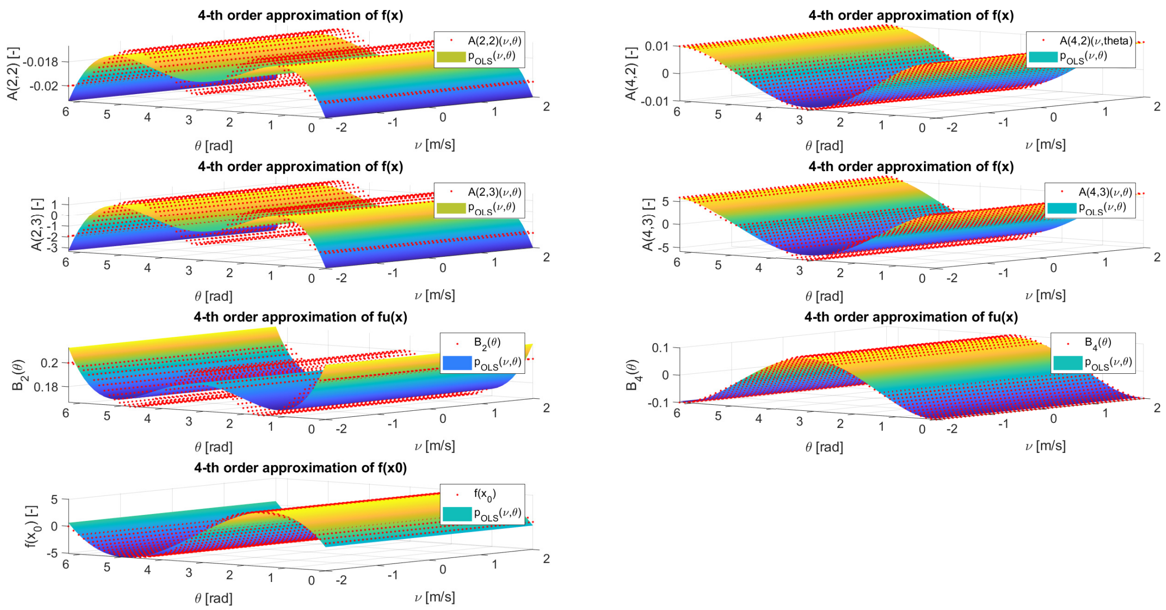

Figure 5.4: Residuals of $\mathbf{Z}$ with multivariate OLS of 4[th] degree D_{multi} over $N_\rho \times N_\rho = 51 \times 51$ data points.

The observed differences in coefficient magnitudes reflect the distinct functional forms of the cart's and pendulum's motions. The cart's acceleration, resembles a near-quadratic relationship and can be adequately captured by the low order 4th degree polynomial. However, the pendulum's angular acceleration, characterized by sinusoidal dynamics due to its oscillatory nature, requires higher degree polynomial to effectively model its periodic behavior.

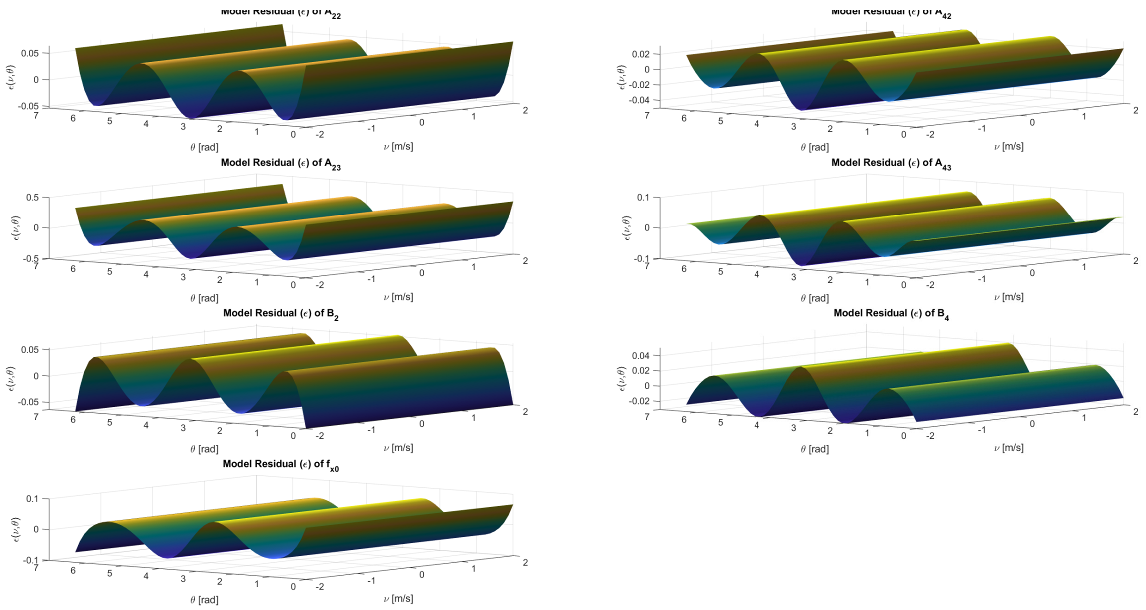

Figure 5.5: Estimation of **Z** with multivariate OLS of 4th degree D_{multi} over $N_\rho \times N_\rho = 51 \times 51$ data points.

Figure 5.5 also supports this claim, as, similar to the spline residuals using Equation 64 in Section 2.5, it shows for the multivariable OLS that the highest magnitudes come from residuals for estimating $\widetilde{\mathbf{A}}_{23}$ and $\widetilde{\mathbf{A}}_{43}$. However, the distribution of the residuals does show a difference for some of the estimated values, as they are not mostly focused in the center of the scheduling parameter grid, as seen in the B-spline residual analysis. This is most likely due to a worse approximation, than B-spline, at $d = 4$ of the estimated values ($\widetilde{\mathbf{A}}_{22}$, $\widetilde{\mathbf{A}}_{23}$, and $\widetilde{\mathbf{B}}_{2}$) as seen in Figure 5.4.

5.3. Comparing Polynomial Methods with Multivariate B-Spline

A more informative comparison is achieved by examining a cross-section of the surface plots with $N_\rho = 51$ data points, enabling a graphical comparison of all polynomial estimators. The approximation capabilities of the simplex B-spline with a lower degree are illustrated in Figure 5.6, where it can be seen that for all estimated vectors in **Z**, the spline matches the data better that the OLS approximates at the provided degree, for the same amount of data-points.

Figure 5.7 shows a comparison of all the proposed scheduling functions, in which the number of points is varied with respect to the polynomial order. The plot is generated for a simulation with $T_{sim} = 40$ and compared with the logarithm of the RMSE obtained. The values are derived from a 4th-order Runge-Kutta integration. Several observations can be made. At $d = 4$ and $N_\rho = 51$, the B-spline values are at a minimum and equivalent to those in Table 4 in Section 2.5. It can also be observed that for this simulation time, after $d = 5$, the B-spline maintains stable, low RMSE values for all approximating states. While it is true that the Multivariate OLS at $d = 5$ has a lower minimum than the B-spline, this is not the case for all states. For X_1, the position of the cart, the integrated value, the RMSE of multi-variate OLS is an order higher than that of the B-spline. Additionally, the ZOH constant lines are also plotted, where it can be seen that the minimum RMSE values at the selected simulation time are obtained at $N_\rho = 61$ points. Similarly to the OLS, at this simulation condition, the integration of the cart's position at this number of data points is lower than that of the B-spline.Finally, at $N_\rho = 11$, it can be seen that B-splines require a sufficient number of control points for the degree of the spline to ensure that the recursion and basis function calculations are valid. This is also discussed in Section 2.4, where every simplex in the triangulation $\mathcal{T}$ contains at least $\hat{d}$ non-coplanar data points, meaning that $N_J \geq \hat{d}$. As the simulation for B-spline is run on $[3 \times 3]$ triangulation of $\mathcal{T}_{18}$ simplices and from Equation 3.10, the condition $d \leq 5$ needs to be met.

The results of the 40-second simulation of the IPCM, in which a sinusoidal input force is applied halfway

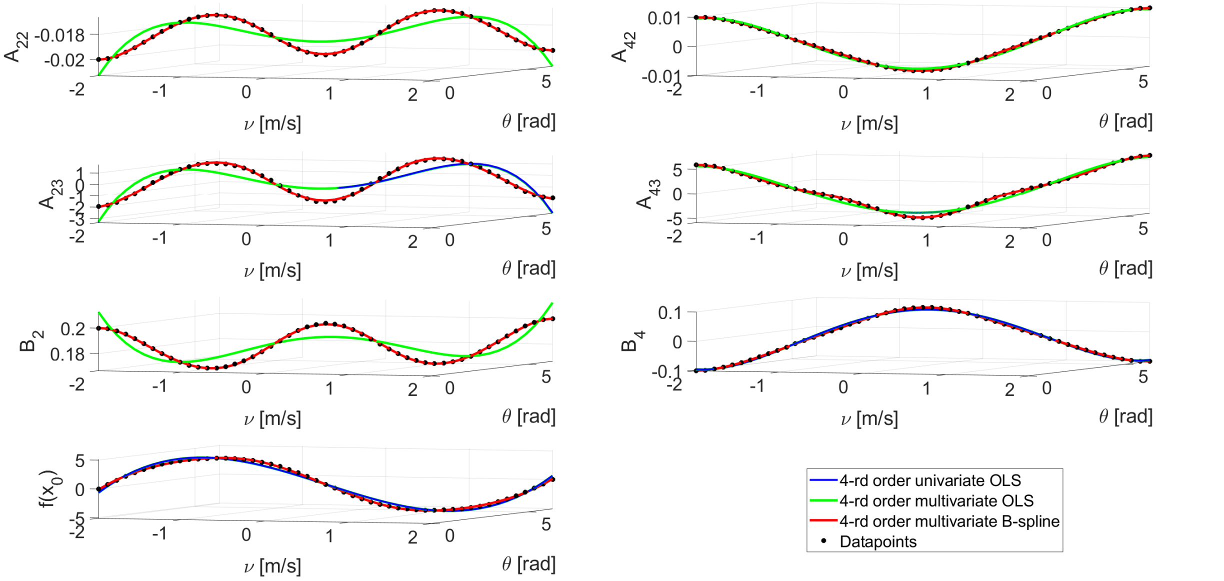

Figure 5.6: Comparison of the polynomial methods approximating the vectors in the **Z** matrix with degree $d = 4$ and $N_\rho = 51$ data points. The spline is in the spline space $s \in S_4^2(\mathcal{T}_{18})$.

through the simulation, are presented in Table 5.1. Notably, for the Euler method, the B-Spline does not produce any values, as is clearly illustrated in Figure 5.9. As discussed in Section 4.4.3, the fixed-step Euler method ($\mathcal{O}(h)$) exhibits limited accuracy due to the significant local truncation errors that accumulate over time, which results in a diverging behavior in the pendulum angle θ. This divergence leads to θ exceeding its bounded range $(0, 2\pi)$, thereby preventing the B-Spline from providing any further estimations beyond this point. It's crucial to recognize that the linear relationship established by OLS methods is derived solely from the observed data within the given range. When the range is exceeded, OLS methods extrapolate and assume that the observed linear pattern will persist indefinitely, which is often not the case. This deviation from the true model can lead to substantial inaccuracies in predictions, as demonstrated in Figure 5.9.

		Root Mean Squared Error (RMSE)			
Method	**Integration**	X_1 [m]	X_2 [m/s]	X_3 [rad]	X_4 [rad/s]
Zero-Order Hold	Euler	0.013245	0.014824	0.039464	0.061496
	Trapezoid	0.012481	0.0050362	0.0054411	0.0091621
	RK4	0.012448	0.0050429	0.0054526	0.0091818
Univariate OLS	Euler	0.021792	0.0098787	0.048841	0.039315
	Trapezoid	0.010166	0.0053941	0.0059723	0.0098187
	RK4	0.010166	0.0053986	0.0059774	0.0098274
Multivariate OLS	Euler	0.033002	0.013107	0.041182	0.053949
	Trapezoid	0.0089243	0.01104	0.014815	0.023669
	RK4	0.008925	0.011043	0.014821	0.023679
B-Spline	Euler	/	/	/	/
	Trapezoid	0.0081887	0.003853	0.0039988	0.006755
	RK4	0.0081884	0.0038474	0.003992	0.006744

Table 5.1: Root Mean Square Error (RMSE) of the estimated states: the position (X_1) and velocity (X_2) of the cart, along with the angle (X_3) and angular velocity (X_4) of the pendulum. The comparison criteria are three integration techniques: Euler, Trapezoidal, and RK4, applied to four different methods: Zero-Order Hold (ZOH), Univariate Ordinary Least Squares (Univariate OLS), Multivariate Ordinary Least Squares (Multivariate OLS), and B-Spline. T_{sim} is 40 seconds.

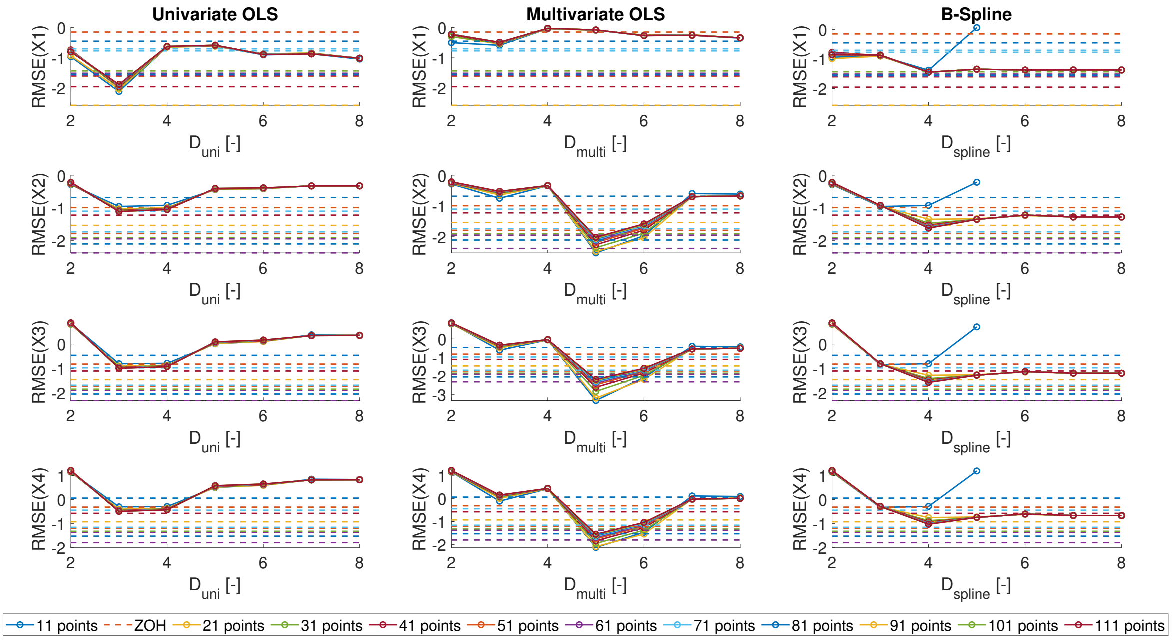

Figure 5.7: Comparison of all the methods based estimation methods in terms of the logarithm of RMSE for a simulation with $T_{sim} = 40$ seconds. B-spline has $[3 \times 3]$ triangulation of $\mathcal{T}_{18}$ simplices. Each line represents a fixed number of scheduling data points N_ρ.

In contrast, the Trapezoidal method ($\mathcal{O}(h^2)$) and Runge-Kutta methods (e.g., RK4, $\mathcal{O}(h^4)$) provide higher-order accuracy and reduces this truncation error which also improves stability of the numerical simulation evident from Figure 5.9. It should be noted, that the difference between Trapezoidal and Runge-Kutta 4th order methods is negligible when comparing them. A sufficiently small step size ($h = 0.001$) minimizes the error in the lower-order Trapezoidal method, making the higher-order accuracy of RK4 of lower impact.

Figure 5.8 shows the absolute error $|\epsilon|$ of the four states for the 3 integration methods. A lower absolute error indicates that the estimator closely follows the true model, suggesting it is accurate. Consistently high error implies a poor match between the estimator and the true model, possibly due to incorrect model assumptions or parameters. It can be seen that indeed B-spline $s_2^4(x_{2601})$ belonging to the spline space $S_4^2(\mathcal{T}_{18})$ shows a consistently lower error amongst the polynomial OLS estimators and the constant ZOH, thus confirming a better model fit.

Additionally, the results illustrate the limited numerical accuracy of the Euler integration method, evidenced by the unbounded growth in the integration of the pendulum angle. This is not observed for the higher-order accuracy integration methods.

5.4. Analysis of B-spline Triangulation, Residuals and Variance

This Section presents a graphical analysis of the rationale for using a 3×3 grid for the triangulation of B-splines. Additionally, it illustrates the relative root mean square error $RMS(\epsilon)$ of the residuals to support the validity of this approach. As shown, for simplex grids smaller than $\mathcal{T}_{18}$, the polynomial OLS values closely approximate the B-spline values. This observation implies that for a spline space S_r^d, even at higher degrees, the difference between the OLS and B-spline estimators is negligible.

The first notable divergence between polynomial approximation and B-splines for this problem appears for simplex grids larger than $\mathcal{T}_{18}$ and for B-spline orders greater than $d = 3$, as depicted in Figure 7 of Section 2.5. However, while the root mean square error (RMSE) decreases for grids exceeding $\mathcal{T}_{18}$, the difference between the OLS estimator and the B-spline estimator remains remains at least 2 orders of magnitude lower on a logarithmic scale.

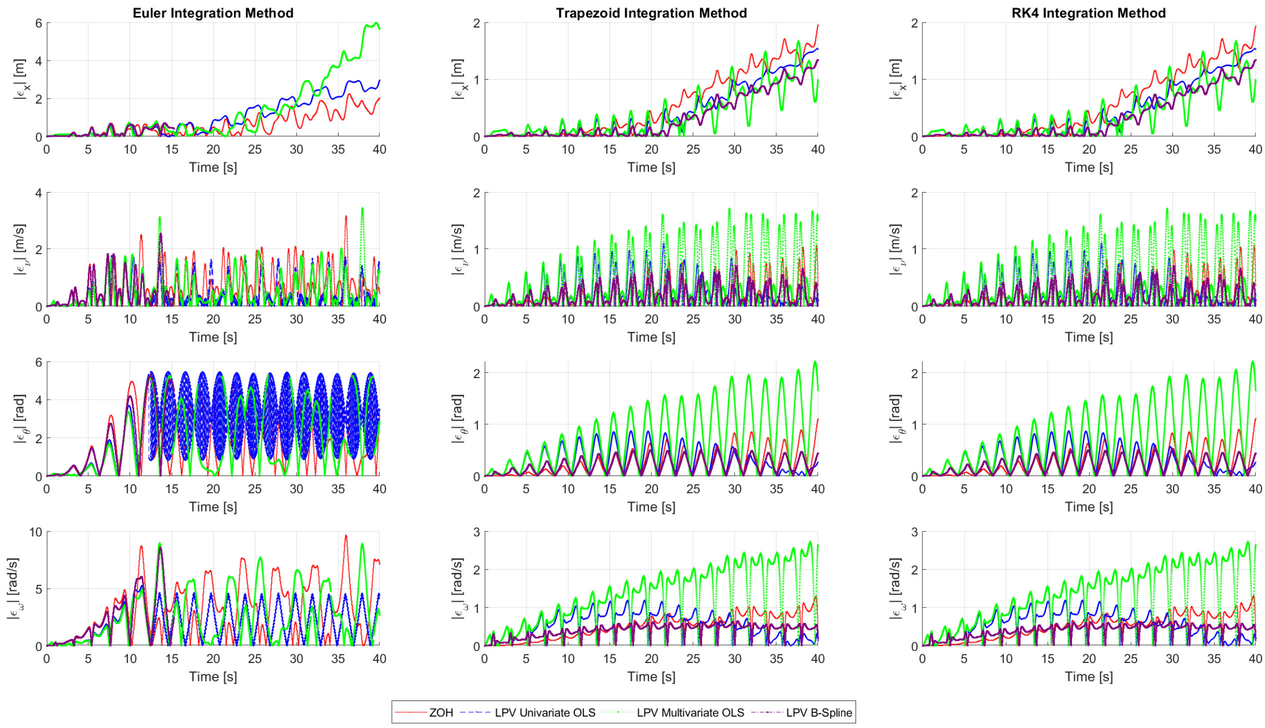

Figure 5.8: Absolute errors of the simulation results comparing the methods with the non-linear system plotted over the 3 integration methods with $T_{sim} = 40$ seconds. Number of points $N_\rho = 51$ and $d = 4$ for polynomial methods. B-spline has $[3 \times 3]$ triangulation of $\mathcal{T}_{18}$ simplices.

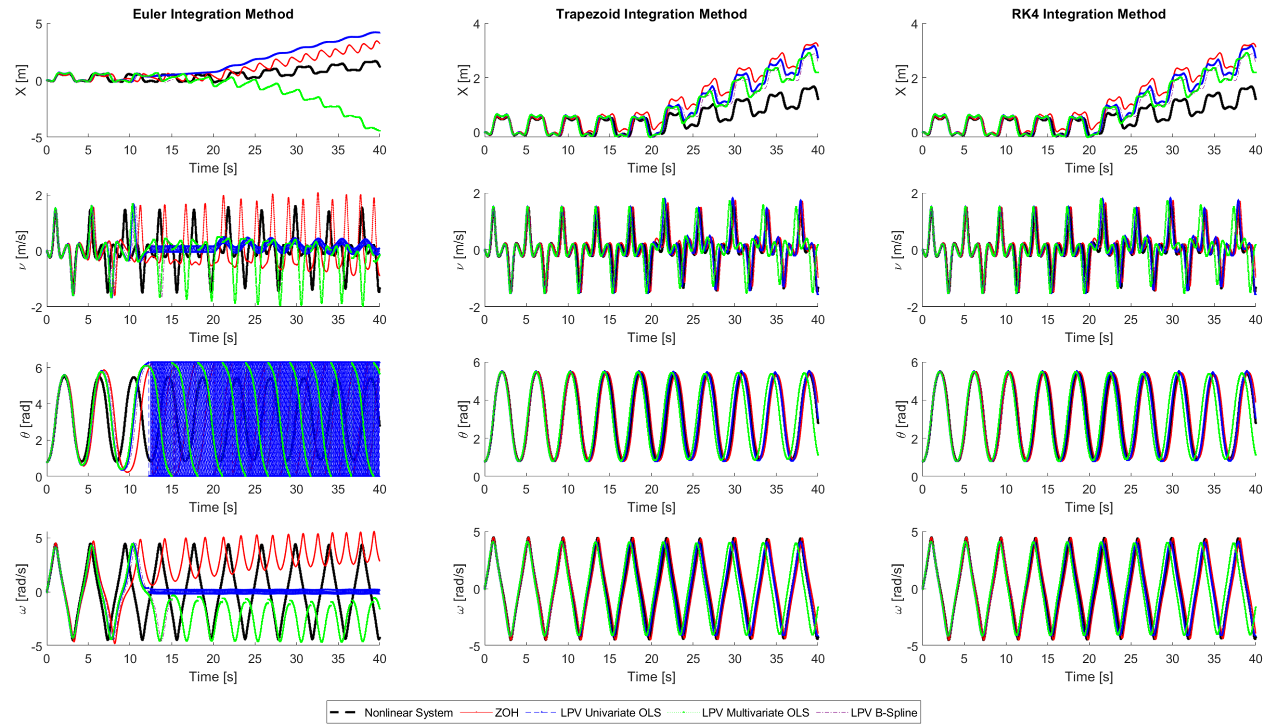

Figure 5.9: Simulation results comparing the methods with the non-linear system plotted over the 3 integration methods with $T_{sim} = 40$ seconds. Number of points $N_\rho = 51$ and $d = 4$ for polynomial methods. B-spline has $[3 \times 3]$ triangulation of $\mathcal{T}_{18}$ simplices.

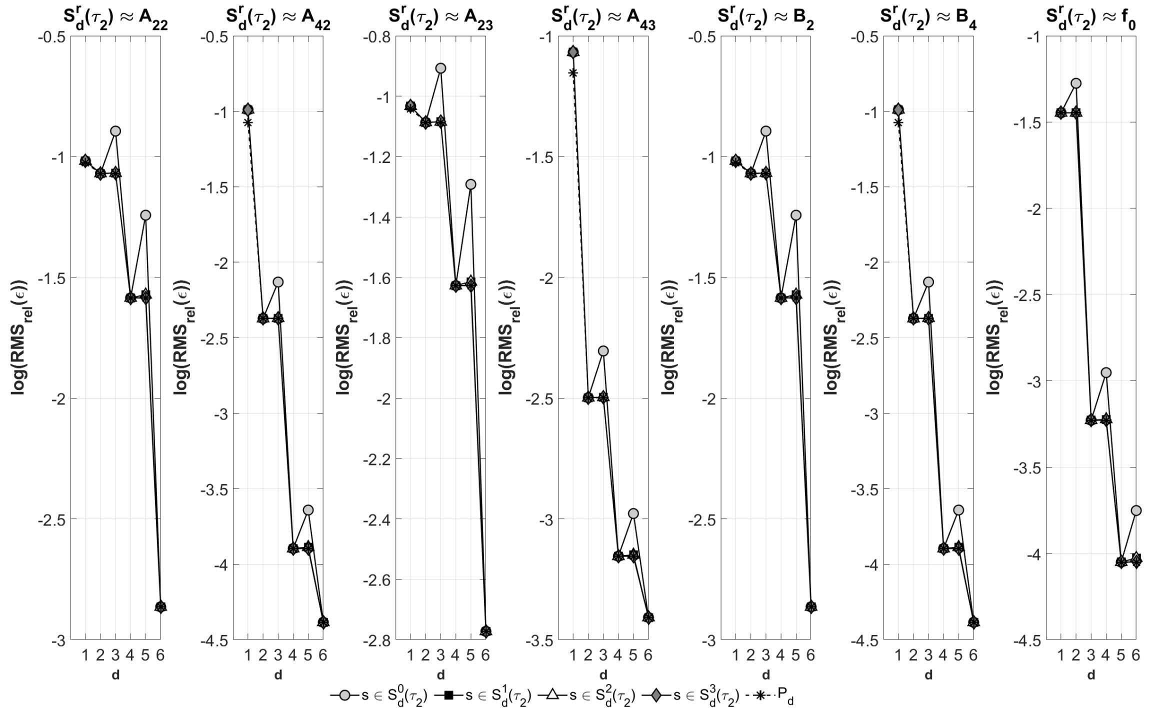

Figure 5.10: Logarithm of the relative Root Mean Squared Error of the residuals for all estimated functions of the LPV model for different spline spaces with varying spline continuity and degree, over a triangulation of $\mathcal{T}_2$ simplices ($[1 \times 1]$ grid) compared to multivariate OLS polynomial of varying degree P_d.

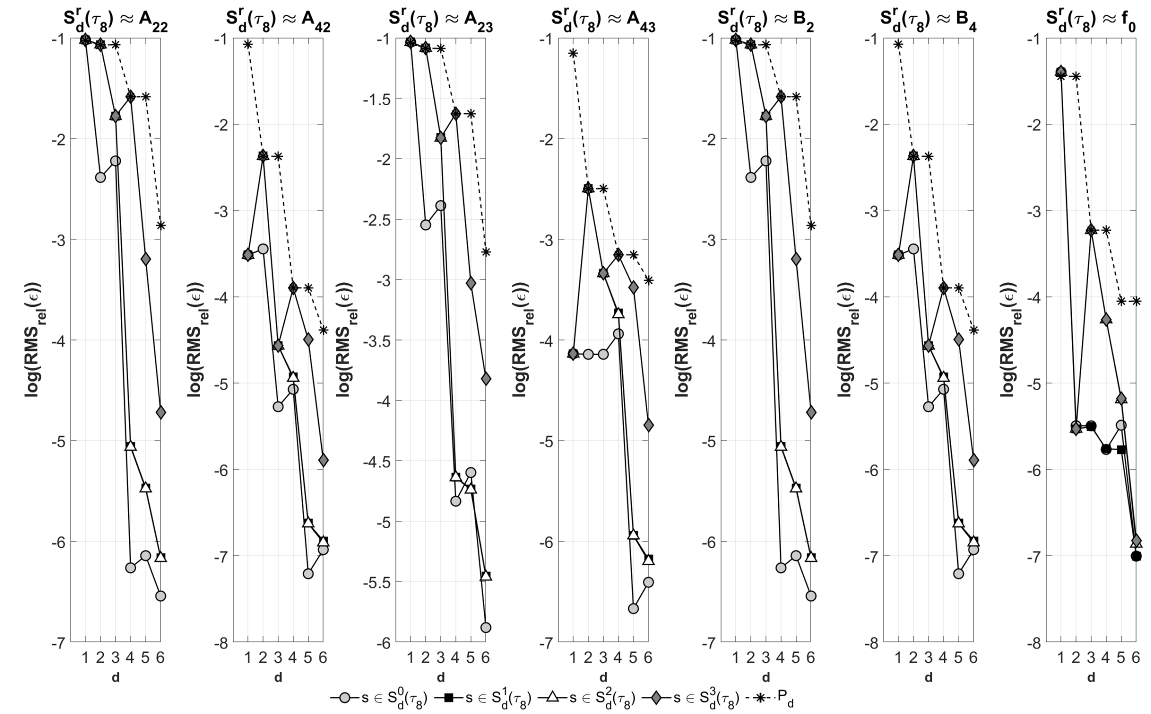

Figure 5.11: Logarithm of the relative Root Mean Squared Error of the residuals for all estimated functions of the LPV model for different spline spaces with varying spline continuity and degree, over a triangulation of $\mathcal{T}_8$ simplices ($[2 \times 2]$ grid) compared to multivariate OLS polynomial of varying degree P_d.

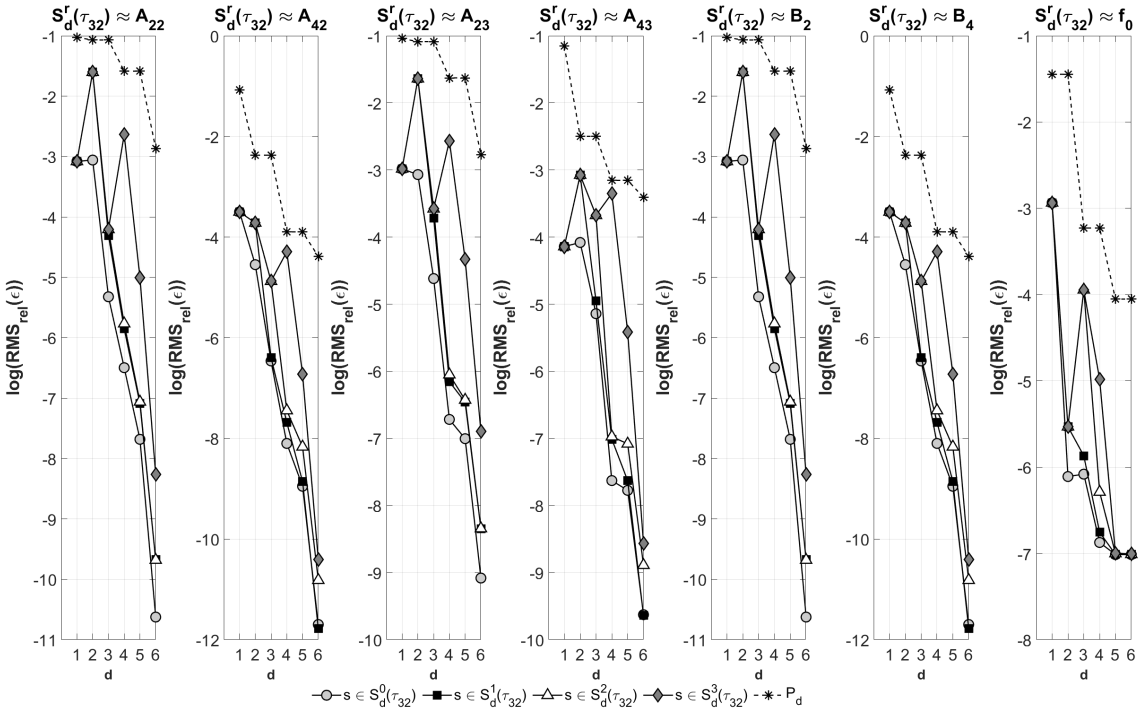

Figure 5.12: Logarithm of the relative Root Mean Squared Error of the residuals for all estimated functions of the LPV model for different spline spaces with varying spline continuity and degree, over a triangulation of $\mathcal{T}_{32}$ simplices ($[4 \times 4]$ grid) compared to multivariate OLS polynomial of varying degree P_d.

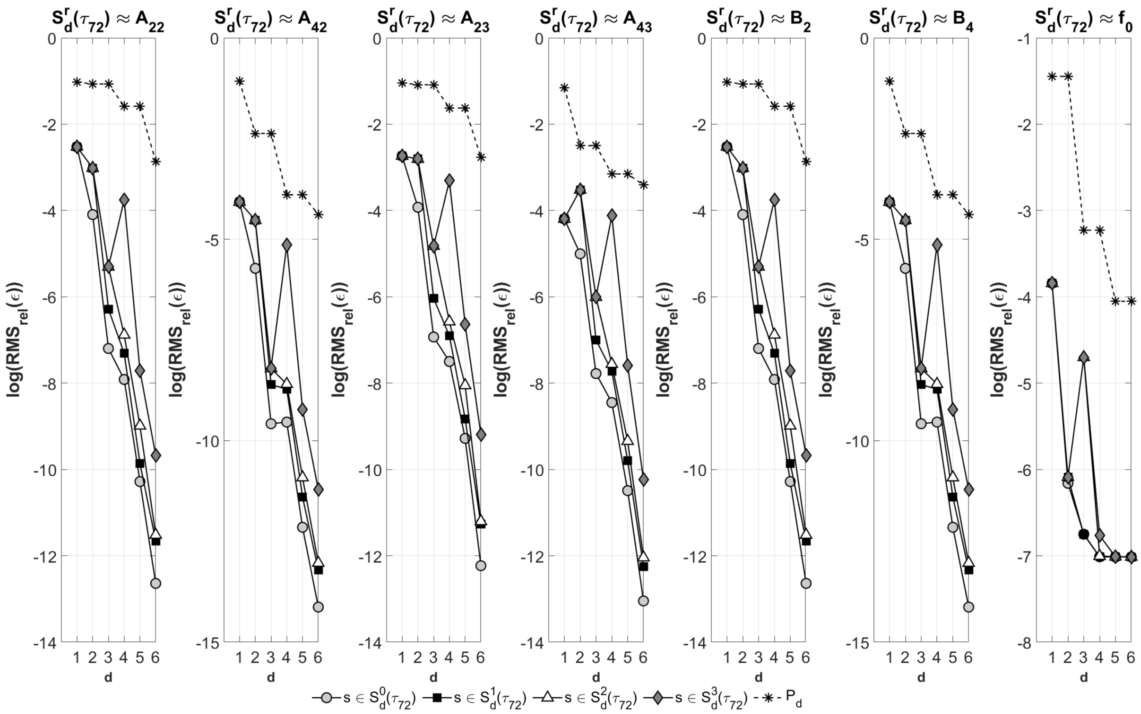

Figure 5.13: Logarithm of the relative Root Mean Squared Error of the residuals for all estimated functions of the LPV model for different spline spaces with varying spline continuity and degree, over a triangulation of $\mathcal{T}_{72}$ simplices ($[6 \times 6]$ grid) compared to multivariate OLS polynomial of varying degree P_d.

Comparing the logarithm of the mean of the variance of B-coefficients $\log\,(\overline{Var(\hat{\mathbf{c}})}$, between the multivariate OLS and the B-spline $s_2^4(x_{2601})$ belonging to the splne space $S_4^2(\mathcal{T}_{18})$ for $d = 4$ and different triangulations can be observed in Figures 5.14 - 5.17. The variance of the multivariate OLS has been computed with Equation 5.1.

$$\log\left(\overline{Var(\hat{\theta}_{OLS})}\right) = \log\left(\frac{\sigma^2}{k}\text{tr}(P)\right) \tag{5.1}$$

where σ^2 is the variance of the residual estimated with $\sigma^2 \approx \hat{\sigma}^2 = \frac{\epsilon^T \epsilon}{n-k}$, with n number of measurements and k number of regressor terms. P is the parameter covariance matrix and the trace of P is given by: $\text{tr}(P) = \sum_{i=1}^{k} p_{11} + p_{22} \dots p_{kk}$. The variance of the B-coefficients is computed using Equation 5.2.

$$\log\,(\overline{Var(\hat{\mathbf{c}})}) = \log\left(\frac{1}{\mathcal{T}_J \cdot \hat{d}} \sum_q Var(\hat{\mathbf{c}})_q\right) \tag{5.2}$$

It can be seen that the mean of the variance of OLS estimates is typically lower than that of ECOLS due to the difference in model flexibility. OLS freely adjusts the coefficients to minimize the residual, resulting in a more uniform and often lower variance across the estimated parameters. In contrast, ECOLS imposes additional restrictions on the coefficients, such as smoothness or boundary conditions ($\hat{\mathbf{c}} = \arg\min J(\mathbf{c}),$ subject to $\mathbf{H} \cdot \mathbf{c} = 0$ constraint), which effectively reduce the model's flexibility, by limiting the degrees of freedom available for parameter estimation, often leading to increased variance for the coefficients that remain free. As a result, the average variance across all coefficients tends to be higher in constrained OLS compared to the unconstrained case across parameters.

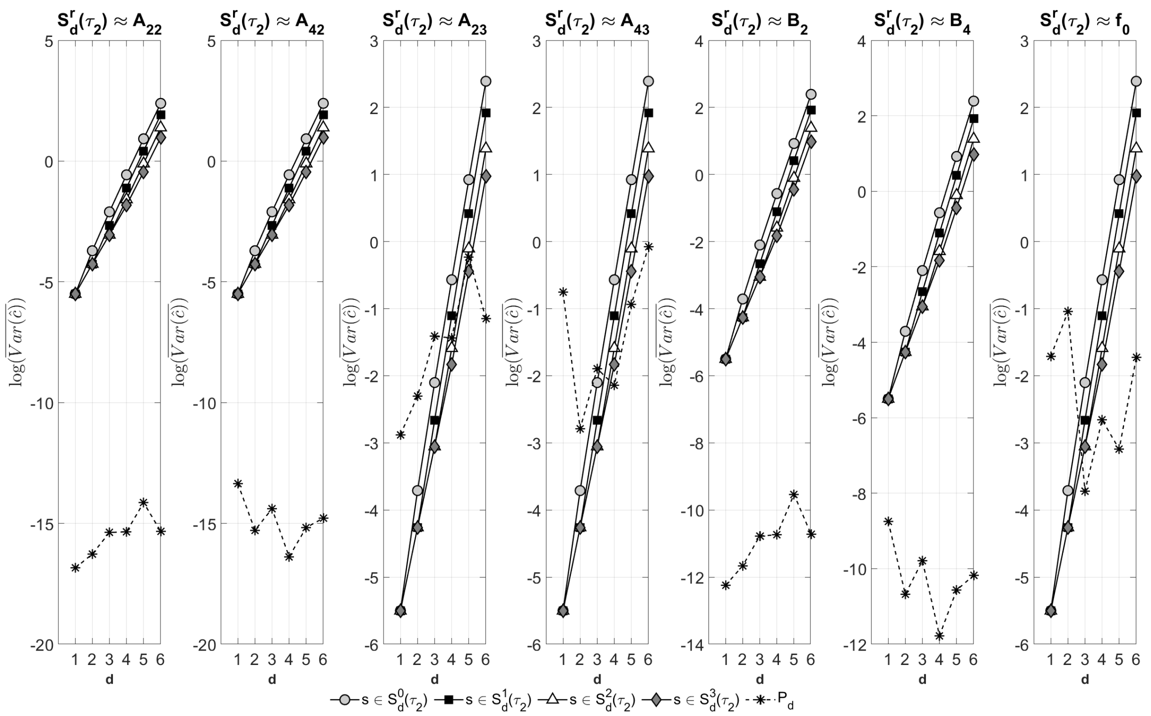

Figure 5.14: Logarithm of the mean of the Variance of the residuals for all estimated functions of the LPV model for different spline spaces with varying spline continuity and degree, over a triangulation of $\mathcal{T}_2$ simplices ($[1 \times 1]$ grid) compared to multivariate OLS polynomial of varying degree P_d.

It should be noted that, given the global approximation of the spline space and the absence of noise or regularization, the mean of the variance per estimated parameter $\log\,(\overline{Var(\hat{\mathbf{c}})}$, remains the same. This is because the variance is calculated based on the global B-coefficients, which depend solely on the fixed structure of the spline basis including the degree of the spline and the simplex construction ($\mathcal{T}_J \cdot \hat{d}$), which are the same for all estimated parameters in **Z**. It does however change based in continuity as observed in the Figures 5.14 - 5.17.

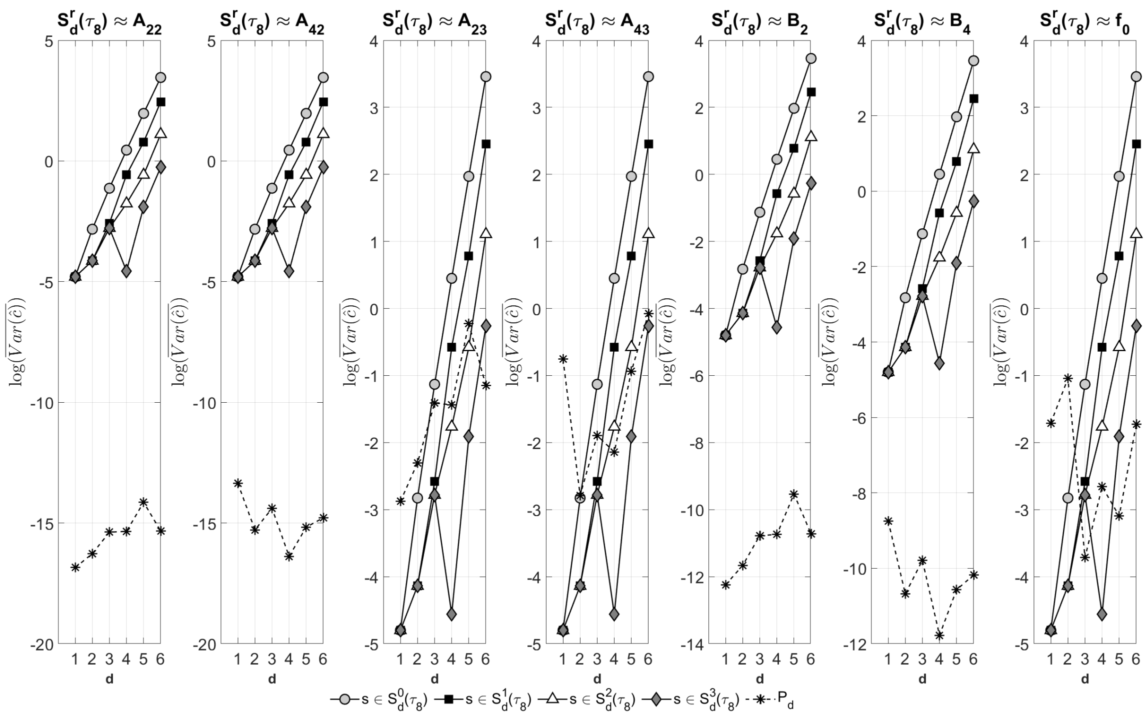

Figure 5.15: Logarithm of the mean of the Variance of the residuals for all estimated functions of the LPV model for different spline spaces with varying spline continuity and degree, over a triangulation of $\mathcal{T}_8$ simplices ($[2 \times 2]$ grid) compared to multivariate OLS polynomial of varying degree P_d.

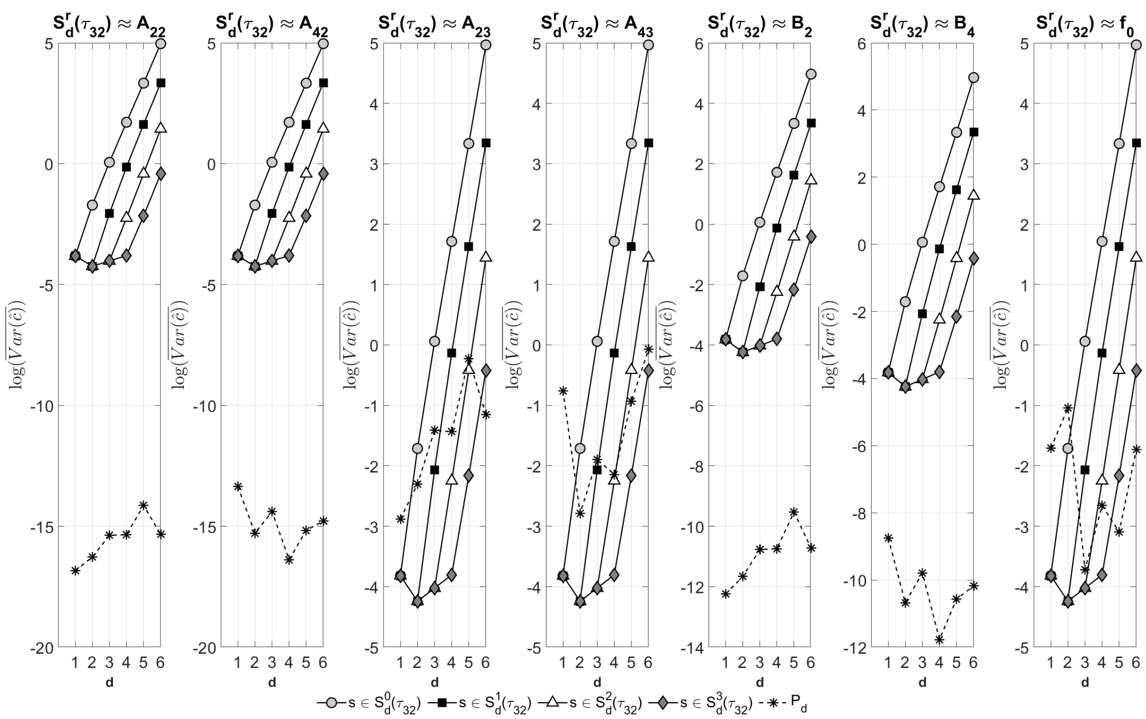

Figure 5.16: Logarithm of the mean of the Variance of the residuals for all estimated functions of the LPV model for different spline spaces with varying spline continuity and degree, over a triangulation of $\mathcal{T}_{32}$ simplices ($[4 \times 4]$ grid) compared to multivariate OLS polynomial of varying degree P_d.

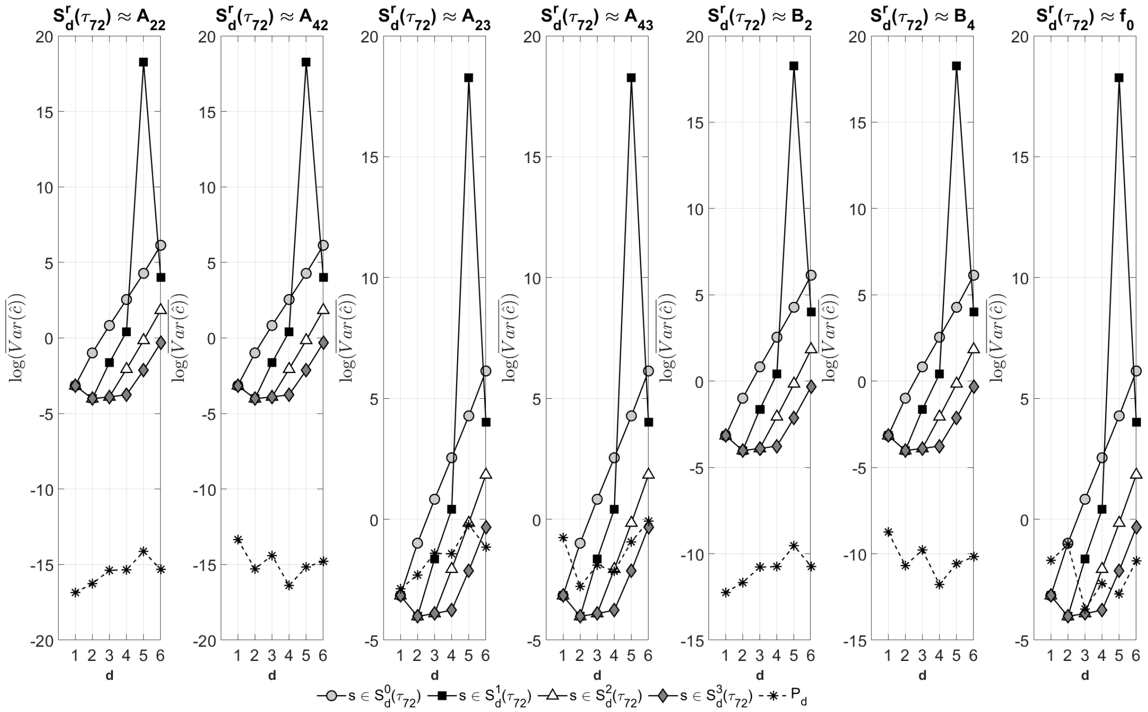

Figure 5.17: Logarithm of the mean of the Variance of the residuals for all estimated functions of the LPV model for different spline spaces with varying spline continuity and degree, over a triangulation of $\mathcal{T}_{72}$ simplices ($[6 \times 6]$ grid) compared to multivariate OLS polynomial of varying degree P_d.

5.5. Linear Quadratic Controller Application to B-Spline LPV Model

This section describes a basic application of an Linear Quadratic Regulator (LQR) controller to the B-spline LPV model defined that was done in order to see if the IPCM leads to a stabilized solution (pendulum remains upward), when starting with initial vector $X_0 = [0\ 0\ \frac{\pi}{4}\ 0]^\mathsf{T}$ and comparing to the non-linear model. LQR was chosen as unlike PID, which considers error between plant output and setpoint that can lead to instabilities as discussed for ZOH in Section 5.1, LQR focuses on minimizing state deviations and control effort based on a continuous state-space model, ensuring smoother and more stable control even in the presence of discontinuities. Since the non-linear system is represented by interpolating LTI models to form an LPV model, which is readily available, LQR presents a good choice as it assumes full access to the state vector and provides full state feedback. Additionally, in [64], attempt has been made to combine LQR and splines, which did result in steady-state errors in the dynamics of the model approximated.

The quadratic performance index over an infinite period of time, is calculated using Equation 5.3[69].

$$J_{lqr} = \int_0^{+\infty} \left(X(\tau)^T Q x(\tau) + u(\tau)^T R u(\tau) \right) d\tau \tag{5.3}$$

where $Q = Q^T \geq 0$ and $R = R^T > 0$ with $Q \in \mathbb{R}^{n_x \times n_x}$ and $R \in \mathbb{R}^{n_u \times n_u}$. By minimizing J, the optimal cost is found by:

$$J_{min} = \widetilde{X}_0^T P \widetilde{X}_0$$

where matrix P is the solution of the Algebraic Riccati Equation and $\widetilde{\mathbf{X}}_0$ is the position of the IPCM where the pendulum is inverted, meaning $\widetilde{\mathbf{X}}_0 = [0\ 0\ 0\ 0]^\mathsf{T}$ in Figure 4.1.

In order for the B-spline LPV model to give finite results, the simplex grid needs to be adjusted such that the motion of the pendulum is captured which will exceed the previous grid. This means that the data points are spread on a square grid $(\nu, \theta) \in \mathbb{R}^2$, $[\nu_{\text{min}}, \nu_{\text{max}}] \times [\theta_{\text{min}}, \theta_{\text{max}}] = [-2, 7] \times [-\pi, 2\pi]$. The LQR simulation with ZOH was first run to determine these grid maximum and minimum values, indicating the motion over the 40-second simulation period.

The closed loop dynamics of the B-spline model are approximated by Equation 5.4

$$\dot{\mathbf{X}} = \widetilde{\mathbf{f}}_0(\mathbf{X}_0, u_0) + \left(\begin{bmatrix} 0 & 1 & 0 & 0 \\ 0 & \widetilde{\mathbf{A}}_{22}(\rho_0) & \widetilde{\mathbf{A}}_{23}(\rho_0) & 0 \\ 0 & 0 & 0 & 1 \\ 0 & \widetilde{\mathbf{A}}_{42}(\rho_0) & \widetilde{\mathbf{A}}_{43}(\rho_0) & 0 \end{bmatrix} - K(\rho_0) \begin{bmatrix} 0 \\ \widetilde{\mathbf{B}}_2(\rho_0) \\ 0 \\ \widetilde{\mathbf{B}}_4(\rho_0) \end{bmatrix} \right) (\mathbf{X} - \widetilde{\mathbf{X}}_0) \tag{5.4}$$

where $K(\rho_0) = R^{-1}\widetilde{\mathbf{B}}(\rho_0))^T P$ is the optimal state feedback gain and is obtained by invoking the `lqr` MATLAB script. The state is then integrated using Runge-Kutta 4th order integration method. The LPV state space $\widetilde{\mathbf{A}}(\rho_0)$ and $\widetilde{\mathbf{B}}(\rho_0)$ are scheduled using the B-spline $s_2^4(x_{2601})$ belonging to the spline space $S_4^2(\mathcal{T}_{18})$.

To verify the effectiveness of the method, the weights R and Q are chosen as follows: Since the input u is scalar, $R = 1$, as initially suggested in [69]. The weight Q is selected by assigning non-zero values only to the states that need to be regulated (scheduled states $\zeta = [\nu\ \theta]$ of the LPV model), while the remaining states are assigned zero or a very small value. Since the scheduling states for the LPV model were cart velocity ν and pendulum angle θ the matrix $Q = diag(Q_{11}, Q_{22}, Q_{33}, Q_{44})$ results in $Q = diag(0.001, 100, 100, 0.001)$. Values of 100 are taken for the scheduled states to get a faster convergence to $\widetilde{\mathbf{X}}_0$. To obtain an optimal value of the weighting matrix Q a sweep of Q_{ii} is needed such that an analalysis of the performance of the closed loop system is examined. This analysis is in terms of settling time, overshoot/undershoot, control amplitude and rate, gain-phase-delay margins and other control parameters suggested in [69], which were not taken into account in this research.

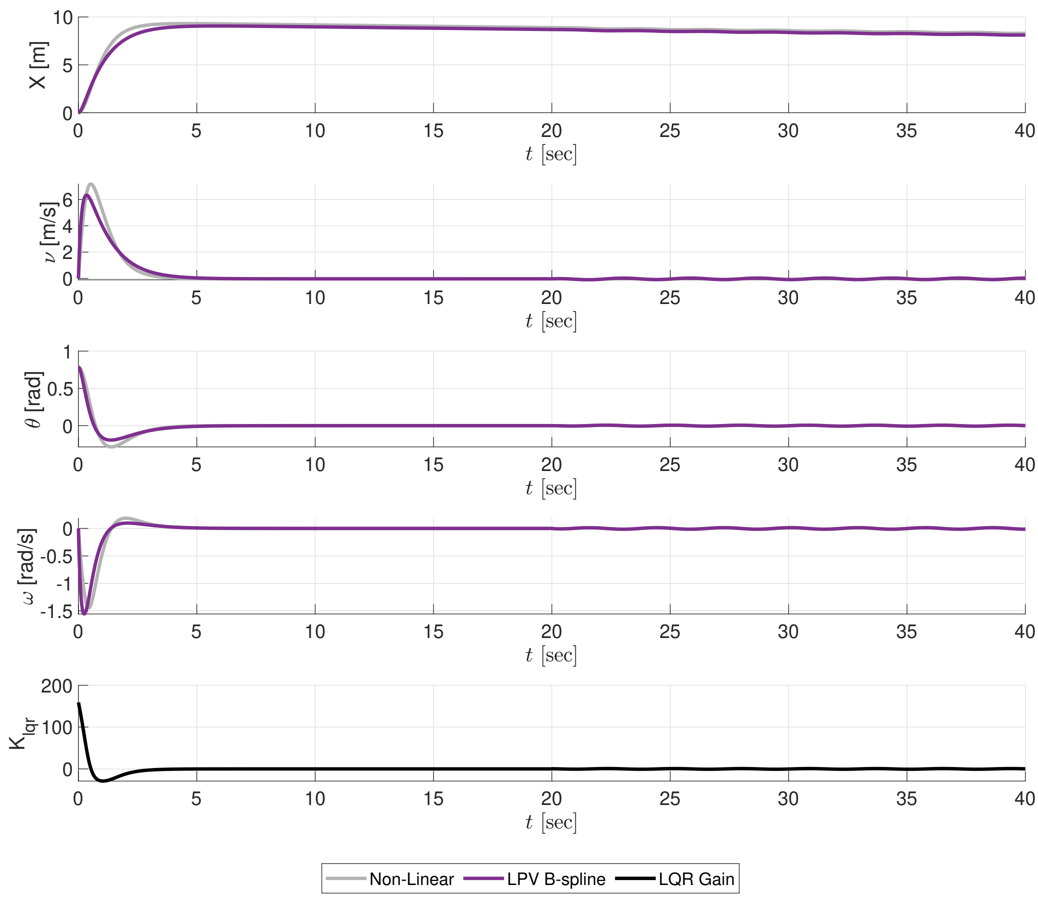

Figure 5.18: Simulation results comparing the LPV B-spline method with the nonlinear system implemented with an LQR controller. The state vector **X** of the IPCM is plotted over the simulation time $T_{sim} = 40$ seconds. A force is applied at $T_{sim}/2$ with an amplitude of $A_m = 1$, and the LQR gain is also plotted. The LPV B-spline is given by $s_2^4 \in S_4^2(\mathcal{T}_{18})$, which has a $[3 \times 3]$ grid of $(\nu, \theta) \in \mathbb{R}^2$ with $[\nu_{\min}, \nu_{\max}] \times [\theta_{\min}, \theta_{\max}] = [-2, 7] \times [-\pi, 2\pi]$.

Using the same settings of the simulation as in Section 4. Simulation Setup of Chapter 2.4, the results are shown in Figure 5.18. It can be seen that a very coarse estimation of the weighting matrix Q and R, the inverted pendulum has both scheduling parameters stabilized within ≈ 5 seconds, while the force applied at 20 seconds with $A_m = 1$ has no significant effect on the ability of IPCM to maintain the setpoint $\widetilde{\mathbf{X}}_0$.

Figure 5.19 shows the trajectory of the pendulum and how it spans over the scheduling parameter grid. The acceleration of the cart is plotted as it gives a better description of how the trajectory of IPCM is evolving. It can be seen that a force with amplitude $A_m = 1$ has no significant effect on scheduling parameter grid. Another notable effect is that the LPV model and the non-linear model do differ in terms of position of the IPCM over the entire simulation, which comes from the fact that position is not actively controlled.

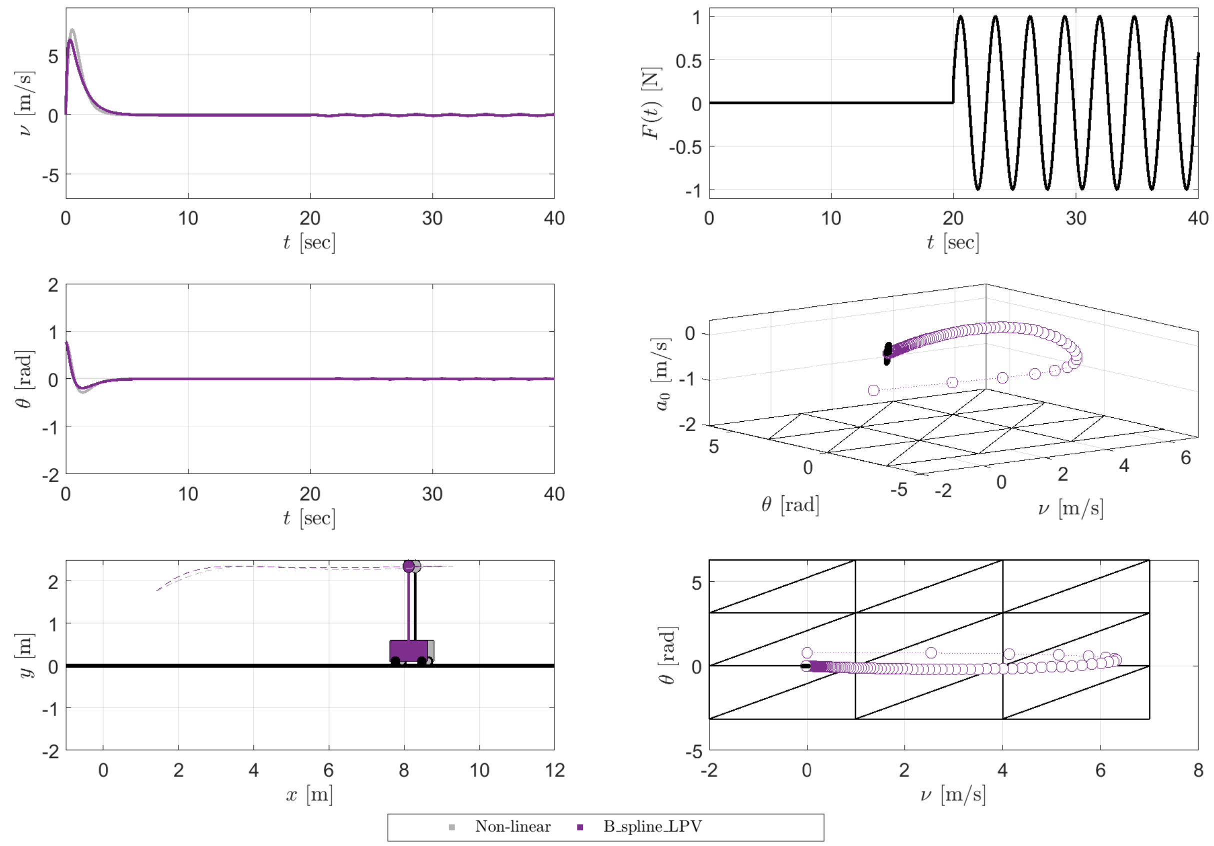

Figure 5.19: Simulation results comparing the LPV B-spline method with the nonlinear system implemented with an LQR controller. The two scheduling states (ν, θ) of the IPCM are plotted over the simulation time $T_{sim} = 40$ seconds, including a visualization of the IPCM and the path taken during the simulation. A force is applied at $T_{sim}/2$ with an amplitude of $A_m = 1$, which is also plotted. The grid of scheduling parameters is shown, with the full data points differentiated as unforced (pink) and forced (black). Additionally, the acceleration of the cart is plotted over the grid, creating a 3D trajectory. The LPV B-spline is given by $s_2^4 \in S_4^2(\mathcal{T}_{18})$, which has a $[3 \times 3]$ grid of $(\nu, \theta) \in \mathbb{R}^2$ with $[\nu_{\text{min}}, \nu_{\text{max}}] \times [\theta_{\text{min}}, \theta_{\text{max}}] = [-2, 7] \times [-\pi, 2\pi]$.

As a final result, to see the effect of the force on stability of the IPCM, the amplitude is changed to $A_m = 10$ and applied immediately to observe the effect and shown in Figure 5.20. Seemingly infinite energy oscillations, that do not subside over time, can be observed around the set point indicating that the controller becomes marginally stable over the simulation time, where the closed-loop poles seem to be on the imaginary axis. An explanation could be that the sinusoidal input of $A_m = 10$ excites an eigenmode of the system, which causes resonant oscillations (likely due to the natural frequency of the pendulum of $\omega_n = \sqrt{\frac{g}{L}}$)) that cannot be stabilized by the LQR controller.

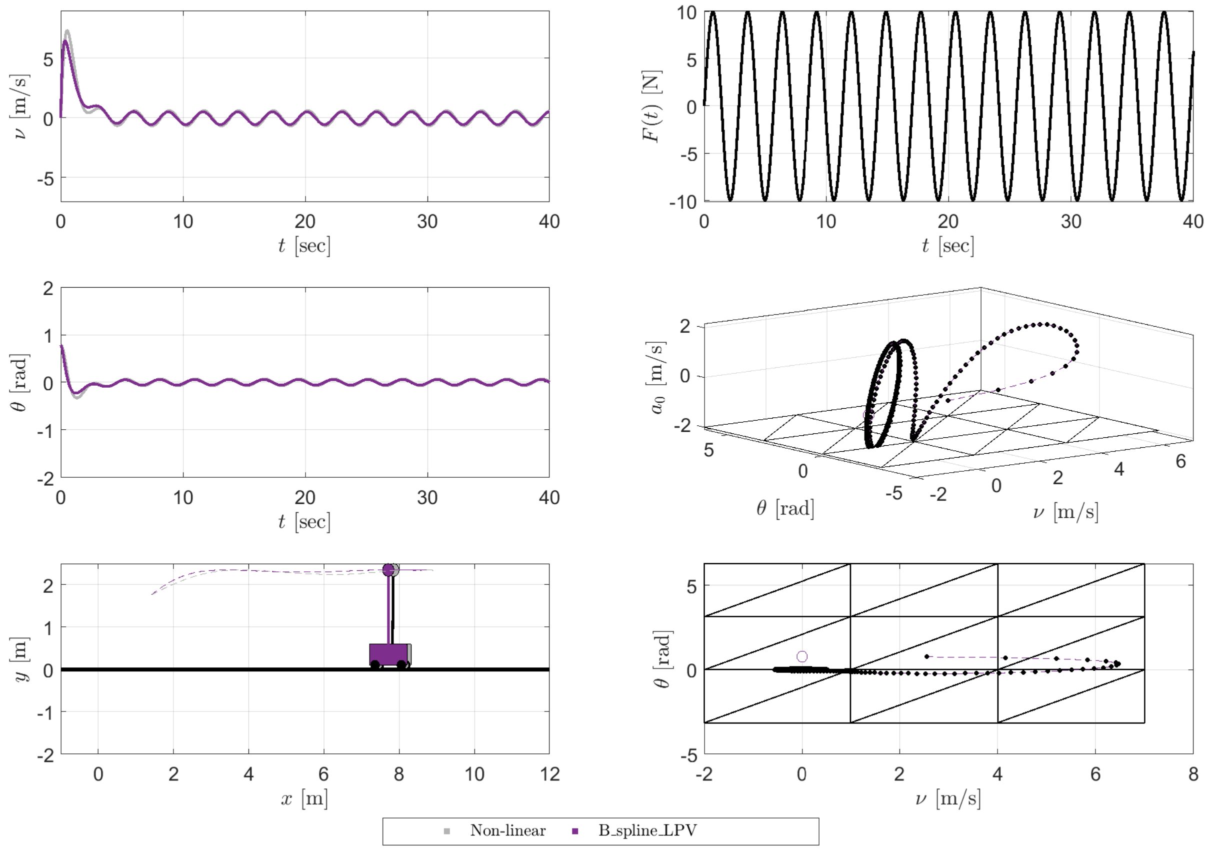

Figure 5.20: Simulation results comparing the LPV B-spline method with the nonlinear system implemented with an LQR controller. The two scheduling states (ν, θ) of the IPCM are plotted over the simulation time $T_{sim} = 40$ seconds, including a visualization of the IPCM and the path taken during the simulation. A force is applied immediately with an amplitude of $A_m = 10$, which is also plotted. The grid of scheduling parameters is shown, with the full data points differentiated as unforced (pink) and forced (black). Additionally, the acceleration of the cart is plotted over the grid, creating a 3D trajectory. The LPV B-spline is given by $s_2^4 \in S_4^2(\mathcal{T}_{18})$, which has a $[3 \times 3]$ grid of $(\nu, \theta) \in \mathbb{R}^2$ with $[\nu_{\text{min}}, \nu_{\text{max}}] \times [\theta_{\text{min}}, \theta_{\text{max}}] = [-2, 7] \times [-\pi, 2\pi]$.

Part IV

Closure

6 Conclusion

6.1. Closing Remarks

The following research has investigated the possibility of Multivariate simplex B-splines offering a viable basis for constructing scheduling functions that can globally approximate a specific type of Linear Parameter-Varying models, which are frequently used for analysis of nonlinear physical systems. The research objective has been defined as and repeated below for convenience.

Research Objective

How can a Linear Parameter Varying (LPV) control method combined with a multivariate simplex B-spline scheduling function address the gap in connecting robust control methods with the complex, non-affine dynamic models?

The results of the investigation demonstrate that multivariate simplex B-splines, deduced by their ability to offer a global approximation through the use of local basis functions across the entire scheduling parameter domain, are well-suited to provide a smooth scheduling function for affine quasi-Linear Parameter varying (qLPV) models. By constraining the range of scheduling variables or bounds of the parameter variations, robustness can be achieved, by making sure the scheduling function remains finite, single-valued and continuous (*well-behaved*) under different operating conditions.

Additionally, when compared to Ordinary Least Squares polynomial methods, such as multivariate OLS, multivariate B-splines, utilizing Constrained OLS estimation for the B-coefficient estimation, yield better estimations of the non-linear model differential equations. This is attributed to the piecewise nature of the polynomials, which are interconnected in such a way as to maintain the continuity of derivatives up to a specified order, determined by the polynomial degree, thereby offering more accurate solution. The results obtained include careful tuning of the spline and simulation parameters (e.g number of simplices, continuity order, number of datapoints, simulation time, input force), which do require optimization. The obtained model for a spline $s_2^4(x_{2601})$ belonging to the splne space $S_4^2(\mathcal{T}_{18})$ is done in this manner, where several criteria for optimum model have been analyzed such as: variance of B-coefficients ($Var(\hat{\mathbf{c}})$), logarithm of the mean variance of all B-coefficients within a single spline function ($\log(\overline{Var(\hat{\mathbf{c}})})$), logarithm of the relative $RMS_{rel}(\epsilon)$ of residuals, RMS of the difference between the non-linear model states and the estimated states and number of (free) unconstrained B-coefficients $\widetilde{\mathbf{c}}$. As discussed in [9], care must be taken when choosing the continuity order as each increase in the level of continuity, decreases the number of free B-coefficients available, which lowers the B-spline ability to fit a given function.

Applying the methodology to a Inverted-Pendulum on a Cart discrete model in open-loop, allows for a well-defined bounded set of scheduling parameters, namely cart velocity ν_0 and pendulum angle θ_0, which shows potential to approximate the entire motion and allows for a robust controller to be applied. One limitation that has emerged in the context of the non-linear model, which is linearized using an affine state-space qLPV (quasi-Linear Parameter-Varying) model, is the reliance on the piecewise constant Zero-Order-Hold (ZOH) method with a single scheduling parameter. While this approach demonstrates low root mean square (RMS) errors across a broad range of scheduling parameter data points, it suffers from a significant drawback. Specifically, piecewise constant methods introduce discontinuities at the points where the scheduling parameter switches from one value to another. These discontinuities can complicate the implementation of a robust controller, as they affect the system stability and performance near the transition points.

6.2. Research Questions

The research questions posed in Section 1.2 are repeated below for convenience.

Research Question 1

What form of LPV mathematical model is applicable to a non-affine dynamic model that can guarantee a certain level of robustness?

1.1 How can the LPV model be parameterized to obtain full state predictions of the dynamics of the non-affine model?

When modeling non-affine dynamic systems, the Jacobian linearized Linear Parameter-Varying (LPV) model offers a mathematical description by utilizing first-order differentiation which is a computationally efficient approach. This efficiency arises from its affine representation, which depends on a limited number of scheduling parameters, simplifying nonlinear dynamics into a series of linear problems reducing the computational complexity. This type of modeling is particularly advantageous for systems characterized by nonlinearities that evolve as a function of operating conditions by local first-order linearization of the nonlinear system dynamics around an operating point (Off-Equilibrium Linearization) that varies with system parameters, creating a quasi-LPV model. To obtain full state predictions, at each point of the scheduling parameter, LTI models have been derived where the affine terms have been contained into $\mathbf{f}_0$ as described by Equation 3a from 2.2. Simulation results in Figure 9 have shown that this approach allows for a full state-space description of the dynamic states of the model.

1.2 What model LPV structure can be used to enable the application of multivariate splines?

The combination of multivariate splines with affine Jacobian linearized quasi-LPV (qLPV) models offers a powerful approach for modeling nonlinear systems, particularly when the system's behavior depends on scheduling parameters that change smoothly across operating conditions and are already contained in the system's internal states. While the Jacobian linearized qLPV model captures local dynamics accurately by providing a state-space description around a specific operating point, multivariate B-splines approximate the global domain through a global sparse regression matrix $B \in \mathbb{R}^{J \cdot \hat{d} \times 1}$ of scheduling parameters, while also having the property of being linear in the parameters. This approach significantly reduces the computational complexity of parameter estimation, as models that are linear in the parameters require less computational effort compared to nonlinear parameter estimators.

1.3 What validation methods should be employed to ensure that the identified LPV model meet requirements?

Model quality analysis has been performed using several key B-spline metrics such as the logarithm of the relative $RMS(\epsilon)$ of the residuals and logarithm of the mean variance of all B-coefficients $\hat{\mathbf{c}}$, $Var(\bar{\hat{\mathbf{c}}})$. The first metric gives a measure of how well the spline model's predicted values match the estimated qLPV model values. The second shows the uncertainty governed by the basis structures, by computing the the variance of B-splines which is global and independent of the estimated function values. The variance surfaces (Figure 5 of Section 2.5) of the B coefficients serve as means to identify specific regions of the model where local estimator failures occur such as insufficient local data coverage or conditioning, or the presence of incorrect model structures.

Results show that for a $[3 \times 3]$ grid of $\mathcal{T}_{18}$ triangulation, as seen in Figures 5.10 - 5.13, $log(RMS(\epsilon))$ starts showing a significant difference in approximation power compared to polynomial OLS. In terms of low mean variance $\log{(Var(\bar{\hat{\mathbf{c}}}))}$, the selected continuity C^2 shows B-coefficients that are well-conditioned and only show increased value at the edges of the scheduling parameter domain, as seen by Figure 5 of Section 2.5.

Research Question 2

How does the application of multivariate splines enhance the accuracy of the LPV model in predicting the performance of a non-affine system across varying operating regimes?

2.1 How do multivariate splines compare to polynomial methods in terms of root mean square error (RMSE) in parameter estimation?

As observed by the RMSE of the results obtained in Table 4 of Section 2.5, the multivariate simplex B-spline $s_2^4(x_{2601}) \in S_4^2(\mathcal{T}_{18})$ outperforms the polynomial OLS estimators. Furthermore looking at Figures 5.10 - 5.13, at changing spline spaces with continuity degree and number of simplices, it can be seen that for degree higher than $d =$, continuity greater than C^1 and triangulations of more than $\mathcal{T}_8$ for a grid larger than $[2 \times 2]$, the relative $RMS(\epsilon)$ shows that B-spline estimate LPV model far better estimation capability than polynomial OLS of the qLPV functions.

2.2 What is the impact of parameter variability over the entire operating range on the accuracy of spline-based LPV models?

A variation of initial conditions is performed, in order to see the spread of the two scheduling parameters, cart velocity ν and pendulum angle θ on the simplex grid $\mathcal{T}_{18}$. The initial pendulum angle θ_0 has been varied by adding noise following a standard Gaussian distribution ($\mu = 0, \sigma = 1$). It was determined that the pendulum remains within confined bounds of the scheduling parameter grid, even when larger pendulum swings result from the application of the input force. As the parameter space is bounded in the triangulation (see Figure 11 of Section 2.5), the multivariate simplex B-spline $s_2^4(x_{2601}) \in S_4^2(\mathcal{T}_{18})$, can still accurately estimate the qLPV model.

7 Recommendations

This chapter provides a brief overview of the primary recommendations for the future continuation of this research project.

Rec 1
Figure 3.1 from the Literature review has indicated the application of multivariate splines to a highly non-affine aerodynamic model of the ICE aircraft has not yet been performed. Given that simplex B-splines are scalable to any number of dimensions, they offer significant potential for modeling complex, high-dimensional aerodynamic systems, this is the next step that needs to be performed. A selection of scheduling parameters needs to be taken into account, due to the fact that in the literature of the ICE, it has been shown, that parameters like Mach number, altitude or pitch angle offer good choice for scheduling, as the ICE equations of motion can be linearized at a fixed value of these parameters across the flight envelope. A brief methodology of how to achieve this is shown next.

Section 4.3 already describes the EOM's including all the aerodynamic coefficients differentiated per contribution of the control effectors. At the set of trim points, these equations can be linearized and several assumptions can be made. The perturbations from the trim state are assumed to be small, such that the aircraft is in steady-state flight, with forces and moments balanced at the trim condition. Aerodynamic coefficients are considered linear with respect to small changes in flight variables, and higher-order nonlinear effects are neglected. Additionally, the system is assumed to be statically stable, with weak coupling between longitudinal and lateral-directional motions, and the environmental conditions are constant. Care must be taken with the control surface deflections, which constitute a vector of 13 axis-coupled control inputs $\mathbf{u} \in \mathbb{R}^{13}$ as shown in Equation 4.2c. By linearizing the system, control surface deflections and their rates can be assumed to vary linearly with control inputs and simplifications with the control allocation scheme as shown in [63] and [52] can be made. It enables using a linear control allocation, in order to obtain a valid LPV model. Time-varying inputs can be neglected. As shown in [63], replacing the physical control surface deflections u_i with a generalized control or moment command vector δ^* is a smart way to be able to approximate the non-linear dynamics.

The next step would be to apply multivariate simplex B-splines to the linearized aircraft model by first discretizing the input space into a simplex grid, ensuring that the variables are bounded while the control inputs remain within the limits of the linearization, preserving its validity even in the presence of small perturbations. One way of doing this is by using a control selector matrix that will transform the generalized control or moment command vector $\delta^* = [q_{cmd} \;\; p_{cmd} \;\; r_{cmd}]^T$, into the surface deflections by $u = B^+ B^* \delta^*$, where u is shown in Equation 4.2c. Once the scheduling map is created, the piecewise polynomial functions can be used to interpolate between each trim point, creating the model. If the dimensionless moment coefficient C_l from Equation 4.19a in affine form is taken as example, the approximation of the Linear Control Allocation of ICE can be represented as:

$$C_l(\alpha, \beta, p, r, \delta_i) \approx p(b(\alpha, \beta, p, r, \delta_i))$$

with $b(\alpha, \beta, p, r, \delta_i)$ being the barycentric coordinates system of the B-spline, while $C_l(\alpha, \beta, p, r, \delta_i)$ is a function of the physical counterparts. The barycentric coordinate transformation is the given by:

$$b(\alpha, \beta, p, r, \delta_i) = A_t \begin{bmatrix} \alpha & \beta & p & r & \delta_i \end{bmatrix}^T + k$$

where A_t and k are dependent on the selected simplex geometries, as shown in [60]. As researched in [70], a transformation matrix Λ can be derived such that a translation between physical coefficients and B-coefficients can be performed, due to Λ being invertible. Writing the resulting spline function in physical coefficients can be done with Equation 7.1[60].

$$p(x) = B^d(b(x)) \cdot \Lambda^{-1} \cdot \hat{c}_p \tag{7.1}$$

where $\hat{c}_p$ are the physical coefficients projected to P-coefficient space with $\Gamma_p = \text{null}(H \cdot \Lambda^{-1})$. With this relation polynomial model structures for the aerodynamic forces and moments can be related to multivariate spline polynomials in barycentric coordinates.

The main concerns with this approach would include the risk of oversimplification when approximating highly nonlinear behaviors, leading to inaccuracies in the model for large perturbations, extreme flight conditions or errors if the grid resolution is insufficient. Additionally, the Linear Control Allocation strategy is computationally efficient but may lead to substantial allocation errors in the nonlinear regions of the flight envelope, as noted in [70].

Rec 2

A subsequent step in this research direction should focus on applying the proposed scheduling function within a closed-loop LPV framework (e.g., Gain-scheduled Proportional-Integral-Derivative (PID), Linear Quadratic Regulator (LQR) or even Model Predictive Control (MPC) controllers), with a primary area of investigation being the evaluation of control stability and performance under varying operational conditions. In Section 5.5, LQR controller has been applied to the demonstrator where it can be seen that a single LQR controller can keep the pendulum inverted of the IPCM. It turned out that the main difficulty with controlling the LPV model is estimating the affine term of the function $\widetilde{\mathbf{f}}_0$, where in the case analyzed was not done, as it would cause instability and divergence of the controller. The LPV estimation of the state-space $A(\rho)$ and input space matrices $B(\rho)$, on the other hand, do yield a LQR controller that can bring the angle and velocity to the required setpoint. Eventhough they can be brought to the required setpoint, the LQR controller shown is not an optimal controller and further performance analysis of the closed loop system in terms of settling time, over/undershoot, control amplitude, rate, gain-phase-delay margins needs to be done. This can be performed by sweeping the weight matrices Q and R between a particular range that would balance performance and robustness, as explained in [69]. Higher diagonal values of Q would increase performance, while higher diagonal values of R would make the controller more robust.

As analyzed in [64], when applying LPV models to highly non-linear flight control systems, gain scheduled LQR controllers have shown to be needed as the control area did not consist of a sequence of equilibrium points across the analyzed flight envelope. Therefore, this approach requires scheduling parameters each possessing a separate controller. As described in this work, due to significant changes in aerodynamic parameters, the resulting shifts in aircraft dynamics can cause a flight mode that is stable and well-damped in one condition to become unstable or insufficiently damped in another [64]. This is also expected if such controller is implemented for ICE, as the control inputs are coupled, which means that any small deflection would lead to rapid changes in the dynamics and closed-loop performance. Thus a future improvement would require for the design of a optimal gain-scheduled controller that can cope with varying changes of dynamics over the entire operating envelope.

Rec 3

In this experiment, a grid was employed as the scheduling parameter domain, which did not appear to fully utilize all of the simplices, as seen from the highest error in the residuals. To improve on this, it would be beneficial to optimize the simplices using Constrained Delaunay Triangulation (CDT) or Type I/II hypercube triangulation method. If looking at Section 5.5, specifically Figure 5.20, for the LQR implementation, it can be seen that when a controller is implemented, the variation of the velocity component is much grater compared to the pendulum angle, thus necessitating an adjustment in grid size. For the bi-variate parameter case, a Constrained Delaunay Triangulation that refines adaptively using curvature-based error estimation, where control points are placed in regions of high curvature while keeping a coarser representation in flatter regions can be used. If higher-dimensional scalability is required, Type I/II hypercube triangulation method should be better as it decomposes an n-dimensional hypercube into simplices that can be structurally connected in multiple dimensions. Using either of these techniques, will allow for grid refinement that can improve the LPV B-spline estimation by minimizing the residual error.

References

[1] Michael G. Safonov. “Origins of robust control: Early history and future speculations”. In: *Annual Reviews in Control* 36.2 (2012), pp. 173–181. DOI: 10.1016/j.arcontrol.2012.09.001.

[2] Christian Weiser et al. “Design and flight test of a linear parameter varying flight controller”. In: *CEAS Aeronautical Journal* 11 (Aug. 2020). DOI: 10.1007/s13272-020-00461-y.

[3] Lennart Ljung. “Estimating Linear Time-Invariant models of nonlinear time-varying systems”. In: *European Journal of Control* 7.2-3 (2001), pp. 203–219. DOI: 10.3166/ejc.7.203-219.

[4] R. Tóth et al. “Identification of nonlinear process models in an LPV framework”. In: *IFAC Proceedings Volumes* 43.5 (2010). 9th IFAC Symposium on Dynamics and Control of Process Systems, pp. 877–882. DOI: 10.3182/20100705-3-BE-2011.00145.

[5] Tom Antonius Henricus Bloemers. “Data-Driven Linear Parameter-Varying Control: A Frequency-Domain Approach”. English. Proefschrift. Phd Thesis 1 (Research TU/e / Graduation TU/e). Electrical Engineering, Mar. 2023.

[6] Andrés Marcos et al. “Development of Linear-Parameter-Varying Models for Aircraft”. In: *Journal of Guidance, Control, and Dynamics* 27.2 (2004), pp. 218–228. DOI: 10.2514/1.9165.

[7] Simon Hecker. “Generating structured LPV-models with maximized validity region”. In: *IFAC Proceedings Volumes* 47.3 (2014). 19th IFAC World Congress, pp. 6901–6906. DOI: 10.3182/20140824-6-ZA-1003.02461.

[8] Dora Turk et al. “Identification of Linear Parameter-Varying Systems Using B-splines”. In: *2019 18th European Control Conference (ECC)* (2019), pp. 3316–3321. DOI: 10.23919/ECC.2019.8795917.

[9] Coen C. de Visser. “Global Nonlinear Model Identification with Multivariate Splines”. Available at https://resolver.tudelft.nl/uuid:6bc0134a-0715-4829-903d-6479c5735913. PhD thesis. Control & Operations (Aerospace Engineering) (TU Delft), 2011.

[10] LI Wen-qiang et al. “Robust Controller Design to Uncertain Nonlinear Tailless Aircraft”. In: *IFAC Proceedings Volumes* 41.2 (2008). 17th IFAC World Congress, pp. 5980–5985. DOI: 10.3182/20080706-5-KR-1001.01009.

[11] Ismael Matamoros. “Nonlinear Control Allocation for a High-Performance Tailless Aircraft with Innovative Control Effectors”. MA thesis. Delft University of Technology, 2017.

[12] I.V.van der Peijl. “Physical Splines for Aerodynamic Modelling of Innovative Control Effectors”. MA thesis. Delft University of Technology, 2017.

[13] Mark van den Aarssen. “Distributed Approach for Aerodynamic Model Identification of the ICE Aircraft”. MA thesis. Delft University of Technology, 2018.

[14] B. Hooij. “Online Distributed Approach for Aerodynamic Model Identification of the ICE Aircraft”. MA thesis. Delft University of Technology, 2020.

[15] M.J Lai et al. *Spline Functions on Triangulations*. Cambridge University Press, May 2010. DOI: https://doi.org/10.1017/CBO9780511721588.

[16] Michael Safonov. “Recent advances in robust control, feedback and learning”. In: *AIAA Guidance, Navigation, and Control Conference and Exhibit* (Aug. 2003). DOI: 10.2514/6.2003-5831.

[17] K. Zhou et al. *Robust and Optimal Control*. Feher/Prentice Hall Digital and. Prentice Hall, 1996.

[18] Roland Toth. *Modeling and identification of Linear Parameter-Varying systems*. Germany: Springer, 2010. DOI: 10.1007/978-3-642-13812-6.

[19] Peter Gaspar Olivier Sename et al. “Robust Control and Linear Parameter Varying approaches: Application to Vehicle Dynamics”. In: Springer Berlin, Heidelberg, Jan. 2013. DOI: 10.1007/978-3-642-36110-4.

[20] Hussam Atoui et al. “Toward switching/interpolating LPV control: A review”. In: *Annual Reviews in Control* 54 (Aug. 2022). DOI: 10.1016/j.arcontrol.2022.07.002.

[21] Corentin Briat. *Linear Parameter-Varying and Time-Delay Systems. Analysis, Observation, Filtering & Control*. Springer, Jan. 2015.

[22] Gijs Hilhorst et al. “Control of linear parameter-varying systems using B-splines”. In: *2016 IEEE 55th Conference on Decision and Control (CDC)*. 2016, pp. 3246–3251. DOI: 10.1109/CDC.2016.7798757.

[23] P. den Boef et al. “On Behavioral Interpolation in Local LPV System Identification”. In: *IFAC-PapersOnLine* 52.28 (2019). 3rd IFAC Workshop on Linear Parameter Varying Systems LPVS 2019, pp. 20–25. DOI: 10.1016/j.ifacol.2019.12.341.

[24] Ian R. Petersen et al. “Robust control of uncertain systems: Classical results and recent developments”. In: *Automatica* 50.5 (2014), pp. 1315–1335. DOI: 10.1016/j.automatica.2014.02.042.

[25] Randy A. Freeman et al. *Robust Nonlinear Control Design*. Boston, MA: Birkhäuser Boston, 1996. DOI: 10.1007/978-0-8176-4759-9.

[26] Lennart Ljung. *System Identification: Theory for the User*. 2nd ed. Upper Saddle River, NJ 07458: Prentice Hall PTR, 1997.

[27] Rik Pintelon et al. *System Identification: A Frequency Domain Approach*. 2nd ed. John Wiley & Sons, Inc., Hoboken, New Jersey, 2001.

[28] Damien Guého et al. “Advances in System Identification: Theory and Applications”. In: *2021 60th IEEE Conference on Decision and Control (CDC)*. 2021, pp. 22–30. DOI: 10.1109/CDC45484.2021.9683394.

[29] Vladislav Klein. “Estimation of aircraft aerodynamic parameters from flight data”. In: *Progress in Aerospace Sciences* 26.1 (1989), pp. 1–77. DOI: 10.1016/0376-0421(89)90002-X.

[30] H. J. Tol et al. “Nonlinear Multivariate Spline-Based Control Allocation for High-Performance Aircraft”. In: *Journal of Guidance, Control, and Dynamics* 37.6 (2014), pp. 1840–1862. DOI: 10.2514/1.G000065.

[31] Coen C. de Visser et al. “A new approach to linear regression with multivariate splines”. In: *Automatica* 45.12 (2009), pp. 2903–2909. DOI: 10.1016/j.automatica.2009.09.017.

[32] Carl de Boor. “B-form basics. In:G. Farin, ed., Geometric modeling: Algorithms and new trends”. In: *Society For Industrial and Applied Mathematics* (Jan. 1987), pp. 131–148.

[33] Tim Visser et al. “Quadrotor System Identification Using the Multivariate Multiplex B-Spline”. In: AIAA Atmospheric Flight Mechanics Conference, 2015. DOI: 10.2514/6.2015-0747.

[34] HJ Tol et al. “Multivariate spline-based adaptive control of high-performance aircraft with aerodynamic uncertainties”. In: *Journal of Guidance, Control, and Dynamics: devoted to the technology of dynamics and control* 39.4 (2016), pp. 781–800. DOI: 10.2514/1.G001079.

[35] K. M. Dorsett et al. *Innovative Control Effectors (ICE)*. Tech. rep. ADB212813. Wright Laboratories, Wright-Patterson AFB, OH, 1996.

[36] K. M. Dorsett et al. *Innovative Control Effectors (ICE), phase 2*. Tech. rep. ADB232172. Wright Laboratories, Wright-Patterson AFB, OH, 1997.

[37] Michael A. Niestroy et al. “A Tailless Fighter Aircraft Model for Control-Related Research and Development”. In: *AIAA Modeling and Simulation Technologies Conference* (2016). DOI: 10.2514/6.2017-1757.

[38] Cameron James Segard. “Control Law Synthesis for Lockheed Martin’s Innovative Control Effectors Aircraft Concept”. MA thesis. Western Michigan University, 2019. URL: https://scholarworks.wmich.edu/masters_theses/4300.

[39] Christian Hoffmann et al. “A Survey of Linear Parameter-Varying Control Applications Validated by Experiments or High-Fidelity Simulations”. In: *IEEE Transactions on Control Systems Technology* 23.2 (2015), pp. 416–433. DOI: 10.1109/TCST.2014.2327584.

[40] Jean-Marc Biannic. “Linear Parameter-Varying Control Strategies for Aerospace Applications”. In: *Robust Control and Linear Parameter Varying Approaches: Application to Vehicle Dynamics*. Berlin, Heidelberg, 2013, pp. 347–373. DOI: 10.1007/978-3-642-36110-4_14.

[41] G. Papageorgiou et al. “Taking robust LPV control into flight on the VAAC Harrier”. In: *Proceedings of the 39th IEEE Conference on Decision and Control (Cat. No.00CH37187)*. Vol. 5. 2000, 4558–4564 vol.5. DOI: 10.1109/CDC.2001.914633.

[42] Hassène Gritli et al. “LMI-based synthesis of a robust saturated controller for an underactuated mechanical system subject to motion constraints”. In: *European Journal of Control* 57 (2021), pp. 179–193. DOI: 10.1016/j.ejcon.2020.04.004.

[43] Steven Snyder et al. “Adaptive control for Linear Parameter-Varying systems with application to a VTOL aircraft”. In: *Aerospace Science and Technology* 112 (2021), p. 106621. DOI: 10.1016/j.ast.2021.106621.

[44] J. Mohammadpour et al. *Control of Linear Parameter Varying Systems with Applications*. SpringerLink : Bücher. Springer New York, 2012.

[45] Bassam Bamieh et al. “Identification of linear parameter varying models”. In: *International Journal of Robust and Nonlinear Control* 12.9 (2002), pp. 841–853. DOI: https://doi.org/10.1002/rnc.706.

[46] S. F. Armanini et al. “Global Linear Parameter-Varying Modeling of Flapping-Wing Dynamics Using Flight Data”. In: *Journal of Guidance, Control, and Dynamics* 41.11 (2018), pp. 2338–2360. DOI: 10.2514/1.G003505.

[47] Chris Verhoek et al. “Deep-Learning-Based Identification of LPV Models for Nonlinear Systems”. English. In: *61st IEEE Conference on Decision and Control*. 61st IEEE Conference on Decision and Control, CDC 2022, CDC 2022 ; Conference date: 06-12-2022 Through 09-12-2022. United States: Institute of Electrical and Electronics Engineers, 2023, pp. 3274–3280. DOI: 10.1109/CDC51059.2022.9992609.

[48] Roland Toth et al. “On the Discretization of Linear Fractional Representations of LPV Systems”. In: *IEEE Transactions on Control Systems Technology* 20.6 (2012), pp. 1473–1489. DOI: 10.1109/TCST.2011.2164921.

[49] Qinghua Zhang. “LPV System Local Model Interpolation Based on Combined Model Reduction”. In: *IFAC-PapersOnLine* 51.15 (2018). 18th IFAC Symposium on System Identification SYSID 2018, pp. 1104–1109. DOI: 10.1016/j.ifacol.2018.09.046.

[50] Jong-Yeob Shin et al. “Quasi-Linear Parameter Varying Representation over Non-trim Region”. In: *AIAA Guidance, Navigation, and Control Conference and Exhibit* (2004). DOI: 10.2514/6.2004-5423.

[51] Andres Marcos et al. “Application of LPV/LFT Modeling and Data-Based Validation to a Re-Entry Vehicle”. In: *AIAA Guidance, Navigation, and Control Conference* (2009). DOI: 10.2514/6.2009-5634.

[52] Jeffrey Barker et al. “Flight control of a tailless aircraft via linear parameter-varying techniques”. In: *Guidance, Navigation, and Control Conference and Exhibit*. American Institute of Aeronautics and Astronautics Inc. (AIAA), 1999. DOI: 10.2514/6.1999-4133.

[53] James Buffington et al. “Synthesis and analysis of dynamic inversion and LPV tailless flight control law designs”. In: *Guidance, Navigation, and Control Conference and Exhibit* (1998). DOI: 10.2514/6.1998-4248.

[54] A.G.Sparks. “A gain-scheduled H_∞ control law for a tailless aircraft”. In: *Proceedings of the 1998 IEEE International Conference on Control Applications* (1970). DOI: 10.1109/cca.1998.728594.

[55] Sudchai Boonto et al. “Closed-loop identification of LPV models using cubic splines with application to an arm-driven inverted pendulum”. In: *Proceedings of the 2010 American Control Conference, ACC 2010* (2010), pp. 3100–3105. DOI: 10.1109/acc.2010.5531139.

[56] Jan De Caigny et al. “Polynomial spline input design for LPV motion systems”. In: *International Workshop on Advanced Motion Control, AMC* 1 (2008), pp. 86–91. DOI: 10.1109/AMC.2008.4516046.

[57] Rob Stolk. “Minimum drag control allocation for the Innovative Control Effector aircraft”. MA thesis. Delft University of Technology, 2018.

[58] Spilios Theodoulis. *AE4351 Robust Flight Control: 0.0-Course Intro*. https://brightspace.tudelft.nl/d2l/le/content/498827/viewContent/3140645/View, last accessed on 07.05.2024. TU Delft Aerospace Engineering. 2023.

[59] Coen C. de Visser. *AE4320 System Identification of Aerospace Vehicles: Lecture 7,8: Parameter Estimation*. https://brightspace.tudelft.nl/d2l/le/content/398004/viewContent/2275186/View, last accessed on 02.07.2024. TU Delft Aerospace Engineering. 2022.

[60] Coen C. de Visser. *AE4320 System Identification of Aerospace Vehicles: Lecture 10,11: Introduction to Multivariate Splines*. https://brightspace.tudelft.nl/d2l/le/content/398004/viewContent/2275187/View, last accessed on 11.08.2024. TU Delft Aerospace Engineering. 2021.

[61] Zhimin Zhang et al. “Convergence and Gibbs’ phenomenon in cubic spline interpolation of discontinuous functions”. In: *Journal of Computational and Applied Mathematics* 87.2 (1997), pp. 359–371. DOI: 10.1016/S0377-0427(97)00199-4.

[62] Coen C. de Visser. *AE4311 - Nonlinear and Adaptive Flight Control Lecture 9: Control Allocation, Part 2*. https://brightspace.tudelft.nl/d2l/le/content/397986/viewContent/2331531/View, last accessed on 20.09.2024. TU Delft Aerospace Engineering. 2021.

[63] James Buffington et al. “Synthesis and analysis of dynamic inversion and LPV tailless flight control law designs”. In: *Guidance, Navigation, and Control Conference and Exhibit*. Aug. 1998. DOI: 10.2514/6.1998-4248.

[64] N.G.M. Rademakers et al. “Modelling and gain scheduled control of a tailless fighter”. In: *2004 5th Asian Control Conference* 1 (Aug. 2004), 374–382 Vol.1. DOI: 10.1109/ASCC.2004.184792.

[65] Javier Aracil et al. “The inverted pendulum: A benchmark in nonlinear control”. In: Jan. 2004, pp. 468–482. DOI: 10.1109/WAC.2004.185364.

[66] John Deyst et al. *Lecture 10: Friction in Lagrange’s Formulation*. https://ocw.mit.edu/courses/16-61-aerospace-dynamics-spring-2003/resources/lecture10/, last accessed on 07.05.2024. Massachusetts Institute of Technology. 2003.

[67] Seif-El-Islam Hasseni et al. “Robust LPV control applied to a personal pendulum vehicle”. In: *2017 18th International Conference on Sciences and Techniques of Automatic Control and Computer Engineering (STA)*. 2017, pp. 6–11. DOI: 10.1109/STA.2017.8314871.

[68] Coen C. de Visser. *AE4320 System Identification of Aerospace Vehicles: Lecture 7,8: Parameter Estimation*. https://brightspace.tudelft.nl/d2l/le/content/398004/viewContent/2275186/View, last accessed on 11.08.2024. TU Delft Aerospace Engineering. 2021.

[69] Spilios Theodoulis. *AE4351 Robust Flight Control: 3.2-Linear Quadratic Regulator (LQR)*. https://brightspace.tudelft.nl/d2l/le/content/498827/viewContent/3156385/View, last accessed on 15.02.2024. TU Delft Aerospace Engineering. 2023.

[70] H. J. Tol et al. “Nonlinear Multivariate Spline-Based Control Allocation for High-Performance Aircraft”. In: *Journal of Guidance, Control, and Dynamics* 37.6 (2014), pp. 1840–1862. DOI: 10.2514/1.G000065.